Nanoparticle-based routes to functional microstructures

Mayes, Eric Leigh

Award date:
2001

Awarding institution:
University of Bath

NANOPARTICLE-BASED ROUTES TO FUNCTIONAL MICROSTRUCTURES

submitted by **ERIC LEIGH MAYES**

for the degree of Ph.D.

of the University of Bath

2001

ProQuest LLC
789 East Eisenhower Parkway
P.O. Box 1346
Ann Arbor, MI 48106-1346

ABSTRACT

The production of nanoparticle-based microstructures was studied using three distinct fabrication methodologies – surface conjugation, infiltration and incorporation.

Nanoparticulate magnetite (Fe_3O_4), gold, cadmium sulphide (CdS), and silica (SiO_2) were prepared and used for the dip coating of spider dragline silk. The resulting coated composite fibres were measured by stress/strain analysis, which showed that the mechanical properties of the hybrid materials were nearly identical to native silk. Scanning electron microscopy and energy dispersive x-ray analysis were used to evaluate continuity and penetration of the coatings, which were shown to be continuous and restricted to the near surface regions of the silk microstructure.

Nanoparticulate magnetite was infiltrated by a reverse swelling method into a bacterial thread microstructure (bionite) produced by slow withdrawal of multicellular fibres from a web culture. Electron microscopy confirmed complete infiltration of the microstructure, and magnetic studies using a superconducting magnetometer confirmed that the composite was a superparamagnet at room temperature. Anisotropic magnetic behaviour was shown in field orientation measurements, due to strain-induced anisotropy produced during the preparation of the thread composite.

Organo-magnesium silicate clays, magnetite and iron-containing protein (ferritin) nanoparticles were incorporated into cement blends. The blends were formed in moulds prepared by a lithographic process, and analysed for porosity, smoothness

and mould fidelity. Scanning electron microscopy and energy dispersive x-ray analysis were used to evaluate the continuity of the dispersants. In the case of magnetite and ferritin, homogenous dispersions were confirmed, and in all cases high fidelity replication of the moulds was achieved.

A novel nanoparticle synthesis involving the polymerisation of pyrrole subunits in the presence of the iron oxide core of ferritin was attempted. UV/Visible spectroscopy showed the onset and growth of pyrrole polymerisation. Transmission electron microscopy suggested nanoparticles of polypyrrole were not formed within the protein cavity, but that flakes of polypyrrole entrapped empty protein shells.

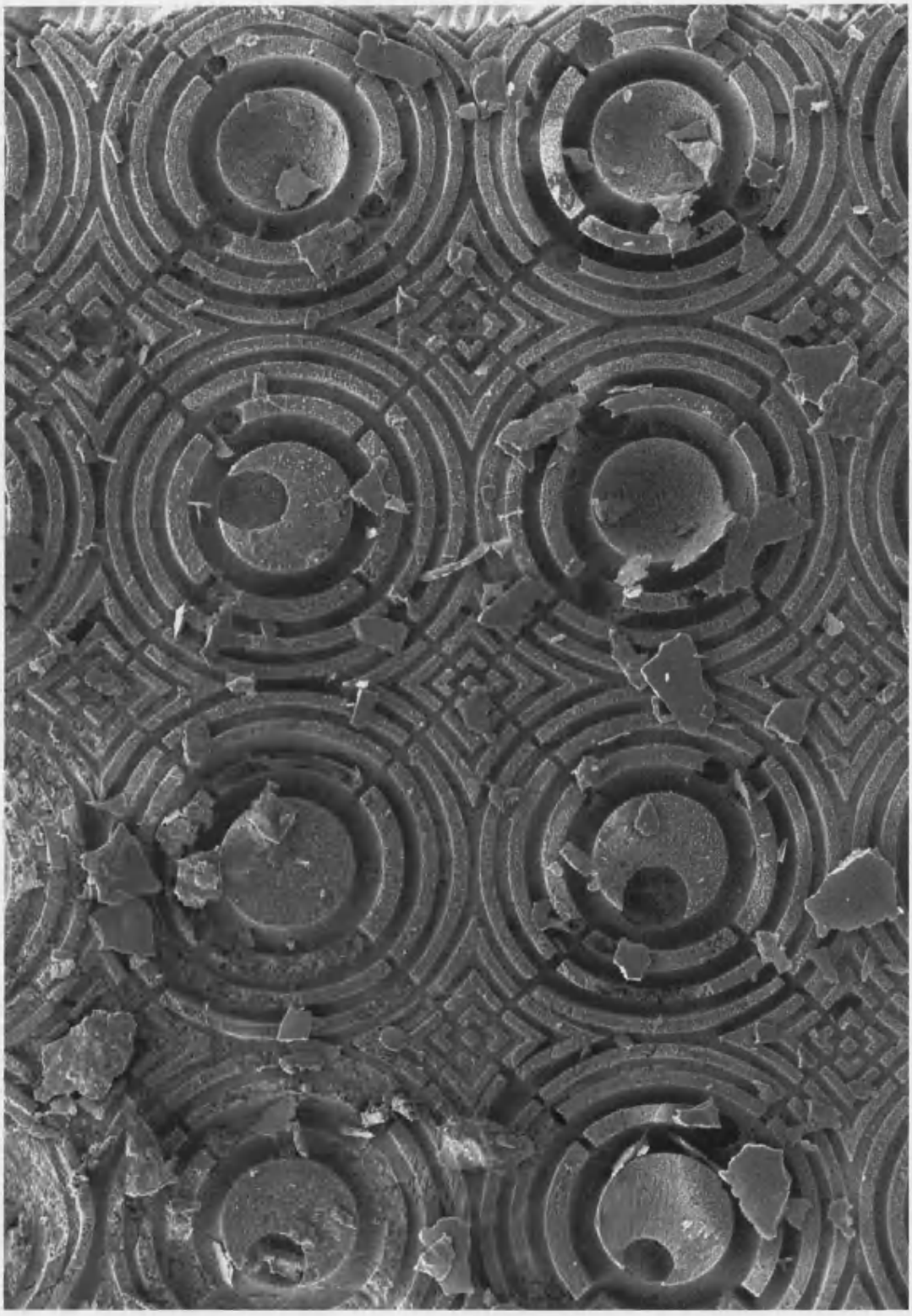

Composite cement microstructure – Chapter 5

To my family

ACKNOWLEDGMENTS

I would first like to thank Prof. Stephen Mann for giving me the opportunity to study and work with him and his group. Not only have I become a better scientist and thinker, but I have grown more than I would have ever imagined. I appreciated his patience and support with my diverted projects, but particularly that he never wavered from keeping me focused on finishing this document. Mostly I thank him for his friendship and fellow musical creativity which has kept me balanced throughout my time in the UK.

I would like to thank British Nuclear Fuels plc for supporting my postgraduate studentship. Harry Eccols, Teresa Kearney, David Goddard and Martin Green were most supportive and helpful, outside of their financial assistance and encouragement.

I would like to thank the technicians at the University of Bath for their assistance in preparing and analysing the samples contained in this thesis. Alan Carver analysed samples using atomic absorption. Ursula Potter, Glen Love and Hugh Perrott instructed on the use of scanning and transmission electron microscopies, and helped in preparing samples for thin-sectioning.

From my spider days, I want to sincerely thank Fritz Vollrath at the University of Århus for his hospitality, conversations and interest. My time in Denmark is a jewel to keep, and I am very thankful for the conversations and time with Shao, Thiemo and Helene. The work on the magnetic bionites would not have been possible without the efforts of David Awschalom and Mark Field at UCSB, to whom I owe a bit of my magnetic awareness. The cement materials would not have been possible

without the ideas and collaborative network of Paul Barnes at Birkbeck College. I appreciated him and his group (Sally and David) with whom I travelled and drank about Germany, meanwhile producing some interesting microstructures.

I want to thank Prof. Mann's diverse research group. Kim, who was the first person I met in the UK, instructed me on the use of the transmission electron microscope, prepared hydrophobic ferritin samples to support one chapter of this thesis, but most importantly has become a good friend. Sandi, Dominic, Sean, Steve (Simso), Jeremy, Benedict, Nicki, Wayne, Harish, Chris and Simon all taught me something, but mostly shared some very good times. Further chemists (Gini, Gail, Gus, and Neil) rounded out my experiences in many non-chemical ways. Also, musicians other than Steve kept me balanced, for which I thank Jon, Ian, Mark, Jason, and Cress.

I am very appreciative of those associated with my diverted projected of NanoMagnetics. Malvin, you gave me a second degree I did not even expect and made me a part of your family. I am forever grateful. I thank those that believed in the project: Chris, Duncan, Alan, Hitesh, Geoff, Peter, Don, John, Greg, Shahaf, and Roger, but especially those who made it work: Kim, Barnaby, Jason, Oksana, Angela and Kevin. Most recently I thank the new team for humouring me while I completed this document: Brendan, Chris, Jim, Artur, David, Richard and Angus.

I thank my teachers who had such an influence over my life – Jan Spears and Charles Hughes are two of so many who kindly encouraged me. The most important teachers have been my parents who have guided me even though they probably do

not believe they did. I will not even attempt to thank you for everything you have done in a few short sentences, but know how much I appreciate you.

Most importantly, I thank my friend and wife Anna. While this thesis gives me a degree, you have given me purpose. Your support and love (especially during the preparation of this document) are more than I could ever have hoped for. As I complete this portion of my academic life, I eagerly anticipate a lifetime of further learning by your side.

CONTENTS

ABBREVIATIONS

AA – Atomic absorption spectroscopy

AFM – Atomic force microscopy

ASID – Attached scanning imaging device

CRT – Cathode-ray tube

DNA – Deoxyribonucleic acid

EDXA (or EDX) – Energy dispersive X-ray analysis

G – Gauss, CGS unit of magnetic flux density (equivalent to $1x10^{-4}$ Tesla)

MEMS – Microelectromechanical systems

MFM – Magnetic force microscopy

Oe – Oersted (equivalent to 1 G in vacuum)

RNA – Ribonucleic acid

SEM – Scanning electron microscopy

SPM – Scanning probe microscopy (includes AFM, MFM and STM)

SQUID – Superconducting quantum interference device

STM – Scanning tunnelling microscopy

TEM – Transmission electron microscopy

UV/VIS – Ultraviolet and visible spectroscopy

CHAPTER ONE

GENERAL INTRODUCTION

FORWARD

The theme of this thesis is the creation of micron-scaled structures with functionality partially provided by the introduction of nanoparticulate materials. The nanoparticles were organised at different length scales and integrated using three principal fabrication methods – surface conjugation, infiltration and incorporation. Each method represents a balance between nano- and micron-scale control, as will be shown through the following chapters. A range of nanoparticles was selected to represent a variety of functionalities including optical, conductive, semi-conductive, and magnetic. In each experimental chapter, this range is integrated into a microstructure that is analysed for its ability to organise the nanoparticles, as well as evaluated in terms of enhanced functionality and integrity as a microstructured composite.

Chapter 1 begins with an introduction to the routes for producing nanoparticle-based microstructures. It then reviews nanoparticle production methods, proceeding to greater control over particle size and morphology. Finally, three general methods for the production of functional microstructures are discussed, specific examples of which are highlighted in subsequent chapters.

1.1 INTRODUCTION

Arising in part from the invention of the transistor, microtechnology has developed over the past five decades into a substantial part of the world economy and become ubiquitous enough even to be found in shoes! Optimised for greater efficiency and speed, microtechnology has employed increasingly finer control over structure, now measured in hundreds of nanometers. During this period many disciplines converged on controlling microstructure, producing not only faster electronics but also stronger materials. To continue the developmental trend, microtechnology is becoming nanotechnology. The idea of extending microstructural processing methods (such as lithography) to produce nanometer-scaled structures is termed the "top-down" approach. Yet chemists and biologists have long been working with materials at the nano-scale, and propose that functional materials can be grown or assembled from the "bottom-up". Tools potentially at their disposal range from the apparent simplicity of crystallisation to the complexity of a single cell developing into a hedgehog. In the fog where "top-down" and "bottom-up" meet is the current state of nanotechnology.

Standing alone, the cutting-edge examples of "top-down" and "bottom-up" do not yet exhibit the type of functionality that nanotechnology promises. Most likely some of the first useful "nanotechnology" materials will combine the best of both approaches, resulting in enhanced-function microstructured materials. "Top-down" approaches currently offer lithography that can reproduce features between 10 and 100 nanometers. "Bottom-up" approaches currently offer not only size- and compositionally controlled nanoparticles, but also naturally produced, well-ordered microstructures, such as bacteria and silks.

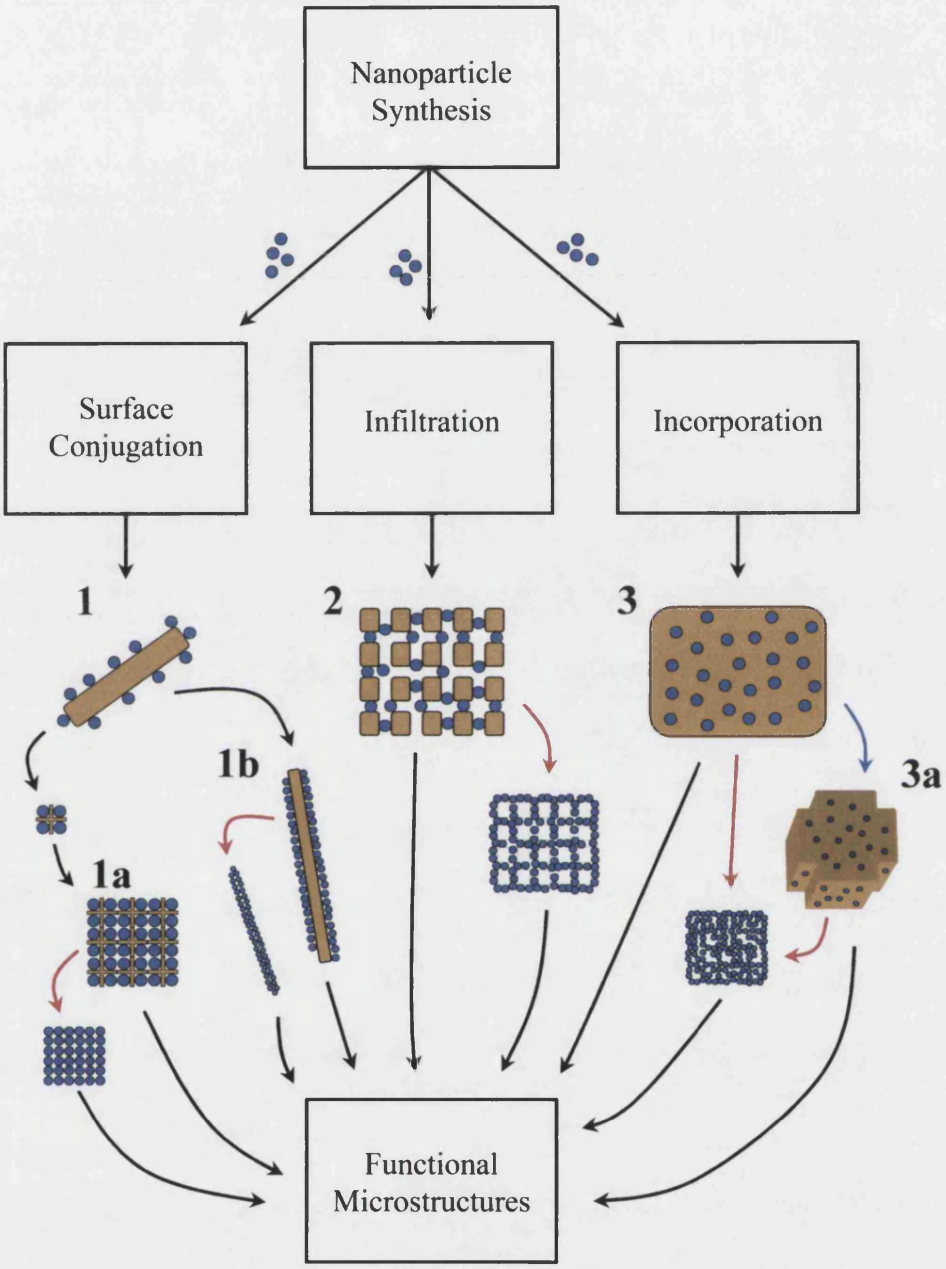

Figure 1.1 Nanoparticle-based routes to functional microstructures. Red lines denote template or matrix removal processes, such as calcining. The blue line denotes microscaled processing, such as moulding or machining.

The production of functional nanoparticle-based microstructures can be abstracted to three general methods. All are dependent on the production of well-controlled nanoparticles with wide-ranging functionality. However, functionality can come from both the properties of the nanoparticle and the form of the final microstructure. The first method can be termed "surface conjugation", in which nanoparticles are reactively coupled to a surface or template. Surface conjugation can lead to micron-scaled coatings (Figure 1.1(1b)), but when the template is appropriately selected or designed, it can lead to organised micro-assemblies (Figure 1.1(1a)). The second method can be termed "infiltration", in which reactive coupling may occur, but entrapment of nanoparticles within micro- or nanoscaled pores or channels is the primary mechanism (Figure 1.1(2)). The third method can be termed "incorporation", in which nanoparticles are blended to make a heterogeneous composite (Figure 1.1(3)). This composite may be microstructured by the nature of its production, or it may be moulded or machined into a final form (Figure 1.1(3a)). In all cases, the template or heterogeneous counterpart can ultimately be removed through chemical or heat processing, leaving a nanoparticulate skeleton of the original form.

Comparing these general methods, control over the nanostructure is diminished from surface conjugation to incorporation. As surface conjugation implies specific attachment across the template surface, and infiltration may involve reactivity, it is expected that some degree of higher scaled order can be imparted to nanoparticles comprising these structures. For the incorporation method, while the nanostructure can be very well defined through moulding or machining, the nanoparticulate component is generally disordered within the bulk of the primary matrix.

1.2 NANOPARTICLE SYNTHESIS

Nanoparticles are one of the few well-characterised building blocks for "bottom-up" nanotechnology. While other methods for their production exist (such as vapour-phase synthesis), chemical routes provide the greatest control over their composition and morphology. Regarding functionality, nanoparticles made of metals or alloys exhibit intrinsic properties such strength, wear-resistance, conductivity, semi-conductivity, magnetism, and catalytic activity, while those made of silicates or aluminosilicates exhibit properties such as catalytic activity or porosity. Extrinsically, assemblies of nanoparticles also can have functionality, especially when their sizes or assembled period match the wavelength of electromagnetic radiation. Such materials, known as "photonic crystals" or "photonic band-gap materials", are dielectric structures with a band gap that forbids propagation of a certain wavelength of light. Such functionality is currently desirable in the fields of optical communication, switching, and amplification. There are now many chemical methods for producing nanoparticles, each with their own advantage. This section will proceed through these methodologies in terms of increasing control over size.

Reaction Stabilised Nanoparticles

Nanoparticles can be produced by reduction or precipitation of ions in solution. By thoughtful selection of the reactants, nanoparticles can be stabilised at a particular size in various solvents, or even functionalised for selective adhesion to a surface. Quite often the depletion of reactants also controls the ultimate size of the nanoparticle. However in some cases pH or ion stoichiometry can affect size. A straightforward synthesis of this type is the production of an aqueous dispersion of magnetite. Precipitating iron(II) and iron(III) species in stoichiometric ratios in the

presence of tetramethylammonium hydroxide provides an alkaline sol of magnetite nanoparticles with an average diameter of ~10 nm (Massart, 1981). Single-phase systems have also been extended to stabilise the nanoparticle with ligands. In particular, ~2 nm gold particles can be thiol-ligand stabilised by sodium borohydride reduction of aqueous gold salts in the presence of *p*-mercaptophenol (Brust, *et al.*, 1995). Similar reactions have used alkanethiolate ligands to produce slightly larger, stabilised gold nanoparticles (Figure 1.2) (Chen, 2001).

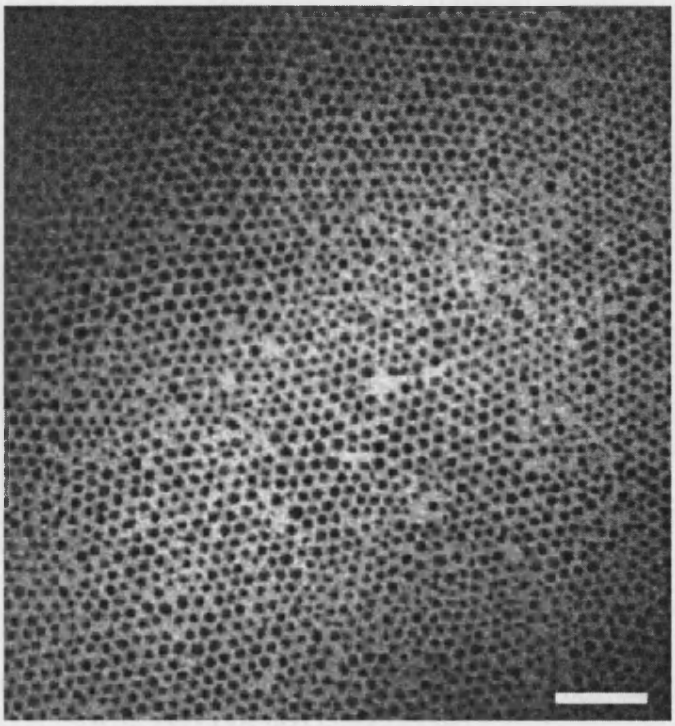

Figure 1.2 TEM micrograph of ~4.7 nm diameter alkanethiolate-protected gold nanoparticles particles deposited onto a SiOx-coated Cu grid (Chen, 2001). Scale bar is 30 nm.

Catalytic nanoparticles such as titanium silicalite-1 and crystalline aluminosilicate (or "zeolite") have also been prepared as single-phase reactions (Zhang, *et al.*, 1995, Schoeman, *et al.*, 1993). In the later case, aluminium was the growth-limiting reagent. Doubling the total alumina content resulted in an increased yield, but also a corresponding increase in particle size.

Nanoparticles can also be prepared in a single-phase reaction with pre-formed stabilisers. After preparing helical lipid tubules with diameters of 400-1000 nm and lengths of 50-100 μm, gold nanoparticles can be reduced from an aqueous salt by diacetylenic groups on the lipid molecules (Burkett, *et al.*, 1996). The resulting nanoparticles remained associated with the tubules, and even decorated the helical lipid structure. Templates with such localised reaction centres offer control not only over nanoparticle size, but organisation, and represent a worthwhile path in single-phase nanoparticle production.

Surfactant-Derived Nanoparticles

Nanoparticles prepared in the presence of surfactants can also be stabilised, but the primary advantage is the creation of nano-scaled reactors that control size and morphology. One of the most productive surfactant routes is the use of reverse micelles, which are part of the general family of microemulsions. For the preparation of reverse micelles, choice of surfactant is important. Reverse micelles are prepared from surfactants such as bis(2-ethylhexyl)sulfosuccinate sodium salt (or "AOT") that have long hydrocarbon chains in comparison to their polar head group. This structure produces wedge-like shapes that assemble head-first ("reverse" of a standard micelle) into spheres around polar solvents. By dissolving a surfactant in a

nonpolar solvent (such as heptane), then adding a small amount of water while vigorously stirring, reverse micelles are easily obtained (Figure 1.3). This system is ideal for making nanoparticles because they form in the aqueous core where they are protected from agglomeration and precipitation. Additionally, the water core diameter can be tuned by modifying the amount of water added to the solvent, producing nanoparticles of varying diameter. Hence an important parameter in reverse micellar preparations is the molar ratio of water to surfactant, given by "w" where $w = [H_2O]/[surfactant]$.

A good example of a functional nanoparticle prepared using reverse micelles is the semi-conductor, cadmium sulfide (CdS). Nanoparticles were produced by first forming a reverse micelle solution with $w = 5$, then drop-wise adding aqueous cadmium ions. These ions migrated in the solution into the aqueous cores, after which S^{2-} ions were added in the form of sodium sulfide. CdS was consequently precipitated within the reverse micelles giving an average particle diameter of 4 nm (Chandler, *et al.*, 1993). This technique has been extended to magnetic alloys (Duxin, *et al.*, 1997, Duxin, *et al.*, 2000), including some that displayed either preferential growth or coalescence of two micelles to form elongated shapes (Duxin, *et al.*, 1998).

A broader exploration of nanoparticle shape was recently performed using cobalt metal. The reaction in this case was non-aqueous, and involved the thermal decomposition and nucleation of cobalt (in the form of an organometallic) injected into a hot di-surfactant mixture. In particular octacarbonyldicobalt ($Co_2(CO)_8$) is dissolved in *o*-dichlorobenzene, then injected into a refluxing bath of *o*-

dichlorobenzene in the presence of oleic acid and trioctylphosphine oxide (TOPO) (Puntes, *et al.*, 2001). If the reaction is quickly quenched, nanorods of cobalt metal are formed roughly 4 nm in diameter. As the reaction was allowed to evolve over 30 minutes, the rods gave way to the production of 20 nm diameter spherical particles. The relative ratio of the surfactants showed an effect over the growth rates of particular faces of the cobalt nanocrystals, indicating a potential method for further size and shape control.

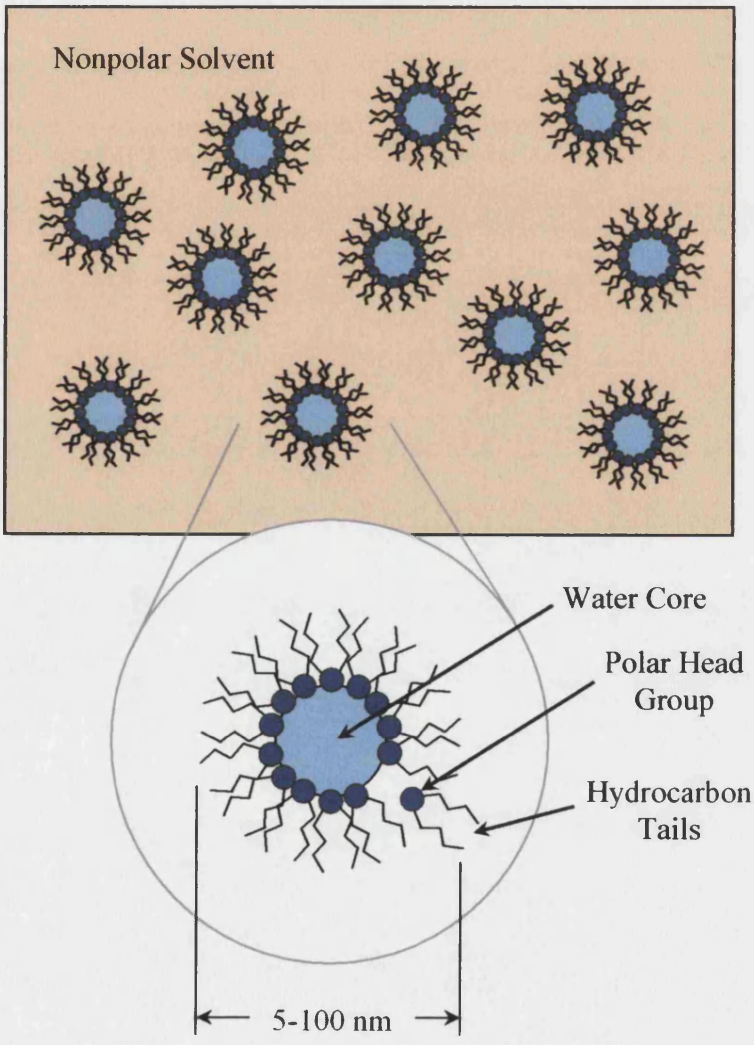

Figure 1.3 Schematic structure of reverse micelles composed of a surfactant such as Aerosol OT (AOT). Precipitation or reduction reactions within the aqueous core produce nanoparticles of corresponding size.

By possibly influencing the growth rates of various crystal faces, this method has also been used to produce a new crystalline form of cobalt (named ε-cobalt), which exhibits a cubic unit cell but is much less dense than both the hcp and fcc structures (Dinega, *et al.*, 1999). As such controllability can be exerted over cobalt, researchers interested in producing magnetic nanoparticles for data storage applications have begun using this di-surfactant method. For example, cobalt nanoparticles that were precisely controlled between 2-11 nm in diameter and showed ferromagnetic behaviour at 5 K have been produced (Sun, *et al.*, 1999). Temperatures lower than room temperature are not practical for data storage, so others have pursued metal alloys that could demonstrate much higher temperature ferromagnetism. Recently the same researchers produced alloys of iron platinum (FePt) with well-controlled sizes between 3-10 nm that exhibited ferromagnetism at ambient temperatures (Sun, *et al.*, 2000). Indeed they even used an assembly of the nanoparticles for micron-scaled magnetic recording.

However, the shape control demonstrated by the surfactant system is not limited to cobalt. Aqueous reverse micelles used for the preparation of barium chromate ($BaCrO_4$) have produced uniform rectangular-shaped particles (Li, *et al.*, 1999). By varying the surfactant ratio, a variety of nanostructures was shown. Surfactant systems have been shown to control particle size and morphology much more than reaction stabilised systems.

Dendrimer-derived Nanoparticles

A method that can exert even greater control over template size is the use of polymeric dendrimers. Dendrimers have been used and developed since the 1980s,

and start with a functional monomeric unit such as an acrylate, ester, or amine (Tomalia, *et al.*, 1997). The monomers are selectively polymerised to form branched structures of arbitrary complexity. "Generation" is a term used to identify the number of polymerisations or branched steps the dendrimer has undertaken. The term implies that the final structure is highly controlled (see Figure 1.4). Dendrimers are commercially available in the size range of 1-15 nm in diameter, so as templates they are potentially versatile. Moreover, tertiary amines present in the structure have been shown to coordinate transition metal ions, so the use of dendrimers for the production of metallic nanoparticles is promising.

Recently, researchers have begun to produce dendrimer-metal composites (Balogh & Laverdure, *et al.*, 1999, Balogh & Valluzzi, *et al.*, 1999). Of particular interest are transition metals with catalytic activity such as copper, gold, platinum and palladium. As an example of a strategy for encapsulating a metal nanoparticle within a dendrimer, a solution of gold ions can be mixed with an aqueous polyamidoamine (PAMAM) dendrimer solution (Figure 1.4). Due to the availability of tertiary amines within their interior, and the fact that tertiary amines are good ligands for many transition metal ions, the gold ions partition into the dendrimer interior. Addition of a reducing agent, such as $NaBH_4$, coalesces the metal ions into a single metal nanoparticle sterically confined to the dendrimer interior. There has yet to be sufficient production of nanoparticles with the dendrimer method, but the size control afforded by the template cannot be dismissed.

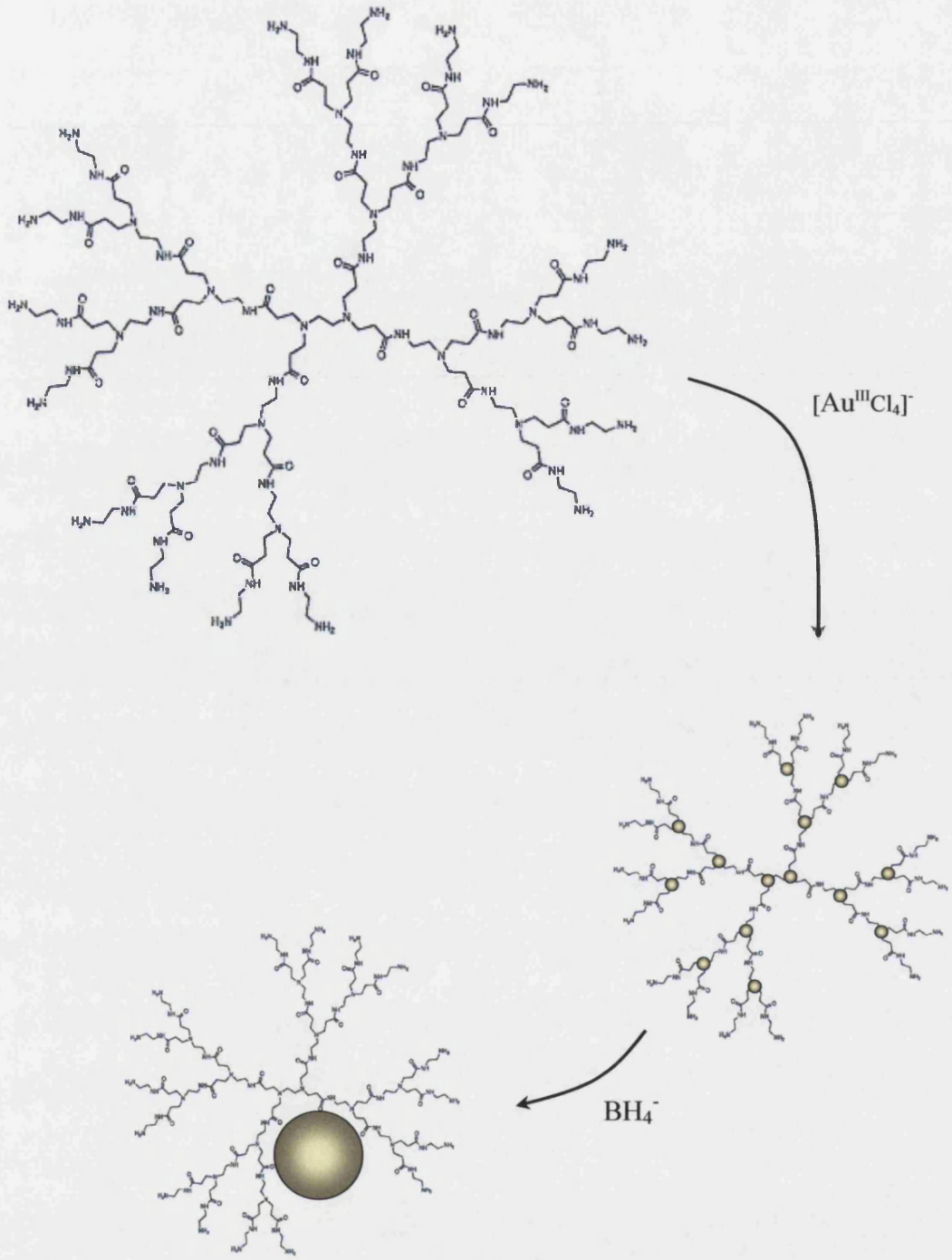

Figure 1.4 Schematic for producing gold nanoparticles using a Generation 2 PAMAM dendrimer (3 nm diameter). Gold ions are added to an aqueous solution of the dendrimer, and locate at the tertiary amines. A reducing agent such as $NaBH_4$ is used to form the final nanoparticle.

Biological Templating

The use of biological systems for the templating of inorganic materials is not new. Indeed nature has been quite deft at it for millennia. Even nanoparticles are not a recent invention, as some living systems already contain proteins surrounding 8 nm diameter iron oxide particles.

One novel biological route to nanoparticles is the use of the tobacco mosaic virus (TMV). TMV particles are 300 nm long, 18 nm wide with a 4 nm diameter inner channel. Recently, TMV particles were use to template amorphous silica by hydrolysing and condensing mixtures of tetraethoxysilane (TEOS) and aminopropyltriethoxysilane (APTES) in the presence of viral rods (Fowler, *et al.*, 2001). Nanoparticle silica spheres, roughly 100 nm in diameter, were formed with porous channels radiating from their core. Apparently TMV particles would bind ends together at a nucleation event, followed by radial silica growth. Later in the reaction, the virus rods would shear, leaving the porous nanoparticles intact. The nanoparticles remained intact upon calcination, which removed the viral proteins.

Continuing with the mineralisation of viruses, other researchers have used spherical cowpea chlorotic mottle viruses (CCMV) as nano-scale reactors. CCMV virons are 28 nm in diameter, with an 18 nm inner cavity. In their native state, the inner cavity is used to carry the RNA that biochemically describes the structural components of the virus. However, the viron can undergo reversible swelling at high pH (Douglas, *et al.*, 1998). Upon swelling at high pH (pH > 6.5), the native RNA can be removed as shown by the schematic in Figure 1.5(top). Following the addition of aqueous molecular tungstate (WO_4^{2-}) species, nanoparticles of paratungstate ($H_2W_{12}O_{42}^{10-}$)

can be precipitated within the viron while lowering the pH and sealing the protein cage (Douglas, *et al.*, 1998, Douglas, *et al.*, 1999). This technique may prove useful for aqueous nanoparticle reactions that occur above pH 6.5, especially as a wide variety of virus capsids exist.

An analogous protein cage to the viron was alluded to at the beginning of this section. Ferritin is a self-assembled, 12 nm diameter iron storage protein involved in biological mechanisms such as haem production. In this role, iron is typically stored as a poorly crystalline nanoparticle of iron(III) oxy-hydroxide (ferrihydrite). The size of the ferrihydrite is constrained by the 8 nm inner cavity of the protein, hinting at its use for the production of alternative mineral nanoparticles. Following reductive removal of the iron(III), the empty cage (apoferritin) has been used for the production of manganese oxide nanoparticles (Meldrum, *et al.*, 1995). It has also been used for the mixed-valence iron oxide, magnetite, increasing the magnetic moment present in the native ferrihydrite (Meldrum, *et al.*, 1991, Meldrum, *et al.*, 1992, Wong, *et al.*, 1998). Extending this approach using transition metal oxides, cadmium sulfide nanoparticles have also been prepared (Wong, *et al.*, 1996). That nanoparticles other than oxides were feasible led to the incorporation of cobalt platinum (CoPt) alloy (Warne, *et al.*, 2000). Similar to the FePt described earlier, such nanoparticle alloys hold promise for high-density data storage.

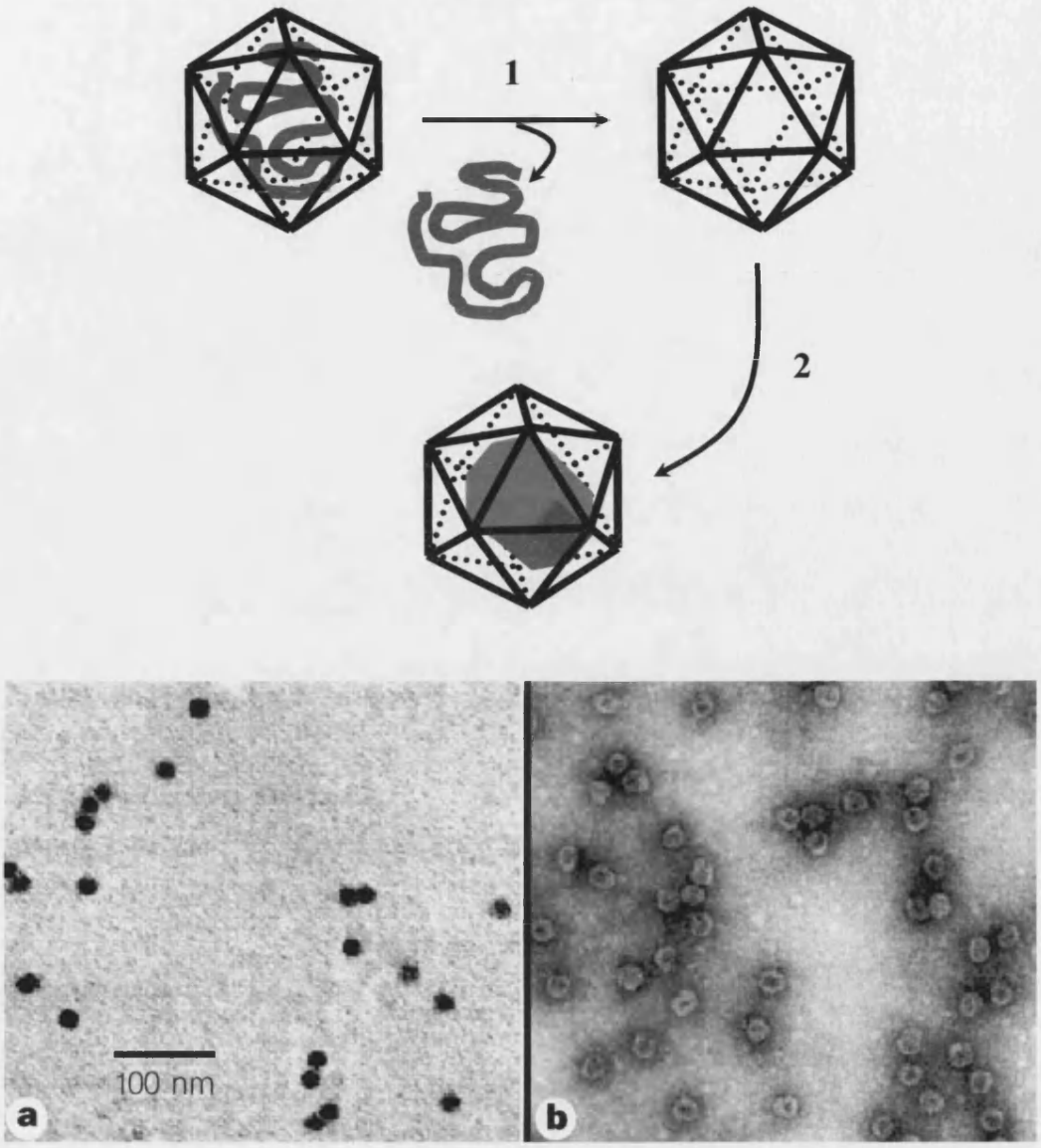

Figure 1.5 Schematic representation of synthetically mineralising a virus particle (top). Step 1 involves the removal of viral RNA and purification of the virus capsid. Step 2 involves the selective mineralisation upon swelling the virus capsid. TEM images (bottom) of synthesised paratungstate nanoparticles (a) and negatively stained composites displaying the intact capsid (b) (Douglas, *et al.*, 1998).

1.3 SURFACE CONJUGATION

In surface conjugation, nanoparticles are reactively coupled to a surface or template. The surface or template may already be microstructured (Figure 1.1(1b)), or smaller subunits may collectively organise or agglomerate to form a microstructure (Figure 1.1(1a)).

One example of this collective organisation is shown in work on gold nanorods conjugated with DNA. Gold nanorods, on average 10 nm in diameter and 50 nm in length, were prepared and electrochemical reduction. Complementary single-stranded DNA with a chemically activated thiol group was reactively attached to the nanorods (Dujardin, *et al.*, 200l). Like sausages closely packed, the complementary DNA strands tied the nanorods into large-scale bundles, some several microns in size. Similar work has been shown with gold nanospheres, but exploiting the highly specific recognition properties of antibodies and antigens. 12 nm diameter gold particles had either of two different antibodies chemisorbed onto them, and were then mixed 1:1 in the presence of a synthetic antigen (Mann, *et al.*, 2000). The reaction produced 3 μm wide filaments, macroscopic in length, of densely packed gold nanoparticles. While unable to control solid angle coordination, these techniques can very tightly regulate the distance between adjacent nanoparticles. Possibly in conjunction with more anisotropic shapes these techniques will exhibit the greatest control over both nano- and micro-length scales. One candidate would be nanoparticles prepared using reverse micelles of $Ba(AOT)_2$ and Na_2CrO_4-containing NaAOT microemulsion droplets (Li, *et al.*, 1999). The resulting nanoparticles were prismatic rectangles, which agglomerated into chains with inter-

particle spacing of 2 nm (Figure 1.6). Further aggregation of the chains produced a 2-D square lattice with regular periodicity.

One example of a pre-existing microstructured surface is the nanoparticulate zeolite decoration of 640 nm diameter polystyrene spheres (Rhodes, *et al.*, 2000, Mann & Davis, *et al.*, 2000). By alternatively adsorbing a cationic polyelectrolyte followed by a negatively charged silicalite, composite layers were built to form a thick shell. The resulting nanostructure could then be calcined to remove the latex template, resulting in a hollow zeolite sphere. These spheres occasionally close-packed (likely due to drying for microscopy), and could potentially be sintered together to form larger, ordered microstructures stemming from the regular packing of monodisperse latex spheres.

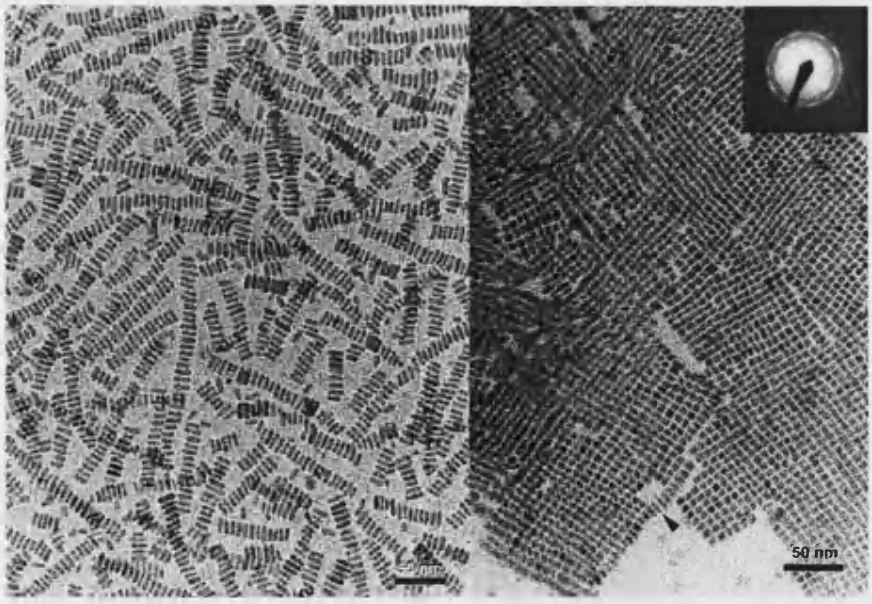

Figure 1.6 TEM images showing ordered chains (left) and close-packed chain arrays (right) of prismatic $BaCrO_4$ nanoparticles. Inset electron diffraction pattern (right) indicates the crystals are single-domain and elongated along the crystallographic *a* axis (Li, *et al.*, 1999).

To serve as inspiration for what types of microstructures are possible through surface conjugation, a set of naturally occurring calcite structures should be reviewed. Certain types of algae, referred to as coccolithophores, produce intricate scales of calcite called hetercoccoliths throughout their life cycle (Young, *et al.*, 1992). In some species, less intricate scales called holococcoliths are produced early in their life cycle. These microstructures are composed of rhombohedral calcite nanocrystals, and display a diversity of shapes specific to the coccolithophore (Figure 1.7). Holococcoliths are thought to result from extracellular mineralisation, but exhibit fine control over nanoparticle size and arrangement that extends to reproducible microstructures 2-3 μm in diameter.

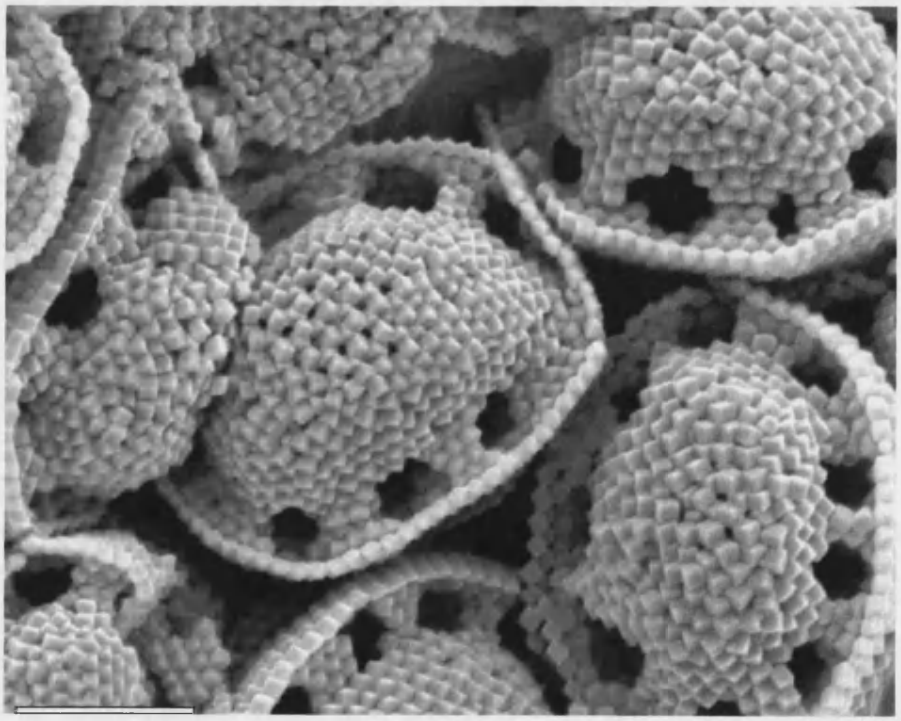

Figure 1.7 SEM image of holococcoliths from *Calyptrosphaera pirus*. Scale bar = 1 μm (Photo courtesy of Dr. Jeremy Young, The Natural History Museum, London).

1.4 INFILTRATION

For infiltration routes to functional microstructures, the associated nanoparticles may engage reactively with the template, but are often entrapped passively within micro- or nanoscaled pores or channels within the matrix (Figure 1.1(2)).

One route to highly ordered templates for infiltration is the crystallisation of monodisperse latex or silica particles. Infusing the resulting 3-D crystals with nanoparticles, and subsequently removing the template can produce microporous nanocomposites. Such microstructured materials with ordered arrays of pores have been produced using gold nanoparticles (Velev, *et al.*, 2000). As the templating particle size can be selected, pore sizes ranging from 150 nm – 1 μm are obtainable. Such a route offers functionality not only through the selection of nanoparticles, but also through the patterned microstructure that could potentially serve as a photonic band gap material.

A second, less ordered template is a bionite. Bionites are composite materials ~30 μm wide, produced by mineralising a bacterial thread complex. The thread complexes are produced from arrays of individual bacterial fibres which supercoil together, leaving axially aligned microstructured channels. Bionites have been prepared using two methods. The first was by introducing soluble metal salts into cultures of the bacteria, exploiting the metal-binding carboxylate groups. Salts of $FeCl_3$, $CaCl_2$ or $CuCl_2$ were incorporated into the cultures, with the metal content present throughout the fibre at 6-10 wt% (Mendelson, 1992). The second method involved incorporating preformed nanoparticles into the native or pre-washed fibre-like complex. One such example was formed by dipping a thread into an alkaline

solution containing surfactant-stabilised tetraethoxysilane (TEOS) (Mann, *et al.*, 1997). The resulting composite was calcined to leave intact hollow cylinders of mesoporous silica. A similar example was produced from a solution of 10 nm diameter silicalite nanoparticles, which were infiltrated into a thread by dipping (Zhang, *et al.*, 2000). Upon calcining the composite, an intact zeolite replica of the channel-like microstructure was left. Combining the separation or catalytic properties of the zeolite nanoparticles with the porous channels of the microstructure could provide technological advantages.

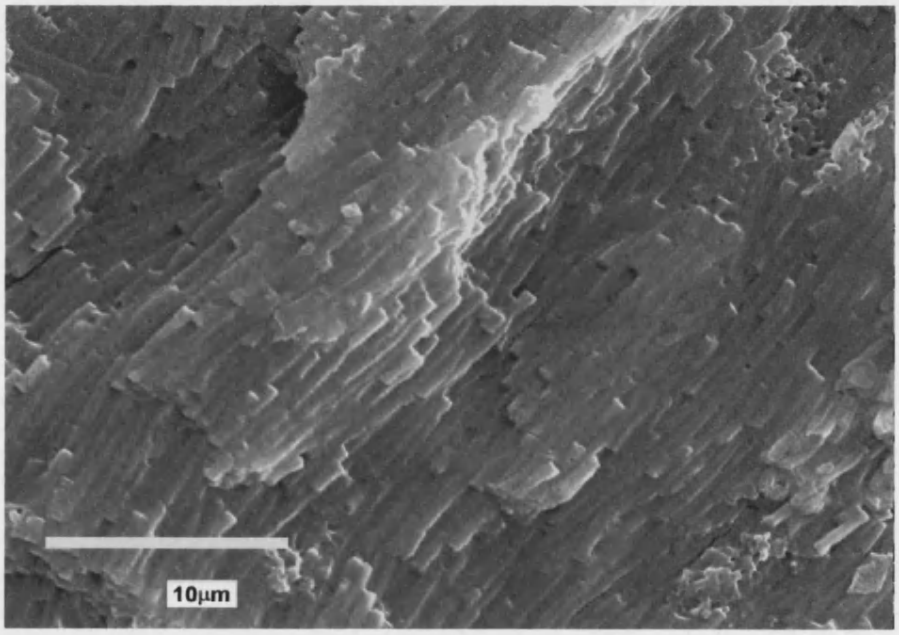

Figure 1.8 SEM side-view of a washed bacterial thread complex, displaying the close packing of individual bacterial fibres.

1.5 INCORPORATION

The final route to functional microstructures presented is the least explored, presumably because incorporation does not exert great control over nanoscale order. It does however allow for tight control over microstructure, and any bulk properties that can be gained through the inclusion of functional nanoparticles brings advantages. To prepare microstructures, nanoparticles are blended to make a heterogeneous composite (Figure 1.1(3)). This composite may be microstructured by the nature of its production, or it may be moulded or machined into a final form (Figure 1.1(3a)).

One recent example was the incorporation of magnetite nanoparticles into a bicontinuous polymeric gel to produce a magnetically active spongelike material (Breulmann, *et al.*, 1998). The same polymeric gel was used with ceramic nanoparticles such as SiO_2 and TiO_2, which formed self-supporting structures upon removal of the gel template (Davis, *et al.*, 2001). However, the overall microstructure in these systems was not controlled other than being of macro scale.

One example of incorporation that did exert control over microstructure was the incorporation of latex spheres in moulded cements (Colston, *et al.*, 1996). The cements were formed in lithographically derived moulds, with the addition of latex nanoparticles. The latex did not provide additional functionality, and was merely present to inhibit coarse crystal growth during the curing of the cement. It did however raise the possibility of dispersing functional nanoparticles within a cement, which could also be microstructured through lithographic patterning.

1.6 Overview of Thesis

The work presented in this thesis is focused on the creation of micron-scaled structures with functionality partially provided by the addition of nanoparticulate materials. By integrating nanoparticles at different length scales using various mechanisms, the production of microstructures is abstracted to three general methods. Chapter 3 discusses the method of surface conjugation using spider dragline silk as a template for coating with a variety of nanoparticles. The structural properties of the composite, as well as the nature and quality of the coatings are investigated. Chapter 4 discusses the method of infiltration, concentrating on a bacterial thread structure for the preparation of magnetic bionites. The magnetic properties of the composite and anomalous anisotropic behaviour are discussed. Chapter 5 discusses the method of incorporation using microstructured cements as the binding matrix for a variety of nanoparticles. Effects on cement microstructure and dispersing of the nanoparticles are discussed. Chapter 6 discusses complex nanoparticles with higher functionality, and investigates the production of protein-encapsulated conducting polymers.

1.7 REFERENCES

Balogh, L., K. S. Laverdure, S. P. Gido, A. G. Mott, M. J. Miller, B. P. Ketchel, and D. A. Tomalia, "Dendrimer-Metal Nanocomposites in Organic/Inorganic Hybrid Materials", *Mat. Res. Soc. Symp. Proc.*, **576**, 69-75 (1999).

Balogh, L., R. Valluzzi, G. L. Hagnauer, K. S. Laverdure, S. P. Gidoand, and D. A. Tomalia, "Formation of Silver and Gold Dendrimer Nanocomposites", *J. Nanoparticle Res.*, **1**(3), 353-368 (1999).

Braun, P. V., P. Osenar and S. I. Stupp, "Semiconducting superlattices templated by molecular assemblies", *Nature*, **380**, 325-328 (1996).

Breulmann, M., H. Cölfen, H. P. Hentze, M. Antonietti, D. Walsh, and S. Mann, "Elastic Magnets: Template-Controlled Mineralization of Iron Oxide Colloids in a Sponge-like Gel Matrix", *Adv. Mater.*, **10**(3), 237-240 (1998).

Brust, M., J. Fink, D. Bethell, D. J. Schiffrin, and C. Kiely, "Synthesis and Reactions of Functionalised Gold Nanoparticles", *J. Chem. Soc. Chem. Comm.*, **90**, 1655-1656 (1995).

Burkett, S. L., and S. Mann, "Spatial organization and patterning of gold nanoparticles on self-assembled biolipid tubular templates", *Chem. Commun.*, 321-322 (1996).

Chen, S., "Langmuir-Blodgett Fabrication of Two-Dimensional Robust Cross-Linked Nanoparticle Assemblies", *Langmuir*, **17**, 2878-2884 (2001).

Chandler, R., S. Bigham, and J. Coffer, "Spectroscopic Analysis of Semiconductor Colloids", *J. Chem. Edu.*, **70**(1), A7-A10 (1993).

Colston, S. L., P. Barnes, H. Freimuth, M. Lacher, and W. Ehrfeld, "Cements: a new medium for micro-engineering structures?", *J. Mat. Sci. Lett.*, **15**, 1660-1663 (1996).

Davis, S. A., M. Breulmann, K. H. Rhodes, B. Zhang, and S. Mann, "Template-Directed Assembly Using Nanoparticle Building Blocks: A Nanotectonic Approach to Organized Materials", *Chem. Mater.*, **13**(10), 3221-3226 (2001).

Dinega, D. P., and M. G. Bawendi, "A Solution-Phase Chemical Approach to a New Crystal Structure of Cobalt", *Angew. Chem. Int. Ed.*, **38**(12) 1788-1791 (1999).

Douglas, T., and M. Young, "Host-guest encapsulation of materials by assembled virus protein cages", *Nature*, **393**, 152-155 (1998).

Douglas, T., and M. Young, "Virus Particles as Templates for Materials Synthesis", *Adv. Mater.*, **11**, 679-681 (1999).

Dujardin, E., L. B. Hsin, C. R. C. Wang, and S. Mann, "DNA-driven self-assembly of gold nanorods", *Chem. Commun.*, 1264-1265 (2001).

Duxin, N., N. Brun, P. Bonville, C. Colliex, and M. P. Pileni, "Nanosized Fe-Cu-B alloys and composites synthesized in diphasic systems", *J. Phys. Chem. B.*, **101**, 8907 (1997).

Duxin, N., N. Brun, C. Colliex, and M. P. Pileni, "Synthesis and magnetic properties of elongated Fe-Cu alloys", *Langmuir*, **14**(8), 1984 (1998).

Duxin, N., W. Wernsdörfer, B. Barbara, D. Mailly, and M. P. Pileni, "Magnetic Properties of an Individual Fe-Cu-B Nanoparticle", *Langmuir*, **16**(1), 11-14 (2000).

Forder, C., S. P. Armes, A. W. Simpson, C. Maggiore, and M. Hawley, "Preparation and Characterisation of Superparamagnetic Conductive Polyester Textile Composites", *J. Mater. Chem.*, **3**(6), 563-569 (1993).

Fowler, C. E., W. Shenton, G. Stubbs, and S. Mann, "Tobacco Mosaic Virus Liquid Crystals as Templates for the Interior Design of Silica Mesophases and Nanoparticles", *Adv. Mater.*, **13**(16), 1266-1269 (2001).

Hall, S. R., W. Shenton, H. Engelhardt, and S. Mann, "Site-Specific Organization of Gold Nanoparticles by Biomolecular Templating", *ChemPhysChem.*, **3**, 184-186 (2001).

Li, M., H. Schnablegger, and S. Mann, "Coupled synthesis and self-assembly of nanoparticles to give structures with controlled organization", *Nature*, **402**, 393-395 (1999).

Mann, S., S. L. Burkett, S. A. Davis, C. E. Fowler, N. H. Mendelson, S. D. Sims, D. Walsh, and N. T. Whilton, "Sol-Gel Synthesis of Organized Matter", *Chem. Mater.*, **9**(11), 2300-2310 (1997).

Mann, S., W. Shenton, M. Li, S. Connolly, and D. Fitzmaurice, "Biologically Programmed Nanoparticle Assembly", *Adv. Mater.*, **12**(2), 147-150 (2000).

Mann, S., S. A. Davis, S. R. Hall, M. Li, K. H. Rhodes, W. Shenton, S. Vaucher, and B. Zhang, "Crystal tectonics: Chemical construction and self-organization beyond the unit cell", *J. Chem. Soc. Dalton Trans.*, 3753-3763 (2000).

Marchessault, R. H., P. Rioux, and L. Raymond, "Magnetic cellulose fibres and paper: preparation, processing and properties", *Polymer*, **33**(19), 4024-4028 (1992).

Massart, R., "Preparation of Aqueous Magnetic Liquids in Alkaline and Acidic Media", *IEEE Trans. Mag.*, **17**(2), 1247-1248 (1981).

Meldrum, F. C., V. J. Wade, D. L. Nimmo, B. R. Heywood, and S. Mann, "Synthesis of Inorganic Nanophase Materials in Supramolecular Protein Cages", *Nature*, **349**, 684-687 (1991).

Meldrum, F. C., B. R. Heywood, and S. Mann, "Magnetoferritin: In Vitro Synthesis of a Novel Magnetic Protein", *Science*, **257**, 522-523 (1992).

Meldrum, F. C., T. Douglas, S. Levi, P. Arosio, and S. Mann, "Reconstitution of manganese oxide cores in horse spleen and recombinant ferritins," *J. Inorg. Biochem.*, **58**, 59-68 (1995).

Mendelson, N. H., "Production and Initial Characterization of Bionites: Materials Formed on a Bacterial Backbone", *Science*, **258**, 1633-1636 (1992).

Ogasawara, W., W. Shenton, S. A. Davis, and S. Mann, "Template Mineralization of Ordered Macroporous Chitin-Silica Composites Using a Cuttlebone-Derived Organic Matrix", *Chem. Mater.*, **12**(10), 2835-2837 (2000).

Puntes, V. F., K. M. Krishnan, A. P. Alivisatos, "Colloidal Nanocrystal Shape and Size Control: The Case of Cobalt", *Science*, **291**, 2115-2117 (2001).

Rhodes, K., S. A. Davis, F. Caruso, B. Zhang, and S. Mann, "Hierarchical Assembly of Zeolite Nanoparticles into Ordered Macroporous Monoliths Using Core-Shell Building Blocks", *Chem. Mater.*, **12**(10), 2832-2834 (2000).

Schoeman, B. J., J. Sterte, and J. E. Otterstedt, "Synthesis and Size Tailoring of Colloidal Zeolite Particles", *J. Chem. Soc. Chem. Comm.*, 994-995 (1993).

Sun, S., and C. B. Murray, "Synthesis of monodisperse cobalt nanocrystals and their assembly into magnetic superlattices", *J. App. Phys.*, **85**(8), 4325-4330 (1999).

Sun, S., C. B. Murray, D. Weller, L. Folks, and A. Moser, "Monodisperse FePt Nanoparticles and Ferromagnetic FePt Nanocrystal Superlattices", *Science*, **287**, 1989-1992 (2000).

Tomalia, D., and R. Esfand, "Dendrons, dendrimers and dendrigrafts", *Chemistry & Industry*, 416-420 (1997).

Velev, O. D., E. W. Kaler, "Structured Porous Materials via Colloidal Crystal Templating: From Inorganic Oxides to Metals", *Adv. Mater.*, **12**(7), 531-534 (2000).

Warne, B., O. I. Kasyutich, E. L. Mayes, J. A. L. Wiggins, and K. K. W. Wong, "Self Assembled Nanoparticulate Co:Pt for Data Storage Applications", *IEEE Trans. Mag.*, **36**, 3009-3011 (2000).

Wong, K. K. W., and S. Mann, "Biomimetic synthesis of cadmium sulfide-ferritin nanocomposites," *Adv. Mat*, **8**, 928-933 (1996).

Wong, K. K. W., T. Douglas, S. Gider, D. D. Awschalom, and S. Mann, "Biomimetic synthesis and characterization of magnetic proteins (magnetoferritin)", *Chem. Mat.*, **10**, 279-285 (1998).

Young, J. R., J. M. Didymus, P. R. Bown, B. Prins, and S. Mann, "Crystal assembly and phylogenetic evolution in heterococcoliths", *Nature*, **356**, 516-518 (1992).

Zhang, G., J. Sterte, and B. J. Schoeman, "Discrete Colloidal Crystals of Titanium Silicate-1", *J. Chem. Soc. Chem. Comm.*, 2259-2260 (1995).

Zhang, B., S. A. Davis, N. H. Mendelson, and S. Mann, "Bacterial templating of zeolite fibres with hierarchical structure", *Chem. Commun.*, 781-782 (2000).

CHAPTER TWO

EXPERIMENTAL METHODS

2.1 METHODS AND INSTRUMENTATION

Water Purification

Domestic water was doubly-distilled in an Aquatron A4D still, with dual boilers. The output water was fed into a Purite Standard Stillplus, comprising a mixed-bed ion exchange column, activated carbon cartridge and 0.2 μm bacterial filter. The resulting output was water of BS 2978 Grade 1 quality, with a standard conductivity of less than 1 μS/cm.

UV/VIS Spectrophotometry

UV/Vis spectra were recorded using a Perkin-Elmer Lambda 6 spectrophotometer. Spectra were typically recorded from 300 to 1100 nm, and samples were prepared in quartz cuvettes with 10 mm pathlength. Disposable polystyrene cuvettes of similar pathlength were only used for coarse measurements. All measurements were taken after allowing the spectrophotometer to thermally stabilise for 1 hour.

Scanning Electron Microscopy (SEM)

Samples were examined using a JEOL 6310 scanning electron microscope operating at 15-20 kV. Samples were typically imaged at magnifications between x100 – x20,000. Higher resolution work was performed using a JEOL 1200 EX transmission electron microscope with an attached scanning imaging device (ASID). The instrument was used with samples up to x50,000. Additional high-resolution work was performed using a JEOL 6400F field emission SEM operating at 30 kV, at the Institute for Microtechnology in Mainz, Germany. All samples were gold coated to prevent the build-up of charge using an Edwards S150B sputter coater.

In SEM a series of components is organised axially in an evacuated column, as shown in Figure 2.1. The first component, an electron gun, produces a stream of monochromatic electrons. This stream is focused to a thin, coherent beam by a condenser lens, typically controlled by a "coarse probe current" knob. This lens is used to both form the beam and to limit the amount of current it contains. The beam is then restricted by a condenser aperture (not shown), which removes high angle electrons, such as those from off the optical axis. The beam next passes through a second condenser lens, which forms the electrons into a thin, coherent beam, typically controlled by a "fine probe current" knob. Next, a set of coils scans (or rasters) the beam in a grid pattern, dwelling on points for a predetermined period of time (typically microseconds). The beam then passes through the objective lens, which focuses the scanning beam onto a portion of the sample. When the beam strikes the sample, incident electrons colliding with an atom in the sample are scattered "backward" 180 degrees, with no appreciable loss of energy in an elastic collision. These "backscattered" electrons are detected and counted for each point on the sample scanned. Each point is then displayed on a CRT with an intensity corresponding to the count or intensity of the backscattered electrons. This process is repeated until the whole sample area is scanned, with a total refresh rate up to 30 times per second. The image can be selectively transferred to film or imaging device other than the CRT, giving a permanent record. For further reading on SEM methods and techniques, see Chescoe, *et al.*, 1990 and Goodhew, *et al.*, 1988.

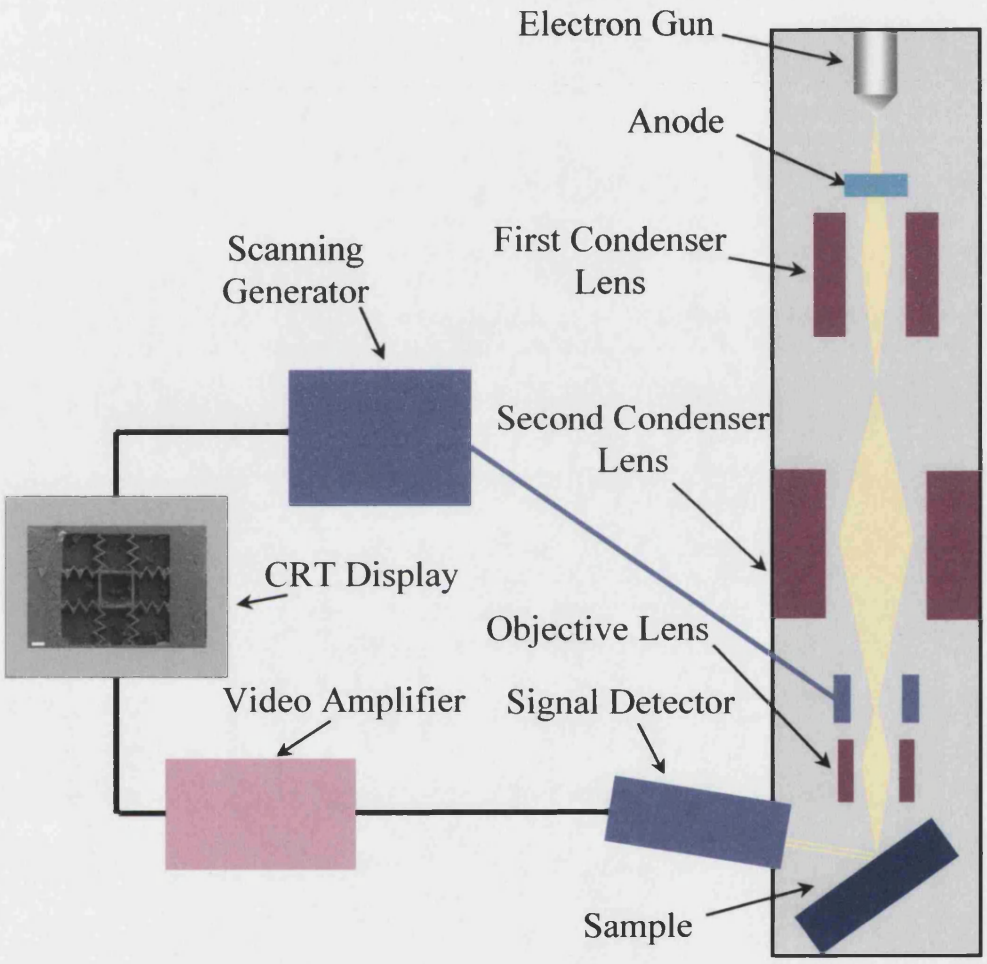

Figure 2.1 Schematic diagram of a scanning electron microscope.

Energy Dispersive X-Ray Analysis (EDXA)

Qualitative elemental analysis was performed on both the JEOL 6310 SEM and the JEOL 2000FX TEM using energy dispersive X-ray analysis (EDXA). Identical Link AN10000 X-ray microanalysis systems were attached to each instrument, outfitted with silicon detectors cooled with liquid nitrogen. The listed limit of detection is of the order of 1-5 wt%, but is dependent on the element. The JEOL SEM was fitted with a removable beryllium window, allowing the detection of lighter elements such as carbon and oxygen. Further, the software was enhanced to allow for elemental mapping analysis across the surface of the sample. For further reading on EDX analysis and techniques, see Goodhew, *et al.*, 1988.

Transmission Electron Microscopy (TEM)

Samples were examined using a JEOL 2000 FX transmission electron microscope operating at 200 kV. This instrument provided magnifications up to x200,000. Samples were typically prepared using carbon sputtered, formvar-covered 3mm copper grids. Between 5-10 µl of liquid sample was applied in a drop to a glazed ceramic tile, with a grid floated upside-down on top. After 5-10 minutes, the grid was removed and allowed to dry protected from contamination.

In TEM a series of components is organised axially in an evacuated column, as shown in Figure 2.2. The first component, an electron gun, produces a stream of monochromatic electrons. This stream is focused to a thin, coherent beam using two condenser lenses. The first lens mostly determines the "spot size" or the size of the final spot that strikes the sample. The second lens changes the size of the spot on the sample, from dispersed field to pinpoint affecting the intensity of brightness. The

beam is then restricted by a condenser aperture (not shown), which removes high angle electrons, such as those from off the optical axis. The resulting beam then strikes the sample, with a portion transmitted to be focused by the objective lens. An objective aperture can further restrict the beam, enhancing contrast by again blocking high angle, diffracted electrons. The focused image is passed along the column through the intermediate and projector lenses, being continuously enlarged. Finally, the image strikes a phosphor screen causing light to be generated in the form of the transmitted image. The darker regions of this image represent those areas of the sample through which fewer electrons were transmitted, being thicker or denser. The lighter regions correspondingly represent areas that are thinner or less dense. The image can be selectively transferred to film or imaging device other than the phosphor screen, giving a permanent record. For further reading on TEM methods and techniques, see Chescoe, *et al.*, 1990 and Goodhew, *et al.*, 1988.

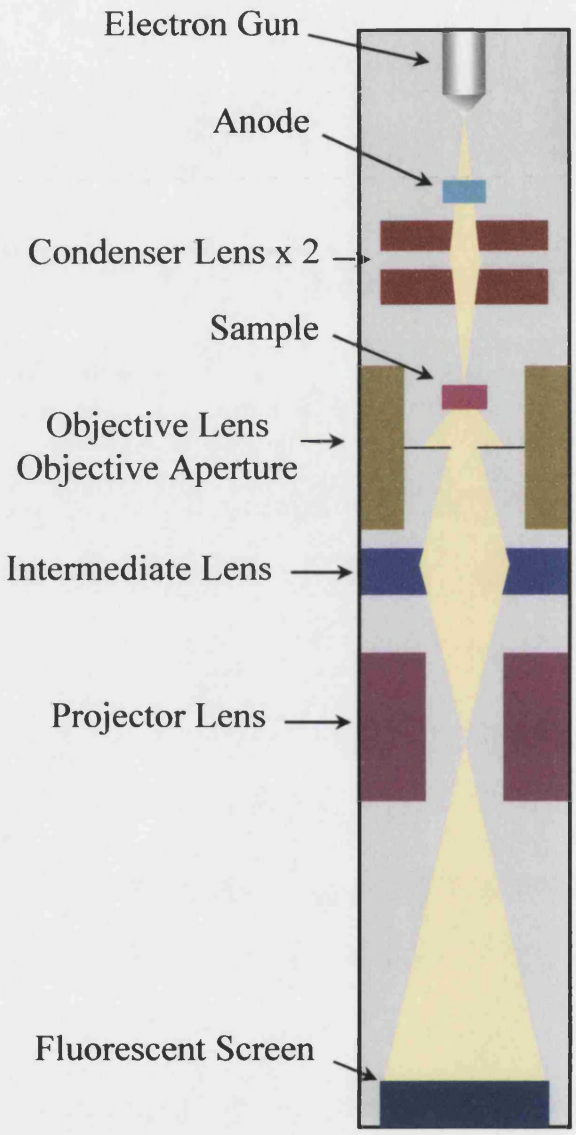

Figure 2.2 Schematic diagram of a transmission electron microscope.

Atomic Force Microscopy (AFM)

Samples were imaged using a Digital Instruments NanoScope IIIa AFM in both contact and tapping modes with etched silicon nitride probes. Contact mode AFM of the cements presented in Chapter 5 utilised an AutoProbe CP (Park Scientific Instruments) at the Institute for Microtechnology in Mainz, Germany, again using etched silicon nitride probes.

Scanning probe microscopy started with the development of the scanning tunneling microscope (STM) in the mid 1980's. An STM works by measuring small changes in tunneling current between a conductive sample and a sharpened metal probe, while rastering in two dimensions over the sample. It provides atomic-resolution topographic images of conducting surfaces. The atomic force microscope (AFM) is an extension of the STM that can image nonconducting surfaces. Instead of measuring the tunneling current between sample and probe, the AFM measures a range of forces between a sharpened probe and the sample. The probe consists of a tip (usually pyramidal) attached to the end of a cantilever that can flex in response to the interaction forces. For small displacements the cantilever obeys Hooke's Law. Hooke's Law is given by F=-kz, where k is a constant which depends of the material composition and geometry of the cantilever (given in N/m), and z is the displacement (given in m). By knowing k and measuring the displacement z, a value of the force between the probe and sample can be determined. To measure the displacement of the cantilever, laser light is reflected from it to a split detector that registers a difference signal (A-B), as shown in Figure 2.3.

AFM can be performed with and without feedback. If feedback is used, a z-axis positioning piezo moves the sample up and down in response to the displacement of the probe. This keeps the probe at a pre-set displacement or, more importantly, keeps the force constant between the sample and tip giving reliable topographic information. If feedback is not used, the instrument operates in constant height mode that can provide atomic-resolution images of extremely flat surfaces. The two most common imaging modes are contact and tapping. In contact mode the tip and sample remain in proximal contact, but a disadvantage is that lateral forces that can cause the sample to move or be damaged by tearing. In tapping mode the cantilever is oscillated at its resonant frequency and positioned such that the tip "taps" the surface of the sample. This imaging mode lessens lateral forces to give a more accurate image, especially of soft samples. By coating standard tips with various materials, the AFM can measure a range of forces including magnetic (MFM), electrostatic and friction. For further reading on SPM methods, see Bonnell, *et al.*, 2001.

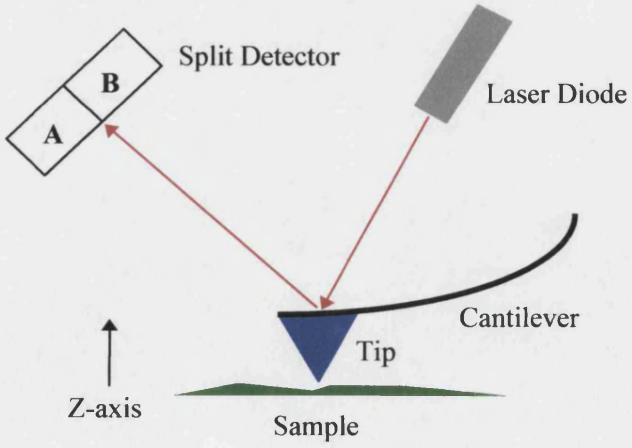

Figure 2.3 Schematic diagram of an atomic force microscope.

SQUID Magnetometry

University of California at Santa Barbara, U.S.A.

Low temperature magnetic measurements were made using an rf superconducting quantum interference device (SQUID) magnetometer, part-built and run by the group of David Awschalom at UC Santa Barbara. A SQUID magnetometer consists of two coupled devices: a flux transformer and a SQUID loop. The flux transformer is a detection coil in which a current is induced by the presence of a changing magnetic field (the sample). This induced current flows through an "input coil", creating an amplified flux that is detected by the SQUID loop. A SQUID loop contains two "Josephson junctions" which are weak links between two superconductors that can support a low current. In the presence of the amplified magnetic flux, the Josephson junctions cause the impedance of the loop to behave as a function of the flux. This impedance is linearised, amplified and processed to reduce noise, then flux-to-voltage measurements are recorded. Simply, the SQUID sensor and electronics package can be thought of as a black box that converts magnetic fields to a voltage, then amplifies the voltage with extremely high gain and low noise. The sensitivity of a SQUID magnetometer can be as high as 10^{-14} Tesla, and tests on samples can be performed in fields up to 5.5 Tesla, and temperatures between 2-400 K.

2.2 REFERENCES

Bonnell, D. A. and B. D. Huey, "Basic Principles of Scanning Probe Microscopy", *Scanning Probe Microscopy and Spectroscopy*, ed. D. A. Bonnell (Wiley-VCH, New York), 7-42 (2001).

Chescoe, D. and P. J. Goodhew, *The Operation of Transmission and Scanning Electron Microscopes*, Oxford University Press/Royal Microscopical Society, Handbook N° 20, U.K. (1990).

Goodhew, P. J. and F. J. Humphreys, *Electron Microscopy and Analysis*, 2nd ed. (Taylor & Francis, London), 39-153 (1988).

CHAPTER THREE

FABRICATION AND CHARACTERISATION OF SILK-FIBRE COMPOSITES INCORPORATING INORGANIC NANOPARTICLES

3.1 INTRODUCTION

In this chapter, nanoparticulate coating and infiltration of spider dragline silk is studied as a method for creating composite materials combining the high strength of natural silk with additional functionality. Dragline silk is dipped into a variety of inorganic nanocolloidal solutions with properties ranging from magnetic to conducting and semiconducting. The silk swells during the solvation process, allowing nanoparticles to infiltrate and/or coat the fibre prior to its withdrawal and drying. The strength and elasticity of the composite fibres are compared with natural silk, and microstructural studies are used to evaluate the uniformity and composition of the coatings. In particular, colloidal magnetite is used to prepare a magnetic silk composite that exhibits macroscopic magnetic behaviour while retaining the high elasticity and modulus of natural silk.

The primary goal of this work is to create composite materials combining the unique mechanical properties of dragline silk with physical properties such as magnetism, electrical conductivity, or semiconductivity. Composites with the high strength of dragline silk and electromagnetic functionality could find applications in areas as diverse as damage-sensitive 'smart' fabrics and microwave attenuation. The work described in this chapter has been published in Advanced Materials (Mayes, *et al.*, 1998).

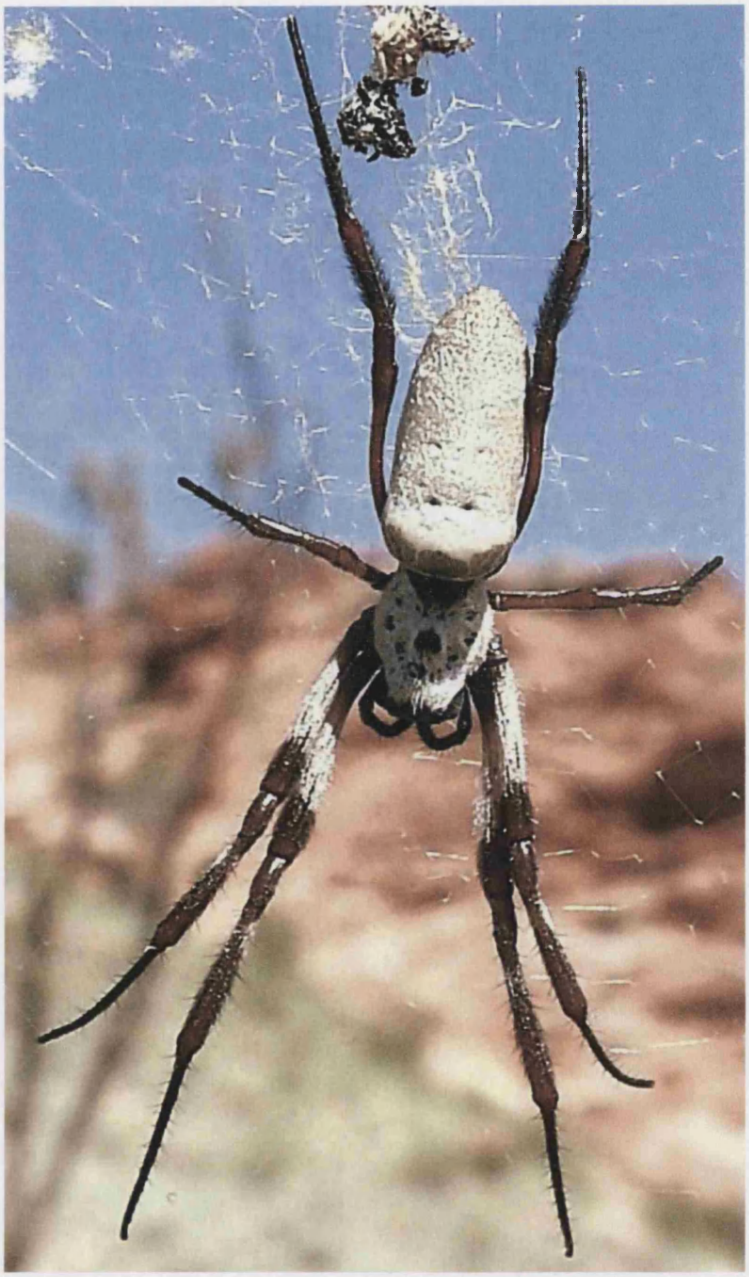

Figure 3.1 Female golden orb weaver, *Nephila edulis* found in eastern Australia (Reproduced with permission from Dr. Robert Raven, Queensland Museum).

Background

Spider dragline silk is a semi-crystalline biopolymer that exhibits a unique combination of high tensile strength, high elasticity and high modulus. The 0.2 to 10 μm diameter fibres have a higher breaking energy than other natural or synthetic fibrous polymers, even exceeding that of high tensile steel and *Kevlar* on a weight-for-weight basis (Gosline, *et al.,* 1986). These fibres have therefore been of great interest for impact-proof and structural fabrics. Moreover, combining these properties with the inherent biocompatibility of silk could produce tear-resistant biomaterials for use in artificial tendons or non-allergenic sutures (Colgin, *et al.,* 1995). A further possibility is to explore the integration of these inherent properties with those of other materials to produce composites for enhanced or entirely new applications. For example, cross-linking of dragline silk fibres with organic polymeric precursors produces an apparent improvement in tensile strength (Dunaway, *et al.,* 1995).

Silks produced by the silkmoths *Bombyx mori* and *Antheraea pernyi* have been used in textiles for centuries, prized for their softness and strength. Enhancing their value is the ability to bind a wide variety of chemical dyes, making them a key commodity of the fashion industry. Consequently, vast cultures of silkmoths constitute a large and profitable industry. Despite the success of silkmoth silk, spiders are the true silk experts, some producing over seven different silks for various applications (Gosline, *et al.,* 1986). In particular, orb-weaving Aranaeid spiders (so called for their production of circular, planar webs up to 1 meter in diameter which entangle prey in an orb of silk) are noted for their strong dragline silk (Figure 3.1). This silk is produced by the major ampullate glands and is used for the frame and radii of the orb

web, as well as the line on which the spider suspends itself. Dragline silk is also highly elastic which is essential to its role in capturing prey, allowing the web to absorb the kinetic energy of an insect while retaining its structure. The balanced properties of the strength and elasticity of dragline silk are due to a composite composition of ordered crystals within amorphous amino acid chains (Vollrath, 1992). Particularly these protein composites consist of crystalline polyalanine β-sheets surrounded by a flexible alanine-rich matrix, confirmed using ^{2}H and ^{13}C nuclear magnetic resonance (NMR) techniques (Simmons, *et al.,* 1994, Kümmerlen, *et al.,* 1996). The crystalline portion of the silk is 20 to 30% by volume, indicating that its cross-linking and reinforcement is important in determining overall structural properties (Simmons, *et al.,* 1996). At least two silk proteins, called fibroins or spidroins, are involved in dragline silk formation, and researchers have begun to map specific protein sequences to these structural regions (Guerette, *et al.,* 1996). Recent comparative analysis of spidroins has shown that their sequence has been highly conserved over nine taxa of *Araneae*, with four key amino acid motifs retained since the Mesozoic era (Gatesy, et al., 2001). However, protein sequence as the sole determinant of silk strength is insufficient.

Efforts to produce spidroins within *Escherichia coli* have yielded aqueous solutions with NMR spectra that resembled re-dissolved natural dragline silk. But the solutions could not be drawn into viable fibres, especially ones to match the mechanical characteristics of natural silk (Fahnestock, *et al.*, 1997). More recently recombinant spidroins have also been produced in potato and tobacco plants (Scheller, *et al.*, 2001). While methods for purifying the proteins make this approach attractive, no fibres were drawn. Researchers modelling the two structural

components have shown quantitatively that the tensile strength, elasticity and shape of the stress/strain curve of dragline silk can be accounted for without any assumptions about the structure of the amorphous chains (Termonia, 1994). However, the maximisation of a semi-ordered state of the amorphous regions around the periphery of the crystallites was shown to be critical. This semi-ordering may occur in the major ampullate glands where liquid-crystalline structure formation has been postulated (Viney, *et al.*, 1994). The glands may provide the structural constraints that determine the size distribution of the crystallites, as well their organisation parallel to the fibre axis. Catching spiders in the act, researchers have cryogenically quenched and microtomed major ampullate glands during the silk spinning process (Willcox, *et al.*, 1996). Subsequent TEM and AFM studies revealed a cholesteric liquid-crystalline phase of spidroins in the early duct of the major ampullate gland, though it is quite likely that further organisation occurs throughout the gland and passing from the spinneret.

The strength of dragline silk seems to be related to the weight of a spider, giving them a margin of safety in falling or escaping (Osaki, 1996). Indeed, experiments comparing the weight of spiders with their respective silk products found that spiders under an applied force produce thicker, stronger and stiffer silks. However, when normalized against the diameter of the silk, it was found that an increased diameter yielded a decreased stiffness (Vollrath and Holtet, *et al.,* 1996). This would not necessarily be expected if the liquid-crystalline structure was the sole component of the fibres. Although silk is a highly hydrophobic, insoluble biopolymer, it has recently been shown that dragline spider silk can undergo a reversible transformation to a super-contracted state when placed in water or polar organic solvents (Shao, *et*

al., 1997). Further, super-contraction in high molarity urea solutions indicated that dragline silk may consist of a fibril tube surrounding a thin core (Figure 3.2) (Vollrath, *et al.,* 1996). Although this structure might be induced by super-contraction, other experiments showed evidence of similar structures for non-contracted fibres. Experiments using AFM on microtomed sections of dragline silk revealed an amorphous inner core surrounded by a fibril-like outer core, both surrounded by a thin skin-like region (Li, *et al.*, 1993, Li, *et al.*, 1994). Indeed this larger-scale structure, combined with the two-component liquid-crystalline phase, may be the key to the extraordinary mechanical properties of dragline silk.

To date, the most successful efforts to produce artificial silks involved the transgenic expression of spidroins in mammalian cells. Bovine mammary epithelial alveolar cells were chosen to express the genes, and the resultant proteins were spun into fibres with mechanical properties similar to natural silks (Lazaris, *et al.*, 2002). The work was performed by Nexia Biotechnologies (Quebec, Canada), though it is ironic to note that bovine cells were used in the successful research rather than their hyped "proprietary transgenic goat technology". The strength of the silk was five to ten times less than native silk, and it remains likely that developing a system closer to natural spinnerets will be the key to producing the best fibres (Vollrath, *et al.*, 2001).

Inspired by the binding of chemical dyes to silkmoth silk, the main section of this work presents an approach to composite silk materials prepared by binding inorganic nanoparticles to the surface and near-surface regions by immersing fibres into colloidal solutions. Super-contraction in these aqueous solutions also offers the possibility of accessing inner binding sites, providing a general route to the

functionalisation of silk fibres. In the final section of this work, the introduction of inorganic nanoparticles into the silk fibre by drawing dissolved silks from solution is explored.

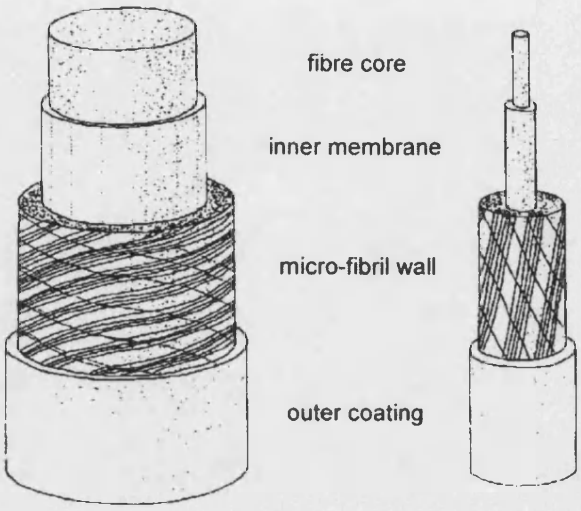

Figure 3.2 Model for the structural organisation of dragline silk. The left shows the super-contracted form, the right is the native state. (Courtesy of F. Vollrath)

Previous Work on Coated Fibres

As the work presented in this chapter was inspired by diverse research and disciplines, the most relevant themes should be summarised to clarify the background. Chemical modification of silk, binding of preformed and *in situ* nanoparticles to fibres, and exploiting the microstructure of fibres are those themes introduced below.

Binding other materials within silk has been performed in an un-contracted state, with researchers cross-linking dragline silk fibres with organic polymeric precursors producing an apparent improvement in the tensile strength (Dunaway, *et al.*, 1995).

While fibres with cross-linked epoxide indicated an enhancement in some samples, the improvements in strength and modulus were small compared to the intrinsic variability of these properties. While there was no statistically significant enhancement in the mechanical properties of the silk, a composite of a biological template and organic polymer was formed without degrading the performance of the fibres.

Magnetite (Fe_3O_4) and maghemite (γ-Fe_2O_3) nanoparticles have been bound to cellulose fibres for the preparation of magnetic paper (Marchessault, *et al.*, 1992). Coatings were prepared from both preformed and *in situ* oxidised nanoparticles, both of which displayed good adherence to the cellulose fibres. Other groups have expanded upon this work using polyester fibres with preformed nanoparticles of magnetite (Forder, *et al.*, 1993). Not only did the nanoparticles adhere to the fibres, but they were also used as a catalyst for a subsequent polymerisation reaction to form a polypyrrole/magnetite coating.

Hollow fibres are used in commercial reverse osmosis seawater desalination membranes and other filtration applications, and are prepared through a spinning process not unlike spider silk (Li, *et al.*, 1994). By forcing molten polymer through a triple orifice spinneret into a cooling bath, hollow fibres with an average diameter of 300 μm were prepared. While not used to bind material in the hollow central channel, these fibres display additional functionality stemming from their microstructure.

3.2 MATERIALS AND METHODS

Colloid Preparation

Four different inorganic colloids were selected for making silk composites. Two hydrophilic colloids were chosen, the first being nanoparticulate magnetite prepared according to Appendix 1. The second was a silica sol (Syton X30) supplied by Monsanto. Two hydrophobic colloids were selected; those being gold nanoparticles suspended in isopropanol and cadmium sulfide suspended in heptane prepared according to Appendices 2 and 3 respectively.

Preparation of Hydrophilic Colloid-Coated Silks

Dragline silk from the Major Ampullate glands of *Nephila edulis* was mechanically drawn from immobilized but fully awake spiders at a speed of 2 cm/s onto 1 cm diameter glass spools. Bundles of around 200 individual silk fibres were prepared by cutting parallel fibres of dragline silk from the 3 cm circumference spools. Initially, bundles of fibres were suspended by tweezers and mechanically lowered into either a water or 1:1 water/methanol sol of 10 to 20 nm diameter superparamagnetic magnetite (Fe_3O_4) particles for 2 minutes. Once it was determined that the colloid would adhere to the silk surface, single fibres were prepared by mounting them across a twin-pronged variable calliper, and mechanically submerging them into the nanocolloidal suspensions (Figure 3.3). After submersion, the fibres were slowly withdrawn from the colloidal sol and allowed to dry in air at ambient temperatures.

Mineralised fibres were embedded in epoxy resin and thin-sectioned for scanning electron microscopy (SEM) and energy dispersive X-ray (EDX) analysis studies

using a JEOL 6310 SEM operating at 20 kV. Samples of both magnetite preparations were analysed in cross-section for the K_α peak of iron.

Silica fibres were coated using an identical protocol, with the exception of the water/methanol solution. These fibres were not thin-sectioned for SEM, as the coating had very poor adherence. The fibres were prepared for mechanical testing as specified below.

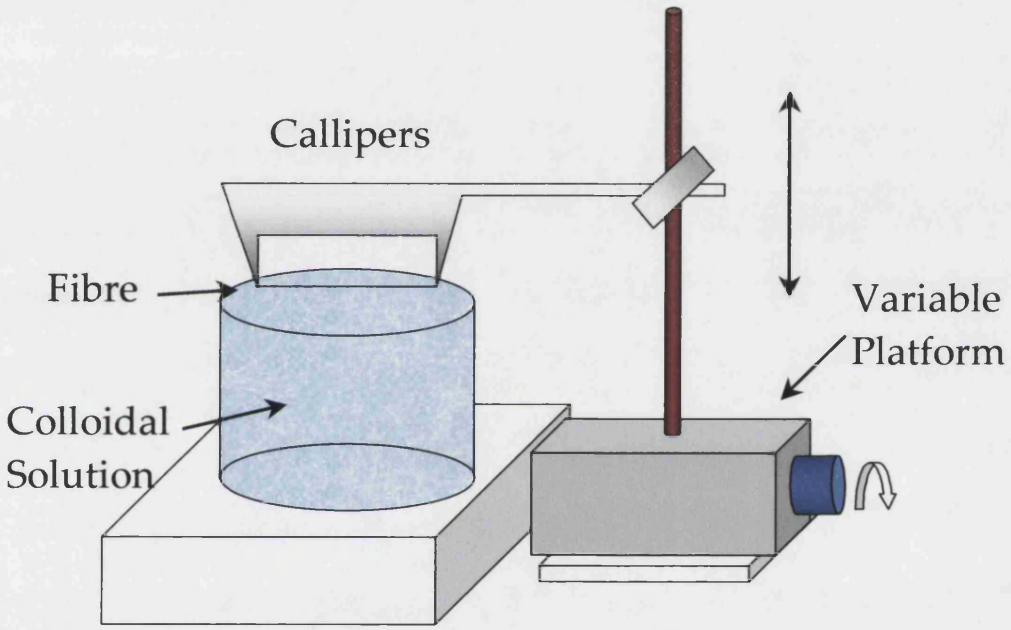

Figure 3.3 Apparatus for preparing silk fibre composites. Either single fibres or bundles are attached between the tines of the callipers, and then lowered into the solution for a set period.

Preparation of Hydrophobic Colloidal Coated Silks

Composites of silk and hydrophobic nanoparticles were prepared following the procedure described above. For gold composites, individual fibres mounted on twin-pronged callipers were submerged for 2 minutes in a sol of 3 nm gold particles that

were functionalized with *p*-mercaptophenol. Air drying of the dipped samples produced dark purple fibres with uniform and stable metal coatings. The gold coating was particularly resilient to subsequent washings with water and sonication. For cadmium sulphide composites, fibres were coated in hydrophobic 4.4 nm diameter particles of cadmium sulfide. Both composites were also prepared for mechanical testing in the procedure described below.

Mechanical Testing

Mechanical testing was performed on single fibres of the magnetite-silk composites, which were attached to the twin arms of a custom-built stress-strain gauge using cyanoacrylate adhesive (Kohler, *et al.*, 1995), with hysteresis cycles and breaking strength measurements performed at ambient conditions of 29 °C and 34 % relative humidity. The measured stress was normalised using average fibre diameters determined by SEM (mean diameter = 3.1 ± 0.5 μm). The custom stress-strain gauge consisted of a FORT 10 force transducer (World Precision Instruments) and a Pen Motor Assembly (Hewlett Packard).

Preparation of Polymer-Coated Silks

Silk fibres coated in the electrically conducting polymer polypyrrole were prepared by a two-step procedure employing Fe^{III}-catalysed oxidative polymerisation. Iron-coated fibres were prepared by dipping fibres in a 1 M $FeCl_3$ solution for 30 minutes and air-drying overnight. The resulting fibres were brown/yellow in colour after drying of the Fe^{III} salt solution. The fibres were mounted then submerged in pyrrole for 2 minutes, removed, then rinsed with water to quench polymerisation. After drying in air, dark greenish-black fibres coated in polypyrrole were produced.

Although the Fe^{III} layer appeared to be stable, the polymer coating could be partially removed by sonication or mechanical flexing.

Preparation of Artificial Silks

An alternative methodology was attempted to produce silk composites. Instead of using naturally drawn fibres, silk was first dissolved in a high molarity salt solution. A selection of colloids was then added to the dissolved silk solution, and "artificial" composite fibres were drawn from the solution using a wire hook. The most promising starting solution was prepared using calcium nitrate and methanol. A number of alternative salts were tested including Guanidine-Cl, LiBr, and LiCl/Urea, but none yielded fibres when combined with colloidal material.

3 mg of *Nephila edulis* silk was dissolved in $Ca(NO_3)_2$/ MeOH (1.5 ml, 6M). A 0.1 ml aliquot was then added to 5 ml of 1M NaCl in a petri dish. 20 µl of a colloidal suspension was mixed with the solution, and then fibres were readily drawn by plucking the surface of the solution with a wire hook (Figure 3.4). Once a fibre was hooked, it was transferred to a rotating microscope slide which drew fibres at a rate of 0.7 cm/s using an electric motor. This process was repeated for colloidal materials including magnetite, silica and gold. The best composite fibres were prepared with a 10% by volume additive fraction of colloid, as higher fractions appeared to mechanically overload the drawn silk. Finally, pyrrole was used in place of the colloidal material. It was hoped that exposing this composite fibre to an aqueous iron(III) salt would form polypyrrole within the fibre.

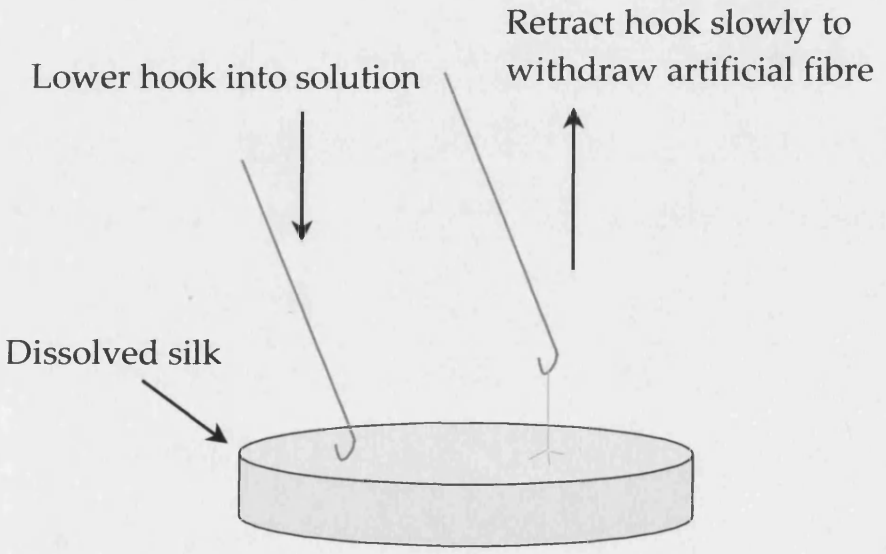

Figure 3.4 Schematic for drawing artificial silk fibres.

3.3 RESULTS

General Characteristics

Native dragline silks were either translucent white or golden yellow. The golden yellow silk comes from the same spider, but is a seasonal variation, apparently changing colour to match autumnal leaves (Osaki, 1989). For colloidal sols with dark colour (magnetite and gold), the fibres were obviously coated having taken on the respective colour of the sol. Silica coated fibres exhibited a bright white colouration which flaked during manipulation, indicating an even coating but with poor adherence. The cadmium sulphide fibres exhibited no visual differences to native silk. Regardless of coating or solvent, all fibres qualitatively retained their native strength and flexibility during manipulation.

Raising hopes of nanoparticle penetration throughout the silk fibre, all thin-sectioned native fibres showed high resin penetration when prepared for SEM cross-sectional studies. This was evidenced by the surface of the fibre matching the texture of the resin itself (Figure 3.5). In some cases, the fibre was mechanically torn by the sectioning knife, indicating an internal, fibril structure (Figure 3.6). The fibrils were oriented parallel to the fibre axis and 10-50 nm in diameter (Figure 3.6C), and appeared to be closely packed in regions, adhering to one another when torn apart.

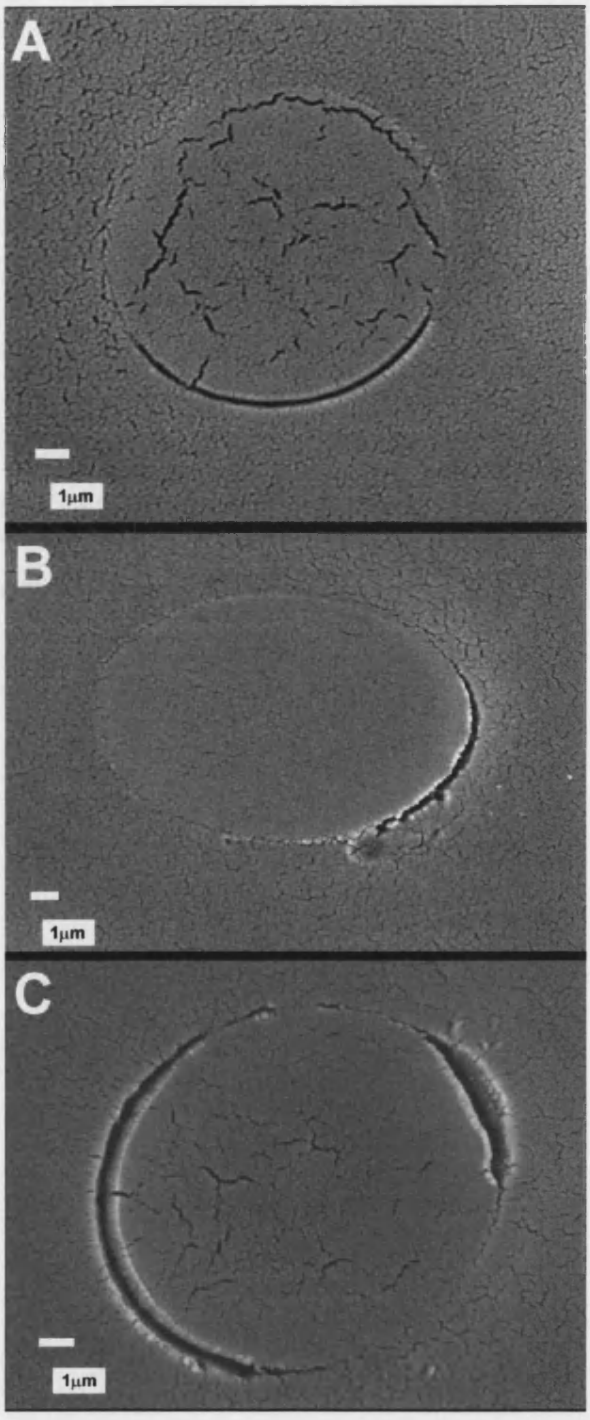

Figure 3.5 SEM cross-sections of bare dragline fibre, displaying complete resin infiltration. Scale bars = 1 μm.

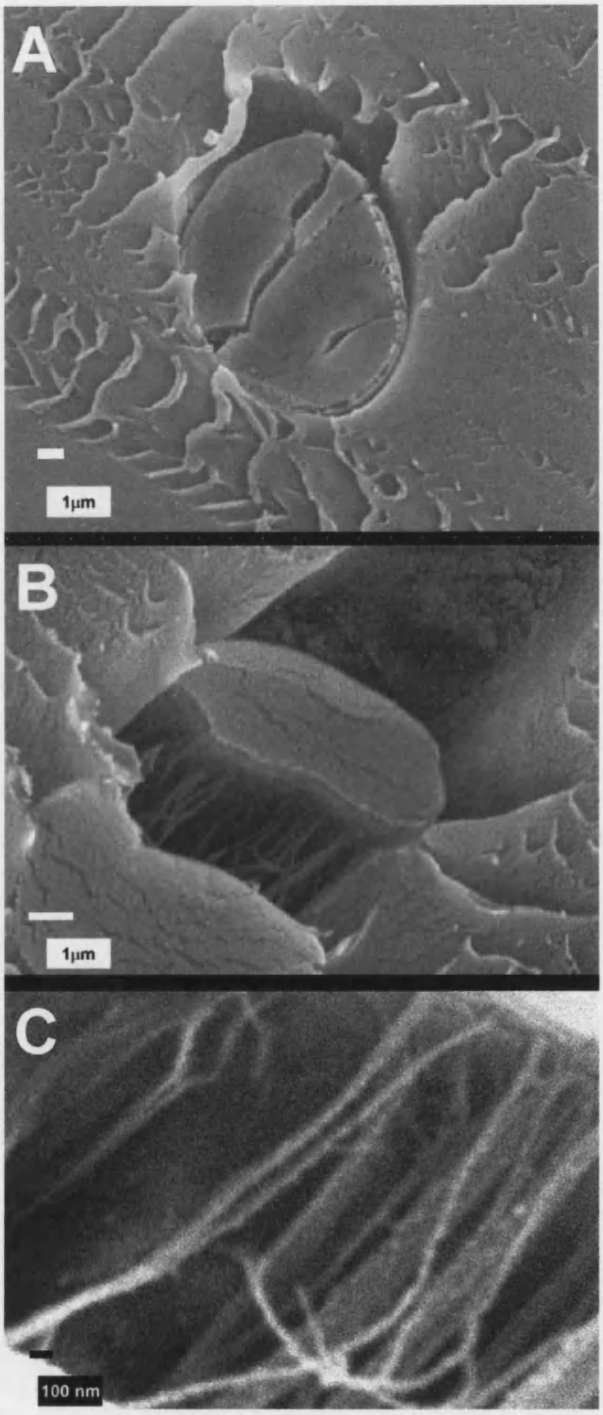

Figure 3.6 Progressive magnification SEM images of damaged fibre opening to reveal either fibrils or resin formed between fibrils. Fibres appear 10-50 nm in diameter. Top and middle scale bars = 1 µm, bottom bar = 100 nm.

Magnetite Coated Silks

Magnetite coated fibres were optically dark brown, but the colour of individual fibres proved difficult to capture on film. Depending on the orientation of the fibre to the light source, fibres appeared either dark brown or bright white/gold (Figures 3.7A and B respectively). However, when grouped in bundles, the mineralised colour could be captured (Figure 3.7C). The fibres had a very dense and coherent film of nanocrystallites over the surface (Figures 3.8A and B). Higher magnification (Figure 3.8C) showed that the magnetite-silk composites displayed some surface roughness, indicating that the thickness of the mineral films was substantial. However, the mineralised fibres retained their natural flexibility without significant disruption of the magnetite coating (Figure 3.8D). Moreover, the combination of intrinsic mechanical and fabricated magnetic properties enabled dried fibres to be oriented in the presence of an external magnetic field because fibres suspended against gravity tracked the position of a strong magnet. This was observed by fixing the fibres with tweezers in the presence of a 1.5 cm diameter neodymium-iron-boron slug (Figure 3.9).

The intensity of the iron K_α peak was recorded for the multiple cross-sections of the water and water/methanol-prepared samples. EDX analysis of sectioned magnetite-silk fibres showed high intensities for iron around and possibly within the surface regions of the composites (Figure 3.10). Analysis of the iron K_α peak intensities of cross-sectioned fibres showed that similar iron adherence was achieved for composites prepared from water or water/methanol solvents. Samples that were extensively washed in water or water/methanol for 2 minutes remained dark brown in colour but had reduced iron contents as shown by EDX analysis of cross-sectioned

material. Similar observations were made for magnetite-silk fibres that had been sonicated for 1 hour in water or water/methanol mixtures.

Stress-strain gauge measurements on individual magnetite-silk fibres showed negligible differences in mechanical properties between the native and composite fibres (Table 3.1). Magnetite composites prepared in water showed a 37% higher initial modulus compared with native or water/methanol-prepared silks (Figure 3.11). The breaking strengths for the composites and native silk were similar, but the water/methanol-prepared samples showed a 50% increase in breaking elongation compared to the water-only preparation (Figure 3.12). These mechanical properties were consistent with recent studies of *Araneus diadematus* dragline silk exposed to different solvents (Shao, *et al.*, 1997).

	Initial Modulus [x 10^9 N/m^2]	Breaking Strength [x 10^8 N/m^2]	Breaking Elongation [%]
Control Bare Silk	1.1 ± 0.1	2.5 ± 0.1	22 ± 2.0
Magnetite (H_2O)	1.5 ± 0.2	2.2 ± 0.3	18 ± 2.0
Magnetite (CH_3OH/H_2O)	1.1 ± 0.1	2.3 ± 0.2	28 ± 1.0
Gold	1.2 ± 0.3	2.8 ± 0.1	25 ± 7.0
Cadmium Sulfide	1.4 ± 0.3	2.2 ± 0.4	19 ± 2.0
Silica	1.9 ± 0.5	2.9 ± 0.3	22 ± 5.0

Table 3.1 Mechanical properties of *Nephila edulis* silk composites

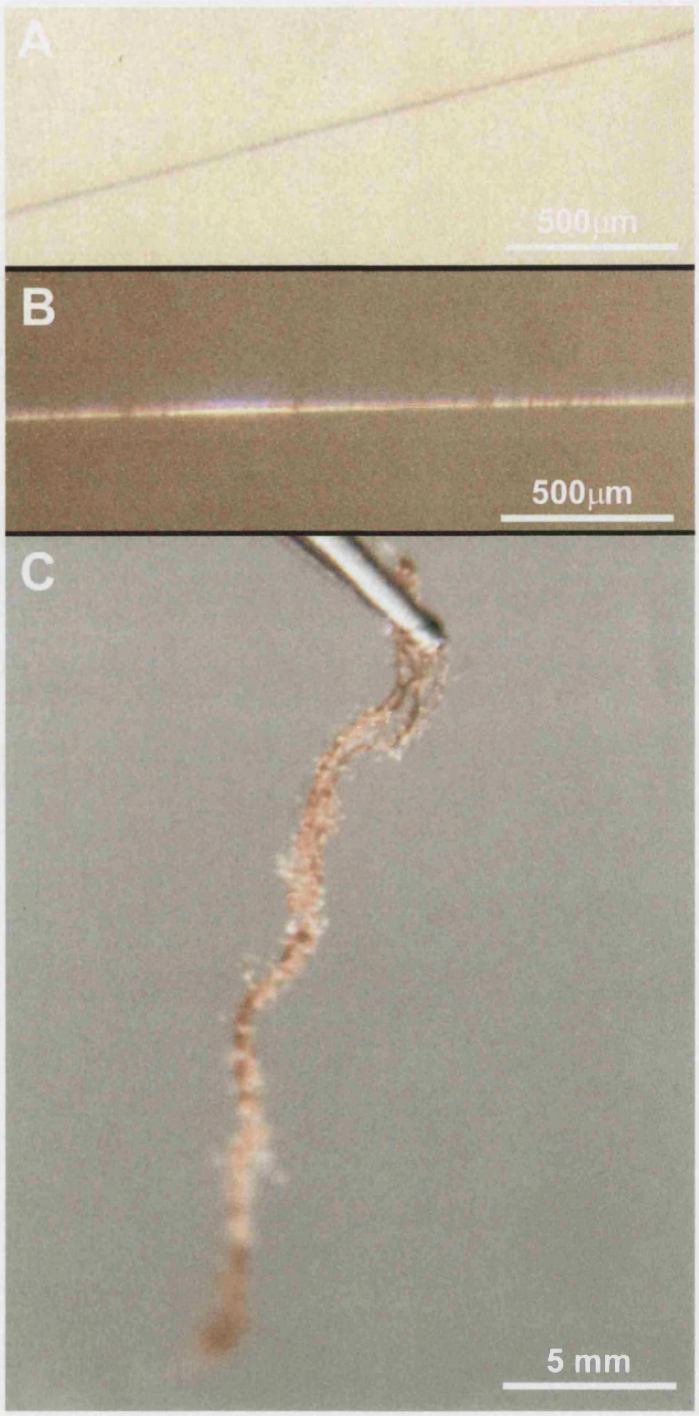

Figure 3.7 Optical micrographs of individual magnetite coated silk fibres (A,B) and fibre bundle (C).

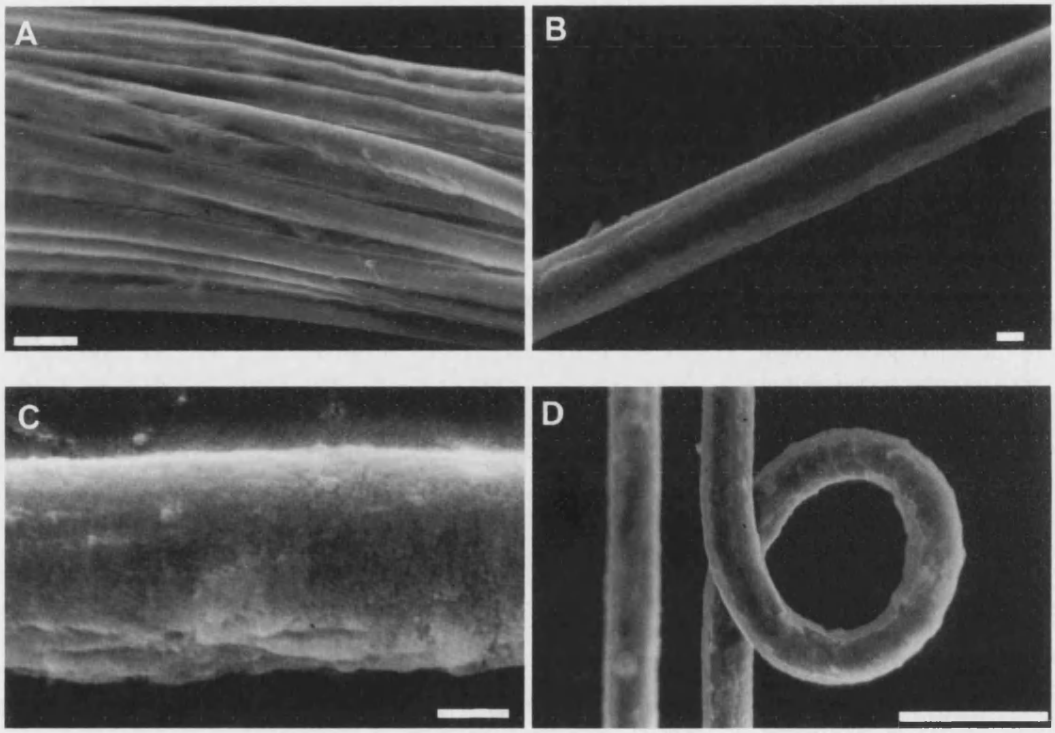

Figure 3.8 SEM images of magnetite-coated silk fibres. (a) low magnification image showing bundle of magnetite-coated spider silk fibres, scale bar = 10 μm. (b) individual silk fibre with magnetite surface film, scale bar = 1 μm. (c) higher magnification image showing surface texture of the magnetite layer, scale bar = 1 μm. (d) magnetite-silk fibre displaying retained flexibility without significant loss of the mineral phase, scale bar = 10 μm.

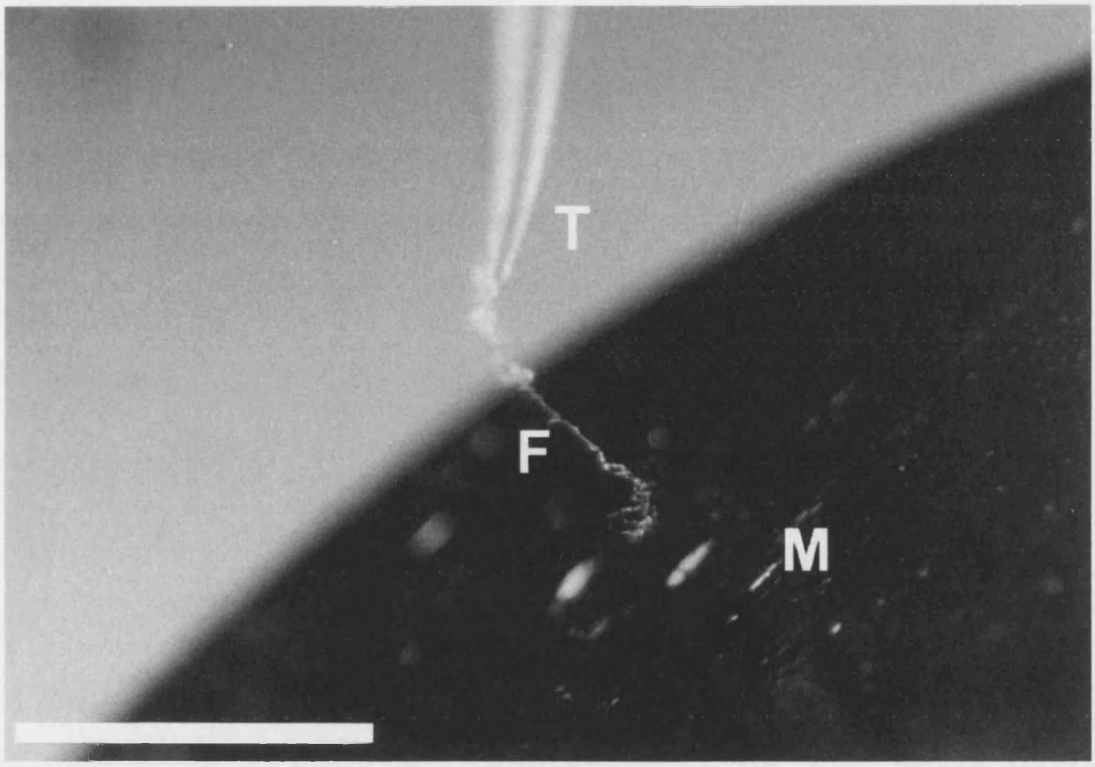

Figure 3.9 Optical image illustrating magnetic attraction of a magnetite-silk fibre (F) to an external magnet (M). The fibre is held on the end of vertically aligned tweezers (T). Scale bar = 5 mm.

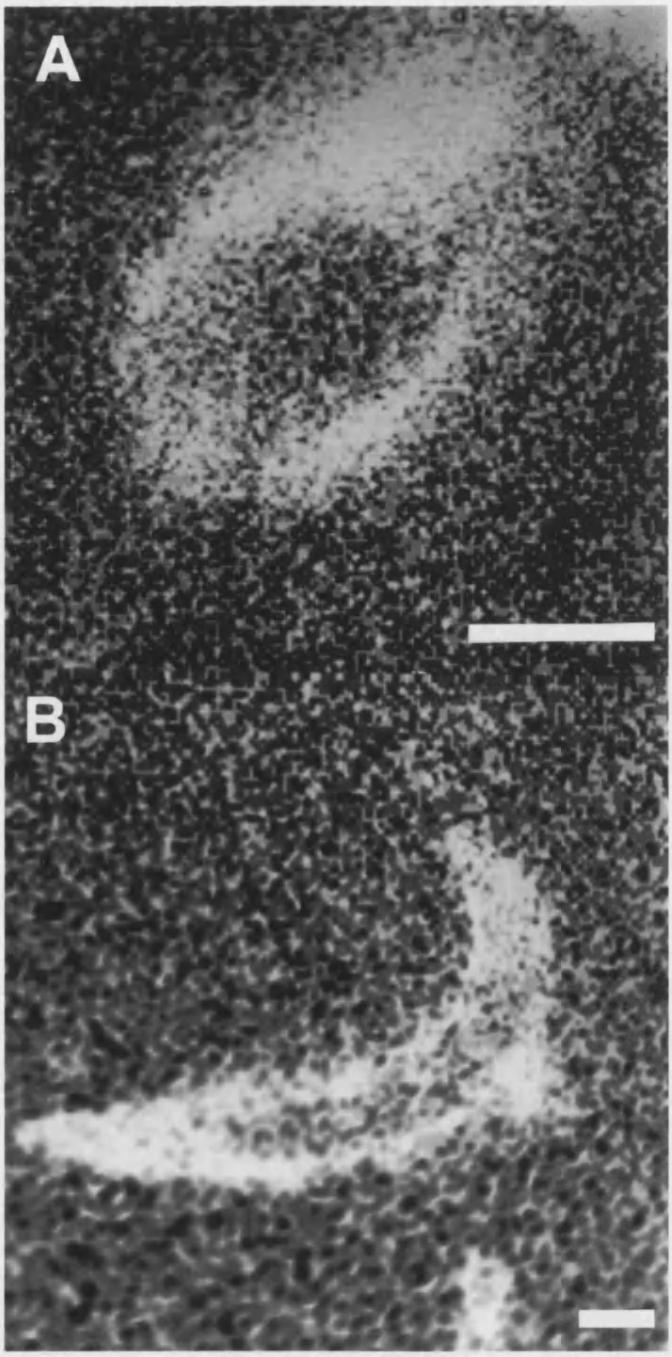

Figure 3.10 Energy dispersive X-ray spatial mapping images for iron in magnetite-silk fibres sectioned (a) approximately perpendicular to, and (b) oblique to the fibre axis. Both scale bars = 1 μm.

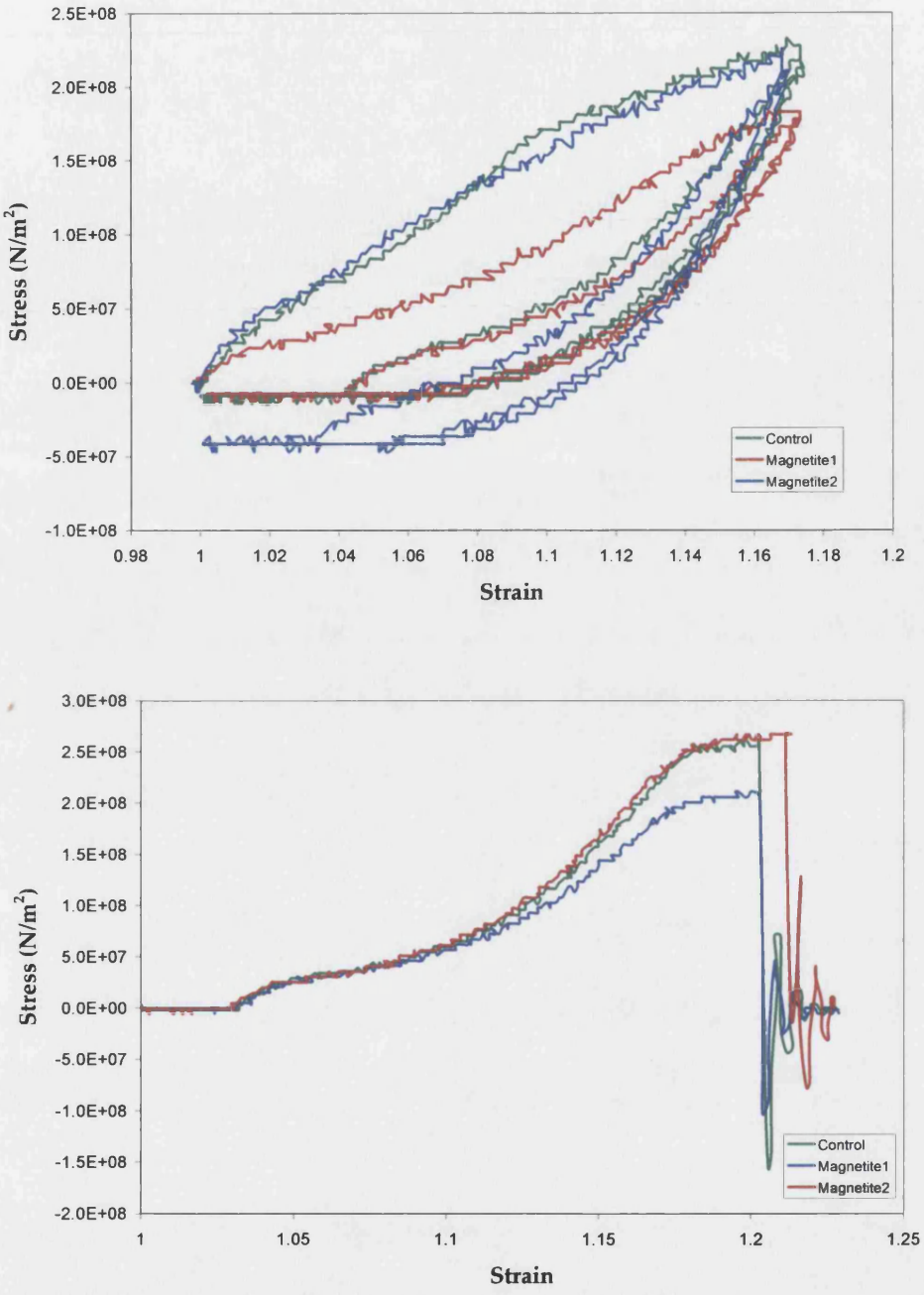

Figure 3.11 Stress-strain curves for a control (unmodified) silk fibre and magnetite-coated silk fibres showing (above) hysteresis, and (below) breaking points.

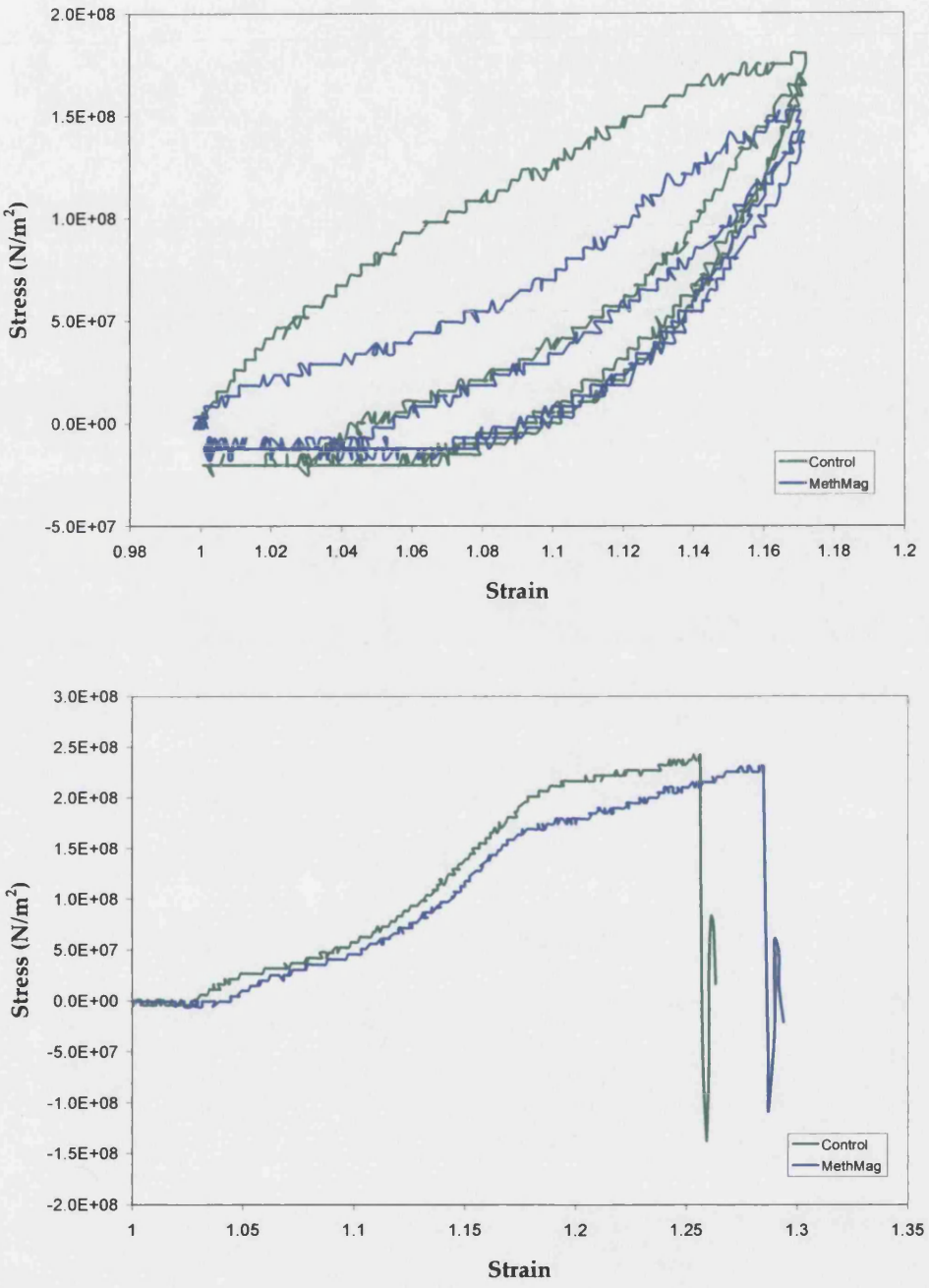

Figure 3.12 Stress-strain curves for a control (unmodified) silk fibres and magnetite in 1:1 methanol-coated silk fibre showing (above) hysteresis, and (below) breaking points.

Gold Coated Silks

Fibres coated with gold colloid were purple, and resistant to flaking or discolouration during flexing or sonication in water. SEM micrographs revealed a texture similar to the magnetite composites, though less rough indicating either a more uniform coverage or less material (Figure 3.13, top). EDX analysis of the fibres showed the characteristic strong K peaks for gold, even from focusing on single fibres (Figure 3.13, bottom). Mechanical testing showed an initial modulus and breaking strength similar to native silk (Figure 3.14 and Table 3.1). There may have been an increase in breaking elongation (Figure 3.14), though this is likely due to the slippage of the fibre within the glued support. Supporting this is that the fibre reached similar strain before breaking (Figure 3.14).

Cadmium Sulphide Coated Silks

Fibres coated with cadmium sulphide appeared optically no different to native silk. However, SEM micrographs revealed a smooth and continuous skin over the surface of the fibres (Figure 3.15). EDX analysis of the fibres showed characteristic peaks for cadmium sulphide (Figure 3.15, inset). Mechanical testing again showed similar initial modulus to native silk (Table 3.1), though samples were notably weaker. Many samples broke prior to testing, leaving only one for cycling comparison (Figure 3.16). That the fibres broke slightly earlier is due to their comparatively low breaking strength and elongation (Figure 3.16 and Table 3.1).

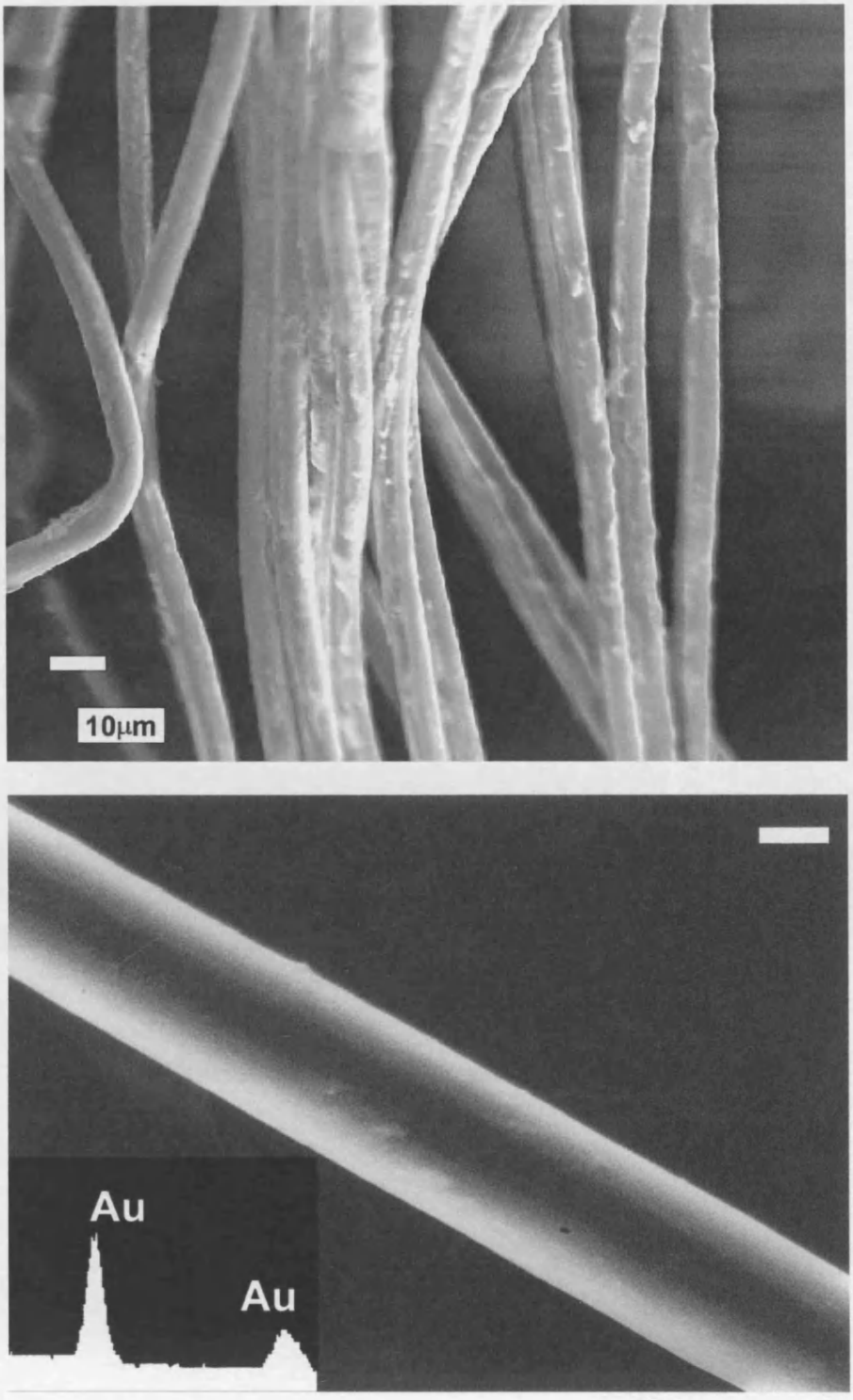

Figure 3.13 SEM images of silk fibre composites prepared with gold nanoparticles, with inset EDX analysis. Scale bar = 1 μm in lower micrograph.

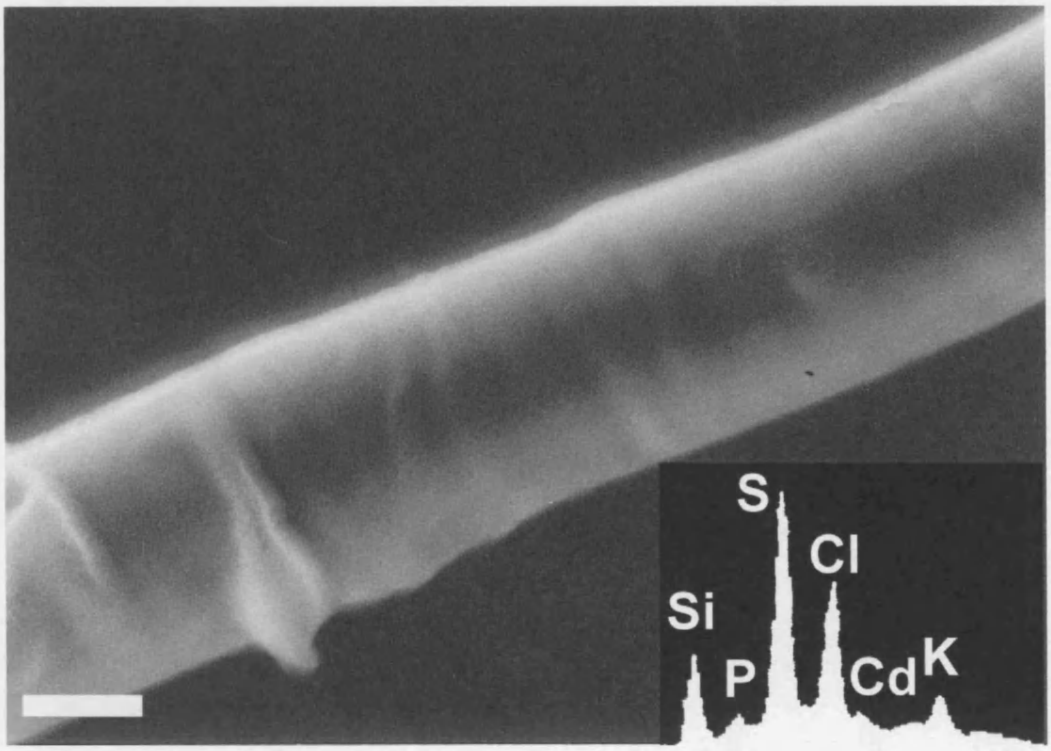

Figure 3.15 SEM image of silk fibre composite prepared with cadmium sulfide nanoparticles, with inset EDX analysis. Scale bar = 1 μm.

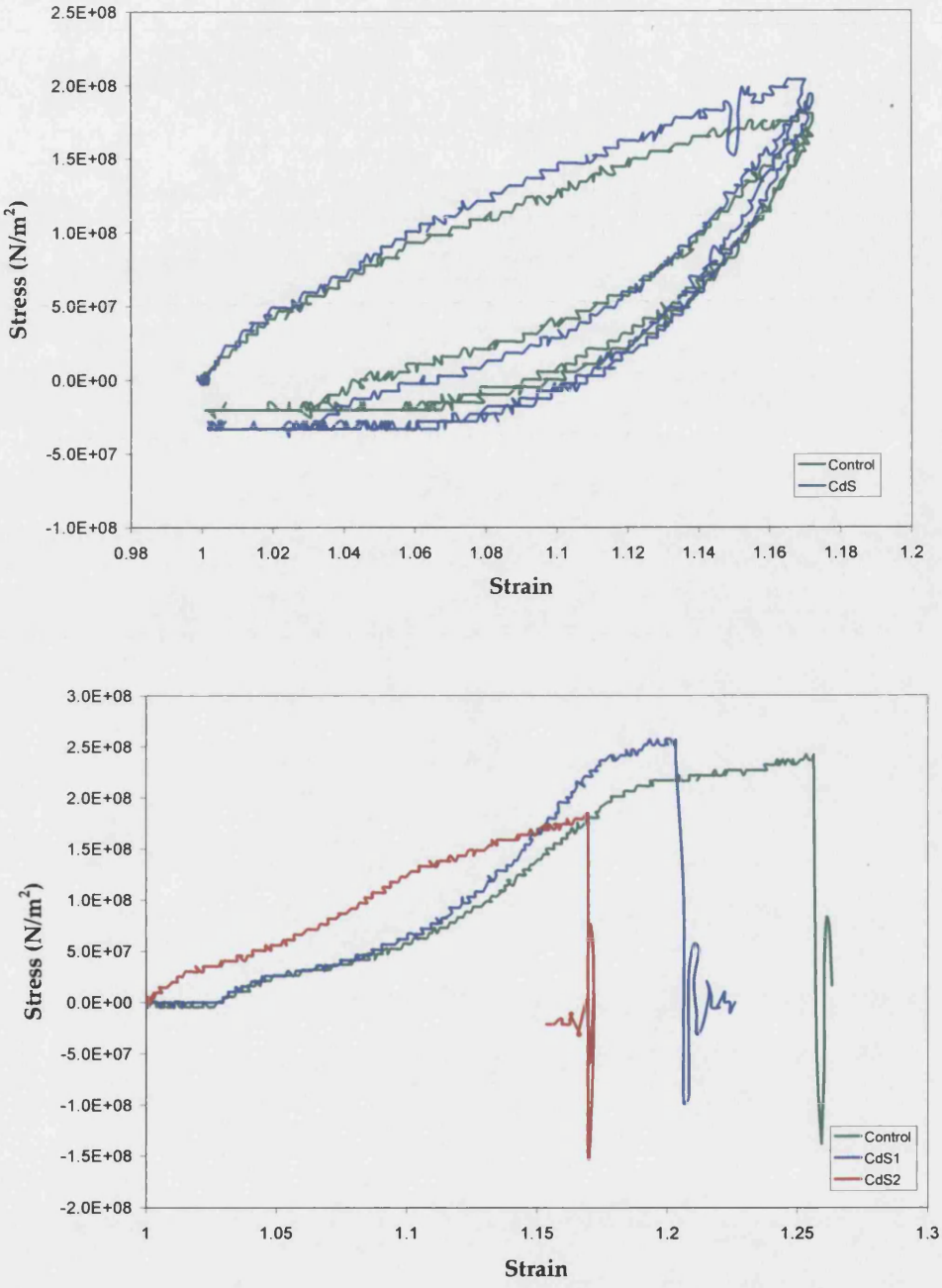

Figure 3.16 Stress-strain curves for a control (unmodified) silk fibre and cadmium sulfide-coated silk fibres showing (above) hysteresis, and (below) breaking points.

Silica Coated Silks

The silica coated fibre composite was optically bright white, but produced flakes during manipulation. SEM micrographs of the silk showed that it did not coat evenly, often producing flakes that would fall during microscopy (Figure 3.17). However, it did show a strong silica signal in EDX analysis (Figure 3.17, inset). Possibly the fibre remained coated with a thin skin of silica underneath the larger flaking material. Mechanically, it was broadly similar to the native fibre (Table 3.1 and Figure 3.18). The composite displayed a slightly higher initial modulus, possibly due to an enhanced support from a silica skin. If it did exist, this skin did not survive the cycling test (Figure 3.18), further supporting the complete flaking of silica from the fibre. There again appeared to be an increase in breaking elongation for one sample (Figure 3.18), but this is likely due to the slippage of the fibre within the glued support.

Polymer-Coated Silks

The silks were first coated with Fe(III) producing a yellow/brown silk which retained material during mechanical manipulation. After the composite was reacted with pyrrole, the fibres became dark green/black and material would flake during manipulation. SEM micrographs revealed a similar flaking structure with patchy coverage (Figure 3.19). EDX analysis showed characteristic peaks for iron (Figure 3.19, inset), indicating not all of the iron was lost during the polymerisation of pyrrole. The fibres were crudely tested for conductivity, but exhibited a very high resistance likely due to poor polypyrrole coverage. No mechanical tests of the polymer-coated silks were performed.

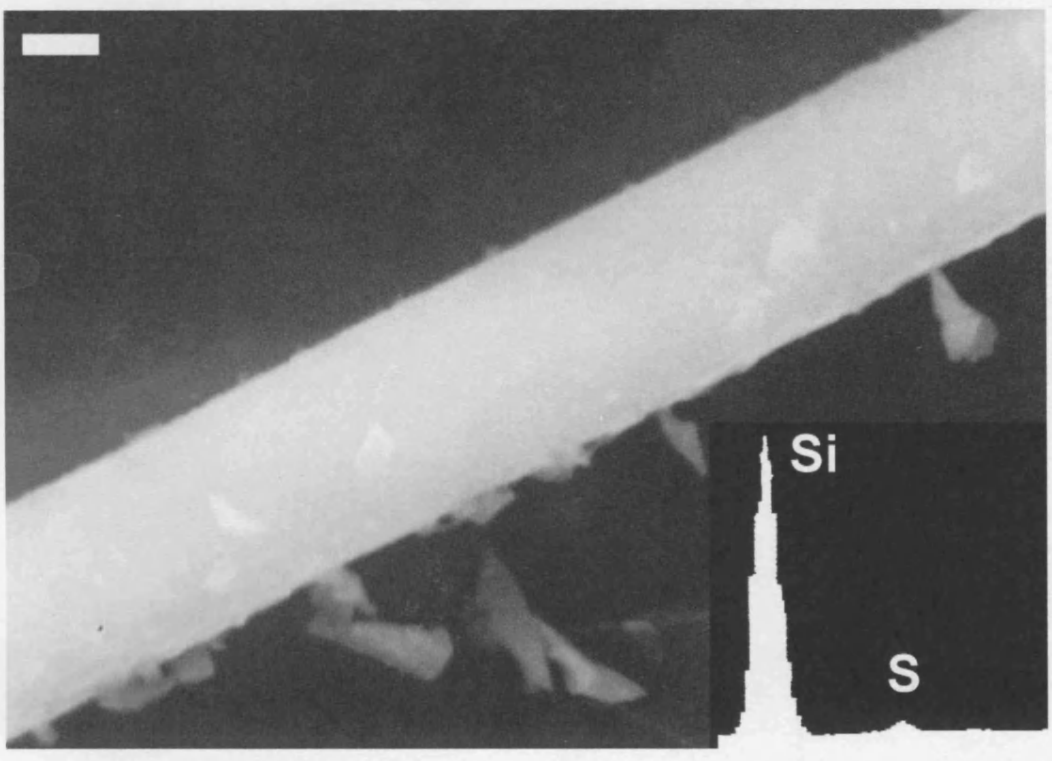

Figure 3.17 SEM image of silk fibre composite prepared with silica nanoparticles, with inset EDX analysis. Scale bar = 1 μm.

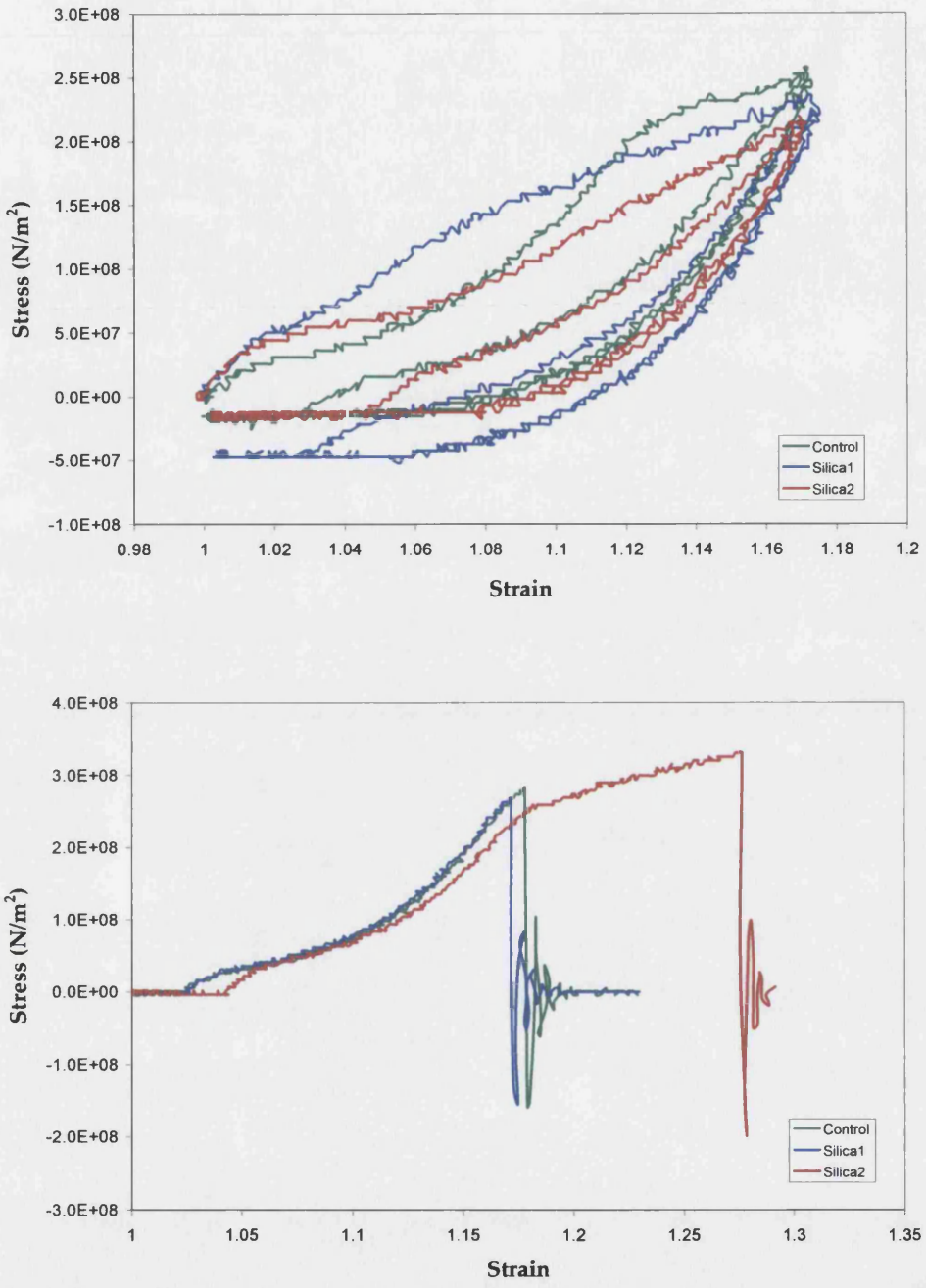

Figure 3.18 Stress-strain curves for a control (unmodified) silk fibre and silica-coated silk fibres showing (above) hysteresis, and (below) breaking points.

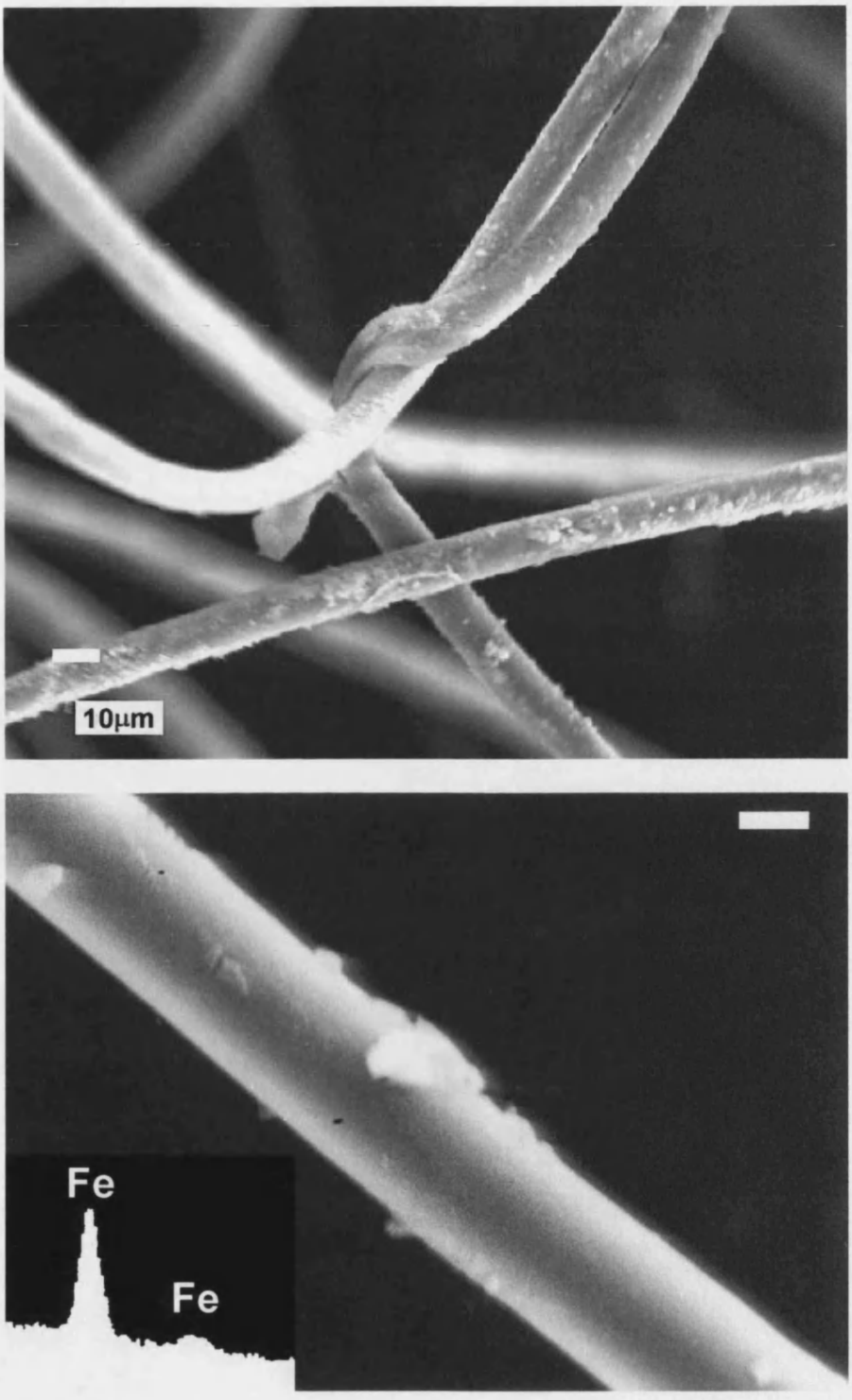

Figure 3.19 SEM images of silk fibre composites with precursor Fe(III) (top), and polypyrrole coating (bottom), with inset EDX analysis. Lower scale bar = 5 μm.

Artificial Silks

Artificial control silks were easily drawn from starting solutions, indicating a sufficient concentration for preparing composite fibres. Strong silks were prepared using a solution of Guanidine-Cl (6M) in Tris-Cl (50mM) at pH 8. But composite fibres could not be drawn when colloidal material was added, as the colloid would precipitate. Other salt solutions tested included LiBr and LiCl/Urea, but neither produced a self-supporting silk with or without colloidal material.

Only hydrophobic gold composite silks prepared in $Ca(NO_3)_2$/ MeOH were successfully drawn (Figure 3.20). Composites made with the hydrophobic gold colloid produced easily drawn silks that appeared to have gold homogeneously dispersed along the fibre. The fibres were not robust enough for embedding in resin and thin-sectioning, so whether the gold spread throughout the fibre is unknown. Both hydrophilic colloids (magnetite and silica) dispersed into the silk solution heterogeneously. While the magnetite colloid could draw, it would break upon drying in regions of heterogeneous magnetite concentration. The fibres drawn from these solutions were not very robust and produced very short fibres, though with characteristic colour in patches along the fibre. Pyrrole dispersed uniformly into the silk solution and produced smooth and easily drawn fibres, but the silk could not be introduced to an iron(III) solution without re-dissolving.

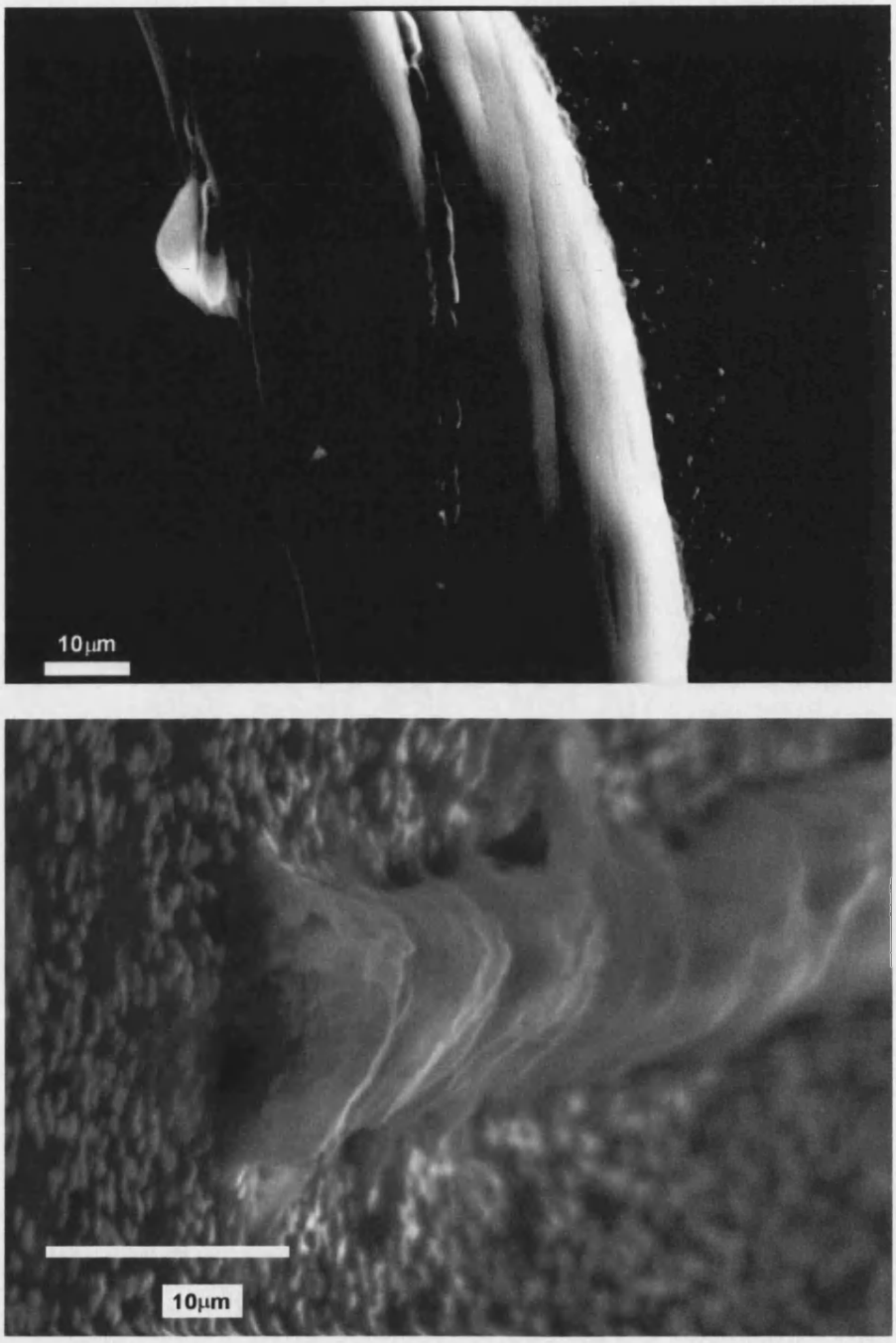

Figure 3.20 SEM images of artificially drawn silk incorporating colloidal gold.

3.4 DISCUSSION

Hydrophilic and Hydrophobic Colloid Adhesion Mechanisms

All of the composites fabricated indicate that mineral-coated silk fibres can be readily produced by a straightforward approach using nanoparticle suspensions. The method is versatile, easy to perform, and environmentally benign, suggesting that a wide range of silk-fibre hybrids could be routinely fabricated using this approach. Upon first consideration, the use of dragline spider silk as a fibrous template for the adsorption of magnetite nanoparticles into film coatings is somewhat surprising, as the hydrophobic nature of the biopolymer should be incompatible with the charged and hydrated nature of the iron oxide surfaces. Indeed, use of hydrophobic nanoparticles, such as ligand-capped gold or surfactant-encapsulated cadmium sulfide nanoparticles, dispersed in organic solvents improved the wetting and mechanical stability of the inorganic coatings. It remains the case, however, that the magnetite coatings were well-defined and relatively stable when adsorbed from aqueous solutions.

One possibility is that there are hydrogen bonding interactions at the oxide-silk interface. Recent observations have shown that immersion of spider silk fibres in water and other polar solvents induces reversible structural changes, consistent with hydrogen bonding networks within the near-surface structure of the silk (Shao, *et al.*, 1997). In principle, oxo- and hydroxyl species on the mineral surface could bind to polar amino acids that are exposed by interaction with solvent molecules. The collective outcome of such processes would be dependent on the binding site density that is probably enhanced by the nanoparticles having a relatively large number of polar surface sites due to the high surface area to volume ratio. Moreover, the small

dimensions appear to be important for determining the structural integrity of the coatings, presumably because the nanoparticles give rise to close packed and highly consolidated aggregates during drying. In contrast, coatings prepared from aqueous suspensions of sub-micrometer size particles, such as the colloidal silica, were extremely fragile and flaked off the silk fibres during manipulation of the sample. Similar considerations were discussed for nanocolloids used for the fabrication of ordered silica macrostructures within bacterial templates (Davis, *et al.,* 1997).

Solvent Effects on Breaking Strength and Elongation

Of the mechanical tests performed, the largest variances came from the water/methanol magnetite, hydrophobic gold, and hydrophilic silica composites. While these variances were notable, they were not generally outside the standard deviation for each mechanical parameter. However, for the silica composites, the initial modulus was consistently higher than native silk. This is likely due to a thick skin of self-supporting silica that is not chemically associated with the composite fibre. This is indicated by the cycling of the composite, which indicated a higher modulus but returned to at or below the characteristics of native silk (Figure 3.18). For hydrophobic gold and water/methanol magnetite composites, the breaking strength and breaking elongation were higher than native fibres respectively.

Previous research on the mechanical properties of dragline silk following contraction in solvents generally indicated reversible structural changes (Shao, *et al.*, 1997). However, the breaking strength and elongation increased after air-drying of fibres contracted in methanol, ethanol and butanol. Furthermore, both mechanical parameters increased with increasing solvent molecular weight. For the hydrophobic

gold composites, the breaking strength was consistently higher than native silk while the breaking elongation was within the standard deviation. The colloidal gold was suspended in isopropanol, which likely affected hydrogen bonding in crystalline regions the same as its alkane family. For the water/methanol magnetite composites, the breaking elongation was consistently higher than native silk while the breaking strength was within the standard deviation. Again, this partial increase is likely due to the breaking of hydrogen bonds with methanol. The increase in both breaking strength and elongation may be due to reorganisation of the crystalline regions upon drying, with the hydrogen bond disruption acting as an 'annealing' of the matrix. Indeed the lower initial modulus, but higher strength and elasticity indicate that some organisation may occur during the process of fibre testing. Evidence of such organisation would be seen in multiple hysteresis cycles over minor-loop stress-strain runs, and is suggested for future experiments.

Evidence for Fibril Structure

The coaxial silk structure proposed by Vollrath (Figure 3.2) (Vollrath, *et al.*, 1996), is supported by electron microscopy observations (Figure 3.6). SEM of sectioned, resin-embedded native silk revealed fibrils 10-50 nm in diameter parallel to the fibre axis. The fibrils appeared to be closely packed in regions, adhering to one another, though their composition could not be ascertained. Possibly they are biopolymer threads created by a particular type of spinneret during dragline formation, but they may be resin that was sculpted between even finer axial structures. It is unexpected that these structures appear across the middle section of the fractured fibre. It may be that the coaxial structures proposed are not valid, and dragline fibre consists solely of axially aligned fibrils. Perhaps the dissolving of the fibrils in high molarity

urea caused the amorphous core observed by Vollrath, but cores show in AFM observations did not expose the fibres to high salt solutions (Li, *et al.*, 1993, Li, *et al.*, 1994). The accidental shearing of the fibre during sectioning hints at a technique to further explore the proposed coaxial structure.

Artificial Silks and Composites

Those seeking to mass-produce dragline silk intend to draw it from solution as one would nylon. To do so potentially misses one important part of the silk formation process – the spinneret. However, assuming that the spinneret does nothing more than provide a narrow aperture in which the protein crystallites orient, the meniscus formed at the silk solution/air interface may serve an identical purpose. By dissolving natural silk in high salt concentrations, silks can be reconstructed as in Figure 3.4, though they lack the mechanical robustness of their native state. Many efforts have been made to identify and clone genes related to the production of silk (Hinman, *et al.*, 1992, Beckwitt, *et al.*, 1994, Prince, *et al.*, 1995, and Luciano, *et al.*, 1996). Others have expressed these genes and produced silk-like proteins that exhibit circular dichroism spectra matching dissolved natural dragline silk (Fahnestock and Irwin, *et al.*, 1997 and Fahnestock, *et al.*, 1997). However, none of these artificial silks have yet been drawn into fibres that identically match the properties of native silk. Likely, some micron-scale structure similar to the fibrils is essential to the mechanical performance of dragline silk and is induced by the spinneret. Any processes or additives that interfere with this micron-scale structure will likely decrease the strength and elasticity of fibres, so adding colloidal material is likely to produce weak silks. Possibly colloids may be injected at the time of silk formation at the spinneret to achieve strong silks with enhanced functionality.

3.5 REFERENCES

Beckwitt, R. and S. Arcidiacono, "Sequence Conservation in the C-terminal Region of Spider Silk Proteins (Spidroin) from *Nephlia clavipes* (Tetragnathidae) and *Araneus bicentenarius* (Araneidae)", *J. Biol. Chem.*, **269**(9), 6661-6663 (1994).

Colgin, M. A., and R. V. Lewis, "Spider silk: a biomaterial for the future", *Chem. and Ind.*, **12**, 1009-1012 (1995).

Davis, S. A., S. L. Burkett , N. H. Mendelson, and S. Mann, "Bacterial templating of ordered macrostructures in silica and silica-surfactant mesophases", *Nature*, **385**, 420-423 (1997).

Dunaway, D. L., B. L. Thiel and C. Viney, "Tensile Mechanical Property Evaluation of Natural and Epoxide-Treated Silk Fibers", *J. Appl. Polym. Sci.*, **58**, 675-683 (1995).

Fahnestock, S. R. and S. L. Irwin, "Synthetic spider dragline silk proteins and their production in *Escherichia coli*", *Appl. Microbiol. Biotechnol.*, **47**, 23-32 (1997).

Fahnestock, S. R. and L. A. Bedzyk, "Production of synthetic spider dragline silk protein in *Pichia pastoris*", *Appl. Microbiol. Biotechnol.*, **47**, 33-39 (1997).

Forder, C., S. P. Armes, A. W. Simpson, C. Maggiore, and M. Hawley, "Preparation and Characterisation of Superparamagnetic Conductive Polyester Textile Composites", *J. Mater. Chem.*, 3(6), 563-569 (1993).

Gatesy, J., C. Hayashi, D. Motriuk, J. Woods, and R. Lewis, "Extreme Diversity, Conservation, and Convergence of Spider Silk Fibroin Sequences", *Science*, **291**, 2603-2605 (2001).

Guerette, P. A., D. G. Ginzinger, B. H. F. Weber, and J. M. Gosline, "Silk Properties Determined by Gland-Specific Expression of a Spider Fibroin Gene Family", *Science*, **272**, 112-115 (1996).

Gosline, J. M., M. E. Demont, and M. W. Denny, "The structure and properties of spider silk", *Endeavour*, **10**, 37-43 (1986).

Hasegawa, I., T. Nakamura, S. Motojima, and M. Kajiwara, "Silica Gel-Phenolic Resin Hybrid Fibres: New Precursors for Continuous β-Silicon Carbide Fibres", *J. Mater. Chem.*, **5**(1), 193-194 (1995).

Hinman, M. B. and R. V. Lewis, "Isolation of a Clone Encoding a Second Dragline Silk Fibroin", *J. Biol. Chem.*, **267**(27), 19320-19324 (1992).

Köhler, T. and F. Vollrath, "Thread biomechanics in the two orb weaving spiders *Araneus diadematus* (Araneae, Araneidae) and *Uloborus walckenaerius* (Araneae, Uloboridae)", *J. Exp. Zool.*, **271**, 1-17 (1995).

Kümmerlen, J., J. D. van Beek, F. Vollrath, and B. H. Meier, "Local Structure in Spider Dragline Silk Investigated by Two-Dimensional Spin-Diffusion Nuclear Magnetic Resonance", *Macromolecules*, **29**, 2920-2928 (1996).

Lazaris, A., S. Arcidiacono, Y. Huang, J-F. Zhou, F. Duguay, N. Chretien, E. A. Welsh, J. W. Soares, and C. N. Karatzas, "Spider Silk Fibers Spun from Soluble Recombinant Silk Produced in Mammalian Cells", *Science*, **295**, 472-476 (2002).

Li, S. F. Y., A. J. McGhie, and S. L. Tang, "New Internal Structure of Spider Dragline Silk Revealed by Atomic Force Microscopy", *Biophys. J.*, **66**, 1209-1212 (1994).

Li, S. F. Y., A. J. McGhie, and S. L. Tang, "Comparative study of the internal structures of Kevlar and spider silk by atomic force microscopy", *J. Vac. Sci. Technol. A*, **12**(4), 1891-1895 (1994).

Li, S. G., G. H. Koops, M. H. V. Mulder, T. van den Boomgaard, and C. A. Smolders, "Wet spinning of integrally skinned hollow fiber membranes by a modified dual-bath coagulation method using a triple orifice spinneret", *J. Membrane Sci.*, **94**, 329-340 (1994).

Luciano, E. and G. C. Candelas, "An alanine tRNA gene cluster from *Nephlia clavipes*", *Gene*, **171**, 301-302 (1996).

Marchessault, R. H., P. Rioux, and L. Raymond, "Magnetic cellulose fibres and paper: preparation, processing and properties", *Polymer*, **33**(19), 4024-4028 (1992).

Mayes, E. L., F. Vollrath, and S. Mann, "Fabrication of Magnetic Spider Silk and Other Silk-Fiber Composites Using Inorganic Nanoparticles", *Adv. Mater.*, **10**(10), 801-805 (1998).

Osaki, S., "Seasonal Change in Color of Spiders' Silk", *ACTA Arachnol.*, **38**, 21-28 (1989).

Osaki, S., "Spider silk as mechanical lifeline", *Nature*, **384**, 419 (1996).

Prince, J. T., K. P. McGrath, C. M. DiGirolamo, and D. L. Kaplan, "Construction, Cloning, and Expression of Synthetic Genes Encoding Spider Dragline Silk", *Biochemistry*, **34**, 10879-10885 (1995).

Scheller, J., K-H. Gührs, F. Grosse, and U. Conrad, "Production of spider silk proteins in tobacco and potato", *Nature Bio.*, **19**, 573-577 (2001).

Shao, Z. and F. Vollrath, "Mechanics of spider silk during and after contraction in selected solvents", *Inst. Mater. (London),* 262-265 (1997).

Simmons, A. H., E. Ray, and L. W. Jelinski, "Solid-State ^{13}C NMR of *Nephlia clavipes* Dragline Silk Established Structure and Identity of Crystalline Regions", *Macromolecules*, **27**, 5235-5237 (1994).

Simmons, A. H., C. A. Michal, and L. W. Jelinski, "Molecular Orientation and Two-Component Nature of the Crystalline Fraction of Spider Dragline Silk", *Science*, **271**, 84-87 (1996).

Termonia, Y., "Molecular Modeling of Spider Silk Elasticity", *Macromolecules*, **27**, 7378-7381 (1994).

Viney, C., A. E. Huber, D. L. Dunaway, K. Kerkam, and S. T. Case, "Optical characterization of silk secretions and fibers", *Silk polymers: materials science and biotechnology*, D. Kaplan, W. W. Adams, B. Farmer, and C. Viney (eds), ACS, **544,** 128-136 (1994).

Vollrath, F., "Spider Webs and Silks", *Sci. Amer.*, 52-58 (1992).

Vollrath, F., T. Holtet, H. C. Thoegersen, and S. Frische, "Structural organization of spider silk", *Proc. R. Soc. Lond. B*, **263**, 147-151 (1996).

Vollrath, F. and T. Köhler, "Mechanics of silk produced by loaded spiders", *Proc. R. Soc. Lond. B*, **263**, 387-391 (1996).

Vollrath, F. and D. P. Knight, "Liquid crystalline spinning of spider silk", *Nature*, **410**, 541-548 (2001).

Willcox, P. J., S. P. Gido, W. Muller and D. L. Kaplan, "Evidence of a Cholesteric Liquid Crystalline Phase in Natural Silk Spinning Processes", *Macromolecules*, **29**, 5106-5110 (1996).

CHAPTER FOUR

FABRICATION AND CHARACTERISATION OF MAGNETIC BIONITE STRUCTURES

4.1 INTRODUCTION

In the previous chapter, the coating of individual fibres of spider silk with magnetic nanoparticles was described. In this chapter a template offering internal porosity and a greater number of binding sites is used to form magnetic composite threads with a higher loading of material. These composites are called bionites, formed from a mutant strain of the rod-shaped bacterium *Bacillus subtilis*. This strain exhibits suppressed cell separation and can only grow by extension along its long axis to produce multicellular filaments that twist back upon themselves in braids. These braids, or macrofibres, are drawn from solution and dried to form brittle threads 10-20 μm in diameter. These threads are in turn dipped into nanoparticulate solutions of magnetite, swelling in the process to absorb the inorganic material between filaments. The resulting composites are dried to form magnetic bionites, which are characterised using a variety of microscopies and magnetometries.

The primary goal of this work is to characterise magnetic bacterial thread composites, assessing whether their bulk magnetic properties are enhanced during preparation. The work described in this chapter has been published in a series of articles (Davis, *et al.*, 1998, Field, *et al.*, 1998, and Smith, *et al.*, 1998).

Background

Bacillus subtilis is a rod-shaped prokaryotic organism 0.8 μm in diameter and up to 4 μm long. Growth of the bacterial rods proceeds by elongation at a constant diameter followed by periodic partitioning, the ends of the rod being capped with hemispherical poles formed during separation. The 30-40 nm thick cell wall acts as a protective layer between the cell and its environment, allowing passage of all metabolites (Graham, *et al.*, 1994). The Gram-positive wall is typical of prokaryotes in that it comprises the polymeric components of peptidoglycan and teichoic acid. Peptidoglycan is unique to bacteria, providing strength when covalently linked to teichoic acid (Mendelson, 1990). The backbone of peptidoglycan consists of up to 100 repeating disaccharides containing N-acetyl glucosamine and N-acetyl muramic acid. Peptides that can cross-link to one another protrude from each N-acetyl muramic acid residue. These peptides cross-link in an intricate network, interconnected to form a gel-like complex (Mendelson, 1990). Non-crosslinked peptides each have three free carboxyl- and one free amino group, while crosslinked peptides have two additional free carboxyl groups. The teichoic acid component is distributed on the external surface of the well wall, with roughly half of the molecules available for solvation (Doyle, *et al.*, 1975). Phosphate groups of the teichoic acid residues and carboxylate groups of the peptidoglycan contribute to an overall electronegative charge density of the cell wall. Further, peptidoglycan contains hydroxyl and amino functional groups. This combined negative charge density is responsible for a strong metal binding capacity. Indeed the binding capacity of cell walls is often as high as that of commercially available ion exchange resins (Marquis, *et al.*, 1976). However, it is the carboxylate groups in the peptide

moiety of peptidoglycan that are believed to be the primary sites for metal binding (Doyle, *et al.*, 1980).

Bacterial macrofibres are formed from cells of a mutant strain (FJ7) of *Bacillus subtilis*. Lysozyme normally aids in separating the cells, but autolysin activity is reduced in this mutant bacterial strain. The cells therefore grow one-dimensionally through cylinder elongation at a constant diameter (Mendelson, 1992). As each cell grows, it exhibits a slight helical twist in relation to its parent. The resulting chain of cells progresses to a two-dimensional form by bending and twisting, finally becoming a three-dimensional macrofibre when it twists into a helical form (Figure 4.1). This process is self-limiting, growing until it is restricted by geometry, mechanical (fibre stiffness) or physiological (nutrient availability) restraints (Mendelson, 1996). Webs of macrofibres can be mechanically drawn from solution that close-pack at the air/solution interface. When air-dried, a mechanically rigid thread of axially-aligned, multi-cellular filaments is produced. Threads of uniform diameter can be drawn up to 1 m long, with a typical thread containing an estimated 50,000 filaments and at least 10^{10} cells (Thwaites, *et al.*, 1990). Similar to the dragline silk work, stress-strain studies have been performed on these threads (Thwaites, *et al.*, 1989, Thwaites, *et al.*, 1991, and Mendelson, *et al.*, 1989). When dry, the tensile strength and modulus are about 300 MPa and 20 GPa respectively. Although substantially thicker, it is notable that these figures are half that of the strength and modulus of native dragline silk (875 MPa and 11 Gpa respectively). However, such comparison does not extend to hydrated threads.

Bionites are composite materials produced by mineralising these bacterial thread complexes. Previously, bionites have been prepared using two methods. The first was by introducing soluble metal salts into cultures of *Bacillus subtilis*, exploiting the metal-binding carboxylate groups. Salts of $FeCl_3$, $CaCl_2$ or $CuCl_2$ were incorporated into the cultures, with the metal content present throughout the fibre at 6-10 wt% (Mendelson, 1992). The second method involved incorporating preformed colloids into the native or pre-washed fibre-like complex. In this chapter, this second method is used for the preparation of magnetic bionites. Using preformed colloids of spherical magnetite, magnetic bionites were formed and their structure and magnetic characteristics analysed. Anisotropic magnetic behaviour was seen, though unexpected for the isotropic, superparamagnetic magnetite. Possible mechanisms affecting this anisotropy in the magnetite colloid are discussed.

Previous Work on Preformed-Colloidal Bionites

Bionites integrating preformed colloids of silica, magnetite, gold, titania, alumina and the protein ferritin have been prepared in the past (Davis, 1996 and Davis, *et al.*, 1997). With the exception of ferritin, all of the colloids infiltrated the internal microstructure of the fibres, remaining intact even after re-immersing in solution. The mechanism proposed for infiltration is the swelling of the bacterial thread upon dipping it into a colloidal suspension. In pure water, a bacterial thread increases its width by 1.2 times and length by 1.4 times, yet does not fully unravel. The filaments of the thread with their negative surface charges are exposed to the colloidal particles. Mutual negative charges force the particles to infiltrate between the filaments of the thread, rather than deposit onto their surfaces. Bionites prepared

with silica colloid even proved to be self-supporting after calcining the organic components away (Davis, *et al.*, 1997).

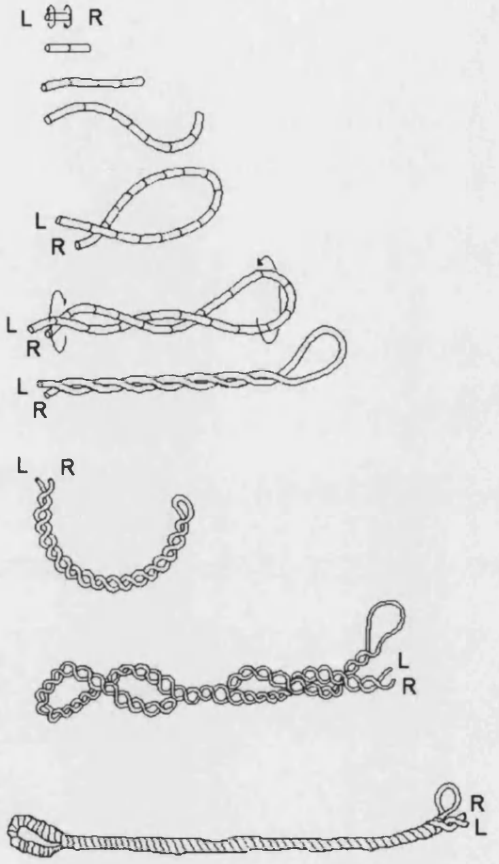

Figure 4.1 Folding pathway of the bacterial thread into a macrofibre (Mendelson, 1990).

While magnetite colloid has been used in the preparation of bionites, full magnetic characterisation was not performed. Indeed, the only method for assessing the magnetic properties of the composite was to suspend the bionite from a magnet. In this chapter, a series of magnetic bionites is prepared with a preformed colloidal magnetite. The resulting composites are fully characterised, and unexpected behaviour is shown and discussed.

4.2 Materials and Methods

Colloid Preparation

A colloidal magnetite (Fe_3O_4) solution was prepared as detailed in Appendix 1.

Preparation of Bacterial Threads

An FJ7 strain of *Bacillus subtilis* was supplied by N. H. Mendelson (Department of Molecular and Cellular Biology, University of Arizona, Tucson). The strain was grown into a culture at 20°C in 8 ml of "Terrific Broth" medium, contained in a sterilised plastic 100x15 mm petri dish. After 24 hours of growth, threads were prepared by drawing multi-cellular filaments from the culture with a nickel-chrome wire hook (Figure 4.2). At the air/solution interface, many filaments were compressed into a thread with parallel strands organised into a pseudo-hexagonal array. The resulting threads were subsequently air-dried, suspended from a solid support for 24 hours. Upon drying they took the form of threads ~20 cm long and 10-20 μm in diameter.

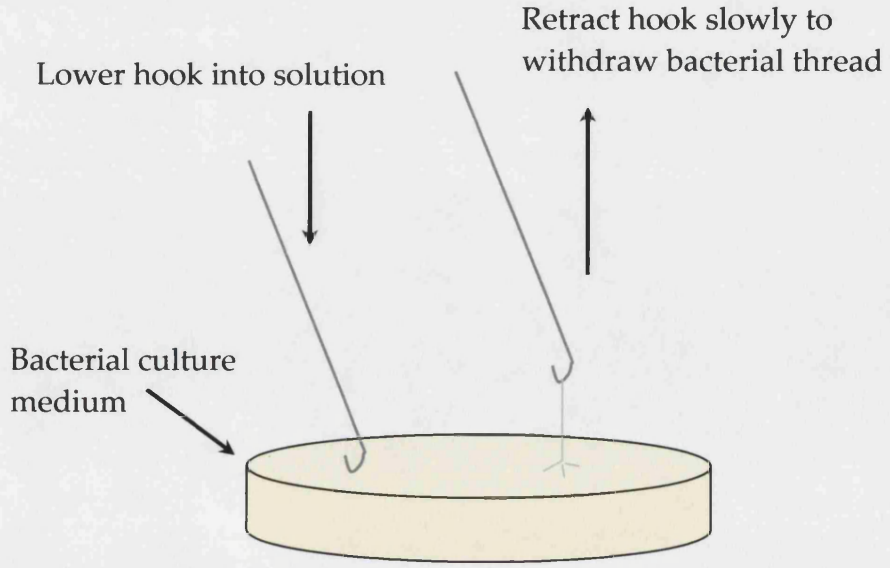

Figure 4.2 Preparation of bacterial threads by constant velocity withdrawing.

Preparation of Bionite Structures

The magnetite bionites were formed by first washing the threads (cut with a scalpel into 2.5 cm sections) in pure water for one minute. The threads were withdrawn then allowed to air dry for 1 hour. The threads were then dipped into the colloidal magnetite solution for one minute and slowly withdrawn while air-drying for an additional hour (Figure 4.3).

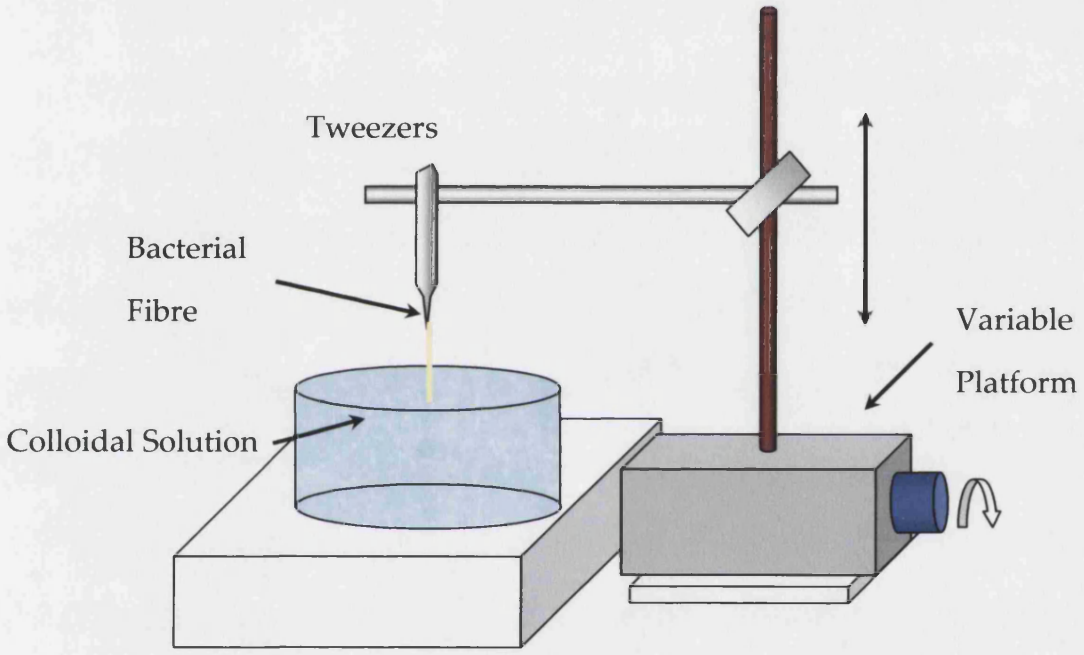

Figure 4.3 Preparation of bionites through dipping in colloidal solutions.

Mircoscopic Characterisation of Magnetite Bionite Structures

Magnetite bionite samples, 2.5 cm in length, were prepared for thin sectioning by suspending them in 50 ml of 1:1 MeOH/H_2O and 0.5 ml silane for one hour. After drying in air for 90 minutes, the threads were embedded in epoxy resin and thin-sectioned for scanning electron microscopy (SEM) and energy dispersive X-ray (EDX) analysis studies using a JEOL 6310 SEM operating at 20 kV. Samples were

also analysed in cross-section for the K_α peak of iron. Thin-sectioned samples were transferred to carbon coated, 3 mm, 200 square mesh copper grids and imaged with transmission electron microscopy (TEM) using a JEOL 2000FX TEM operating at an accelerating voltage of 200kV. The TEM was also used to perform electron diffraction to determine the mineral phase present. Finally, the magnetite samples were imaged in cross-section and longitudinally using atomic force microscopy (AFM), employing a Digital Instruments NanoScope IIIa in both contact and tapping modes.

Magnetic Characterisation of Magnetite Bionite Structures

Magnetisation studies of samples of native threads and magnetite bionites were performed in conjunction with Dr. David Awschalom (University of California, Santa Barbara, Department of Physics). Using a superconducting quantum interference device (SQUID) magnetometer, hysteresis curves at three different temperatures (5K, 300K and 400K) and zero-field cooled studies were performed.

4.3 RESULTS

General Characteristics

Native, washed threads appear yellow/white and are on the order of 10 μm in diameter. Washed threads do not differ significantly (e.g. cleaner) from native threads. SEM of broken cross-sections display individual fibres packed closely in the thread, but the surface texture is smooth at the fibre length-scale. On a 10 μm scale, the outer surface appears bumpy or scaly, but not as organised or regular as a human hair shaft (Figure 4.4 top and bottom). Higher magnification of the threads reveals pseudo-hexagonal packing parallel to the thread axis (Figure 4.5 top and bottom). At this high resolution the surface can be seen to match the texture of closely packed fibres. Quite likely the surface texture observed in Figure 4.4 is the sputtered gold coating to keep the threads from charging during imaging, though possibly there is long-scale waviness in the macrofibres.

Individual fibres are observed to be 0.7 μm in diameter, and quite consistent across the whole surface of the fractures. There appears to be a 0.1 μm skin or film over the thread in Figure 4.5 bottom. This is possibly dissolved peptidoglycan or teichoic acid that somehow became solublised during the washing process.

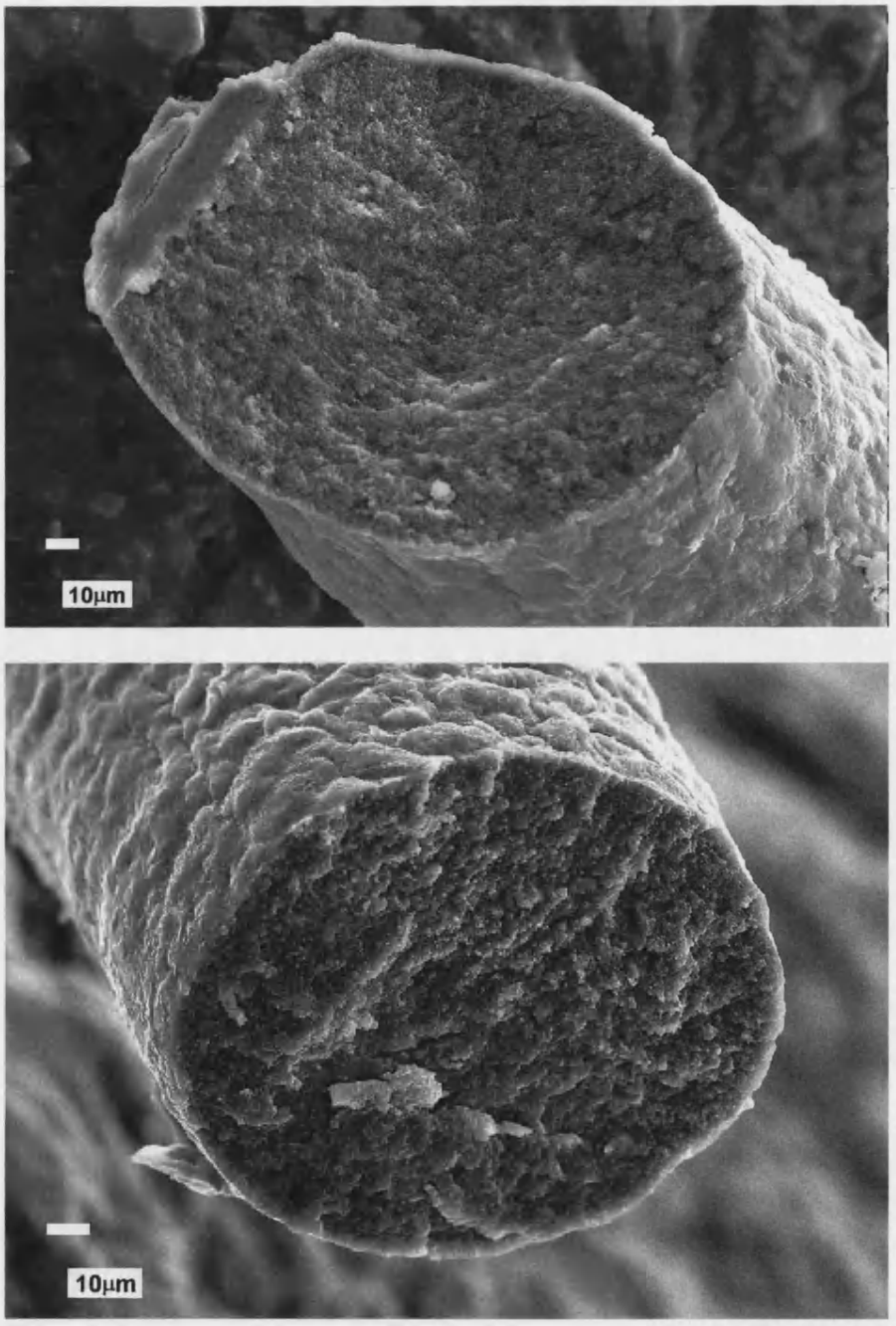

Figure 4.4 SEM images of bacterial thread cross-sections. Scale bars = 10 μm.

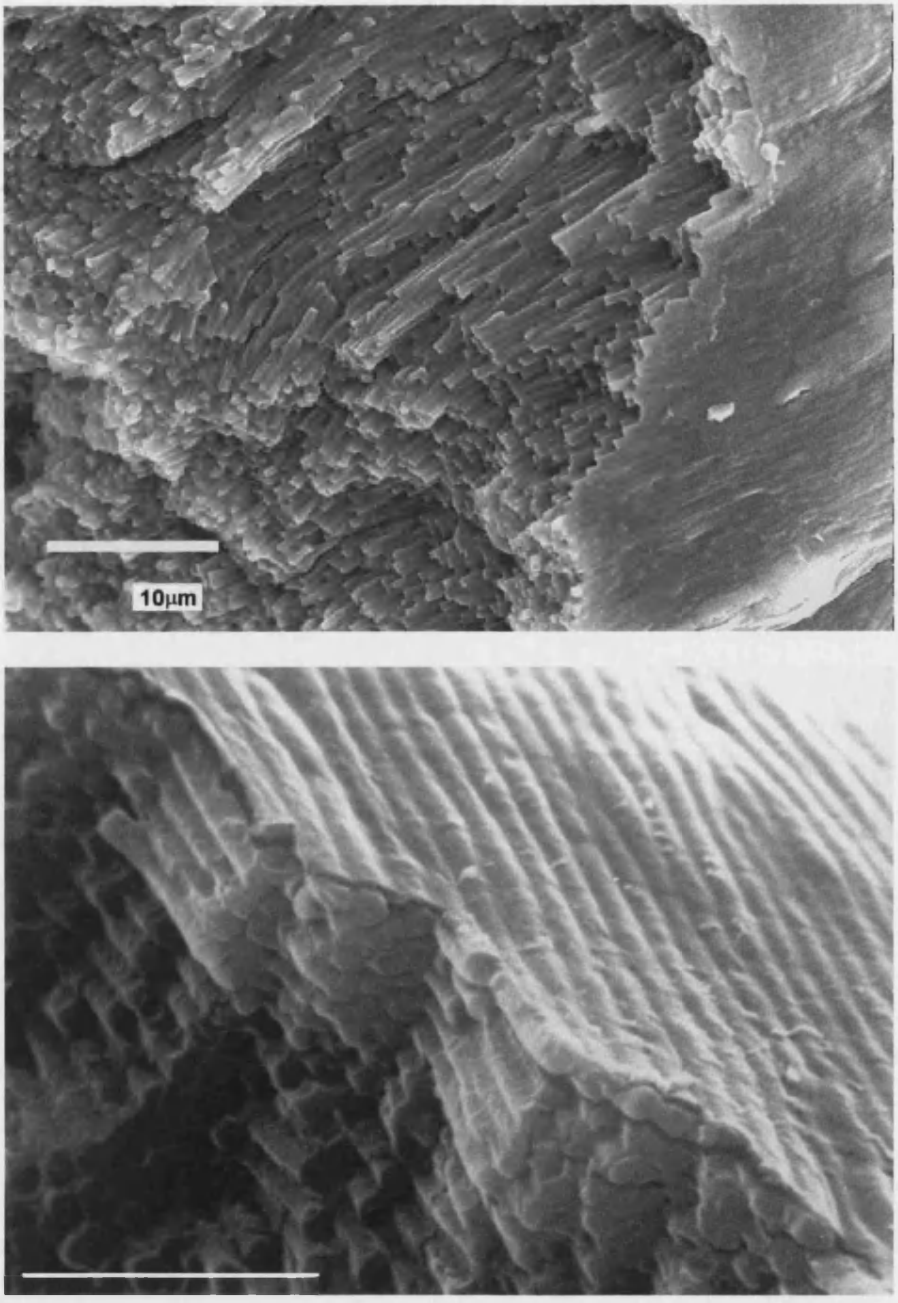

Figure 4.5 SEM images of a broken bacterial thread displaying individual fibres in a pseudo-hexagonal close packing parallel to the thread axis. Scale bars are 10 µm, 5 µm bottom. (Bottom photo courtesy of N. H. Mendelson)

Magnetite Bionites

The magnetite bionites were brittle, dark brown to black threads with diameters between 10 and 20 μm. Although nominally retaining their initial diameter, the threads were on average 10% more massive. The bionites displayed crude magnetic behaviour, such as the magnetite bionite adhering to a permanent magnetic sphere (Figure 4.6).

Microscopic Studies

SEM on bionite cross sections revealed that the fibre structure seen in native, washed threads was intact following impregnation (Figure 4.7 A). EDXA analysis confirmed that iron permeated the thread (Figure 4.7 B). Higher resolution SEM of a cleaved native thread shows tight, hexagonal packing of the fibers (Figure 4.8 A). Indeed the normally cylindrical fibres have taken on a hexagonal profile. SEM of cleaved bionites reveals magnetite between fibres (Figure 4.8 B), with no preferential orientation of the nanoparticles visible.

TEM of the magnetite bionites shows discrete nanoparticles between adjacent fibres. The loading is not uniform across the cross section, but material may have disappeared during sample preparation (Figure 4.9). Electron diffraction displayed the characteristic peaks for magnetite, confirming the intended composite (Figure 4.9, inset).

AFM of the magnetite bionite did not show any nanoparticulate texture, but it did resolve the individual fibres both longitudinally (Figure 4.10 top), and across a cleaved surface (Figure 4.10 bottom). The cross section of the fibre was much too

rough for both contact and tapping mode of the AFM. Quite possibly sectioning with a diamond knife would produce a smooth enough surface for the more detailed imaging befitting the AFM.

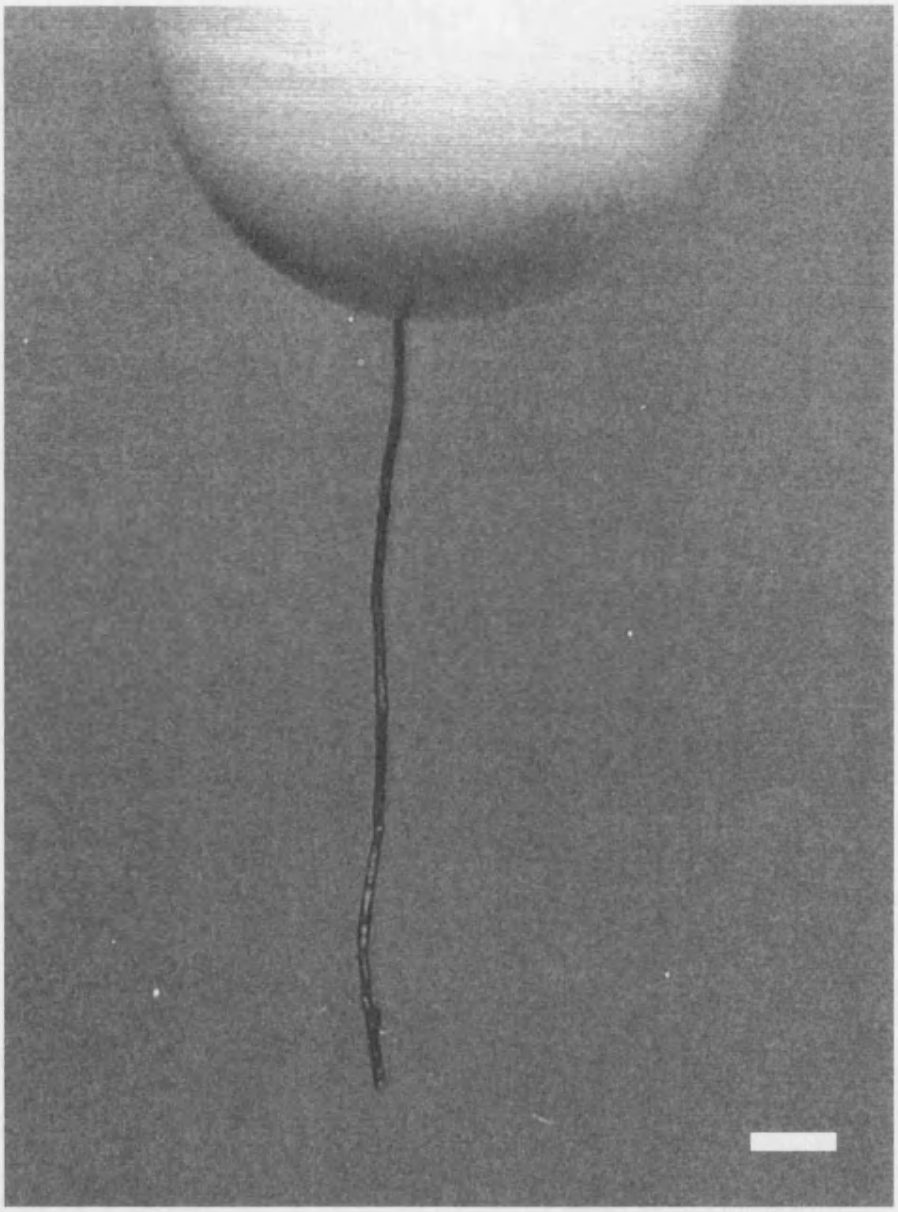

Figure 4.6 Magnetite impregnated bionite suspended from a permanent magnetic sphere. Scale bar 1 mm.

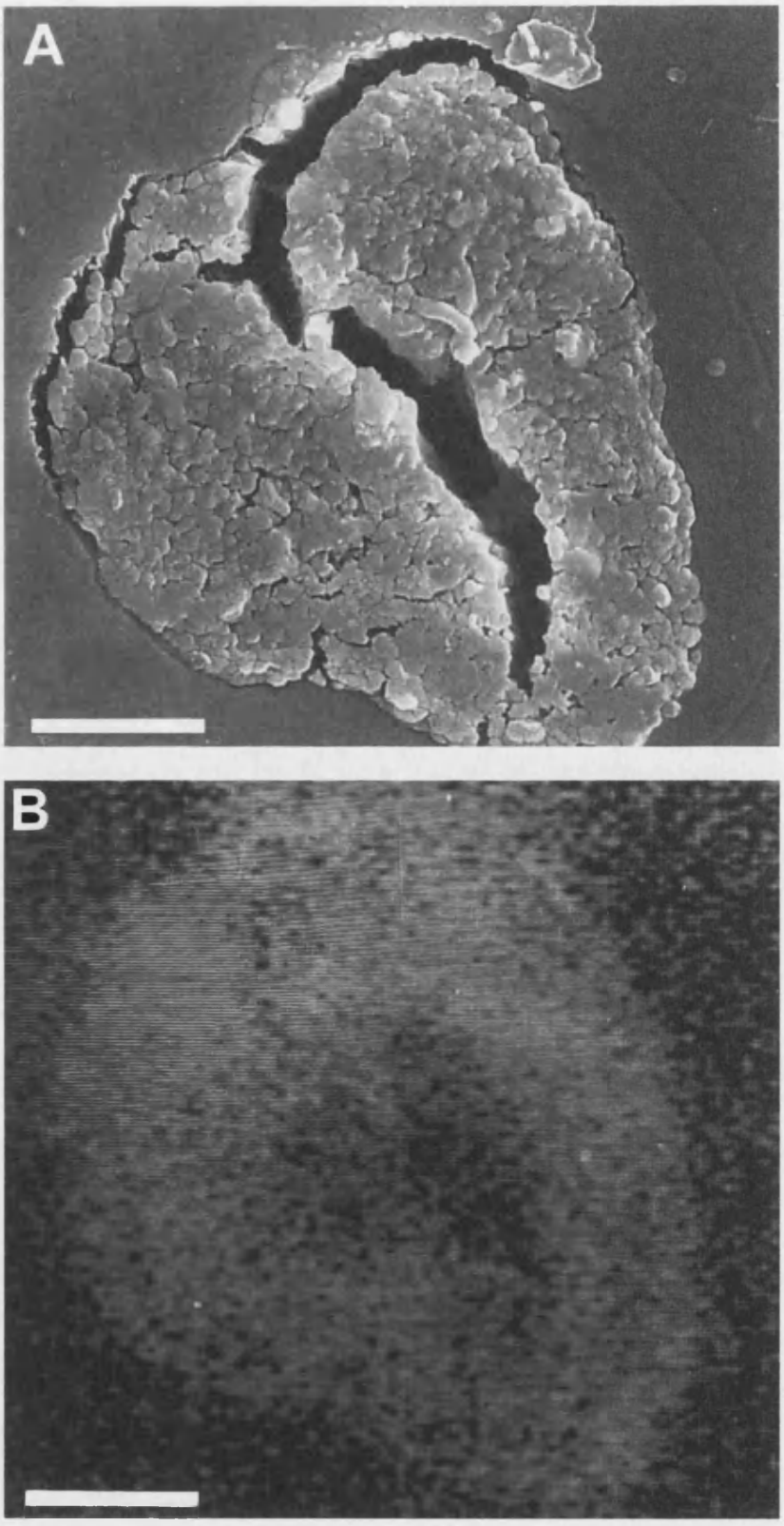

Figure 4.7 SEM cross-section of a resin-embedded magnetite bionite (a) and its corresponding elemental distribution for iron (b). Scale bar 5 μm.

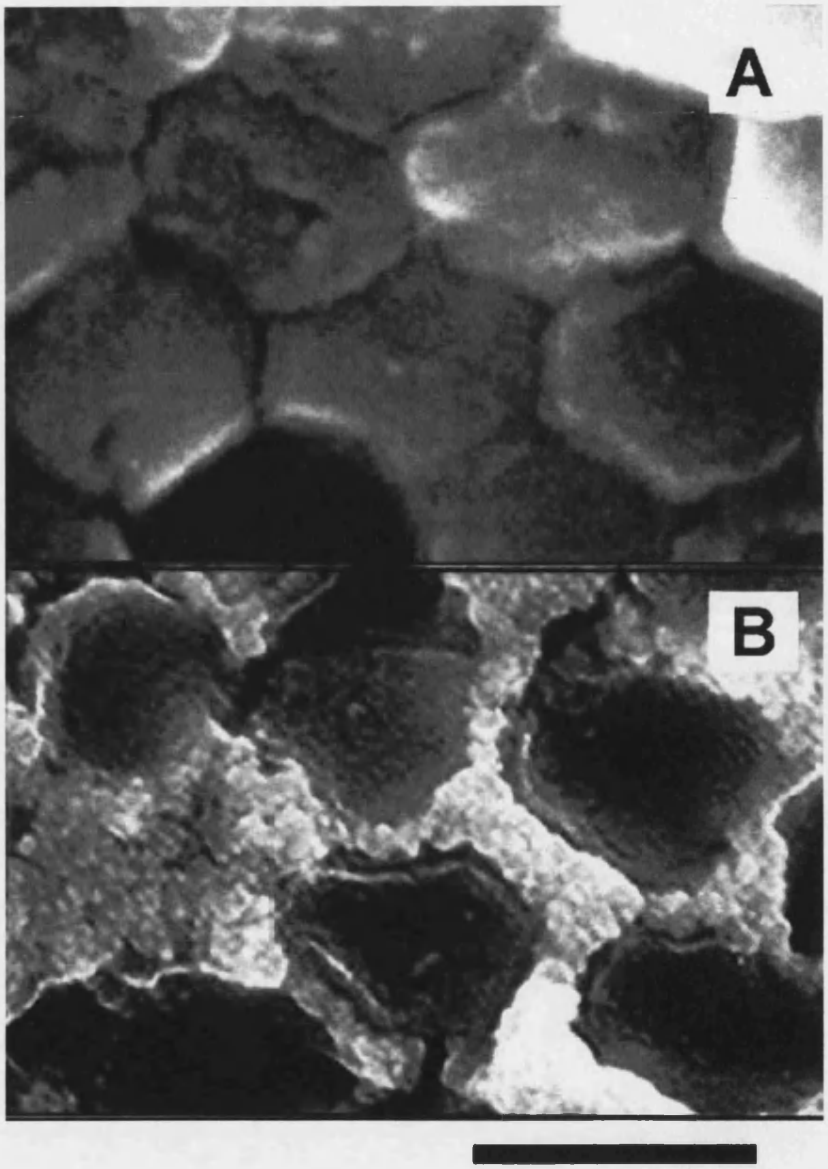

Figure 4.8 SEM cross-sections of a bacterial thread before infiltration (a), and after infiltration with magnetite colloid (b). Scale bar = 0.5 μm.

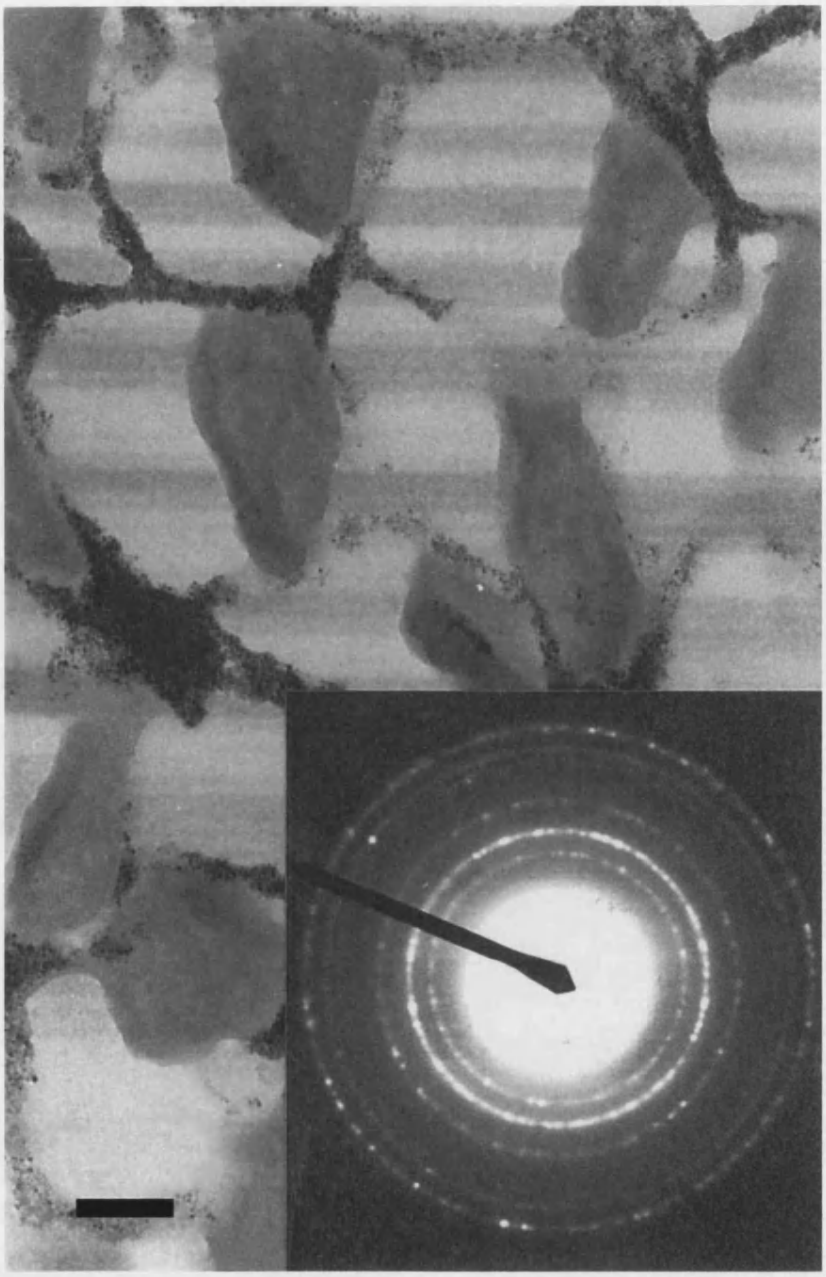

Figure 4.9 TEM micrograph of a transverse thin section of a magnetite bionite showing aggregated Fe_3O_4 nanoparticles (interstitial dark areas), with electron diffraction (inset) confirming the presence of magnetite [d_{hkl} = 0.492 nm (111), 0.300 nm (220), 0.253 nm, 0.212 nm]. Scale bar = 0.2 μm.

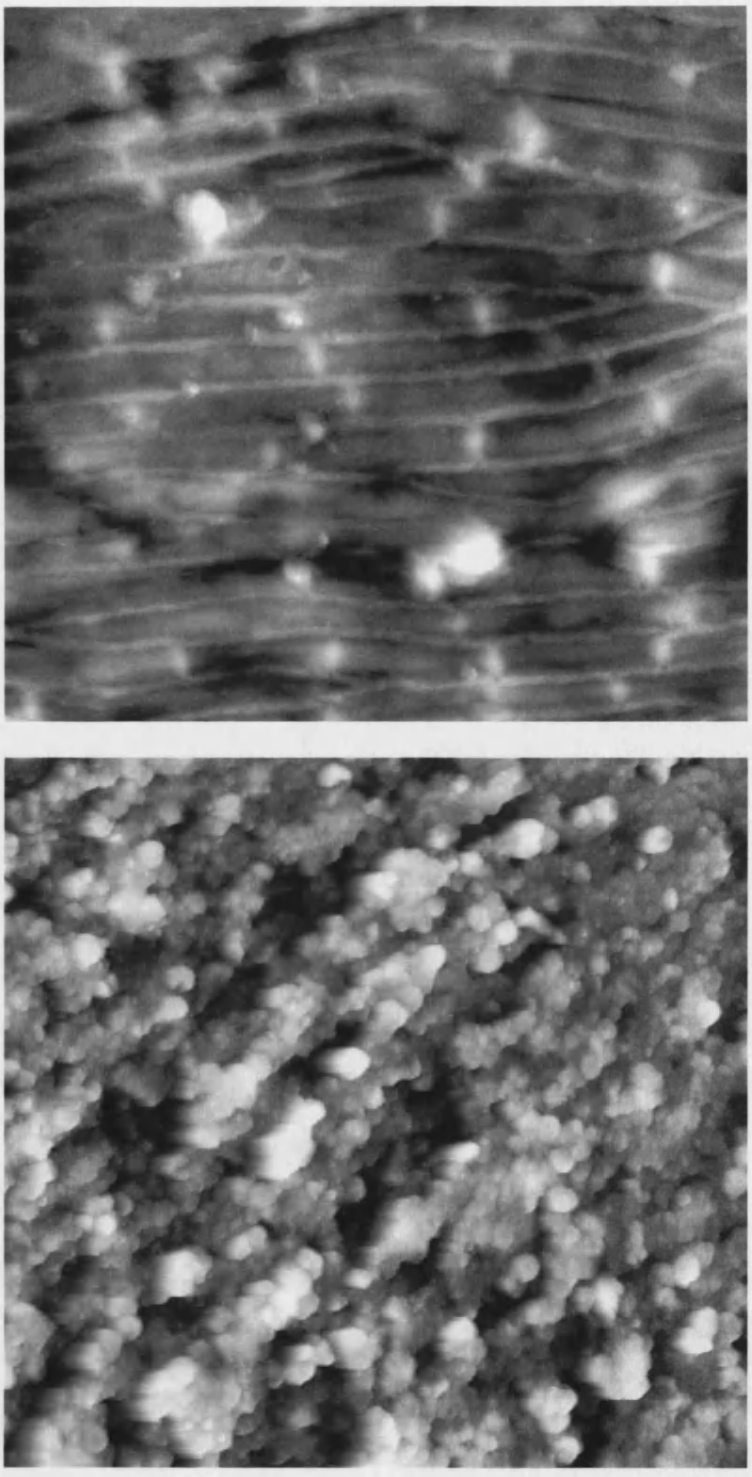

Figure 4.10 10 μm^2 AFM image at 512 samples per line of a magnetite bionite exterior scanned parallel to long axis (top). 20 μm^2 AFM image at 512 samples per line taken over the end of a broken bionite filament (bottom).

Magnetic Studies

The magnetic properties of 1 mm length sections of the bionites were measured in an rf-SQUID. Field loops of the magnetite bionites were sampled at three different temperatures. At 5K hysteresis was observed indicating the magnetite nanoparticles were below their blocking temperature (Figure 4.11). Surprisingly there was a marked difference between the perpendicular and parallel (to the bionite axis) loops. As the temperature increased to 300K and 400K (Figures 4.12 and 4.13), the nanoparticles exceeded their blocking temperature and behaved as superparamagnetic assemblies. Anomalous spikes in these hysteresis curves are caused by electrical noise, and are not related to the sample. However, there remained a difference in saturation magnetisation depending on the orientation of the saturating field. Regardless of temperature, the loops saturated near the same value ($2x10^{-4}$ emu (or $G*cm^3$)).

The temperature dependence of the magnetic moment of the magnetite bionites was measured in a 10 Gauss (G) (or 10 Oersted (Oe)) applied field after the sample was cooled in zero field. The temperature was raised from 5K to 300K while recording the magnetisation of the sample in the applied field. The moments of the particles aligned in the field as temperature increased up to a certain point. At this point the particles lost their preferential orientation – a temperature termed the "blocking temperature." From Figure 4.14, the blocking temperature for the magnetite bionite can be seen to be around 175 K.

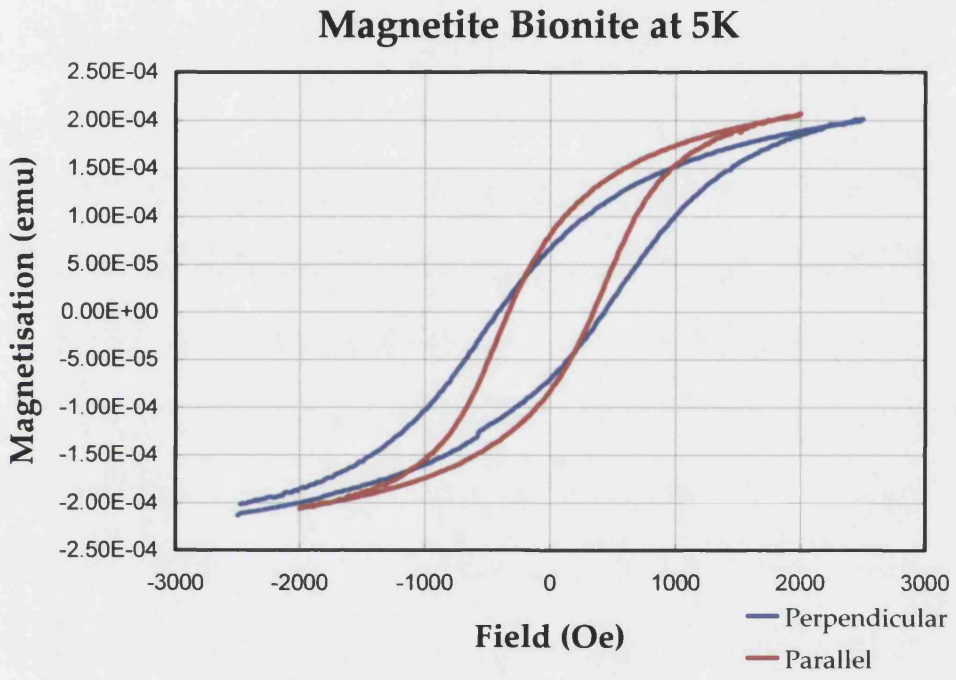

Figure 4.11 M(H) plot of a magnetite bionite at 5 K. Field sampled both parallel and perpendicular to the bionite axis.

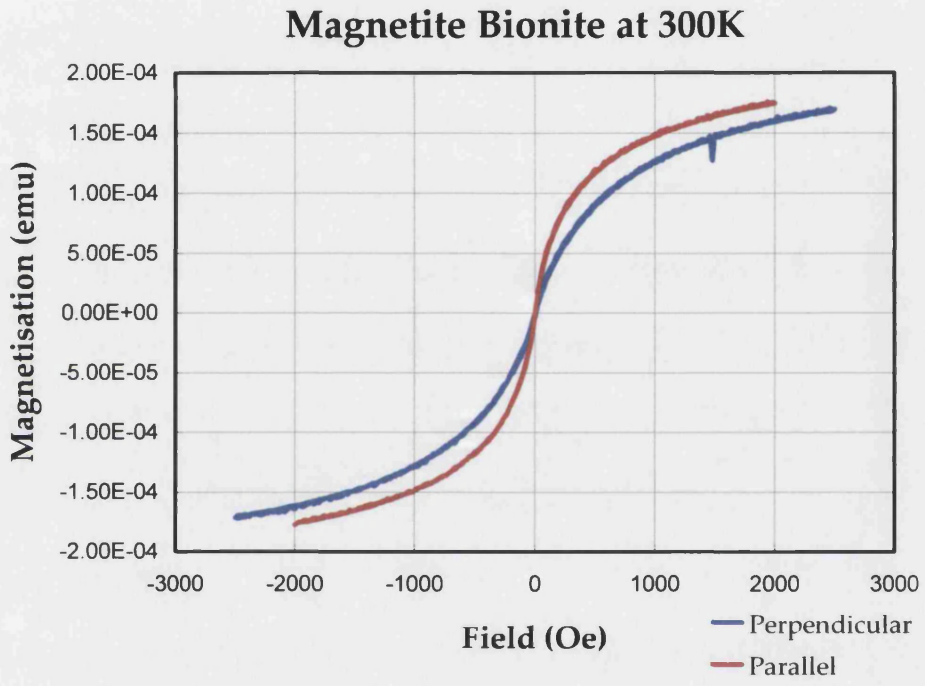

Figure 4.12 M(H) plot of a magnetite bionite at 300 K. Field sampled both parallel and perpendicular to the bionite axis.

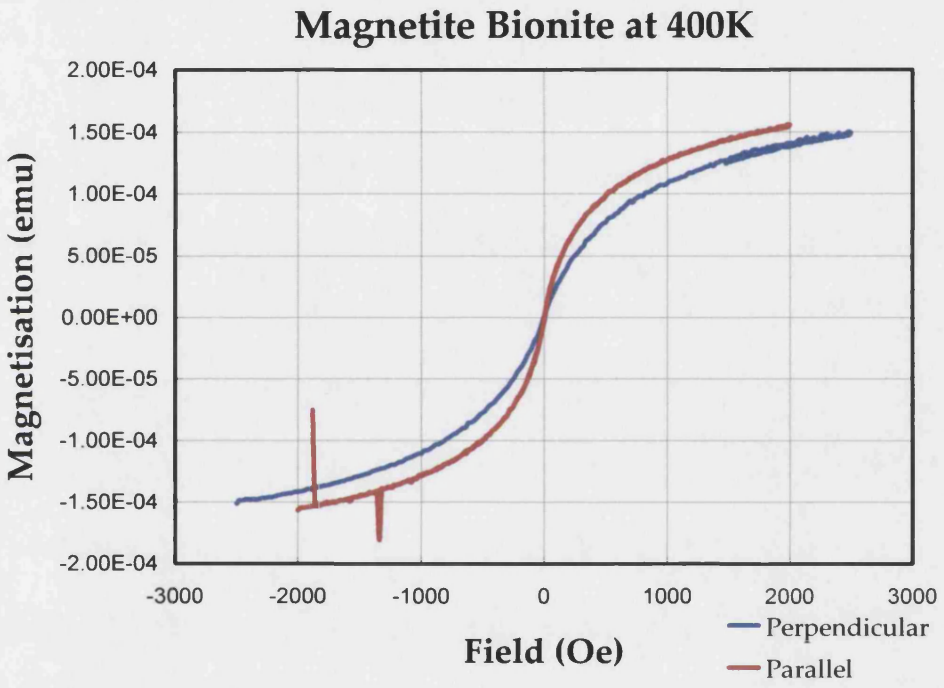

Figure 4.13 M(H) plot of a magnetite bionite at 400 K. Field sampled both parallel and perpendicular to the bionite axis.

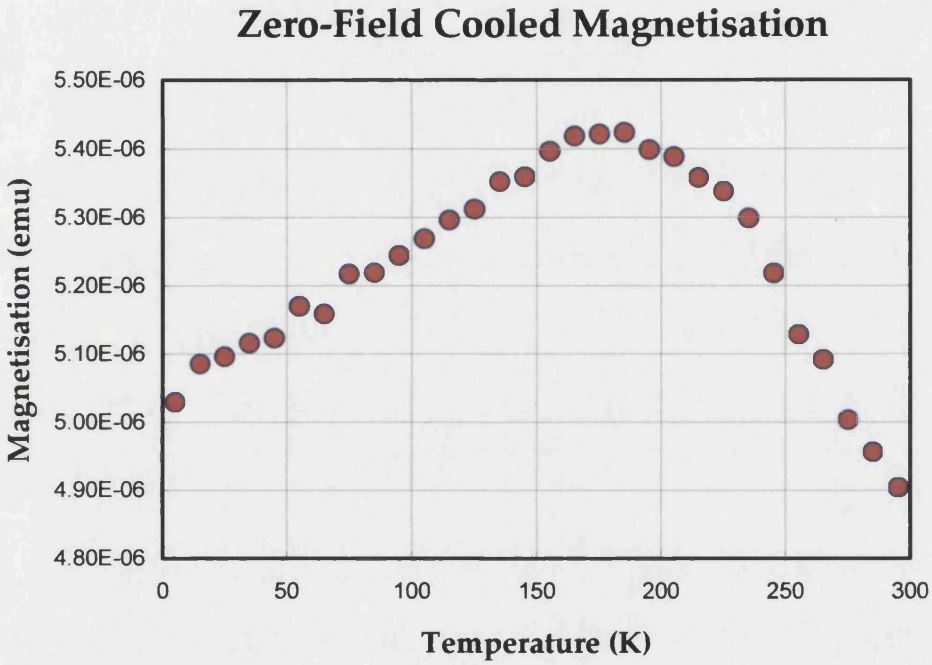

Figure 4.14 M(T) plot along the parallel axis of a bionite in a field of 10 G. Note that the blocking temperature appears at approximately 175 K.

4.4 DISCUSSION

Bionite "Skin" and Dissolution

In the high-resolution TEM images of the bare, washed bionite, a 0.1 μm skin or film over the thread is visible (Figure 4.5). This is possibly dissolved peptidoglycan or teichoic acid that somehow became solublised during the washing process. It could also be a very thin layer of the sputtered gold for microscopy preparation, however TEM studies indicate some dissolving of the bacterial material may occur. In thin-section studies of these bionites, the magnetite acts as a negative stain. It is a common feature of the micrographs to have magnetite only present in a few arcs between adjacent fibres (Figure 4.9). This could be due to colloidal material falling from the fibrous matrix during sample preparation, but could also indicate adjacent fibres dissolving into one another and reforming during the drawing process. Possibly the presence of a trace of surfactant or other bi-layer disruptive agent could dissolve a portion of the fibres during washing or colloidal preparation. Any dissolved material that escaped the confines of the fibrous matrix would coat the outside of the thread upon re-drawing, if proximate at the solution/air interface. Further, any trapped, dissolved material would fill in the voids between fibres, decreasing the locations for colloidal penetration.

Collective Magnetic Behaviour in Bionites

Macro-scaled magnetic material consists of a collection of individual domains, each acting as an individual bar magnet. Normally their collective behaviour is assumed to be identical to the state of each piece of the material, but even if immersed in high, uniform field, some domains may be aligned askew. When all of the domains in a material are aligned in the same direction, the material is termed "saturated".

Depending on the magnetic material, the size at which these bar magnets act as discrete, single domains can range from $5x10^{-7}$ - 0.5 μm^3. If these single-domains become small enough, the energy barrier to overcome in order to reverse their magnetization becomes so small that thermal energy fluctuations can reverse their magnetization even in the absence of an applied field (Neél, 1949). If single-domain elements or particles exhibit this type of behaviour, they are termed "superparamagnetic."

The probability that a particle will have enough thermal energy to overcome its energy barrier $\Delta E = KV$ is given by the Boltzmann factor $e^{-KV/kT}$. In this factor, K is an anisotropy term related to the magnetic susceptibility of the particle with volume V. The total anisotropy is the sum of terms including the magnetocrystalline, shape, and stress anisotropies, but only the magnetocrystalline anisotropy is intrinsic to the particle. The rate of decay of magnetization at a certain time is proportional to the Boltzmann factor and the magnetization of the particle, which can be expressed as:

$$-dM/dt = f_0 M e^{-KV/kT}.$$

The proportionality constant, f_0, is called the "attempt frequency" and has a value of around 10^9 Hz (though seems to be contingent on the material and sampling conditions). It represents the rate at which the particle attempts to overcome the energy barrier through thermal fluctuations and may be thought of as magnetic Brownian motion. The rate of decrease of magnetization can also be described as M/τ, where τ is the magnitude of the time for the decrease in magnetization. The previous equation can therefore be re-expressed as:

$$1/\tau = f_0 e^{-KV/kT}.$$

Further, as the value of $1/\tau$ is strongly dependent on both the volume (V) and temperature (T) in the equation, a limit can be imposed. The upper limit of volume for single domain behaviour (V_p) imbues a limit on the $1/\tau$ term of 10^{-2} Hz. Therefore the decay can be expressed as:

$$10^{-2} = 10^{9}\, e^{-KVp/kT}.$$

Solving this equation, KV_p/kT is roughly equal to 25. With rearrangement, the equation can be expressed as: $V_p = 25kT/K$, where k is Boltzmann's constant, T the blocking temperature of the particle in degrees Kelvin, and K the absolute value of the anisotropy of the material. Using this equation, it is possible to experimentally verify the volume of a particle by knowing its blocking temperature and anisotropy constant. In the case of the magnetite bionite, the blocking temperature was determined to be 175 K by Figure 4.14. The magnetocrystalline anisotropy constant for magnetite is -1.1 x 10^5 ergs/cm^3. Therefore, the particle volume is expected to be 5.7 x 10^{-18} cm^3. Assuming a spherical particle, the calculated diameter would be 22 nm, which is only slightly outside of the 9 nm size range determined by TEM. To account for this slight discrepancy, the total anisotropy may be a combination of both magnetocrystalline and shape anisotropies. Indeed TEM observations often indicate facets to the magnetite nanoparticles. Regardless, it was shown that the magnetic behaviour of the magnetite bionites is represented by a collection of individual superparamagnetic particles – a material termed a superparamagnet.

Anisotropy of Bionite Magnetisation

In all of the hysteresis curves, it is notable that the saturation magnetisation is higher for bionites saturated in a field along their axis (Figures 4.11-4.13). In colloidal suspension, magnetite nanoparticles are free to rotate. As this is their state when

introduced to the macrofibre, they should be expected to be randomly oriented inside the organic matrix. However there is a clear anisotropy between the saturation field orientations. A possible explanation is that the magnetite particles have an associated shape that becomes preferentially oriented within the thread matrix. However, from the TEM studies, the particles appear spherical. A more likely explanation for this anisotropy is that while drawing the thread from solution, there is a highly compressive force acting radially inward, towards the axis of the fibre. The randomly oriented magnetite particles experience this directional force, which induces corresponding stress anisotropy. Lowering the compressive force by varying the humidity of the air at the interface may be one way to test this hypothesis.

4.5 REFERENCES

Davis, S. A., "Biomineralization and Biomimetic Synthesis", *PhD Thesis* (University of Bath), 140-354 (1996).

Davis, S.A., S. L. Burkett, N. H. Mendelson, and S. Mann, "Bacterial templating of ordered macrostructures in silica and silica-surfactant mesophases", *Nature*, **385**, 420-423 (1997).

Davis, S. A., H. M. Patel, E. L. Mayes, N. H. Mendelson, G, Franco, and S. Mann, "Brittle Bacteria: A Biomimetic Approach to the Formation of Fibrous Composite Materials", *Chem. Mater.*, **10**, 2516-2524 (1998).

Doyle, R. J., M. L. McDannel, J. R. Helman, and U. N. Streips, "Distribution of teichoic acid in the cell wall of Bacillus subtilis", *J. Bacteriol.*, **122**, 152-158 (1975).

Doyle, R. J., T. H. Matthews, and U. N. Streips, "Chemical basis for selectivity of metal ions by the *Bacillus subtilis* cell wall", *J. Bacteriol.*, **143**, 471-480 (1980).

Field, M., C. J. Smith, D. D. Awschalom, N. H. Mendelson, E. L. Mayes, S. A. Davis, and S. Mann, "Ordering nanometer-scale magnets using bacterial thread templates", *App. Phys. Lett.*, **73**(12), 1739-1741 (1998).

Graham, L. L., and T. J. Beveridge, "Structural differentiation of the *Bacillus subtilis* 168 cell wall", *J. Bacteriol.*, **176**, 1413-1421 (1994).

Marchessault, R. H., P. Rioux, and L. Raymond, "Magnetic cellulose fibres and paper: preparation, processing and properties", *Polymer*, **33**(19), 4024-4028 (1992).

Marquis, R. E., K. Mayzel, and E. L. Carstensen, "Cation exchange in cell walls of gram-positive bacteria", *Canadian Journal of Microbiology*, **22**, 975-982 (1976).

Mendelson, N. H. and J. J. Thwaites, "Cell Wall Mechanical Properties as Measured with Bacterial Thread Made from Bacillus subtilis", *J. Bacteriol.*, **171**(2), 1055-1062 (1989).

Mendelson, N. H., "Bacterial macrofibres: the morphogenesis of complex multicellular bacterial forms", *Sci. Progress Oxford*, **74**, 425-441 (1990).

Mendelson, N. H., "Self-Assembly of Bacterial Macrofibers: A System Based Upon Hierarchies of Helices", *Mat. Res. Soc. Symp. Proc.*, **255**, 43-54 (1992).

Mendelson, N. H., "Production and Initial Characterization of Bionites: Materials Formed on a Bacterial Backbone", *Science*, **258**, 1633-1636 (1992).

Mendelson, N. H., "Bacterial fibers and their mineralised products: bionites", *Biomimetic Materials Chemistry*, ed. S. Mann (VCH Publishers, U.K.), 279-313 (1996).

Neél, L., "Theorie du trainage magnetique des ferromagnetiques en grains fins avec applications aux terres cuites", *Ann. Geophys.* **5**, 99-136, (1949).

Smith, C. J., M. Field, C. J. Coakley, D. D. Awschalom, N. H. Mendelson, E. L. Mayes, S. A. Davis, and S. Mann, "Organizing Nanometer-Scale Magnets with Bacterial Threads", *IEEE Trans. Mag.*, **34**(4), 988-990 (1998).

Thwaites, J. J. and N. H. Mendelson, "Mechanical properties of peptidoglycan as determined from bacterial thread", *Int. J. Biol. Macromol.*, **11**, 201-206 (1989).

Thwaites, J. J. and N. H. Mendelson, "Mechanical Properties of Bacterial Fibres", *Mat. Res. Soc. Symp. Proc.*, **174**, 179-185 (1990).

Thwaites, J. J. and N. H. Mendelson, "Mechanical Behaviour of Bacterial Cell Walls", *Adv. Micro. Physio.*, **32**, 172-222 (1991).

CHAPTER FIVE

INCORPORATION OF INORGANIC NANOPARTICLES INTO CEMENT MICROSTRUCTURES

5.1 INTRODUCTION

In the previous chapter, nanoparticles of magnetite were incorporated into the porous microstructure of a bacterial thread. In this chapter a range of nanoparticles and reactive inorganic additives are combined with a cement blend that is subsequently moulded into predefined microstructures. Continuing the theme of adding functionality to microstructures, this work introduces the ability to control microstructure beyond linear, fibrous templates. Indeed an infinite variety of microstructures can be defined using lithographic techniques then faithfully replicated with a functional, composite cement. Stemming from the development of microelectromechanical systems (MEMS) that are typically limited to materials such as polycrystalline silicon, metals, and polymers, structures presented in this chapter permit magnetic, biological and host-guest reactive functionality.

The primary goal of this work is to create composite materials with well-defined microstructures and functionality beyond that currently available to MEMS. Inexpensively produced microstructured cements with electromagnetic, bio- or chemically active functionality could find applications in areas such as electromagnetic band-gap modification, micro-reactors, and biological sensors. The work described in this chapter has been published in the Journal of Materials Science Letters (Colston, *et al.*, 2000).

Background

The past fifteen years have seen the development, production and implementation of microstructures with applications as diverse as accelerometers, bio-assays, opto-electronics, and chemical mixers. These MEMS often require a high aspect ratio that can be realized through a process called LIGA (a German acronym of lithography, galvanoformung und abformung). LIGA employs X-ray lithography to pattern a thick photoresist that is selectively removed to form a template for metalisation or further patterning. This technique is becoming pervasive, as it is not constrained to materials such as polycrystalline silicon or electrodeposited metals like traditional MEMS processes. Such materials are inadequate for applications requiring strength, wear- and heat-resistance, or transparency. LIGA has been used to fabricate heat-resistant ceramic microstructures prepared through a process of stamping cast ceramic films with microstructured metallic dies, followed by sintering (Knitter, *et al.*, 1996). While this process allows the use of ceramics, microstructures are not uniformly reproduced.

LIGA has also been combined with injection molding of amorphous thermoplastics such as polymethylmethacrylate (PMMA), introducing not only transparent polymer MEMS for optical applications, but a mould for materials with high strength and heat-resistance (Piotter, *et al.*, 1997). Demonstrating higher feature replication, ceramic precursor slurries have been pressure-molded into PMMA microstructures, followed by pyrolytic removal of the moulds leaving ceramic microstructures (Ritzhaupt-Kleissl, *et al.*, 1996). This process inspired the use of cements for the production of composite microstructures.

Cement Microstructures

Using polymer moulds, poured cement microstructures can reproduce horizontal features to a high resolution. Compared with ceramic microstructures that experience shrinkages up to 50%, cement microstructures display no measurable shrinkage and do not require a sintering step (Colston, *et al.*, 1996). Micron-scale resolution is achieved for features in the plane of the moulds, with complete replication of the lateral mould dimensions. In the vertical direction, the replication is 90-100% depending on the height of the features. The mechanism by which the microstructures form smooth surfaces and intersections with sub-micron dimensions is essentially hydrate growth outwards from initial cement grains towards the mould faces. Cement grains have an average size of 20 μm, with a broad size distribution from 10 to 60 μm. Growth within the mould depends on the hydration mechanisms involved, so cement choice is important for the best replication. Tricalcium silicate (C_3S in shorthand, where C is CaO, S is SiO_2) is the major component in Portland cements, and its hydration reaction is generally summarised by: $2C_3S + 7H \rightarrow C_3S_2H_4 + 3CH$ (where H is shorthand for H_2O). The formation of the main C-S-H product is topotactic, where the hydration products grow outward from the initial C_3S grains, continuing for many hours until the free water is fully used. The C-S-H products interlink in a continuous, self-supporting matrix.

In this chapter, Ordinary Portland Cement (OPC) is used as the microstructured matrix. OPC has a C_3S main component, but also contains other mineralogical phases including aluminates, sulphates, and ferric oxides. The reproduction of microstructures in early work was not always found to be consistent, with the greatest problem being a tendency for structures to crack and break free as a result of

shrinkage or mechanical stressing during demoulding. Therefore a styrene butadiene copolymer latex was added, as it has been shown to form a polymer film which acts as an additional binder between the hydrates and across microcracks and pores (Colston, *et al.*, 1996). To add functionality beyond the self-supporting matrix, powders of lamellar organo-clays, colloidal magnetite or the protein ferritin were blended with the cement or cement/latex slurries. While possibly affecting the hydration or growth mechanisms of the cements in revealing ways, the composites were intended as alternative materials for functional MEMS. The organo-clay composites could be used for catalytic or separation processes, with reactive clays interacting with the fluid flow in a microstructured channel. Conductive or magnetic microcomposites could be used as low-cost actuators, compared with complex, electrostatic combs (Börner, *et al.*, 1996). Inductors (Rogers, *et al.*, 1997) or even microvalves (Yanagisawa, *et al.*, 1995) could be produced using a less expensive cement composite containing magnetic material such as magnetite. Biosensor MEMS employing enzymatic membranes are not mechanically robust, and tend to degrade with time (Wollenberger, *et al.*, 1995). Incorporating enzymes or other biological material within a rigid matrix could resolve this problem.

In this chapter, a series of composites that could address catalytic, electromagnetically actuated, or bio-reactive applications are produced. While their reactivity or device characteristics are not explored, the effect on the final microstructure and uniformity of dispersion of the composites is fully characterised.

5.2 MATERIALS AND METHODS

Organo-Clay Preparation

Powders of lamellar solids were selected for making microstructures with host-guest reactivity. A range of synthetically prepared organo-magnesium silicate clays (containing alkyl, epoxy, methacrylate or polymethacrylate groups covalently linked to the inorganic clay layers) were prepared and gifted by Dr. Nicola Whilton. In particular, three self-named clays, NW38, NW57 and NW53, were used. NW38 is a mixed octyl/methyl clay of methyltriethoxysilane and octyltriethoxysilane, NW57 is an un-polymerised 3-methacryloxypropyltrimethoxysilane, and NW53 is NW57 polymerised with α-azo-iso-butyronitrile.

Colloid Preparation

Two different colloids were selected for making magnetic and bio-active cement microstructures. A hydrophilic, nanoparticulate magnetite was prepared according to Appendix 1. For the bio-active cements, a colloidal, iron-containing protein called "ferritin" was purchased from Sigma (Derived from equine spleen, 10.2 mg/ml, 0.15M NaCl). Ferritin is a 12 nm diameter spherical protein, which self-assembles from 24 identical subunits and is used for iron storage in a wide variety of organisms. The iron is stored in the form of a semi-crystalline oxide, ferrihydrite, inside the 8 nm diameter spherical inner cavity.

Preparation of Microstructured Moulds

Moulds were prepared using the LIGA process by the Institute of Microtechnology in Mainz (Figure 5.1). The first stage of the process is to use deep X-ray lithography to expose a thick photoresist through a mask (Figure 5.1.1). The irradiated parts of

the photoresist are then chemically removed (Figure 5.1.2), and electroplating is used to fill the spaces between unexposed resist with metal (Figure 5.1.3). The resist is then removed leaving a metal mould (Figure 5.1.4) that can be filled with or hot-pressed into a polymer (Figure 5.1.5) to produce a negative mould (Figure 5.1.6). In the work presented here, negative moulds were composed of PMMA and designed for optoelectronic applications. Typically the microstructures consisted of channels with widths of 50-250 μm and vertical depths of 100-130 μm.

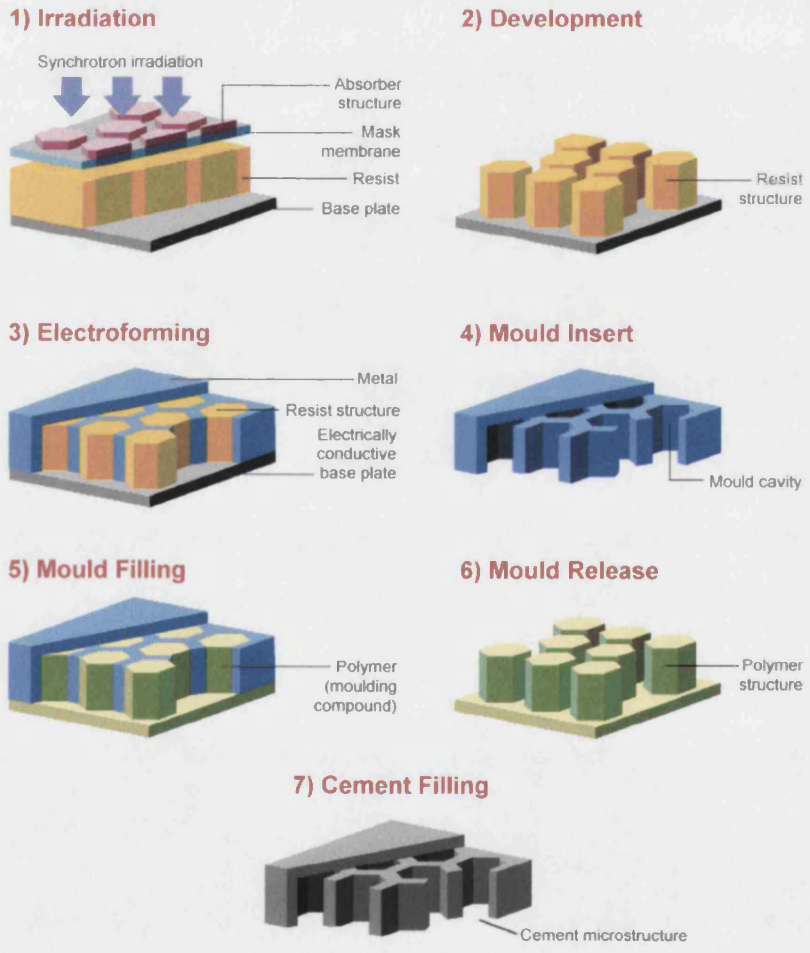

Figure 5.1 LIGA process sequence for producing cement microstructures. (Modified with permission from Dr. Wolfgang Ehrfeld, Institute for Microtechnology Mainz GmbH).

Preparation of Cement Microstructures

For the organo-clay microstructures, 0.1 g of the clay was mixed into 0.8 ml of water, 0.4 g of a liquid emulsion of latex, and 2 g of Ordinary Portland Cement (OPC). For the magnetite and ferritin microstructures, 3 ml of each solution was added to 5 g of OPC and mixed, notably not adding any latex. The slurries of the composite cements were then poured into PMMA moulds and allowed to dry in air for 24 hours. The microstructures were removed from the PMMA moulds by heating in an oven with a cycle of 15 °C per hour up to 400 °C, and then held at 400 °C for 3 hours. This cycle has been shown to reduce the stresses on the composite structure and incidence of bulk fracture (Colston, *et al.*, 1996). A compositional overview of the composite cements is contained in Table 5.1 below.

Material	Form	Particle Size	Level of Addition (% weight of cement)
Ordinary Portland Cement (OPC)	Powder	10 - 100 μm 20 μm average	
Styrene-butadiene latex	Liquid emulsion	0.2 μm average	20% solid polymer
Organo-clays	Slurry	1 - 50 μm	2-5% clay
Magnetite	Colloidal	~ 10 nm	3 ml
Ferritin	Native horse spleen (Sigma 10.2 mg/ml, 0.15M NaCl)	~ 12 nm	3 ml

Table 5.1 Properties of the various materials blended with Ordinary Portland Cement (OPC) to form composite microstructures.

Surface and Compositional Characterisation

Microstructures were characterised with both scanning electron and atomic force microscopies. High resolution SEM was performed using a JEOL 6400F operating at 30 kV, and lower resolution and energy dispersive X-ray (EDX) analysis were performed using a JEOL 6310 SEM operating at 20 kV. Both the magnetite and ferritin composites were analysed for distribution by mapping the K_α peak of iron. Atomic force microscopy (AFM) was performed using etched silicon nitride probes on an AutoProbe CP (Park Scientific Instruments). Some structures were also characterised by optical profilometry using a UBM LaserScan profiler.

5.3 RESULTS

General Characteristics

While occasionally pockmarked by voids, all of the composite cements replicated the moulds faithfully. Typically the microstructures consisted of channels with widths of 50-250 μm and vertical depths of 100-130 μm. Only at 100,000X magnification and higher were structural differences observed between the composites, mainly in the quality of the porosity.

Organo-Clay Cement Structures

Composites containing NW38, displayed the smoothest feature reproduction. The organo-clay cements consistently reproduced uniform features over the whole mould (Figure 5.2, top), as well as the delicate and sharp edge features (Figure 5.2, bottom). Moreover, optical profilometry confirmed uniformity of the depth profile (Figure 5.3), with a consistent trench of 100 μm. EDX analysis of the microstructures, mapping the K_α peaks for silicon and calcium, indicate that silicon is preferentially located at the edges of the feature (Figure 5.4). This may indicate that it is transported during drying and appears to be exclusive of calcium.

Even finer features were replicated, including small "humps" normally used to fasten optical fibres (Figure 5.5, top). The pockmarked quality of the cement composites may be due to the moulds themselves, as those used during preparation were cast-offs from the production of opto-electric components (Figure 5.5, bottom). To assess whether this coarse structure was related to faulty moulds or the cement structure, AFM was performed on various regions of the microstructures. A section from the defective mould of Figure 5.5 was selected for atomic force microscopy,

which indicated a rough surface with features up to 2 μm high (Figure 5.6). Some crystalline structure was evident, and likely calcium hydroxide.

Composites containing NW53 replicated the fine features of a spring-box, but exhibited some sag from the drying process (Figure 5.7, top). Outside of the structure, the composite cement produced a smooth continuous surface with sparse porosity (Figure 5.7, bottom). At higher resolution (Figure 5.8, top), cracking and crystallite formation becomes evident. AFM scans at a similar magnification (Figure 5.8, bottom) indicate a height range of around 400 nm over 5 μm^2. This smoothness is quite similar to the NW38 samples.

Finally, the un-polymerised NW57 displayed a much higher porosity (Figure 5.9) possibly indicating an interaction between the clay and the formation of calcium hydroxide crystallites.

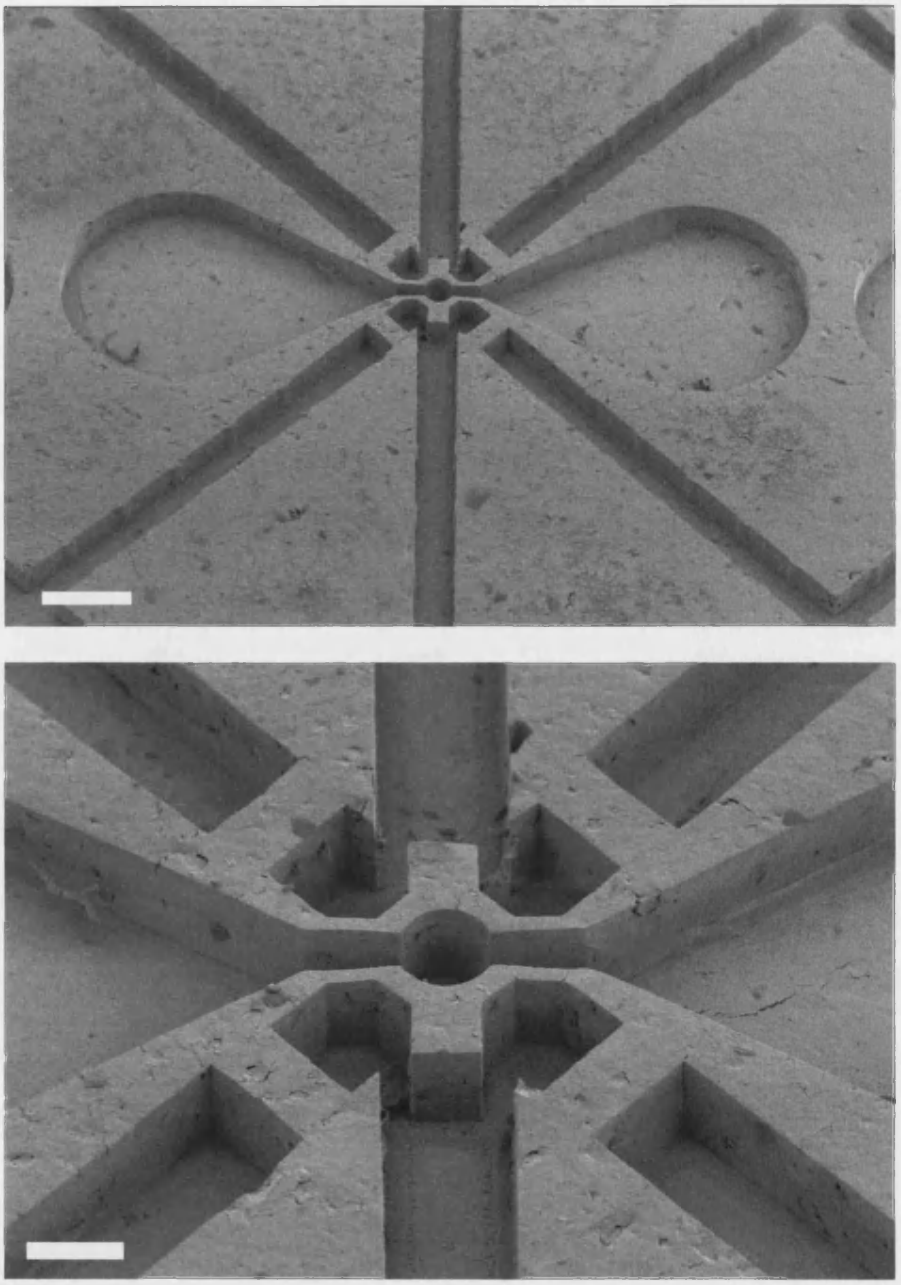

Figure 5.2 SEM of the microstructure of a NW38 composite. Scale bars = 300 μm above and 100 μm below.

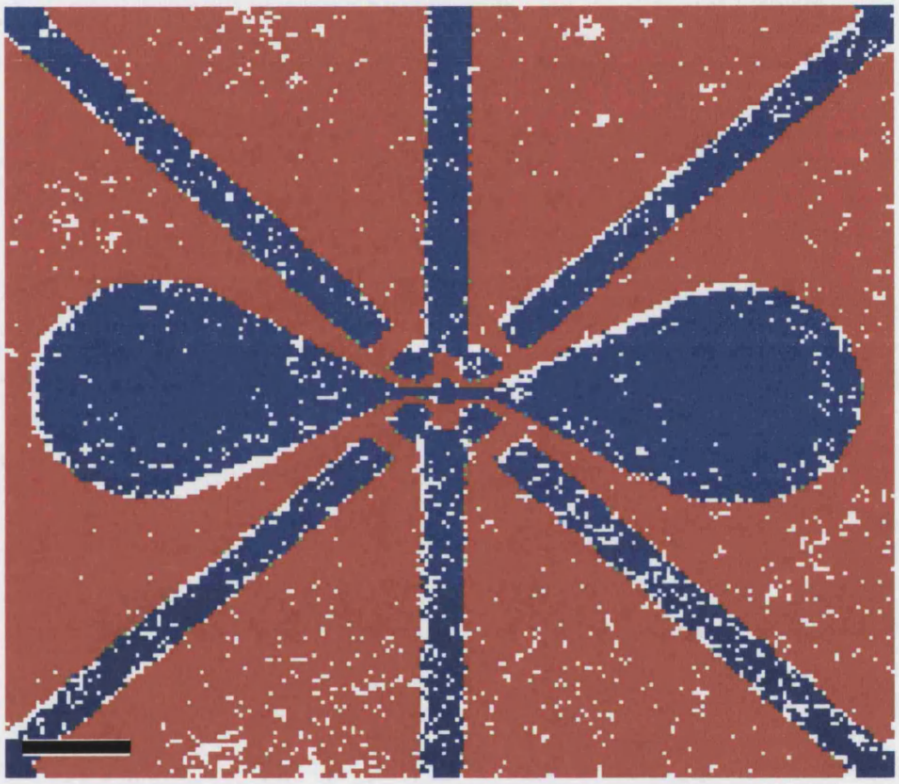

Figure 5.3 Optical profilometer height-field of the feature shown in Fig. 5.2, indicating very uniform profiles and a consistent trench of 100 μm. Scale bar = 300 μm.

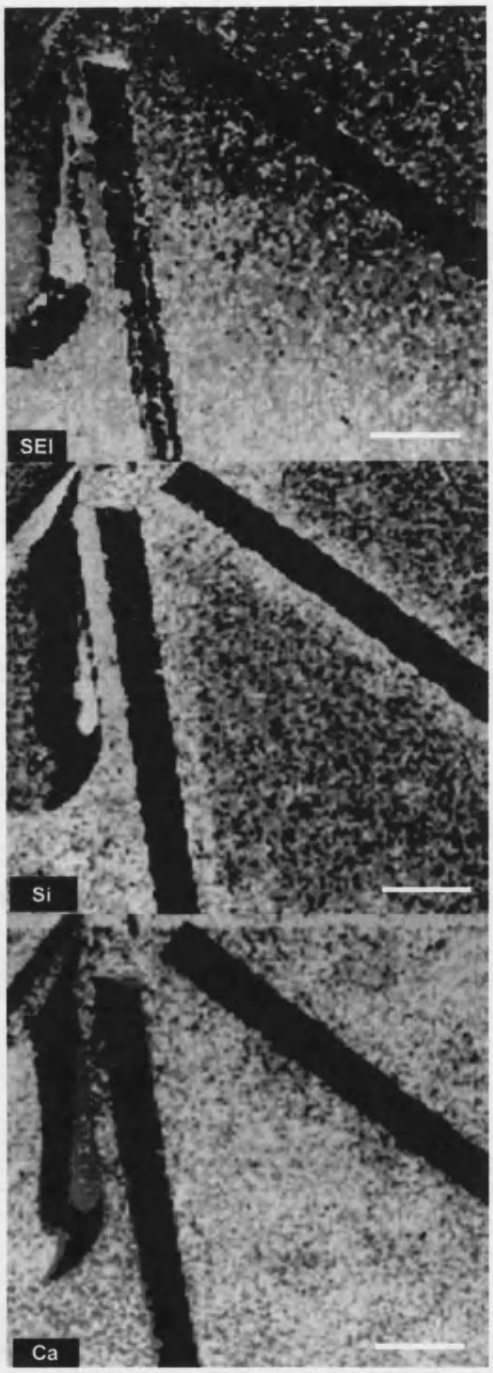

Figure 5.4 EDXA data of the Fig. 5.2 feature, displaying the SEM image (top), distribution of silicon (middle), and calcium (bottom) in the cement. Scale bars = 300 μm.

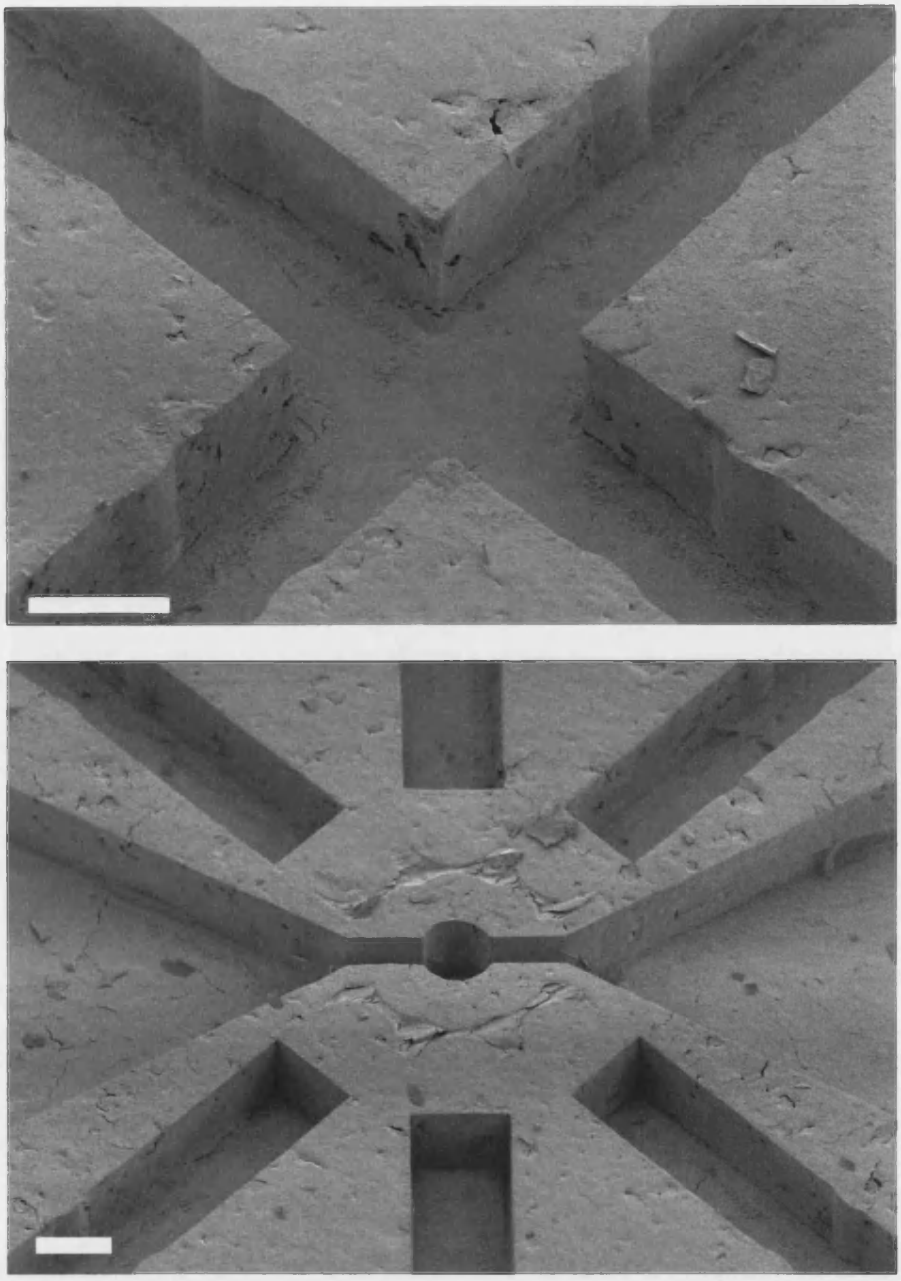

Figure 5.5 Features down to 5 μm reproduced faithfully in the optical structure shown in Fig. 5.2, as seen in the small "humps" normally used to fasten optical fibres (above). Additional optical structures were replicated, but the moulds were defective leading to unwanted filling (below). Scale bars = 100 μm.

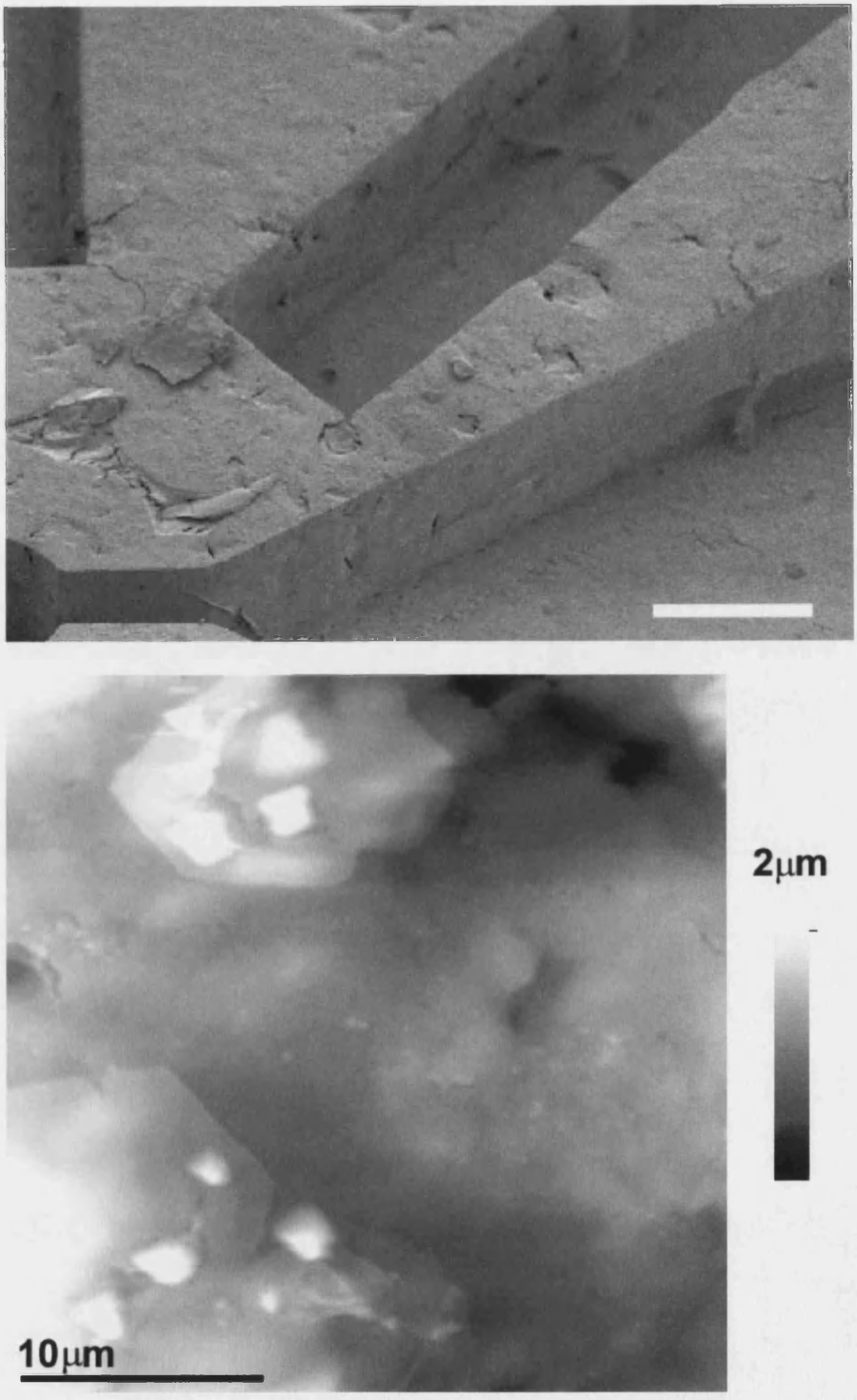

Figure 5.6 AFM scan of a 30 μm^2 area (highlighted at top) revealed features up to 2 μm high, and some crystalline structure likely calcium hydroxide. Scale bars = 100 μm above, and 10 μm below.

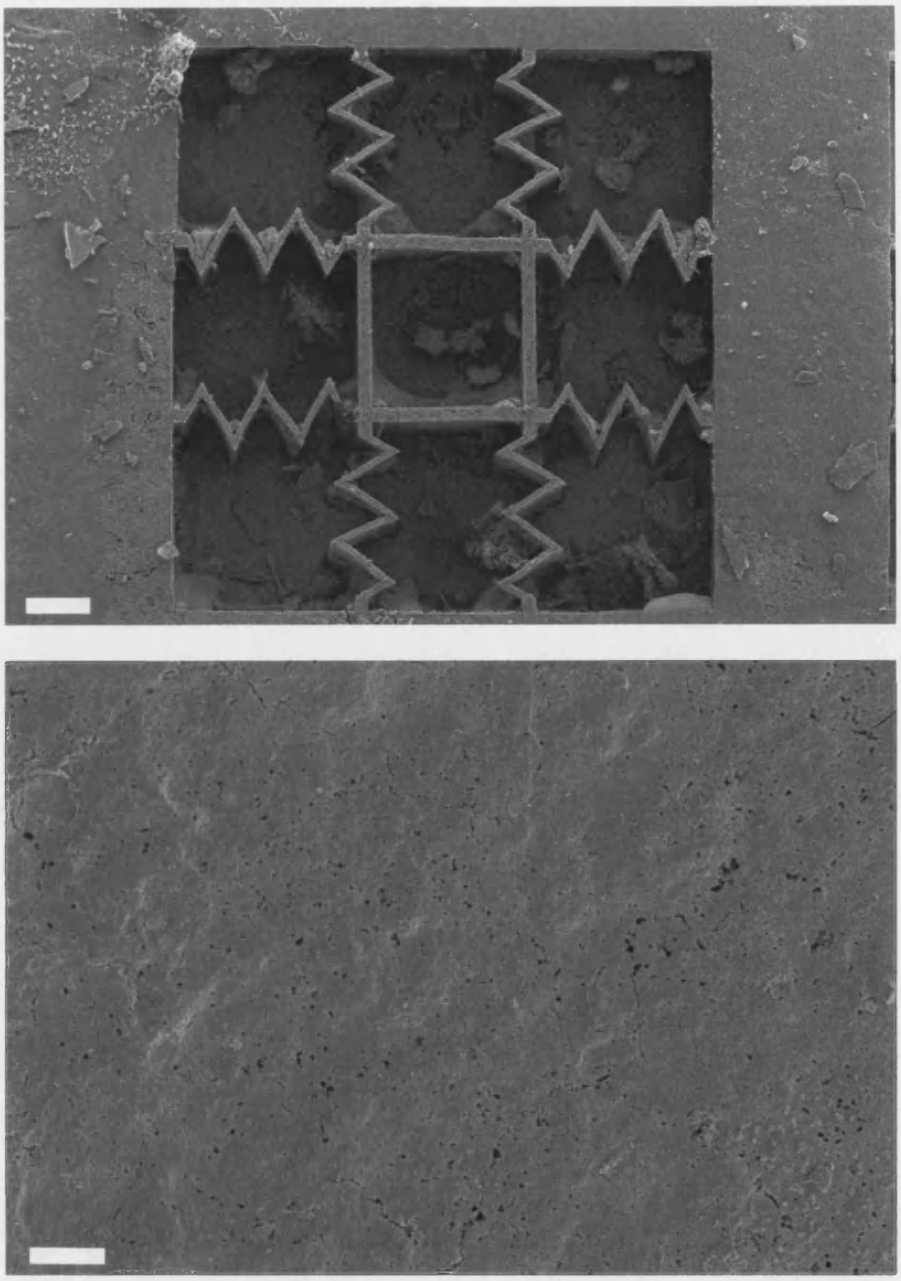

Figure 5.7 SEM micrograph of a NW53 composite in an accelerometer sensor structure (above). Outside of the sensor, the composite remained very smooth (below). Scale bars = 100 μm above, 10 μm below.

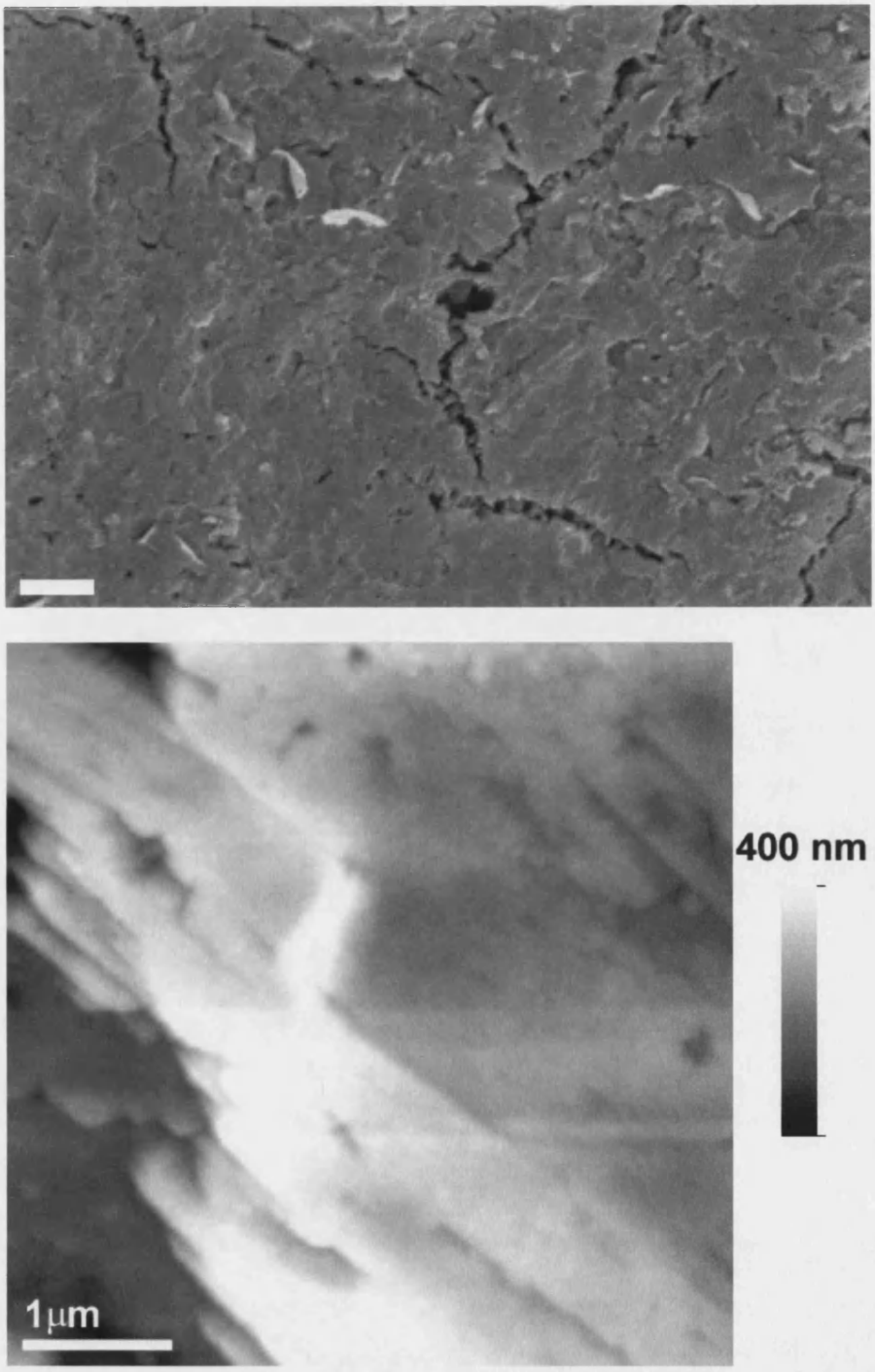

Figure 5.8 Higher magnification SEM of the surface highlights smooth regions associated with crystalline structure, interspersed with cracking (above). AFM scans at a similar magnification (below), indicate a height range of around 400 nm over 5 μm^2. Scale bars = 1 μm.

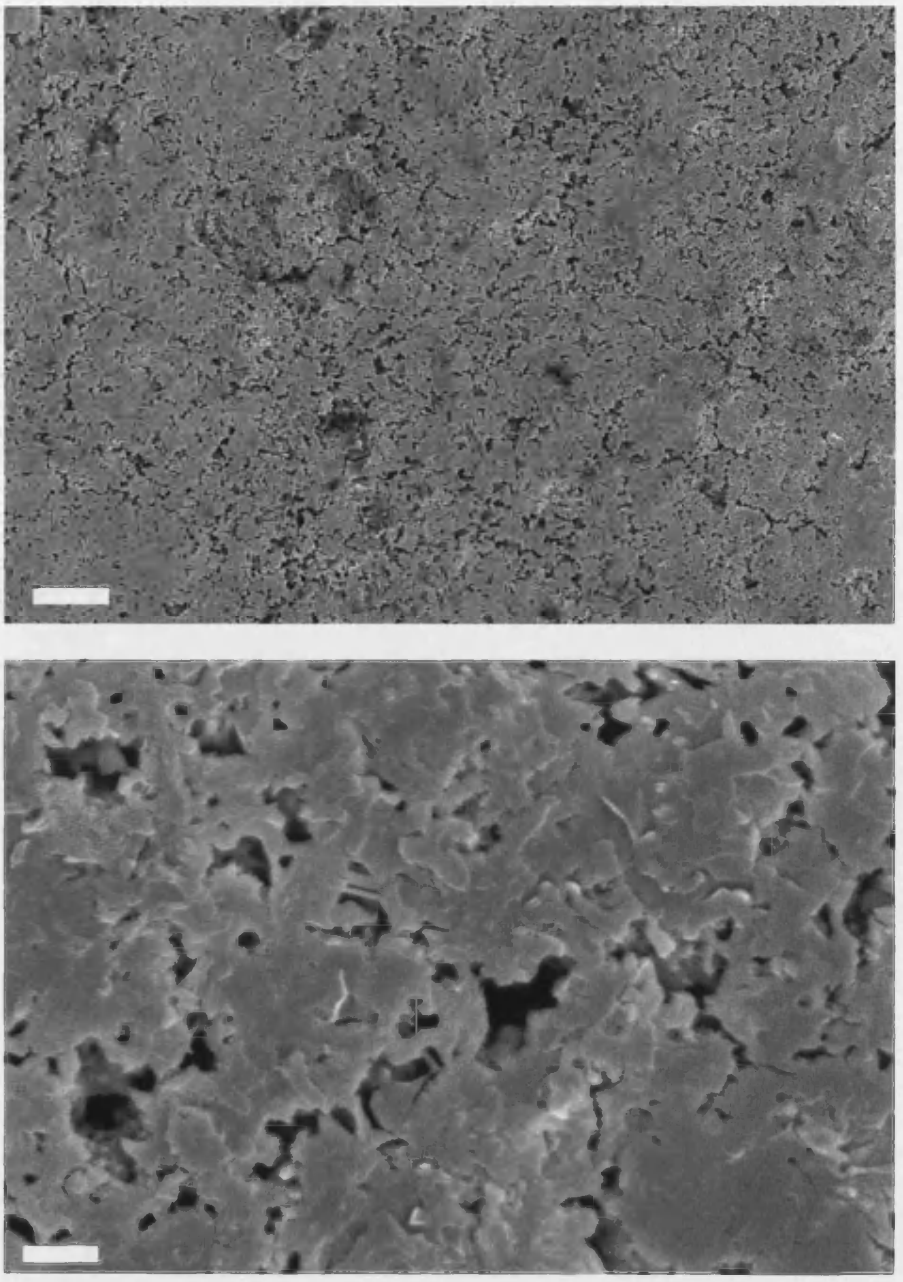

Figure 5.9 SEM micrographs of a replicated planar surface with the NW57 composite, showing higher porosity. Scale bars = 10 μm above, 1 μm below.

Magnetite Cement Structures

Composites involving hydrophilic magnetite did not contain the latex presumed responsible for the apparent smoothness of the microstructures. Although taken off-normal to the surface, SEM micrographs expectedly showed a much rougher texture than the organo-clay composites (Figure 5.10). Crystallite formation is evident, but with some filamentary features within surface cracks (Figure 5.10, bottom).

Higher magnification SEM of the filamentary features between cracks in the magnetite composite indicate that the filaments are on the order of 100 nm in diameter and tend to run through the composite for a few microns (Figure 5.11). Smaller filamentary bundles are also present with significantly smaller diameter and length, appearing on planar surfaces between the larger filaments. These may possibly be calcium silicate salts.

SEM micrographs and their corresponding EDX maps for the K_α peaks of calcium, silicon and iron are indicated in Figure 5.12. The darker rectangular regions correspond to channels in a waveguide structure. Silicon and calcium appear to be exclusive, again indicating the presence of calcium hydroxide instead of calcium silicate hydrate. Irrespective of the formation of these crystals, the magnetite is spread homogenously through the sample.

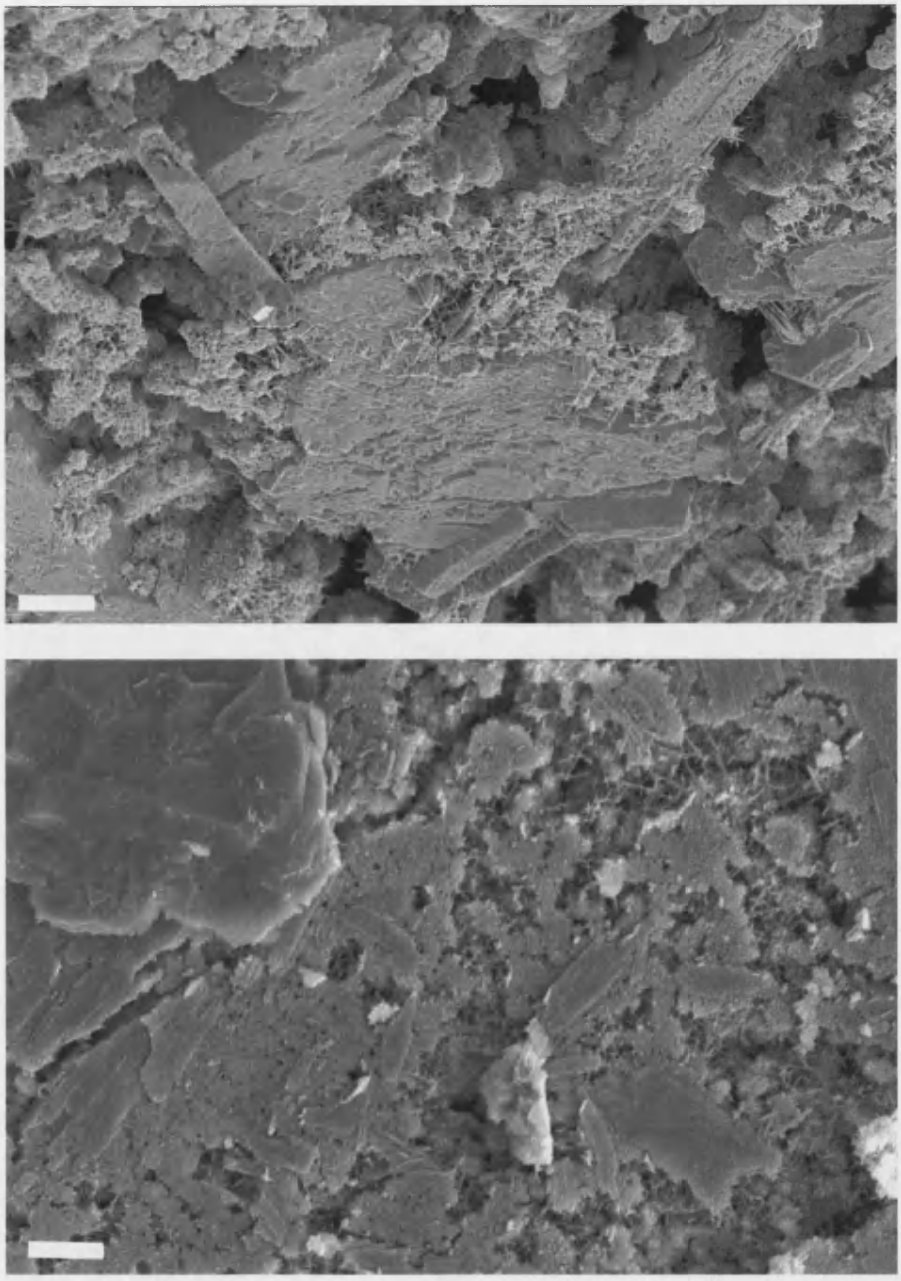

Figure 5.10 SEM micrographs of a planar surface of a magnetite composite cement. Scale bars = 10 μm.

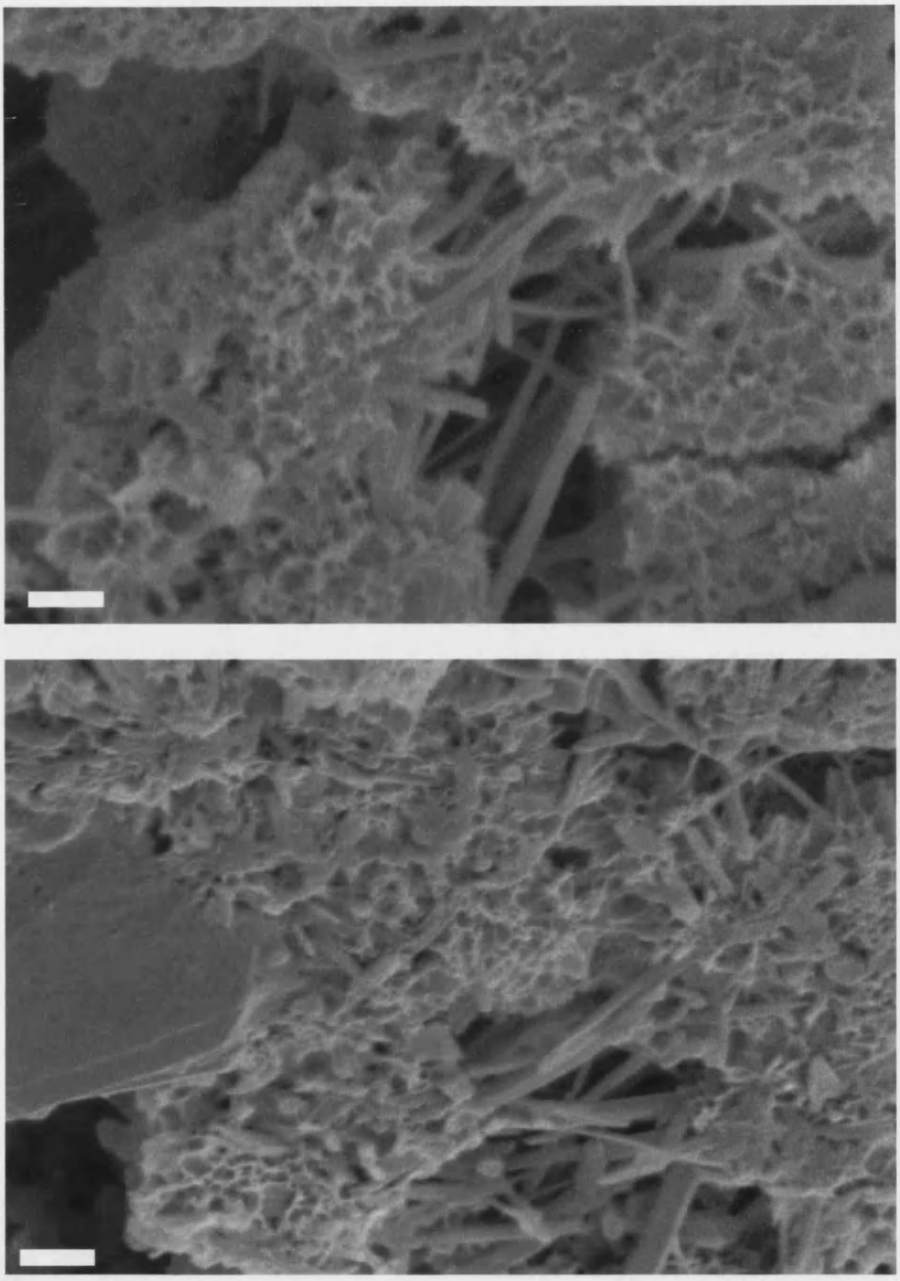

Figure 5.11 SEM micrographs of the filamentary features between cracks in the magnetite composite. Scale bars = 1 μm.

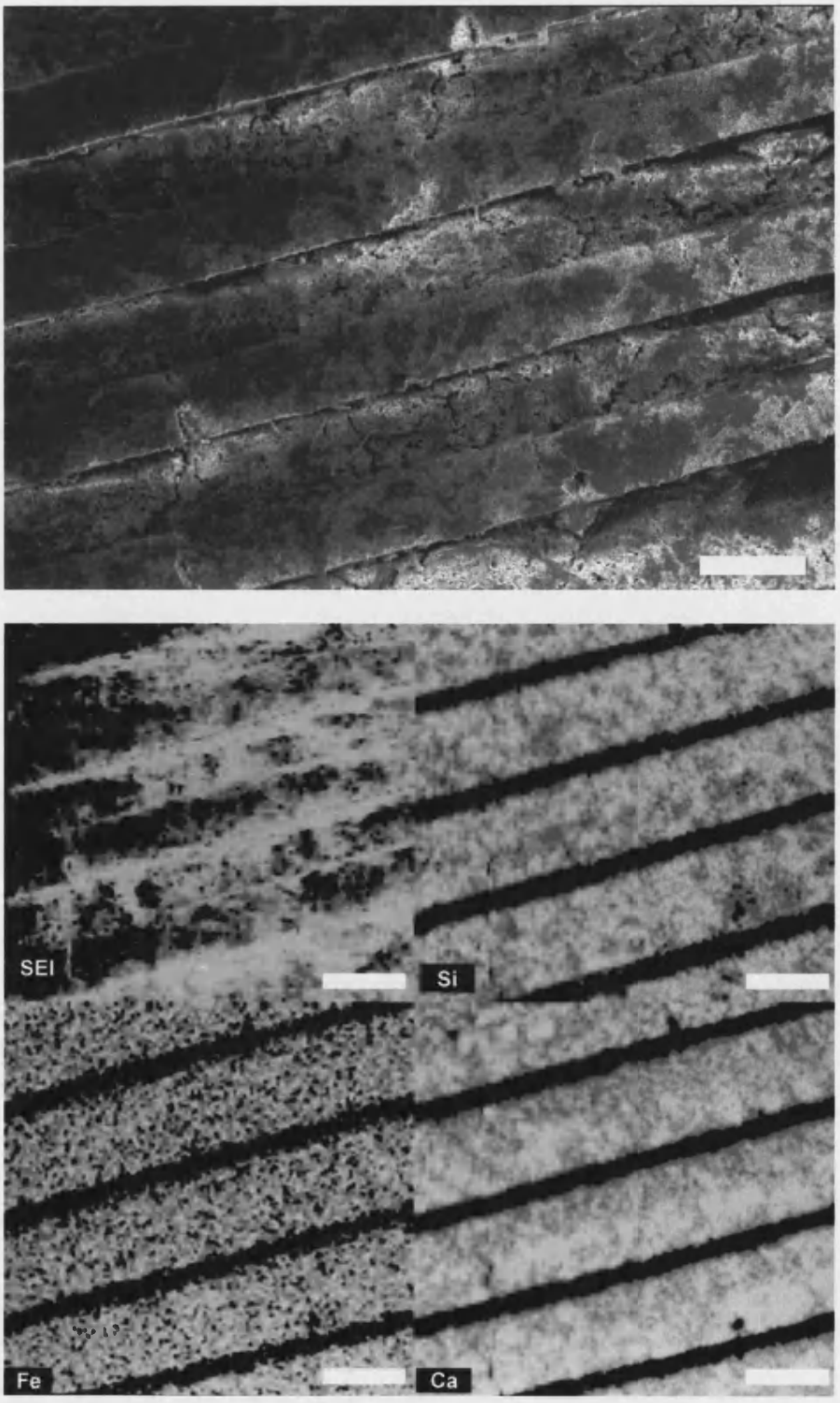

Figure 5.12 SEM micrograph and corresponding EDX maps (Ca, Si, and Fe as indicated) for the magnetite composite. Scale bars = 150 μm top, 100 μm bottom.

Ferritin Cement Structures

As in the magnetite cements, composites involving ferritin did not contain latex. SEM micrographs of a planar surface of the composite are shown in Figure 5.13. While smoother and replicating the surface better than the magnetite composite, the porosity is high and includes a similar filamentary structure within surface cracks.

Higher magnification SEM of the filamentary features between cracks in the ferritin composite again show filaments on the order of 100 nm in diameter, running through the composite alongside a finer filamentary structure (Figure 5.14, top). AFM scans at a similar magnification (Figure 5.14, bottom), indicate a height range of around 700 nm over 5 μm^2 but without resolving the filaments.

SEM micrographs and their corresponding EDX maps for the K_α peaks of calcium, silicon and iron are indicated in Figure 5.15. The darker rectangular regions correspond to channels in a waveguide structure. Silicon and calcium appear to be exclusive, again indicating the presence of calcium hydroxide instead of calcium silicate hydrate. Ferritin was spread homogenously through the sample.

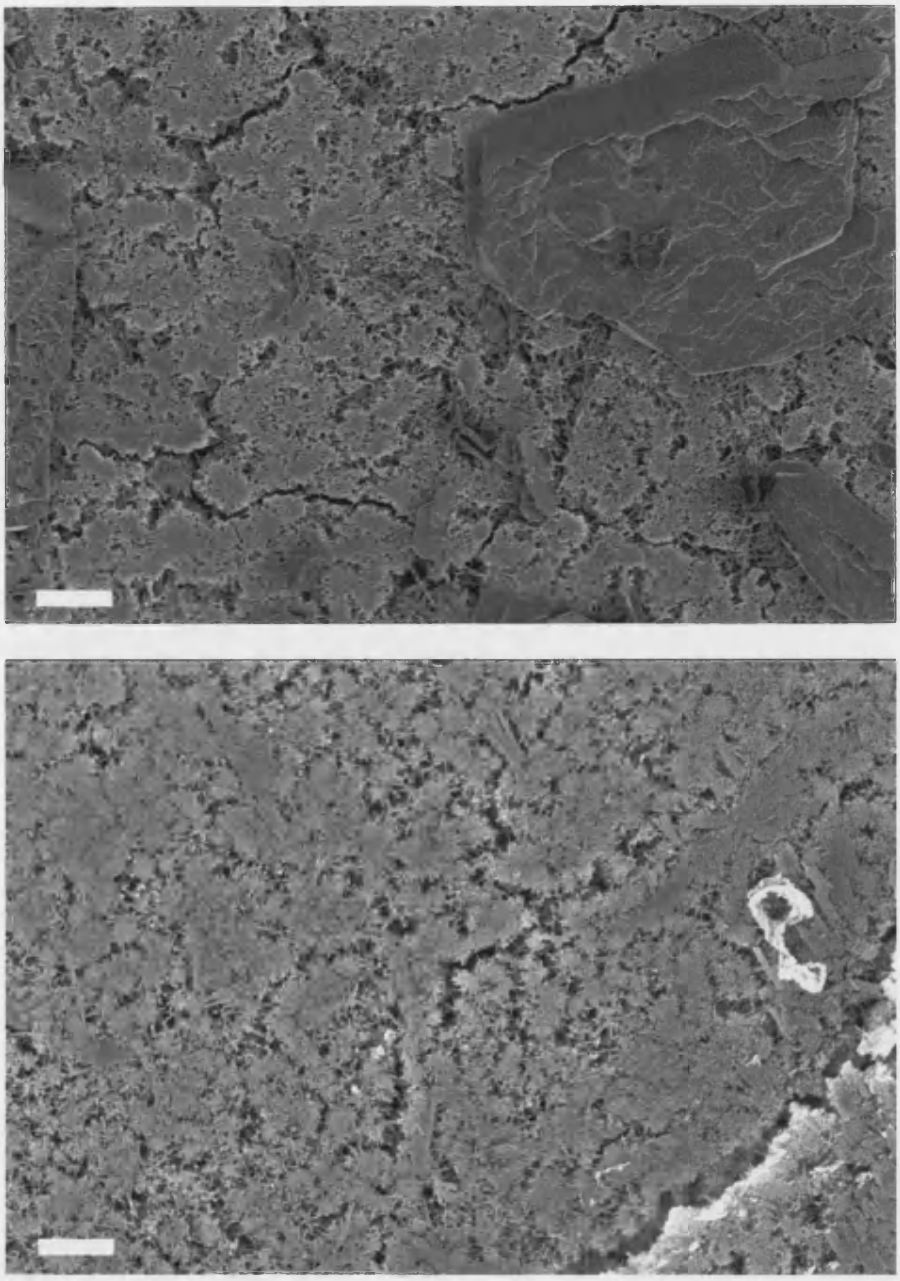

Figure 5.13 SEM of ferritin composite. Scale bars = 10 μm.

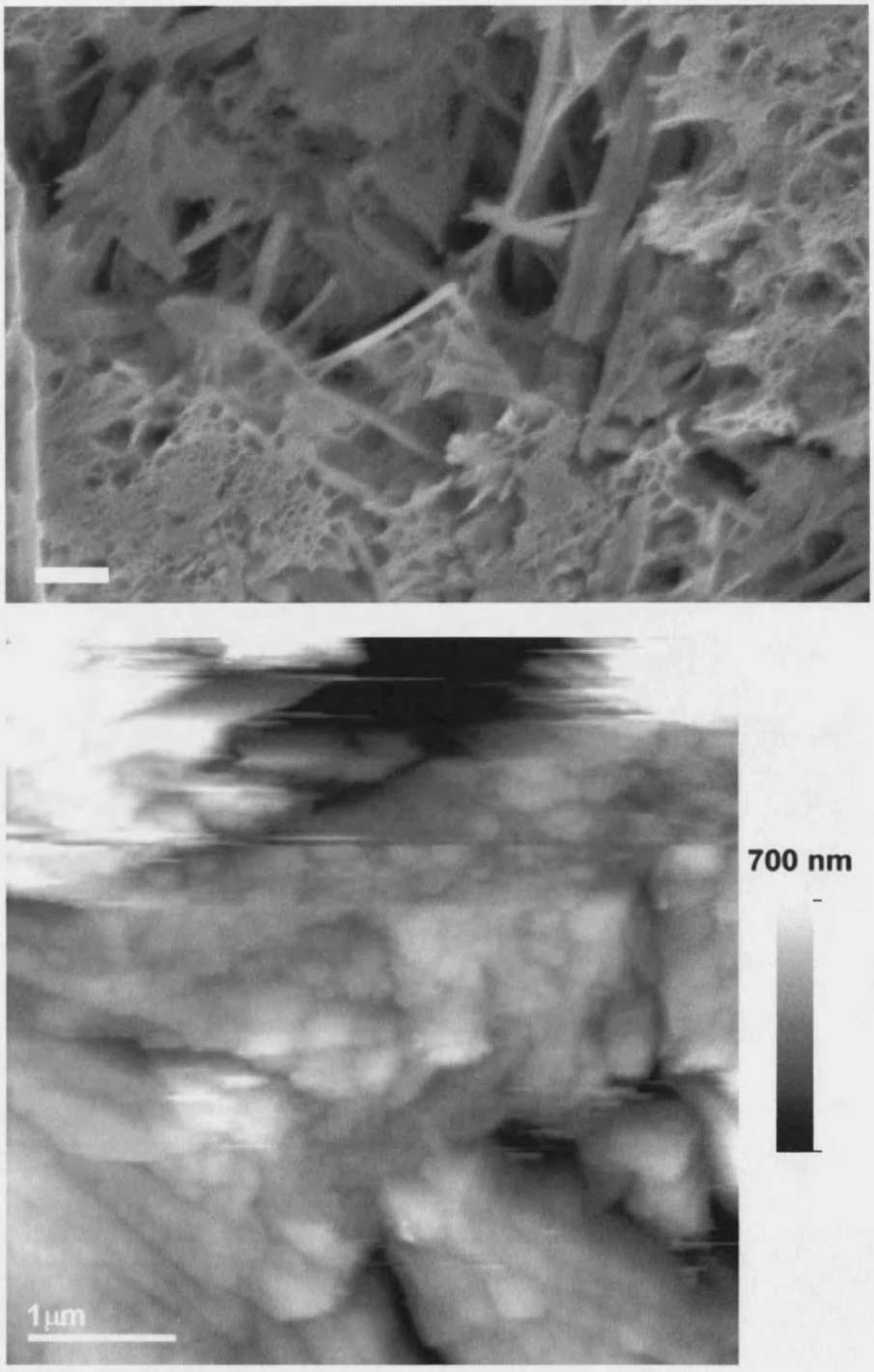

Figure 5.14 SEM micrograph (above) at higher resolution displaying filamentary structure. AFM scan at similar magnification, but without filamentary structure evident (below). Scale bars = 1 µm.

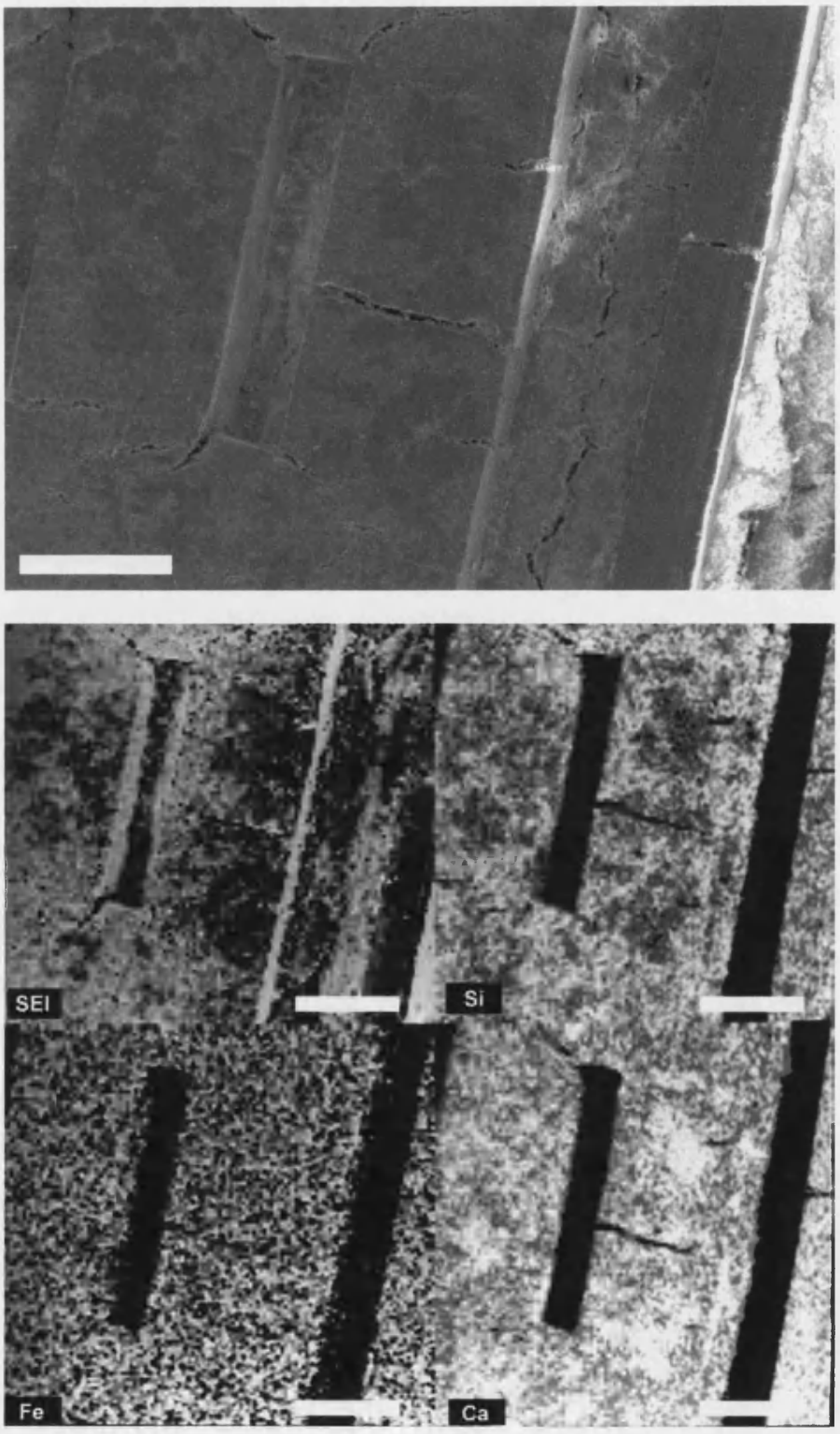

Figure 5.15 SEM micrograph and corresponding EDX maps (Ca, Si, and Fe as indicated) for the ferritin composite. Scale bars = 100 μm.

5.4 DISCUSSION

Dispersion of Colloids in Cement Microstructures

The organo-clay, magnetite and ferritin additives blended well with the powdered cement, dissolving and dispersing in the 60% by mass liquid fraction. The first indication of a good dispersion in the magnetite and ferritin cements was the homogeneous spread of their inherent brownish colour. The white, powdery organo-clays did not significantly affect the colour of the resulting cements. EDX mapping analysis for iron in the magnetite and ferritin cements (Figures 5.12 and 5.15, respectively) showed uniform dispersion across both planar surfaces and microstructured features. Crystalline fractions in the cement showed granularity on the 5 μm scale using EDX mapping analysis for calcium and silicon, indicating the presence of calcium hydroxide and calcium silicate hydrate. Regardless of the location of these differing crystalline regions, the magnetite and ferritin remained evenly distributed. It remains unclear whether the ferritin protein remained intact during the curing of the cement, though it would not be expected to survive the heating conditions required for removal of the PMMA mould. Quite likely the ferritin is carbonised during the heating process, but other mould removal techniques could be employed if biological functionality were required.

For the organo-clay samples, direct measurement of the dispersions using EDX mapping provided little insight. The most conclusive evidence for the uniform dispersion of organo-clays comes indirectly from the difference in porosity between the clay cements. NW57, the un-polymerised form of NW53, yielded composite cements with a much higher porosity than the other two, potentially indicating some reactivity between the clay and the cement during formation. That this higher

porosity was uniform across the surface of the cement (Figure 5.9) indicates that the effect of, hence the presence of, the clay was correspondingly uniform. The remaining clays are less reactive, behaving more like the magnetite and ferritin during the mixing and curing process. It is expected that they were similarly transported and left uniformly dispersed throughout the cement. In summary, the cement mixtures are capable of dispersing and carrying functional materials as micro- or nano-particles within the microstructured features.

Filamentary Structures in Cement

A filamentary texture was observed in both the magnetite (Figure 5.11) and ferritin (Figure 5.14) composite cements. The preparation of these two cements was different from the organo-clays in that no latex was added, and the water content came solely from the solvent of the additives. As the additive weight percent was kept roughly constant, either the presence of additional salts in the magnetite and ferritin sols or the absence of latex is responsible for the filaments. While the ferritin solution contained 0.15M NaCl, it is unlikely that such crystals would exhibit a filamentary form. Moreover, the magnetite composites displayed nearly identical filaments, but the respective sols contained no sodium chloride. Most probably, the composites contained crystals of calcium silicate hydrate that typically form filaments, as latex has been shown to promote the growth of calcium hydroxide to the exclusion of calcium silicate (Grosse, *et al.*, 2001). Further supporting this mechanism, EDX analysis of the latex-containing clay samples showed higher silica concentrations at the edges of features (Figure 5.4), formed last during the hydration process. In contrast, the magnetite (Figure 5.12) and ferritin (Figure 5.15) cements

exhibited a more homogeneous distribution of silica, indicating calcium silicate growth was less inhibited in the absence of latex.

Porosity in Organo-Clay Composites

Composites containing the un-polymerised NW57 produced cements with a much higher porosity than the other clays, potentially indicating some reactivity between the clay and the cement during formation. Possibly it interfered with the dispersing of latex, or inhibited the growth of calcium hydroxide. The uniformly porous surfaces of the cement (Figure 5.9) showed none of the filaments present in the latex-free cements, indicating that calcium silicate hydrate formation was suppressed. Such a mechanism could be further explored with EDX analysis of the surface, observing the uniformity of calcium and silicon concentration. A further possibility is that the surfactant in the latex solution which normally improves contact between the hydrophobic polymer mould and the hydrated cement (Colston, *et al.*, 1996) was disrupted by free methyl groups on the clay.

Functional MEMS

In this work two important abilities have been introduced to materials for MEMS. The first is the ability to change the porosity of a feature, and the second is the ability to disperse functional nanoparticles uniformly throughout a feature. While the complete range of porosities and mechanisms has yet to be explored, this work indicates one could modify the porosity of the composites by deliberately altering the latex or water content of the mix, or possibly inhibit the properties of the surfactant contained in the latex. Applications are conceivable in which a gas or liquid flow proceeds at a controlled rate through a porous cement matrix to interact with reactive

sites for catalysis or detection. By combining the porosity with dispersed proteins, one can envisage sensors that use immobilized proteins within a microstructured matrix to trap drugs or bioactive agents. By dispersing magnetic nanoparticles in a cement, one could possibly prepare actuators that respond to electromagnetic fields. Some traditional actuated MEMS place actuators at the base of a translating feature, but by incorporating the functionality of the nanoparticles, the whole translating feature can become the actuator, reducing complexity. Further, properties not available to traditional MEMS materials such as catalytic, bioactive and magnetic can widen the base of their application. Importantly, new devices are feasible which exhibit control at the mixed length scales of the nanometer (nanoparticles), sub-micron (cement porosity) and 10-100 micron (microstructured features).

5.5 REFERENCES

Börner, M. W., M. Kohl, F. J. Pantenburg, W. Bacher, H. Hein, and W. K. Schomburg, "Movable microstructures made by a sub-micron LIGA process", *Microsystem Technologies 2*, 149-152 (1996).

Colston, S. L., D. O'Connor, P. Barnes, E. L. Mayes, S. Mann, H. Freimuth, and W. Ehrfeld, "Functional micro-concrete: The incorporation of zeolites and inorganic nano-particles into cement micro-structures", *J. Mat. Sci. Lett.*, **19**, 1085-1088 (2000).

Colston, S. L., P. Barnes, H. Freimuth, M. Lacher, and W. Ehrfeld, "Cements: a new medium for micro-engineering structures?", *J. Mat. Sci. Lett.*, **15**, 1660-1663 (1996).

Feiertag, G., W. Ehrfeld, H. Freimuth, G. Kiriakidis, H. Lehr, T. Pedersen, M. Schmidt, C. Soukoulis, and R. Weiel, "Fabrication of three-dimensional photonic band gap material by deep X-ray lithography", *Photonic Band Gap Materials*, ed. C. M. Soukoulis (Kluwer Academic Publishers, Netherlands), 63-69 (1996).

Grosse, C. U., S. U. Köble, and H. W. Reinhardt, "Ultrasound, Scanning Electron Microscopy and Nuclear Magnetic Resonance Spectroscopy - Comparison of Results Investigating the Hydration Process in Cementitious Materials", *Nondestructive Testing & Ultrasonics*, **6**(5), e-Journal (2001).

Hall, C., P. Barnes, J. K. Cockcroft, S. L. Colston, D. Hausermann, S. D. M. Jacques, A. C. Jupe, and M. Kunz, "Synchrotron Energy-Dispersive Diffraction Tomography", *Nucl. Instrum. & Methods in Phys. Res.*, **B140**, 253-257 (1998).

Jawed, I., J. Skalny, and J. F. Young, *Structure and Performance of Cements*, ed. P. Barnes (Applied Science Publishers, London), 237 (1983).

Knitter, R., E. Günther, C. Odemer, and U. Maciejewski, "Ceramic microstructures and potential applications", *Microsystem Technologies 2*, 135-138 (1996).

Piotter, V., T. Hanemann, R. Ruprecht, and J. Haußelt, "Injection moulding and related techniques for fabrication of microstructures", *Microsystem Technologies*, 129-133 (1997).

Ritzhaupt-Kleissl, H. J., W. Bauer, E. Günther, J. Laubersheimer, and J. Haußelt, "Development of ceramic microstructures", *Microsystem Technologies 2*, 130-134 (1996).

Rogers, J. A., R. J. Jackman, and G. M. Whitesides, "Constructing Single- and Multiple-Helical Microcoils and Characterizing Their Performance as Components of Microinductors and Microelectromagnets", *J. Microelectromechanical Systems*, **6**(3), 184-192 (1997).

Schluth, F., "Crystallographically defined pore systems: reaction vessels with molecular dimensions", *Dechema Monographs*, **132**, 71-92 (1996).

Wollenberger, U., R. Hintsche, and F. Scheller, "Biosensors for analytical Microsystems", *Microsystem Technologies 1*, 75-83 (1995).

Yanagisawa, K., H. Kuwano, and A. Tago, "Electromagnetically driven microvalve", *Microsystem Technologies 2*, 22-25 (1995).

CHAPTER SIX

PROTEIN TEMPLATED POLYPYRROLE COMPOSITES: COMPLEX NANOPARTICLES

6.1 INTRODUCTION

In the preceding chapters, nanoparticles of uniform composition were produced to functionalise microstructures. Any additional functionality of the final microstructure was provided by the template, unless an assembly of nanoparticles showed collective behaviour. In this chapter nanoparticles with enhanced functionality are considered which could further enhance the utility of nanoparticulate microstructures. Enhanced functionality can be obtained by structuring the nanoparticles themselves. For example, layered nanoparticles and nanotubes have been created by anodic deposition (Suenaga, *et al.*, 1997). The nanoparticles (and tubes) were composed of alternating layers of graphitic carbon and boron nitride, as well as nanoparticles composed of a small grains of hafnium boride layered with boron nitride and carbon. Such layered nanoparticles not only allow for interesting electronic properties, but also enhanced mechanical properties (e.g. strength and wearability). Nanoparticles with potential in molecular sieving or catalysis have been prepared not through layering, but by using surfactant templates to produce grains of mesoporous silica (MCM-41) (Fowler, *et al.*, 2001).

The goal of the work presented in this chapter is to use the iron oxide core of ferritin as a catalyst for a nanopolymer to be contained within the protein cage. As ferritin can be loaded with iron(III) in the form of ferrihydrite, an organic monomer (pyrrole) that can polymerise in the presence of iron(III) was chosen. Further, polypyrrole is a conducting polymer so monodisperse, protein-coated nanoparticles could be used in composites that exploit electron transport at the nanometer scale.

Background - Ferritin

Ferritin is a storage protein providing biologically available iron for mobilisation in mechanisms such as heam production. The iron is stored typically in a poorly crystalline form as an iron (III) oxy-hydroxide, ferrihydrite (Harrison, *et al.*, 1989). The protein is composed of 24 nearly identical subunits, which self-assemble to form an almost spherical 12 nm diameter cage with a 7.5 - 8.0 nm diameter cavity (Figure 6.1). The assembled structure of the protein contains both hydrophilic and hydrophobic channels permitting the influx of ions and ejection of by-products. The protein is quite robust, being able to withstand high temperatures (65 ^{o}C) and wide pH variations (in the approximate range 4.0 - 9.0) for limited periods of time without significant disruption to the quaternary structure. This stability is a very attractive feature compared to other techniques for nanoparticle synthesis.

The internal cavity can be accessed if the native iron oxide mineral core is first removed by reductive dissolution leaving an empty protein, termed "apoferritin". The cavity of the protein can then be used as a reaction vessel for the production of different mineral phases, such as reconstituting in vitro with iron (Figure 6.2), or oxides of manganese (Meldrum, *et al.*, 1991, 1995) or uranium (Meldrum, *et al.*, 1991). It has also been used for the production of the magnetic iron phase, magnetite (Meldrum, et al., 1992), and *in situ* sulphidation of the native or reconstituted iron oxide core can be performed to produce an iron sulphide core (Douglas, *et al.*, 1995). More recently cadmium sulphide (CdS) (Wong, *et al.*, 1996) and an fcc-ordered magnetic alloy of cobalt/platinum (Warne, *et al.*, 2000: Figure 6.3) have been produced. In all instances the cavity is not only used to confine, but also to control the size of the mineral formed. In this chapter native ferritin with a ferrihydrite core

was intended to be the catalytic centre for the conductive polymer – polypyrrole. The intention was to produce nanoparticles of polypyrrole within the ferritin cavity.

Pyrrole is only slightly soluble in water, so to enhance mixing between ferritin and the monomers the surface of the protein was hydrophobically-modified. Such modified ferritins have enhanced solubility in organic solvents such as dichloromethane (DCM), and to a lesser extent, ethyl acetate and toluene (Wong, *et al.*, 1998, and Wong, *et al.*, 1999). The derivatised proteins are synthesized by alkylation reactions using long chain primary amines (C_n , n = 6, 9, 12, 14, 18) which are covalently coupled to the native protein by nucleophilic substitution at carbodiimide-activated carboxylic acid groups.

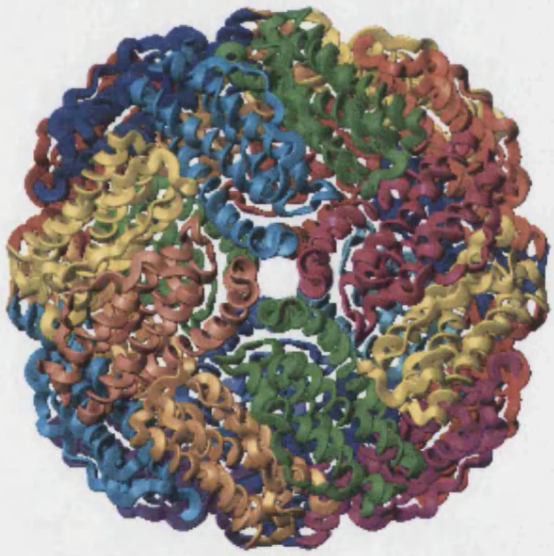

Figure 6.1 Structural representation of the 12 nm-diameter ferritin macromolecule from high-resolution studies (Hempstead, *et al.*, 1997, Bernstein, *et al.*, 1977) prepared using MolMol (Koradi, *et al.*, 1996) and viewed along the 4-fold axis. The 24 protein subunits are individually coloured for structural clarity.

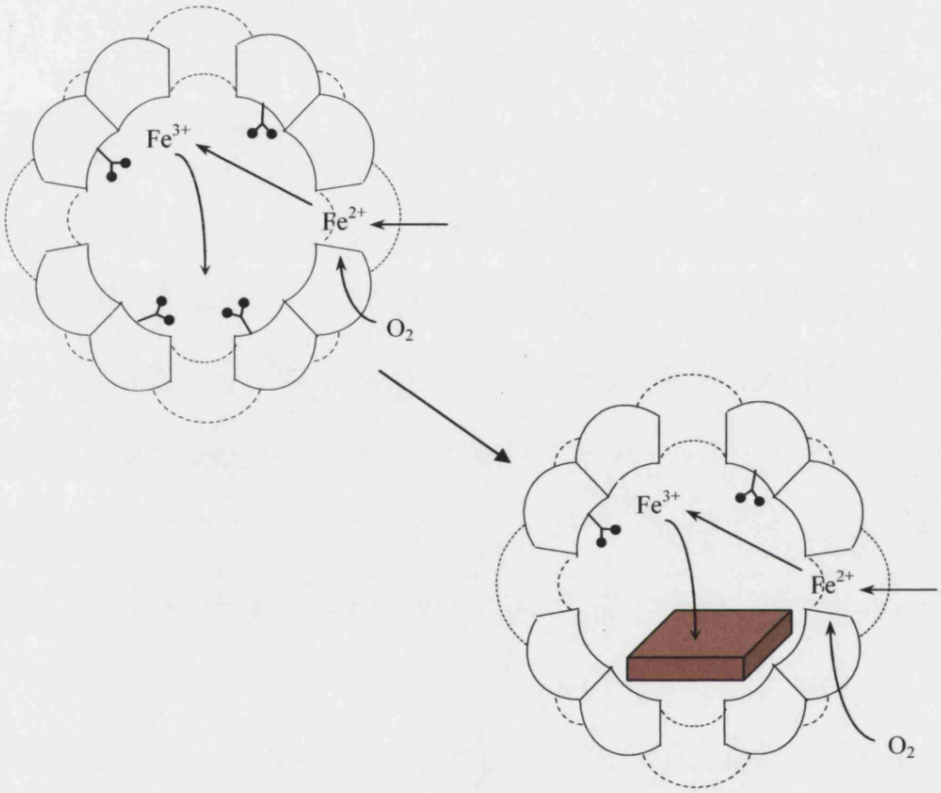

Figure 6.2 Schematic mechanism for the production of an iron(III) oxy-hydroxide core within the ferritin protein. Iron (II) ions enter the protein cavity and are oxidised to iron(III) at reactive centres (top). The iron(III) oxide nucleates and begins to form a core of material (bottom).

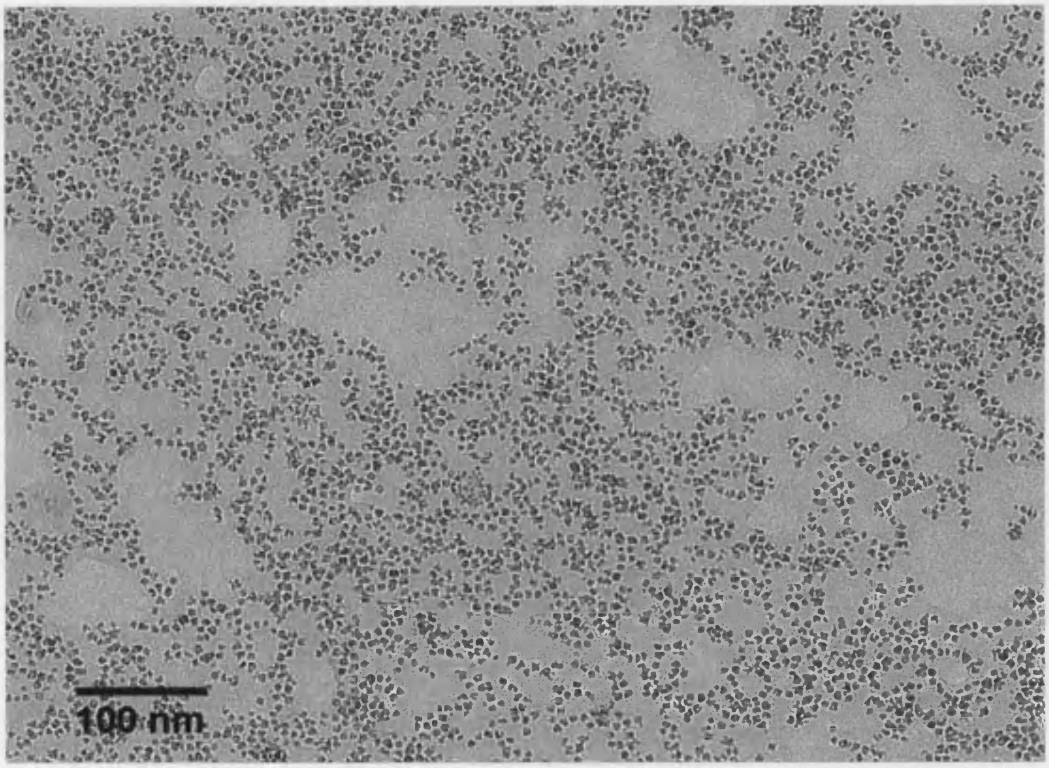

Figure 6.3 TEM micrograph of fcc-ordered cobalt/platinum alloy nanoparticles within the protein ferritin. Electron dense cores are uniformly ~8 nm in diameter (Warne, *et al.*, 2000).

Background - Polypyrrole

There has been much recent interest in nanoscaled polypyrrole structures. Systems that control the structure of the final polymer have mirrored many of the templating methods discussed in the preceding chapters. For example, supercritical carbon dioxide was used during the polymerisation process to produce aggregates of polypyrrole with much finer structure (less globular) than typical aqueous production methods (Kerton, *et al.*, 1997). Others have exerted even more control using spherical latex beads as templates for coating (Lascelles, *et al.*, 1995). Pyrrole has also been stabilised by surfactants and polymerised, controlling the growth and shape of the polymer to yield nanoparticles typically 100-150 nm in diameter (Armes, 1996, Simmons, *et al.*, 1995). Akin to the gold-decorated tubules mentioned in Chapter 1, polypyrrole has also been used to decorate the edges of lipid tubules (Goren, *et al.*, 2000). Most relevant to the proposed material in this chapter, complex polypyrrole nanoparticles have been prepared using tetrachloroauric acid ($HAuCl_4$) as the catalyst for pyrrole (Selvan, *et al.*, 1998). By stabilising tetrachloroauric and pyrrole in copolymer micelles, nanocores of gold coated in polypyrrole were produced typically 20-30 nm in diameter.

The goal of this chapter was to extend the templating nature of ferritin to include the production of a nanopolymer within the protein cage of ferritin. Pyrrole will polymerise into a black/green product in acidic solutions of iron(III) complexes, and the controlled dissolution of the ferrihydrite core was expected to catalyse polymerisation within the protein shell.

As an example of iron(III) reactivity, ions from solvated $FeCl_3$ act as oxidants of the pyrrole. In particular, there are intermediates of $FeCl_3$-pyrrole complexes as the first steps in polymerisation (Planche, *et al.*, 1994). The polymerisation reaction is generically given by the following, where $Pyrrole^{*+}$ is a radical cation:

$$Pyrrole + Fe^{3+} \rightarrow Pyrrole^{*+} + Fe^{2+} \quad (1)$$

$$2Pyrrole^{*+} \rightarrow Pyrrole\text{-}Pyrrole + 2H^{+} \quad (2)$$

$$Pyrrole\text{-}Pyrrole + Fe^{3+} \rightarrow Pyrrole\text{-}Pyrrole^{*+} + Fe^{2+} \quad (3)$$

$$(Pyrrole\text{-}Pyrrole)_n^{*+} + Pyrrole^{*+} \rightarrow (Pyrrole\text{-}Pyrrole\text{-}Pyrrole)_{n+1} + 2H^{+} \quad (4)$$

The radical can dimerise to make bipyrrole (eq. 2) setting two protons free. The polycondensation then proceeds according to equations 3 and 4, until reactants are depleted. The reaction is shown diagrammatically in Figure 6.4 below:

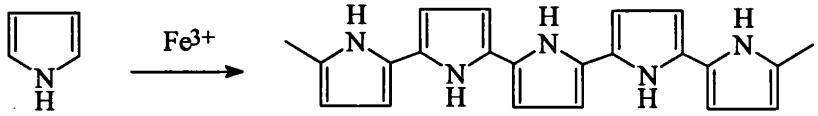

Figure 6.4 Reaction scheme for the polymerisation of pyrrole mediated by iron(III).

While polymerisation of pyrrole with Fe^{3+} is quite rapid, the iron(III) in oxides such as ferrihydrite is not sufficiently soluble for the reaction to occur at normal pH. Therefore pH is an important component in the successful production of polypyrrole using ferritin as a template.

6.2 MATERIALS AND METHODS

Apoferritin Preparation

Horse-spleen ferritin (250 mg from Sigma Aldrich) was placed into a dialysis bag (molecular weight cut-off of 12-14 kDaltons) and diluted with sodium acetate buffer (25 ml of 0.1 M at pH 5.5). The bag was suspended in 800 ml of buffer and purged with N_2 for 30 minutes. Thioglycolic acid (TGA; 2.0 ml of 0.02 M) was then added to the buffer under anaerobic conditions and allowed to stir. A further 1 ml of TGA was added after 2 hours, and then dialysed for another hour. The buffer was then refreshed and purged with N_2 for 30 minutes, with the de-mineralisation procedure repeated until a colourless solution was obtained. The apoferritin solution was then dialysed against saline (0.15 M; 2 litres) and stirred for 1 hour. The saline was refreshed (3 litres) with the bag stirring overnight in a cold room. Finally, the protein concentration was determined using a bichionnonic acid assay (Sigma). One portion of the apoferritin was partitioned for Atomic Absorption (AA) analysis for iron. The partitioned solution was diluted until the iron concentration reached 0.6 parts per million (ppm). The remaining apoferritin solution was used for the procedures outlined below.

Reconstituted Ferritin Preparation

A solution of apoferritin was dialysed against 2-[N-morpholino]ethanesulphonic acid buffer (MES; 0.05 M at pH 6.5). Four aliquots of deaerated ferrous ammonium sulfate (2.78×10^{-6} moles), equivalent to 250 Fe(II) atoms per protein macromolecule for each addition were added at hour intervals. The resulting solution was left to stir overnight, and produced a faintly yellow solution of reconstituted ferritin. One portion of the reconstituted ferritin was mixed in 3:1

Ethanol/Water, and diluted until the iron concentration reached 38.5 ppm by AA. A similar concentration of aqueous ferritin was produced, and the remaining solution was used for the procedure described immediately below.

Derivatised Ferritin Preparation

Nonylamine (1.5 ml of 7.77 mM) was added to THF/H_2O (1:1) to give a final volume of 10 ml. The pH of the solution was adjusted to pH 5.5 with HCl. Apoferritin (10 mg of 2.22 x 10^{-5} mM) was added slowly with the pH being maintained at pH 5.5. The apoferritin concentration corresponded to approximately 700 nonylamine molecules for each carboxylic acid group on the protein, assuming a total of approximately 520 aspartic and glutamic acid residues. 1-(3-dimethylaminopropyl)-3-ethyl carbodiimide hydrochloride (EDC; 150 mg of 0.78 mM) dissolved in 1 ml THF/H_2O (1:1), was added dropwise while continuing to maintain pH 5.5. The pH was monitored and maintained for 2-3 hours, then the reaction mixture stirred overnight at room temperature. The alkylated protein was transferred from the reaction mixture into dichloromethane (DCM) by the addition of small quantities (5-10 mg) of dry sodium chloride. The final, functionalised product can be represented schematically by Figure 6.5. This procedure was used for both apo- and reconstituted ferritin solutions, to produce protein precursors in DCM. The concentration of the reconstituted ferritin was adjusted so that iron was at 38.5 ppm, while the derivatised apoferritin was adjusted to 0.6 ppm iron. Derivatised proteins could also be returned into an aqueous phase by addition of water, which lowered the salt concentration forcing the derivatised proteins out of the DCM. The synthesis of the material described was guided with the help and supervision of Dr. Kim Wong.

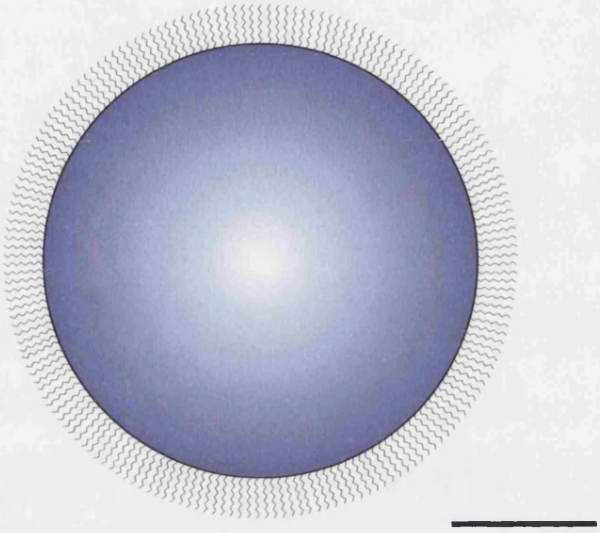

Figure 6.5 Schematic of derivatised ferritin with primary amines of C_9. Scale bar = 3 nm (Drawing courtesy of Kim Wong).

Control Preparation

Ferrihydrite was prepared through hydrolysis of an acidic iron(III) solution. First 250 ml of H_2O was heated in an oil bath to 75 °C. 2.5 g of unhydrolyzed crystals of $Fe(NO_3)_3 \cdot 9H_2O$ were added under rapid stirring. The solution was left for 10-12 minutes during which the solution changed from gold to dark reddish brown. The solution was then cooled rapidly by immersion in an ice bath and finally dialyzed for three days, changing the water several times each day. The resulting pH of the ferrihydrite suspension was pH 2.5. Ferrihydrite solution was diluted such that the final iron concentration was 38.5 ppm as confirmed by AA. An iron(III)Chloride solution was also prepared in water, and diluted such that the final iron concentration was also 38.5 ppm confirmed by AA.

Two-Phase Polypyrrole Preparation

It was expected that the reaction rate would be more rapid when the pyrrole monomers were in contact with the ferritin/iron complexes, so two different experiments were proposed. In both cases, the pH was lowered slightly to allow for iron(III) to reduce and become mobile from the ferritin core, oxidise in solution, then catalyse the polymerisation of pyrrole. The first experiment was to prepare aqueous phase proteins and controls and add 1 ml of pyrrole (Sigma-Aldrich, 98%) while stirring to form two phases. It was expected that reactions would occur at the water/solvent interface, moderating the reaction. The other was to prepare derivatised proteins and controls in organic solvents (DCM and ethanol), such that they would mix into a single phase.

For the two-phase experiment, derivatised reconstituted ferritin, derivatised apoferritin, reconstituted ferritin, apoferritin, $FeCl_3$ and ferrihydrite solutions were prepared such that the iron concentration in the apoferritin samples was 0.6 ppm, and all else were 38.5 ppm. All samples were adjusted to pH 6.9 - 7.1 but not buffered, and then 2 ml of each solution was added to 1 ml of pyrrole and allowed to stir for several days. At regular intervals, the pH of the solutions was recorded and photographs were taken to show the evolution of greenish/black polypyrrole.

One-Phase Polypyrrole Preparation

For the one-phase experiment, derivatised reconstituted ferritin and derivatised apoferritin in DCM, reconstituted ferritin and apoferritin in 1:1 Ethanol/Water, and $FeCl_3$ and ferrihydrite in 3:1 Ethanol/Water were prepared such that the iron concentration in the apoferritin samples was 0.6 ppm, and all else were 38.5 ppm.

All samples were adjusted to pH 6.9 - 7.1 but not buffered, and then 2 ml of each solution was added to 1 ml of pyrrole and allowed to stir into a single phase for several days. At regular intervals, the pH of the solutions was recorded and photographs were taken to show the evolution of greenish/black polypyrrole.

UV/VIS Characterisation of Polypyrrole Composites

Spectra were recorded at the end of the experiments using a Perkin-Elmer Lambda 6 spectrophotometer. Absorbance was recorded from 400 to 1100 nm, and samples were prepared in quartz cuvettes with 10 mm pathlength. All measurements were taken after allowing the spectrophotometer to thermally stabilise for 1 hour. For the two-phase samples, 10 μl of the solution was taken from the bottom of the vial to avoid any pyrrole contamination. It was dispersed into 2 ml H_2O for UV/VIS analysis. In some one-phase systems, a sub-phase would appear which was treated in a similar manner except where noted.

Microscopy of Polypyrrole Composites

Samples were analysed using atomic force microscopy (AFM), using a Digital Instruments NanoScope IIIa in both contact and tapping modes. Transmission electron microscopy was performed using a JEOL 2000 FX operating at 200 kV. Samples were prepared on carbon sputtered, formvar-covered 3 mm copper grids. High resolution SEM was performed using a JEOL 1200 EX transmission electron microscope with an attached scanning imaging device (ASID).

6.3 RESULTS

General Characteristics

Regardless of experiment, the incubation of pyrrole with reconstituted ferritin, $FeCl_3$, and ferrihydrite solutions became darker, indicating the formation of polypyrrole. Apoferritin samples also became darker, but at a much slower rate. All samples became more acidic over the duration of the experiments due to the increase in protons as the reaction proceeded.

Two-Phase Reaction

This experiment evolved polypyrrole in the top (pyrrole-containing) phase of the vial over a period of 20 days. Throughout the reaction, pH decreased as shown in Table 6.1. The top phase of both reconstituted ferritin samples and the controls proceeded to become darker more rapidly than the apoferritin samples, as expected. However, the non-derivatised apoferritin remained a cloudy emulsion throughout the experiment and seemed to produce only a slight amount of the polypyrrole product (Figure 6.6).

Sample	Derivatised Reconstituted Ferritin	Derivatised Apoferritin	Reconstituted Ferritin	Apoferritin	Ferrihydrite Control	$FeCl_3$ Control
26/03/97	6.50	7.30	8.60	8.80	8.50	9.00
27/03/97	6.50	7.20	8.50	8.50	8.70	8.80
30/03/97	6.30	7.00	8.50	7.60	8.30	8.50
02/04/97	6.20	7.00	8.50	8.30	8.50	8.50
07/04/97	6.10	6.80	8.30	8.00	8.50	8.60
11/04/97	6.20	6.90	8.20	7.80	8.30	8.50
15/04/97	6.10	6.20	7.90	7.70	7.70	8.30

Table 6.1 pH values of two-phase samples versus sampling date.

UV/Vis Analysis

Solutions were extracted from the lower phase of the samples which did not obviously contain polypyrrole. It was expected that any polypyrrole formation within the ferritin protein would remain solvated by water. It is a typical signature of polypyrrole of a broad absorbance maximum between 400 and 500 nm (Selvan, *et al.*, 1998). In none of the samples was such a maximum visible (Figure 6.7). However there was an interesting inverse relationship between derivatised and non-derivatised proteins around 980 nm.

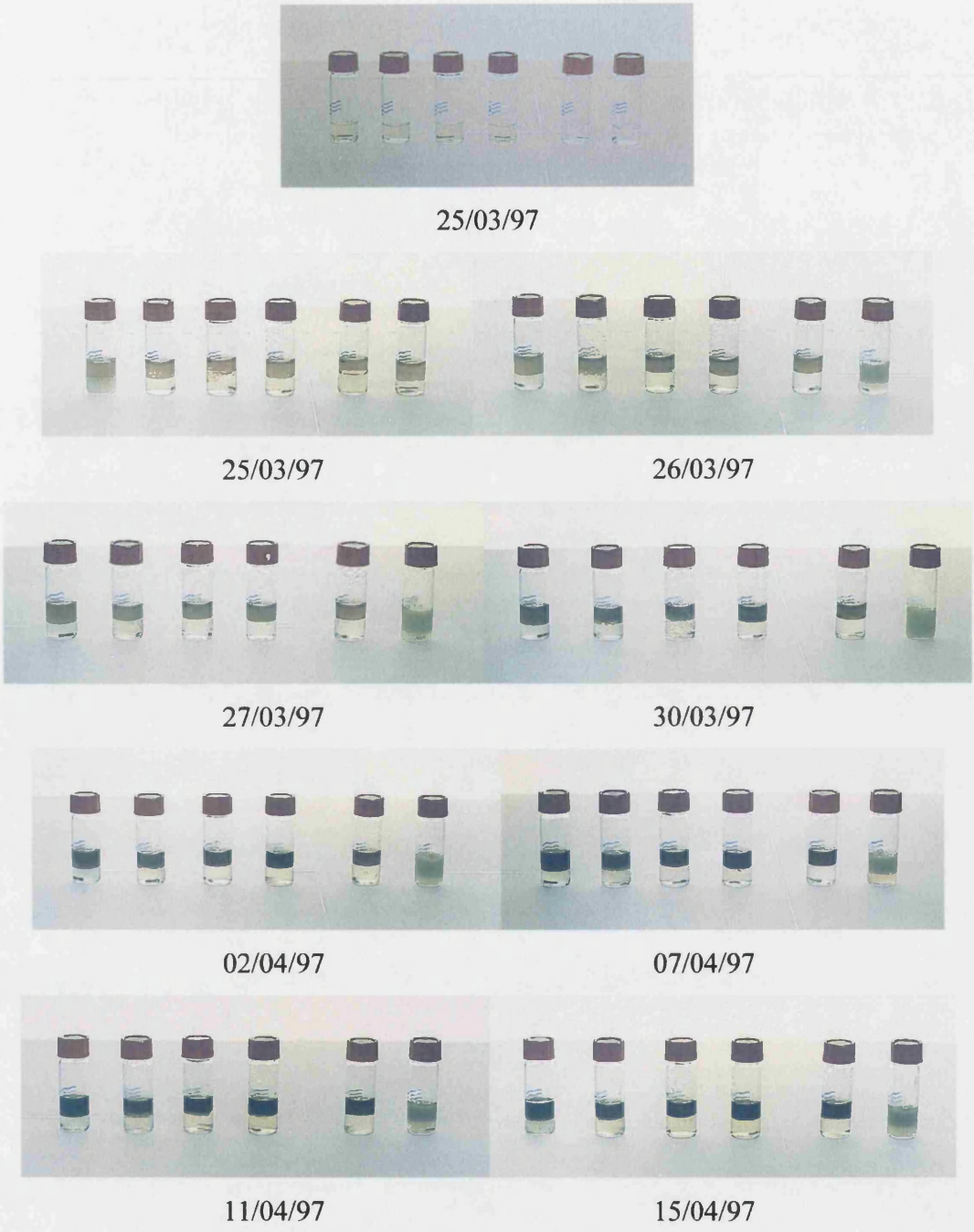

Figure 6.6 2-Phase samples over time (top image without pyrrole). L-R: Derivatised Reconstituted Ferritin, Reconstituted Ferritin, Ferrihydrite Control, Iron(III)Chloride Control, Derivitised Apoferritin, Apoferritin. 1 ml pyrrole added as top phase on 25/03/97.

One-Phase Reaction

This experiment evolved polypyrrole in a single phase over a period of 20 days. Throughout the reaction, pH decreased as shown in Table 6.2. Both reconstituted ferritin samples and the controls proceeded to become darker more rapidly than the apoferritin samples, as expected. The derivatised samples seemed to react more slowly, remaining lighter for a longer period (Figure 6.8). As the colour of these samples was lighter, the derivatised one-phase samples were the most likely candidates for successful production of the protein-encapsulated polypyrrole products. This idea is based on the assumption that smaller polypyrrole particles interfere with light to a lesser degree.

Sample	Derivatised Reconstituted Ferritin	Derivatised Apoferritin	Reconstituted Ferritin	Apoferritin	Ferrihydrite Control	$FeCl_3$ Control
26/03/97	6.50	8.30	8.60	8.40	8.10	7.60
27/03/97	6.24	8.30	8.30	8.50	8.00	7.50
30/03/97	6.30	8.50	8.30	8.20	8.00	7.40
02/04/97	6.09	8.30	8.30	8.20	8.00	7.50
07/04/97	6.00	8.10	8.00	7.90	7.80	7.40
11/04/97	5.80	7.90	7.90	7.70	7.70	7.50
15/04/97	5.84	7.60	7.90	7.70	7.70	7.50

Table 6.2 pH values of one-phase samples versus sampling date

UV/VIS Analysis

In none of the samples was the characterisatic polypyrrole maximum visible (Figure 6.9 and Figure 6.10). It appeared that any characteristic maximum was obscured due to the broad absorbance of iron.

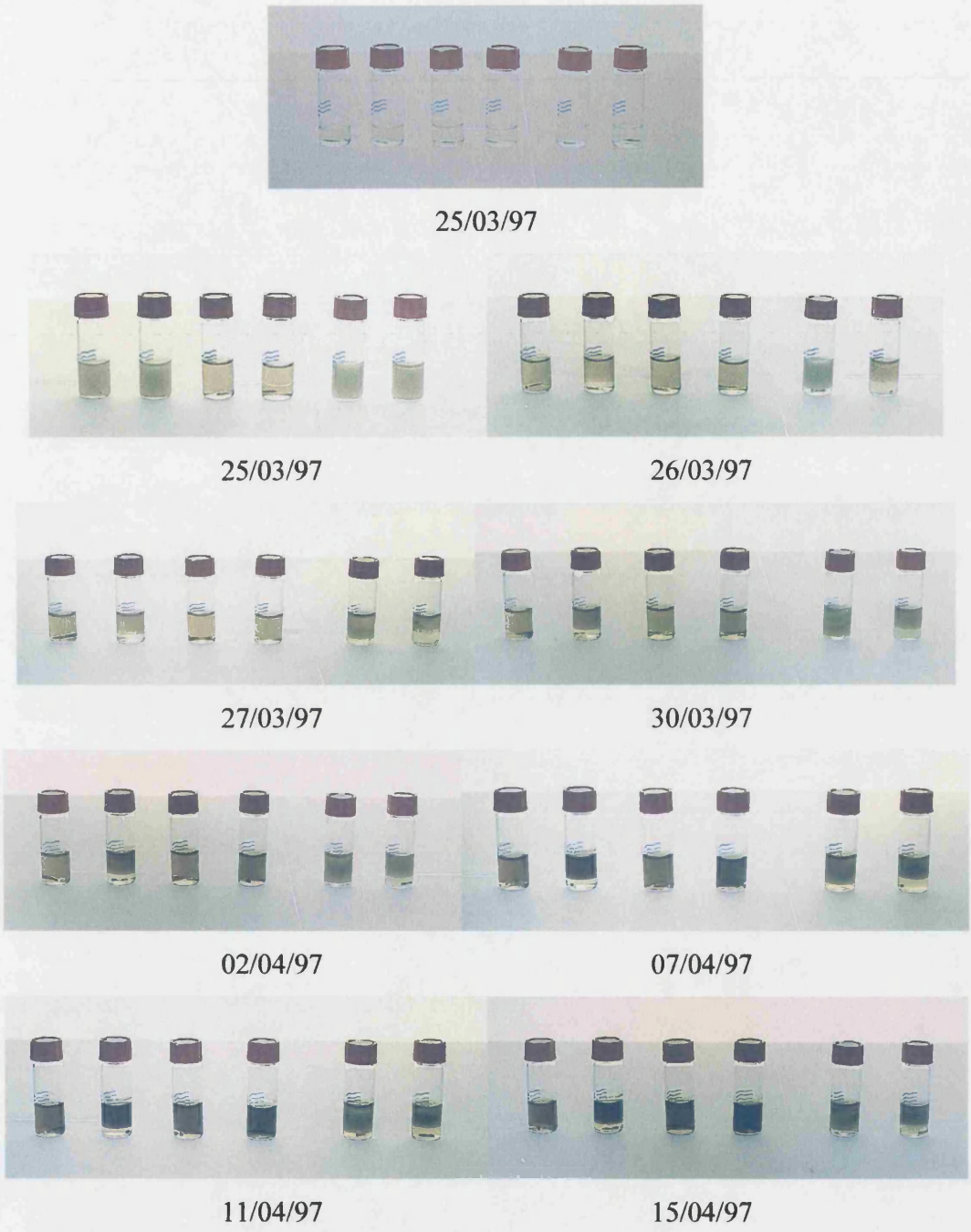

Figure 6.8 1-Phase samples over time (top image without pyrrole). L-R: Derivatised Reconstituted Ferritin, Reconstituted Ferritin, Ferrihydrite Control, Iron(III)Chloride Control, Derivitised Apoferritin, Apoferritin. 1 ml pyrrole mixed into solution on 25/03/97.

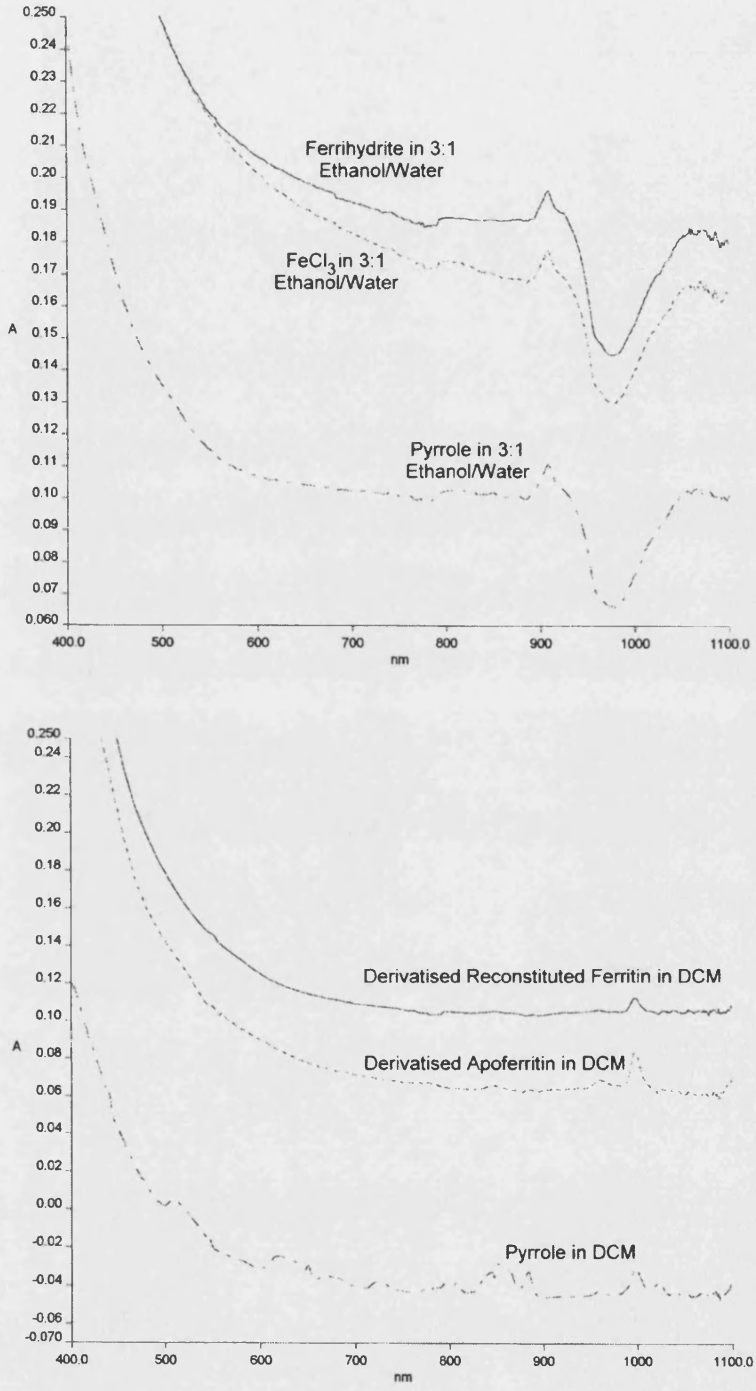

Figure 6.9 1-Phase UV/VIS as controls for solvents. Iron control samples in 3:1 Ethanol/Water compared against pyrrole in Ethanol/Water (Top). Ferritin samples in DCM compared against pyrrole in DCM (Bottom).

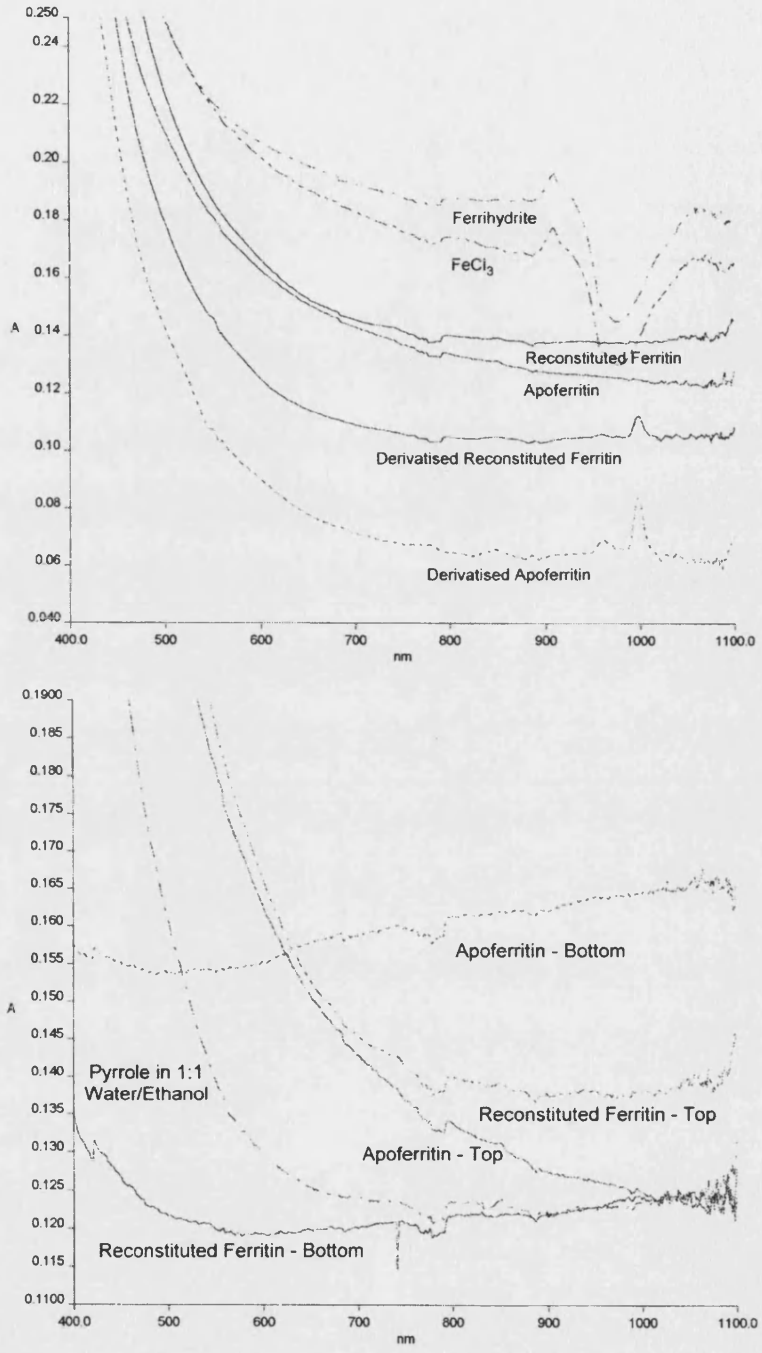

Figure 6.10 1-Phase UV/VIS spectra for samples and controls (Top). Spectra of two different phases which formed over the duration of the reaction, indicating pyrrole remained in the top fraction (Bottom).

Microscopy Analysis

A long-term reaction under harsh conditions might have affected the protein, leading to aggregation or dissolution. To test the integrity of the proteins, atomic force microscopy was performed on both a native ferritin control and the respective apo- and reconstituted ferritin complexes. Samples were deposited onto freshly cleaved mica squares and allowed to sit for one minute. The mica squares were then rinsed with distilled water and dried under nitrogen.

Initial imaging confirmed the presence of intact proteins from single-phase reconstituted ferritin samples (Figure 6.11). Similar images were seen for the remaining ferritin-derived samples, but an unexpected feature was revealed. The imaged material appeared as 60-80 nm diameter bundles which would extend in linear assemblies at micron length scales. More refined examination of these features revealed pentameric assemblies of 12-16 nm diameter subunits comprising the larger bundles (Figure 6.12). These subunits are consistent with ferritin molecules. That this structure was seen for both native ferritin and the polypyrrole/ferritin complexes indicates that the protein remained intact during the reactions.

The unusual samples were also imaged with the attached secondary electron imaging device (ASID) of the JEOL 1200 TEM (Figure 6.13). In this image, there are similar 60-80 nm spherical structures. However, the resolution is not high enough to resolve any finer structure.

Finally transmission electron microscopy of diluted single-phase reconstituted ferritin samples showed many morphologies of semi-electron dense material. Most frequently, assemblies of ~40 nm spheres chained together like sausages (Figure 6.14). While these may have been induced by the presence of ferritin, no indicative iron cores or 12 nm features were visible.

Two regions of one grid containing the same sample showed large electron-dense flakes of material stretching for microns (Figure 6.15). Within these flakes, a repeated, faint circular texture may indicate the presence of the ferritin protein without its iron core.

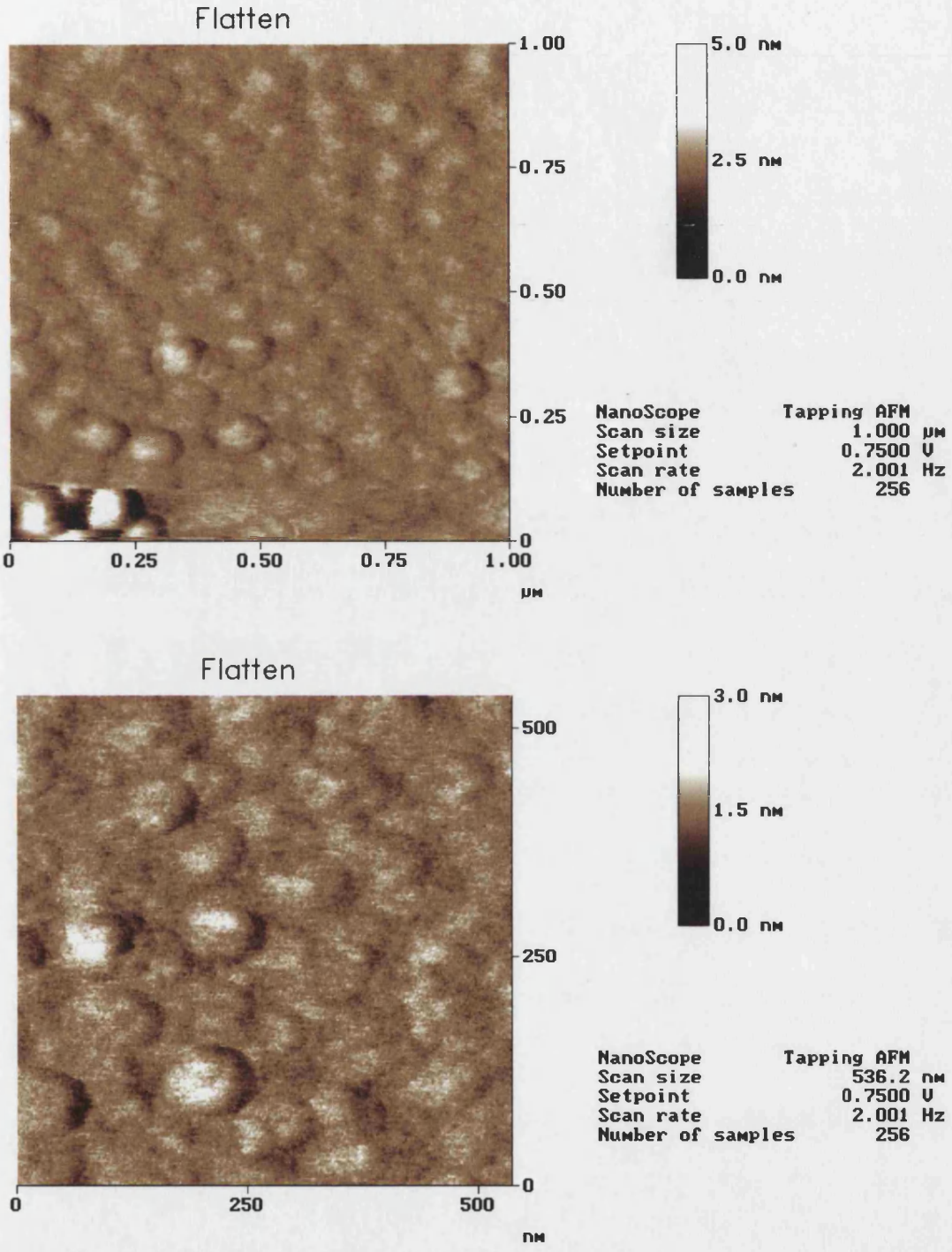

Figure 6.11 Tapping mode AFM of 1-phase reconstituted ferritin/polypyrrole complex on mica. Spherules have a diameter of ~35nm. 1 μm^2 (above) and 500 nm^2 (below) images indicate structure within larger spherules.

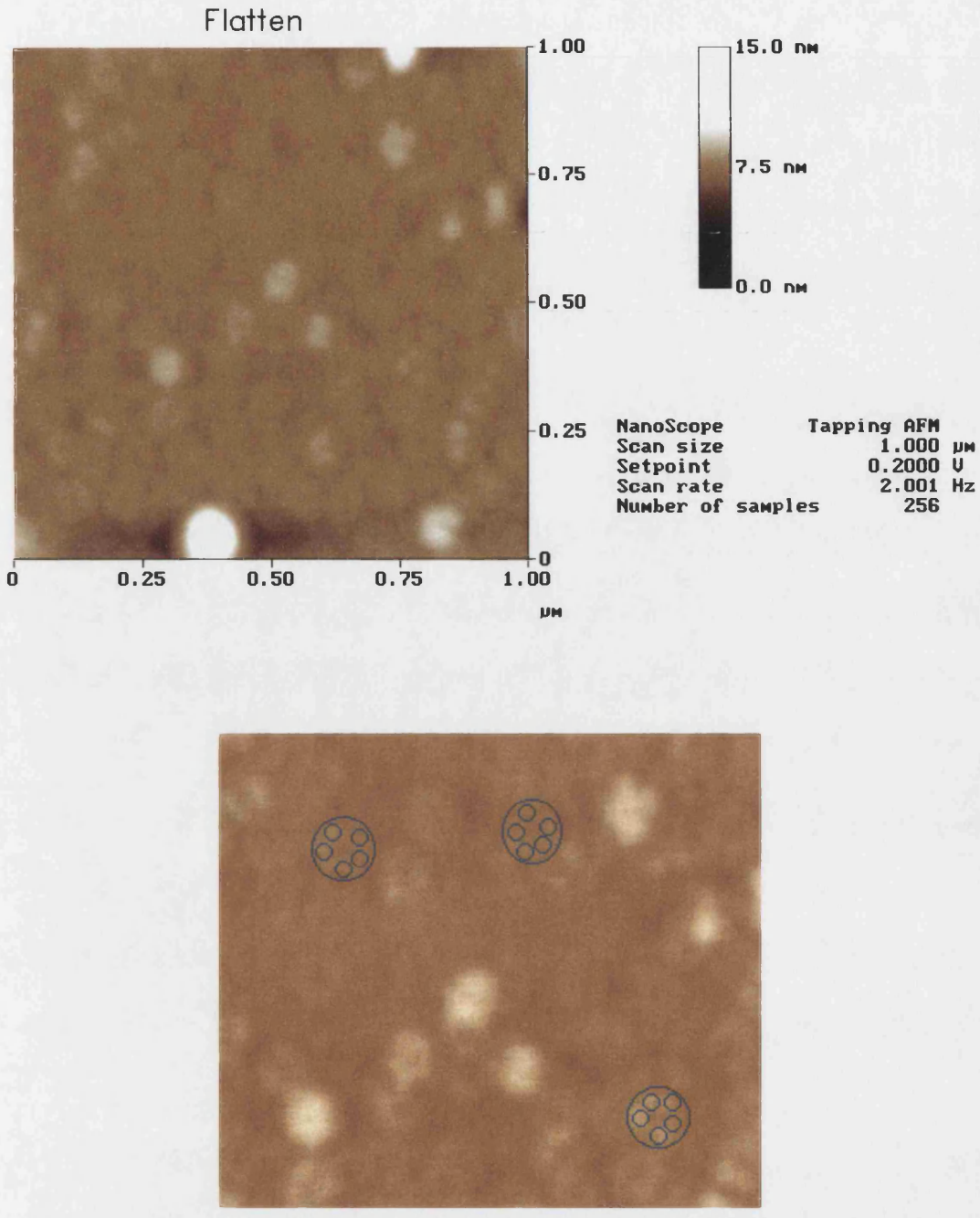

Figure 6.12 Tapping mode AFM of 1-phase reconstituted ferritin/polypyrrole complex on mica. Using less tapping force, an internal structure is revealed (above). 12 nm features can be seen in the larger spherules as indicated by the cartoon overlay (below).

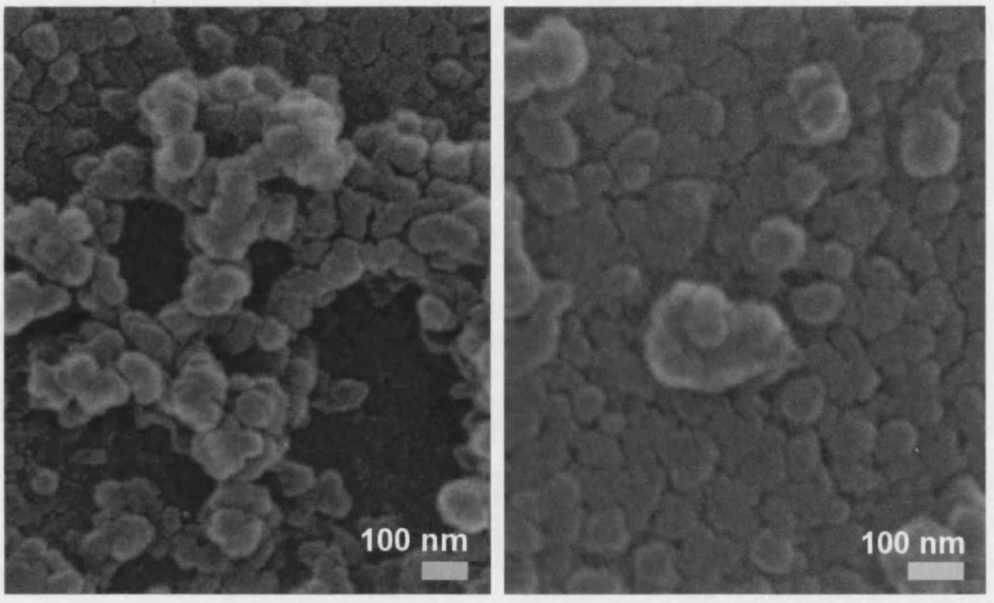

Figure 6.13 High resolution SEM micrographs of large-scale bundles. Average diameter of bundle is ~70 nm.

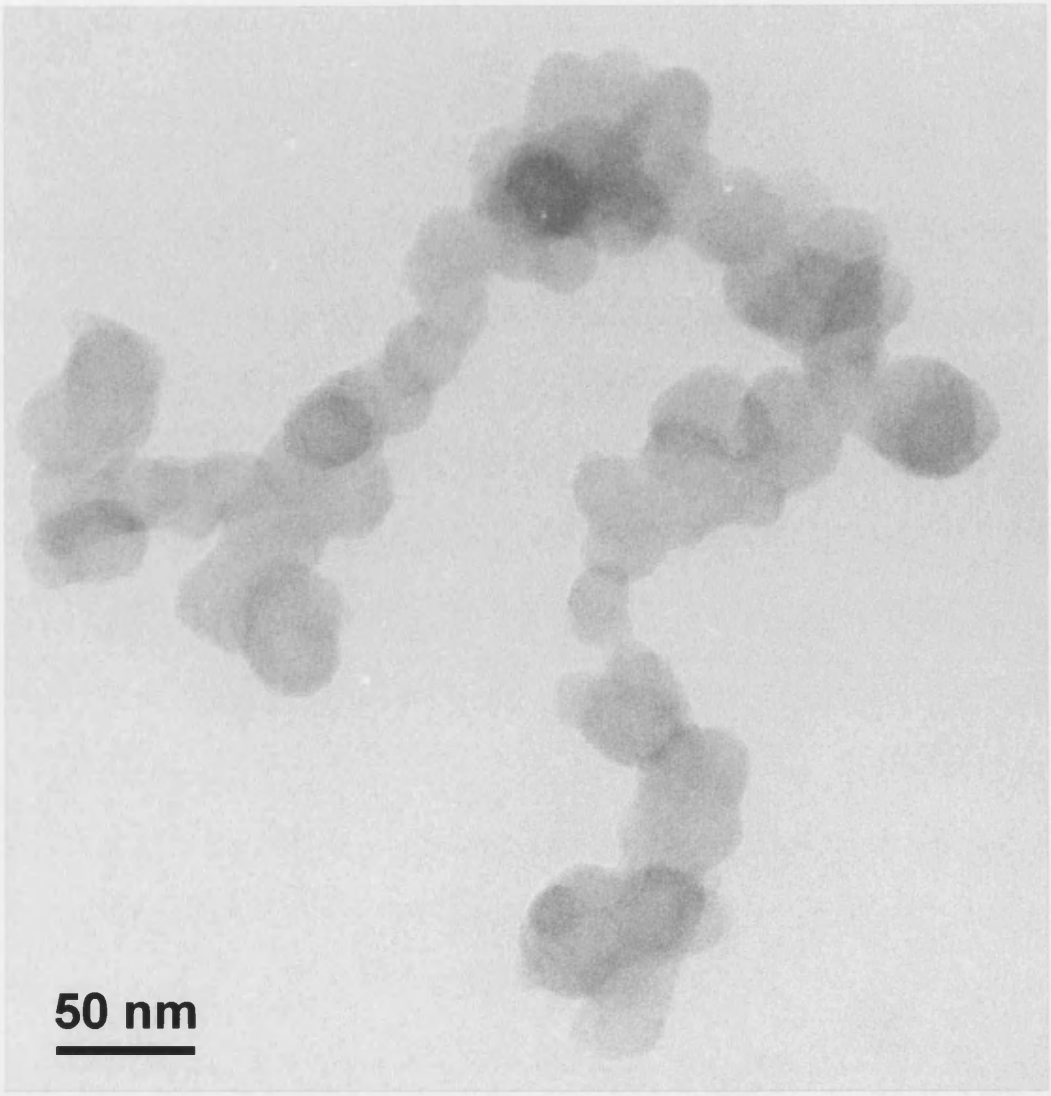

Figure 6.14 TEM of possible polypyrrole complex.

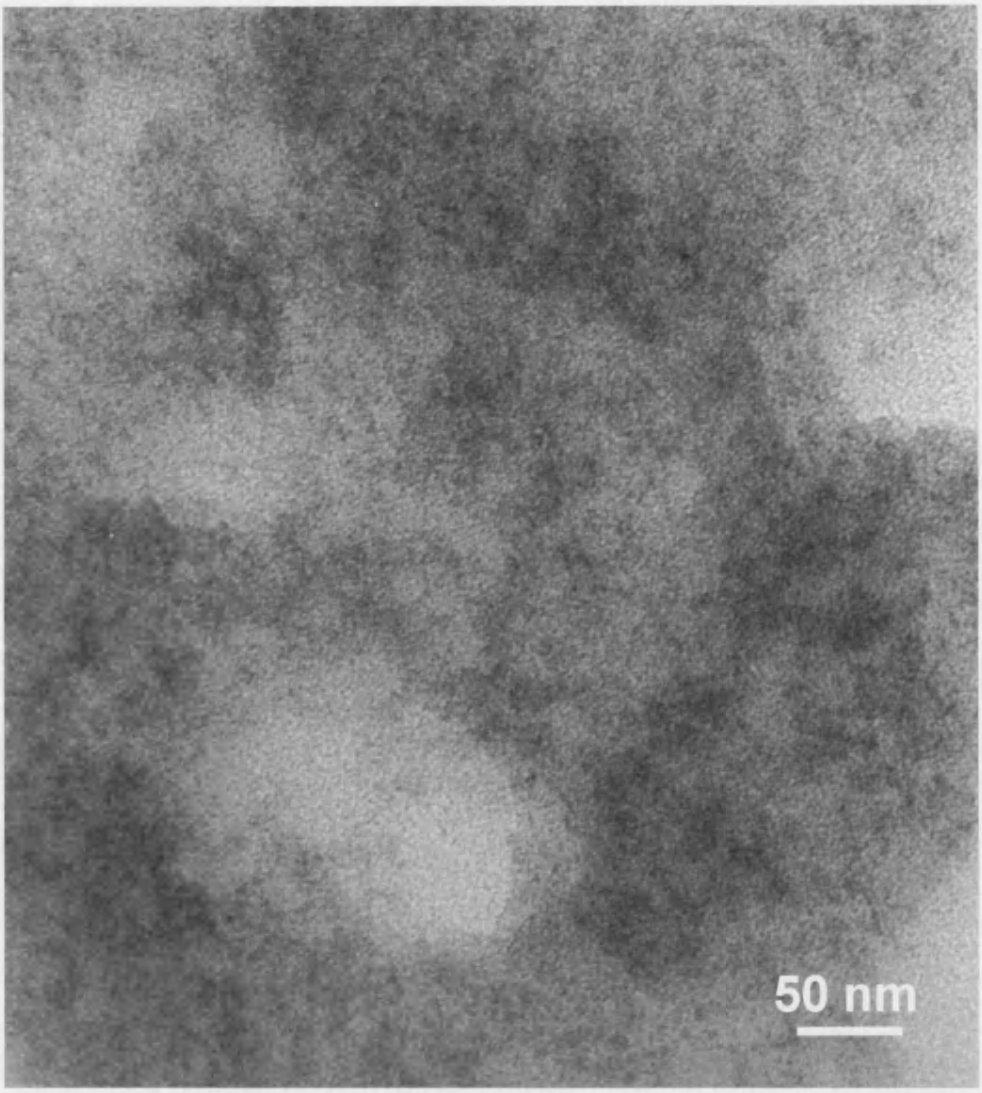

Figure 6.15 TEM of polypyrrole/ferritin complex, with circular texture approximately 12 nm in diameter.

Page left intentionally blank

6.4 DISCUSSION

Polypyrrole Composite

The association of ferritin and polypyrrole was difficult to prove. UV/VIS spectrometry was not sensitive enough to differentiate between the iron core of the protein and the production of polypyrrole. The surface-imaging microscopies of both SEM and AFM did not reveal any structure beyond the pentameric assemblies, which could be a side-effect of the polypyrrole, but are more likely a semi-stable morphology for ferritin (see below). It was evident from visible evaluation that polypyrrole was produced; however the association with ferritin could only be hinted at by the stable suspension of greenish-black colloidal material. Only using TEM, and then only in a small subset of the samples, was a combination of polypyrrole and ferritin evidenced.

Most likely, the iron from within the reconstituted ferritin was slowly reduced then oxidised in solution to form polypyrrole immediately outside the ferritin cavity. Over time, the iron core within ferritin was completely reduced to leave apoferritin surrounded in a polypyrrole mat. These mats then assembled separately or together to form the larger assemblies of electron-dense polypyrrole with apoferritin induced voids.

Ordered Ferritin Structures

The 60-80 nm diameter bundles have been observed previously. Biotinylated ferritin has been absorbed and linked onto streptavidin-coated substrates, and then imaged using AFM (Davies, *et al.*, 1994). AFM of the resulting structures showed similar larger-order assemblies 60-80 nm in diameter. Further, these assemblies would

assemble into long chains that would order over several microns, mirroring samples presented in this chapter (Figure 6.17). Another group imaged similar chains and structures, but were able to distinguish the ferritin subunits using scanning tunnelling microscopy (STM) (Yau, *et al.*, 1995). The group also observed "... ferritin pentamers arranged in rows", and noted that the pentamers appeared to aggregate in groups of three or more giving long-range structure. This STM work further mirrored the AFM images presented in this chapter.

Ferritin mostly produced hexagonally close-packed assemblies, but pentameric assemblies are not completely implausible. The 24 subunits of ferritin order themselves into a close approximation of a rhombic dodecahedron. Each diamond-like side has an obtuse angle of ~109.5°, which is quite similar to the 108° inner angle of a pentagon. Indeed rhombic dodecahedrons can be arranged into a pentagonal unit such that only a 1.5° gap exists between the adjacent sides (Figure 6.18). Quite possibly this structure is semi-stable for packing, and is induced during the drying process.

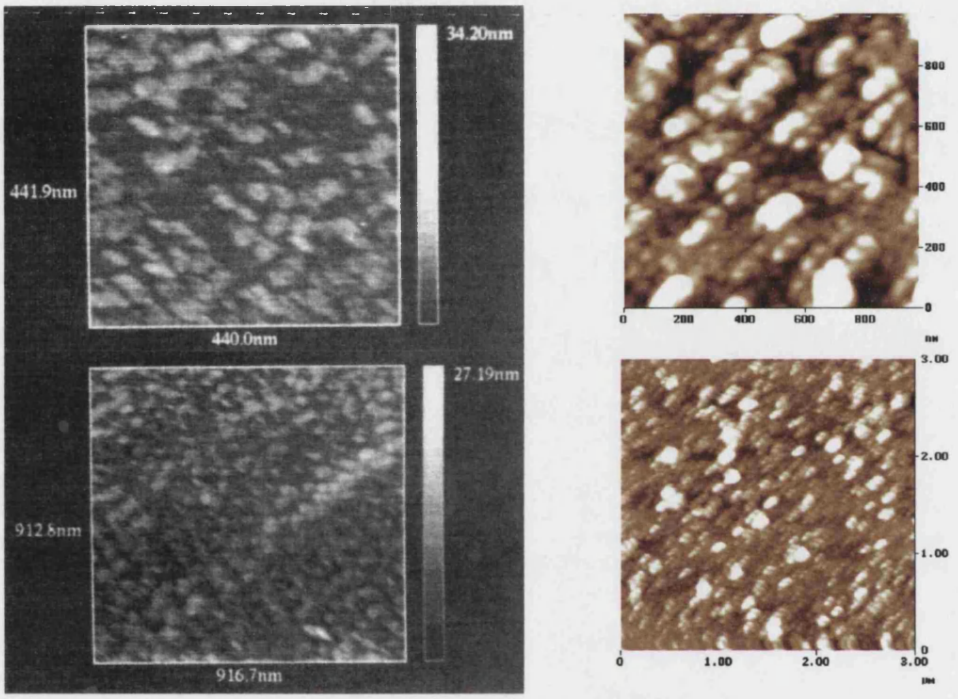

Figure 6.17 SPM images of densely packed ferritin assemblies at different scales. Images on the left are from a ferritin binding study (Davies, *et al.*, 1994), with similar images to the right produced from ferritin deposited onto mica. Spherical features 60-80 nm in diameter form linear arrangements over microns.

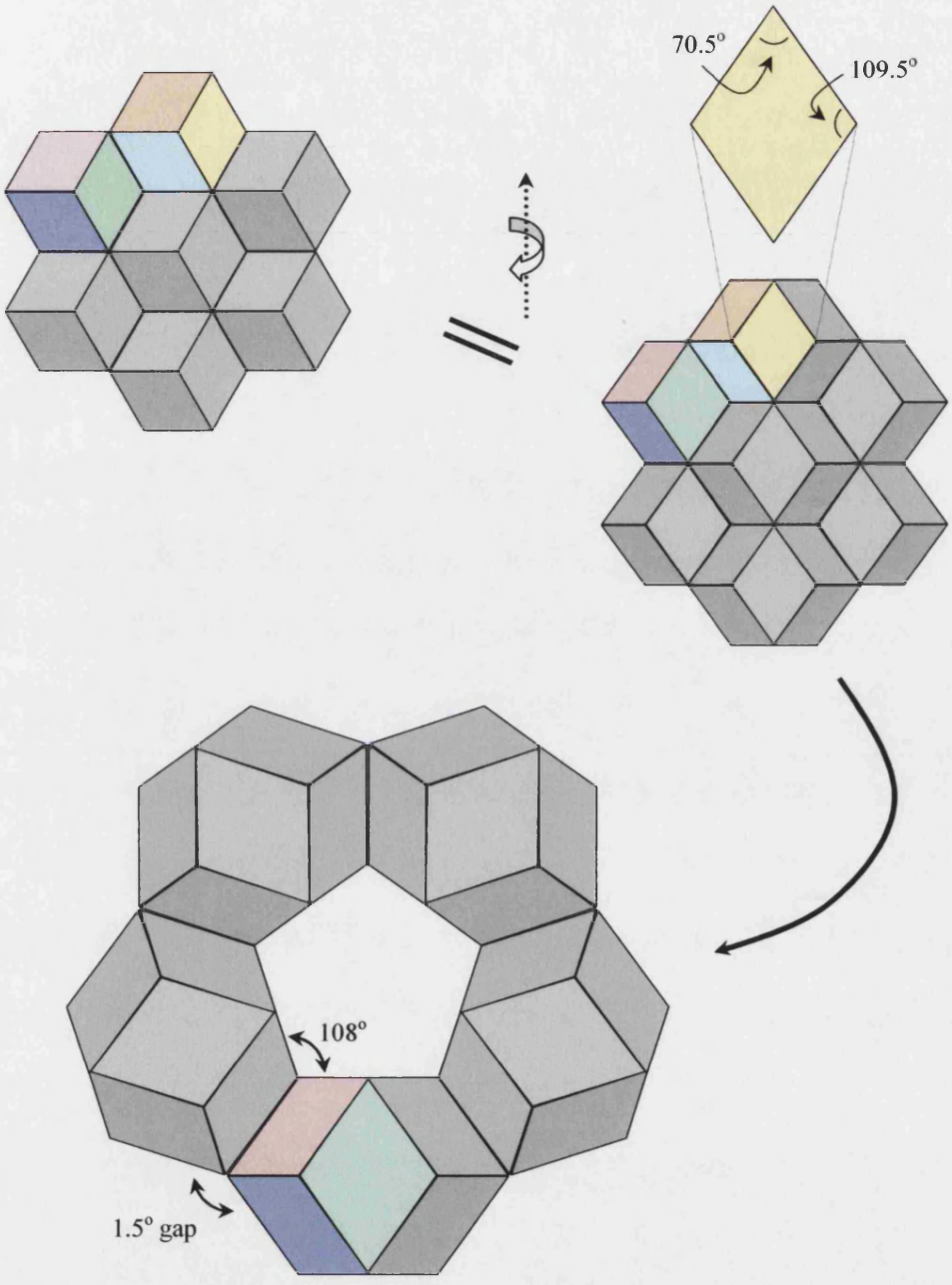

Figure 6.18 Possible scheme for the pentagonal arrangement of ferritin proteins, represented by rhombic dodecahedrons.

6.5 REFERENCES

Armes, S. P., "Conducting Polymer Colloids", *Curr. Opin. Coll. & Inter. Sci.*, **1**(2), 214-218 (1996).

Bernstein, F. C., T. F. Koetzle, G. J. Williams, E. E. Meyer Jr., M. D. Brice, J. R. Rogers, O. Kennard, T. Shimanouchi, and M. Tasumi, "The Protein Data Bank: a computer-based archival file for macromolecular structures", *J. Mol. Biol.*, **112**, 535-542 (1977).

Davies, J., C. J. Roberts, A. C. Dawkes, J. Sefton, J. C. Edwards, T. O. Glasbey, A. G. Haymes, M. C. Davies, D. E. Jackson, M. Lomas, K. M. Shakesheff, S. J. B. Tendler, M. J. Wilkins, and P. M. Williams, "Use of Scanning Probe Microscopy and Surface Plasmon Resonance as Analytical Tools in the Study of Antibody-Coated Microtiter Wells", *Langmuir*, **10**, 2654-2661 (1994).

Douglas T., D.P.E. Dickson, S. Betteridge, J. Charnock, C. D. Garner, and S. Mann, "Synthesis and Structure of an Iron(III) Sulfide-Ferritin Bioinorganic Nanocomposite", *Science*, **269**, 54-57 (1995).

Fowler, C. E., D. Khushalani, B. Lebeau, and S. Mann, "Nanoscale Materials with Mesostructured Interiors", *Adv. Mater.*, **13**(9), 649-652 (2001).

Goren, M., Z. Qi, and R. B. Lennox, "Selective Templated Growth of Polypyrrole Strands on Lipid Tubule Edges", *Chem. Mater.*, **12**, 1222-1228 (2000).

Harrison, P. M., P. J. Artymiuk, G. C. Ford, D. M. Lawson, J. M. A. Smith, A. Treffry, and J. L. White, "Ferritin: Function and Structural Design of an Iron-storage Protein", *Biomineralization: Chemical and Biochemical Perspectives*, ed. S. Mann, J. Webb, and R. J. P. Williams (VHC, Germany), 257-294 (1989).

Hempstead, P. D., S. J. Yewdall, A. R. Fernie, D. M. Lawson, P. J. Artymiuk, D. W. Rice, G. C. Ford, and P. M. Harrison, "Comparison of the three-dimensional structures of recombinant human H and horse L ferritins at high resolution", **PDB ID: 1AEW**, *J. Mol. Biol.*, **268**, 424-448 (1997).

Kerton, F. M., G. A. Lawless, and S. P. Armes, "First example of a conducting polymer synthesised in supercritical fluids", *J. Mater. Chem.*, **7**(10), 1965-1966 (1997).

Koradi, R., M. Billeter, and K. Wüthrich, "MOLMOL: a program for display and analysis of macromolecular structures", *J. Mol. Graphics*, **14**, 51-55 (1996).

Lascelles, S. F., and S. P. Armes, "Synthesis and Characterization of Micrometer-Sized Polypyrrole-Coated Polystyrene Latexes", *Adv. Mater.*, **7**(10), 864-866 (1995).

Meldrum, F. C., V. J. Wade, D. L. Nimmo, B. R. Heywood, and S. Mann, "Synthesis of Inorganic Nanophase Materials in Supramolecular Protein Cages", *Nature*, **349**, 684-687 (1991).

Meldrum, F. C., B. R. Heywood, and S. Mann, "Magnetoferritin: In Vitro Synthesis of a Novel Magnetic Protein", *Science*, **257**, 522-523 (1992).

Meldrum, F. C., T. Douglas, S. Levi, P. Arosio, and S. Mann, "Reconstitution of manganese oxide cores in horse spleen and recombinant ferritins," *J. Inorg. Biochem.*, **58**, 59-68 (1995).

Planche, M. F., J. C. Thiéblemont, N. Mazars, and G. Bidan, "Kinetic Study of Pyrrole Polymerization with Iron(III) Chloride in Water", *J. App. Poly. Sci.*, **52**, 1867-1877 (1994).

Selvan, S. T., J. P. Spatz, H. A. Klok, and M. Möller, "Gold-Polypyrrole Core-Shell Particles in Diblock Copolymer Micelles", *Adv. Mater.*, **10**(2), 132-134 (1998).

Simmons, M. R., P. A. Chaloner, and S. P. Armes, "Synthesis of Colloidal Polypyrrole Particles Using Reactive Polymeric Stabilizers", *Langmuir*, **11**, 4222-4224 (1995).

Suenaga, K. C. Colliex, N. Demoncy, A. Loiseau, H. Pascard, and F. Willaime, "Synthesis of Nanoparticles and Nanotubes with Well-Separated Layers of Boron Nitride and Carbon", *Science*, **278**, 653-655 (1997).

Warne, B., O. I. Kasyutich, E. L. Mayes, J. A. L. Wiggins, and K. K. W. Wong, "Self Assembled Nanoparticulate Co:Pt for Data Storage Applications", *IEEE Trans. Mag.*, **36**, 3009-3011 (2000).

Wong, K. K. W., and S. Mann, "Biomimetic synthesis of cadmium sulfide-ferritin nanocomposites," *Adv. Mat*, **8**, 928-933 (1996).

Wong, K. K. W., N. T. Whilton, H. Cölfen, T. Douglas, and S. Mann, "Hydrophobic Proteins: Synthesis and Characterisation of Organic-Soluble Alkylated Ferritins", *Chem. Comm.*, 1621-1622 (1998).

Wong, K. K. W., N. T. Whilton, H. Cölfen, T. Douglas, and S. Mann, "Synthesis and Characterisation of Hydrophobic Ferritin Proteins", *J. Inorg. Biochem.*, **76**, 187-195 (1999).

Yau, S. T., and Y. Zhou, "Scanning Tunneling Microscopy of Ferritin Nanostructures", *Mod. Phys. Lett. B*, **9**(3&4), 187-193 (1995).

Summary and Future Work

SILK COMPOSITES

The work presented in Chapter 3 demonstrated that a high-strength biopolymer could be enhanced using a variety of functional nanoparticles. Composites with the high strength of dragline silk and electromagnetic functionality could find applications in areas as diverse as damage-sensitive 'smart' fabrics and microwave attenuation. Not only did the work produce a novel set of composite materials, but it also added to the evidence for an internal, fibril structure in spider dragline silk.

Further developments of this work should include the incorporation of a range of smaller nanoparticles with a variety of surface charges in the "artificial silk" system. The artificially-drawn composite silks showed promise, but require a much more thorough investigation of starting silk solutions and colloidal material. Such an experiment might also reveal more about the internal structure of silk, with smaller colloids acting as a negative stain for TEM.

MAGNETIC BIONITES

The work presented in Chapter 4 highlighted that mechanical stress was likely being introduced during the formation of bionites. The bulk magnetic properties of the magnetite nanoparticles showed an anisotropy in magnetisation orientation as well as a possible increase in magnetic anisotropy energy.

This work could be extended by using magnetic nanoparticles with a narrower size distribution and more uniform magnetocrystalline anisotropy. Using these as magnetic standards, any increase in magnetic anisotropy energy could be compared with theoretical predictions for compressive forces at the solution-air interface

during bionite formation. Such a system might prove useful for studying stress-induced anisotropy in magnetic nanoparticles.

CEMENT MICROSTRUCTURES

The work presented in Chapter 5 demonstrated that composite materials with well-defined microstructures and functionality beyond that currently available to MEMS could be formed. Two important abilities were introduced to MEMS materials. The first was the ability to change the porosity of a feature, and the second was the ability to disperse functional nanoparticles uniformly throughout a feature. Based on this work, devices are feasible which concurrently exhibit control at the nanometer, sub-micron and 10-100 micron length scales.

Further developments of this work should include device testing to verify that nanoparticle functionality is retained and transferred. For instance, a magnetite composite should be mobile in a magnetic field and a gold composite should demonstrate an enhanced electrical conductivity. Also, methods of removing moulds without high temperatures should be explored to retain the functionality of any dispersed biological materials.

PROTEIN/POLYPYRROLE COMPOSITES

The work presented in Chapter 6 indicated that iron(III) from the iron oxide core of ferritin can act as a catalyst for the polymerisation of pyrrole. However, it was undetermined whether polypyrrole became the intended nanopolymer contained within the protein cage.

Outside of using other spectroscopies (such as FTIR and Raman, or electrospray mass spec.) to determine the relationship between polypyrrole and ferritin, other synthetic strategies should be tried. A thorough investigation of whether pyrrole subunits can enter the apoferritin macromolecule should be performed. If the subunits can indeed enter the empty protein, a reverse strategy of adding iron(III) ions to solution containing pyrrole/ferritin complexes may produce the intended results.

APPENDICES

APPENDIX 1 MAGNETITE NANOPARTICLE PREPARATION

Magnetite Colloid Preparation

A colloidal magnetite (Fe_3O_4) sol was prepared in alkaline media according to a previously reported procedure (Massart, 1981). Dropwise additions totalling 50 ml of 1 M tetramethylammonium hydroxide ($Me_4NOH{\cdot}5H_2O$) were added to a stirred mixture of 2.1 M iron(III) chloride hexahydrate (2.3 g $FeCl_3{\cdot}6H_2O$ in 4 ml H_2O) and 6.0 M ammonium iron(II) sulfate (1.69g $Fe(NH_4)_2(SO_4)_2$ in 1 ml of 2 M HCl). The resulting black sol was stirred at room temperature for 1 hour, sonicated in a water bath for 1 hour, and finally centrifuged at 20,000 rpm for 2 hours. The supernatant was decanted and the pellet resuspended in water by sonication. The centrifugation and washing procedures were repeated and the resuspended sol was filtered through a 13 mm diameter, 0.2 μm nitrocellulose membrane. The final colloidal solution had a pH of 9.3. The negatively charged magnetite nanocolloid was used as a suspension either in water or in a 1:1 methanol/water mixture.

Particle Size Determination

The resulting solution responded quickly in the presence of a magnetic field, indicating the saturation of the iron(II) atoms in the crystalline lattice. Transmission electron microscopy revealed a moderate distribution of approximately spherical particles (Figure A1.1), which were recorded from a set of regions across the microscope grid. The particle size distribution was plotted (Figure A1.2) showing an average particle diameter of 8.9 ± 2.3 nm.

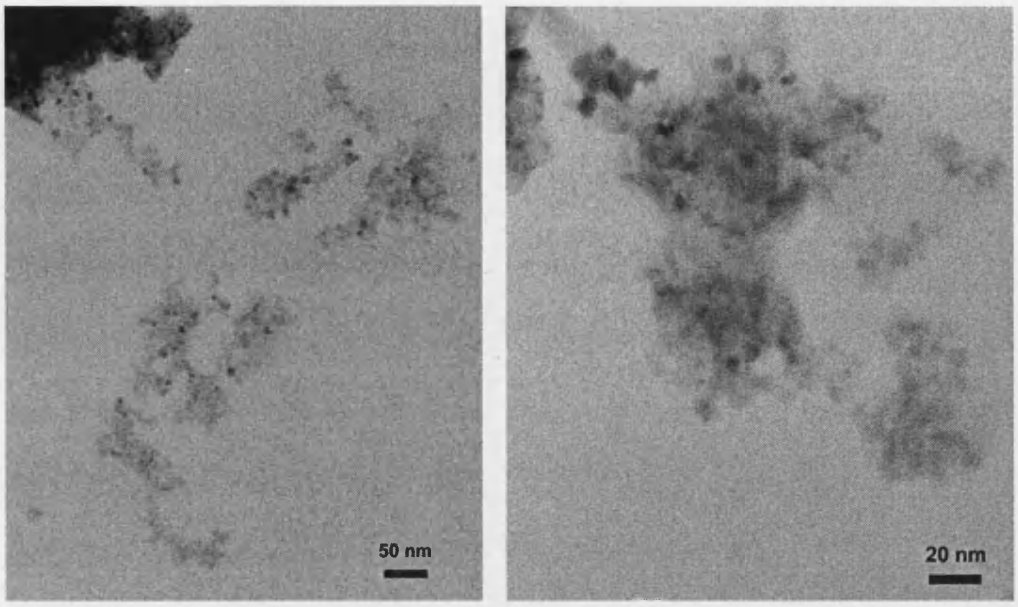

Figure A1.1 TEM micrographs of colloidal magnetite sample.

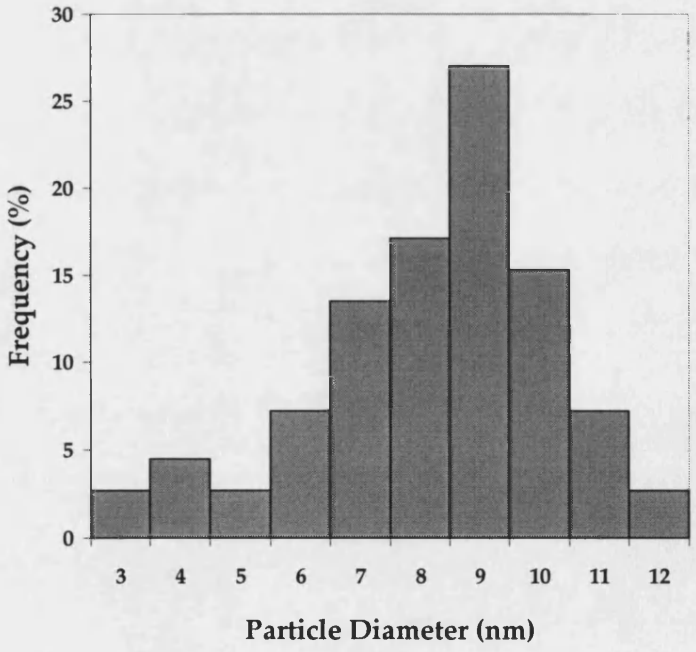

Figure A1.2 Histogram of magnetite colloid size distribution.

REFERENCES

Massart, R., "Preparation of Aqueous Magnetic Liquids in Alkaline and Acidic Media", *IEEE Trans. Mag.*, **17**(2), 1247-1248 (1981).

APPENDIX 2 GOLD NANOPARTICLE PREPARATION

Gold Colloid Preparation

A colloidal, thiol-functionalised gold sol was prepared according to a previously reported procedure (Brust, *et al.*, 1995). Hydrogen tetrachloroaurate trihydrate (0.30 g $HAuCl_4 \cdot 3H_2O$) was dissolved in 150 ml methanol in a 250 ml round-bottom flask, yielding a yellowish solution. *p*-Mercaptophenol (3.3 g) was added to the solution followed by 3 ml of acetic acid. The acetic acid addition is to prevent the deprotonation of *p*-Mercaptophenol. 30 ml of freshly prepared 0.4 M aqueous sodium borohydride ($NaBH_4$) were added carefully in 1 ml portions with vigorous stirring. Upon each addition, the solution immediately turned brown indicating the formation of the gold colloid. After the complete addition of the reducing agent, the solution was stirred for an additional 1 hour. The solvent was then removed under reduced pressure using a rotary evaporator with water aspirator vacuum, keeping the temperature at 40 °C. The remaining dark-brown residue was thoroughly washed with diethyl ether, though most of the solid remained stuck to the flask upon multiple washings. The residue was washed with water and vacuum filtered, then dissolved in isopropanol for the final wash. The isopropanol was removed under reduced pressure to yield approximately 0.2 g of product, which was finally resuspended in 50 ml isopropanol (4 mg/ml).

Samples were prepared for TEM by evaporation of a droplet onto an amorphous carbon film supported by a copper mesh grid. The corresponding electron diffraction pattern confirmed polycrystalline face centred cubic (fcc) gold as indicated by the respective [111], [200], [220], [311], [222], and [400] planes (Figure A2.1).

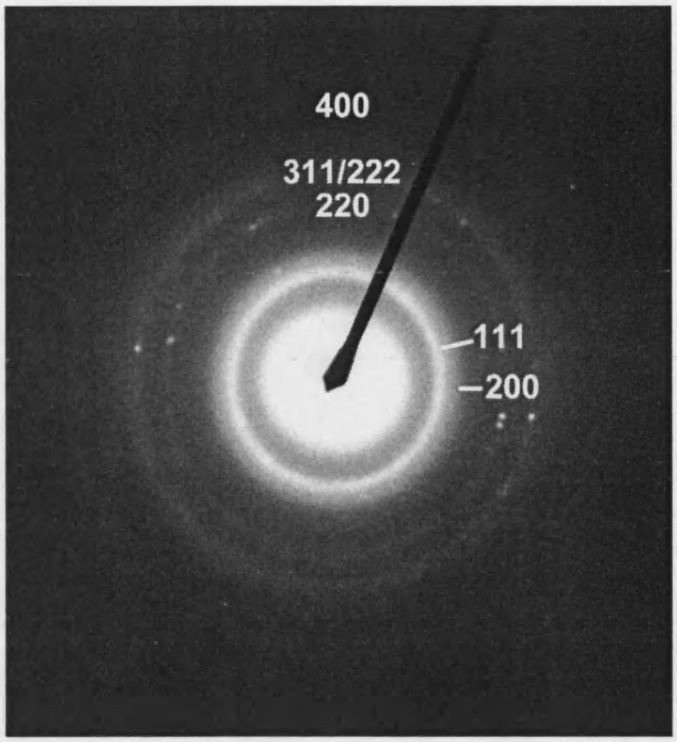

Figure A2.1 Electron diffraction pattern from gold colloid.

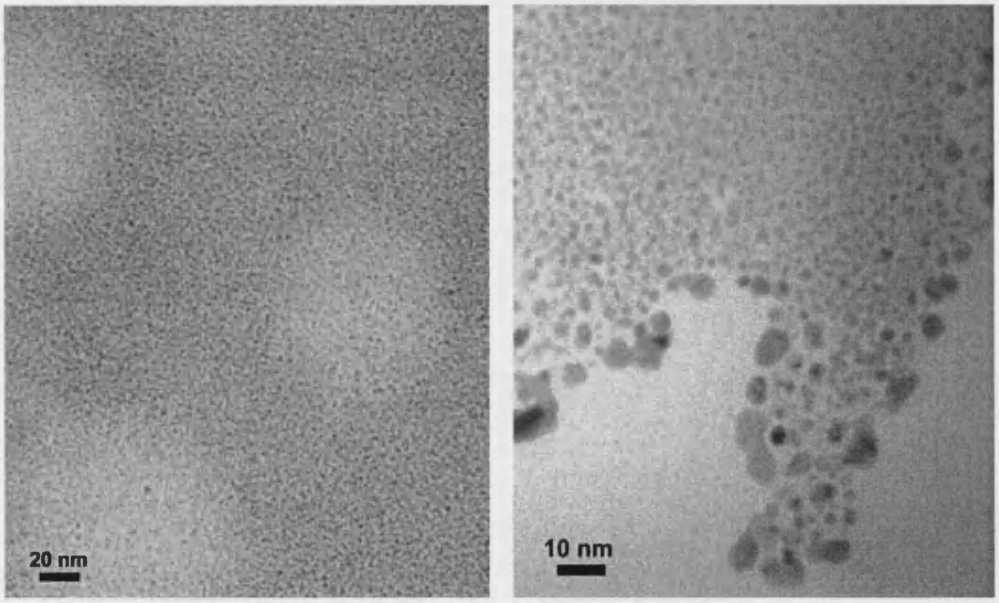

Figure A2.2 TEM micrographs of colloidal gold sample.

Particle Size Determination

Transmissions electron microscopy revealed a moderate distribution of spherical particles (Figure A2.2), which were recorded from a set of regions across the microscope grid. The particle size distribution was plotted (Figure A2.3) showing an average particle diameter of 2.9 ± 1.8 nm.

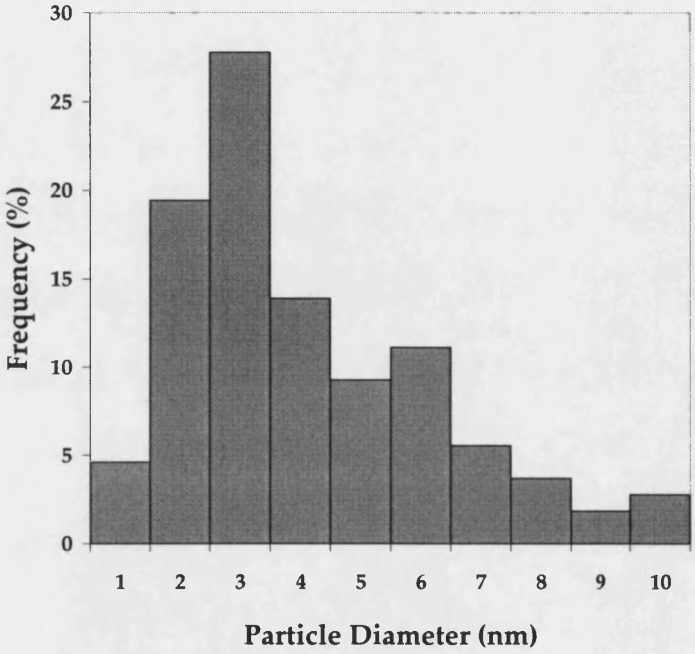

Figure A2.3 Histogram of gold colloid size distribution.

REFERENCES

Brust, M., J. Fink, D. Bethell, D. J. Schiffrin, and C. Kiely, "Synthesis and Reactions of Functionalised Gold Nanoparticles", *J. Chem. Soc. Chem. Comm.*, **90**, 1655-1656 (1995).

APPENDIX 3 CADMIUM SULFIDE NANOPARTICLE PREPARATION

Cadmium Sulfide Colloid Preparation

A colloidal cadmium sulfide (CdS) sol was prepared in reverse micelles according to a previously reported procedure (Chandler, *et al.*, 1984). Reverse micelles were prepared by dissolving 1.67 g of AOT surfactant in 65 ml of heptane, followed by drop wise addition of 338 µl of water while stirring vigorously in a round-bottom flask. The homogeneous mixture was purged with nitrogen and 5 µl of 1M cadmium nitrate pentahydrate ($Cd(NO_3)_2 \cdot 4H_2O$) was then added via a microliter syringe to 10 ml of the stirred reverse micelle solution. 5 µl of 1 M sodium sulfide (Na_2S) was slowly added and the solution was stirred for 20 minutes until stabilised following the schematic of Figure A3.1.

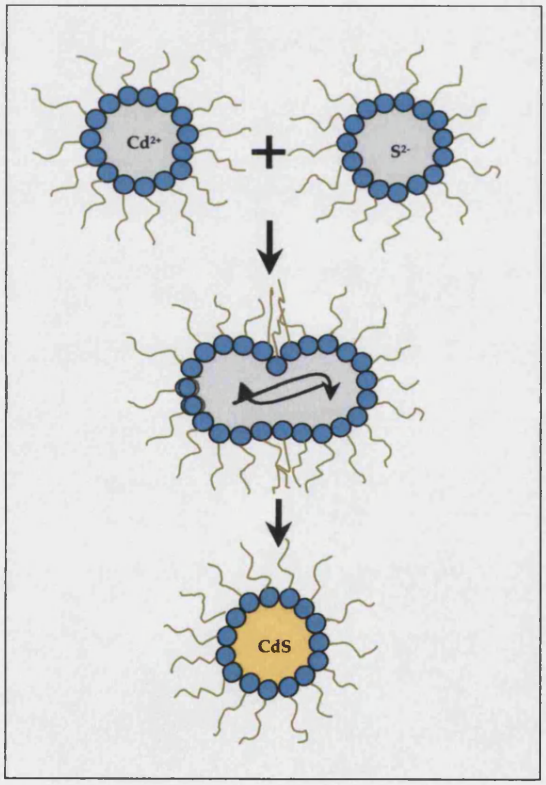

Figure A3.1 Schematic representation of formation of CdS nanoparticles within reverse micelles.

Particle Size Determination

The UV-Vis spectra of the solution was recorded on a Perkin-Elmer Lambda 6 spectrophotometer between 300 and 600 nm. The absorption edge was approximated by determining the intersection of a straight line extrapolated from the baseline and a line drawn from the ascending slope at the onset of absorption (Figure A3.2). The absorption edge was determined to be 428 nm, corresponding to a mean particle diameter of 4.4 nm.

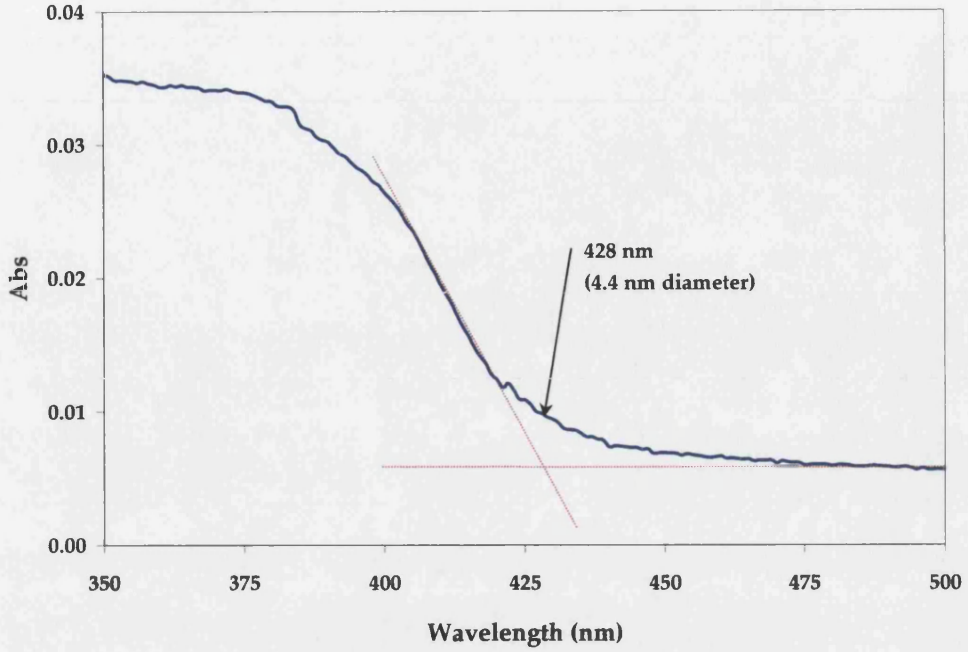

Figure A3.2 UV/Vis Spectra of CdS solution, displaying characteristic 'hump' near 400 nm. Absorption edge determined to be 428 nm, indicating average particle diameter of 4.4 nm.

REFERENCES

Chandler, R., S. Bigham, and J. Coffer, "Spectroscopic Analysis of Semiconductor Colloids", *J. Chem. Edu.*, **70**(1), A7-A10 (1993).

ADVANCED MATERIALS

In conclusion, this work reports the first high resolution ^{13}C NMR study of the organic superconductor κ-$(ET)_2$-$Cu[N(CS)_2]Br$ via MAS and cross-polarization techniques with ^{13}C-enriched ET molecules. The Knight shift tensor of the central carbon atoms has been derived. A lowering of the symmetry below 273 K has been deduced from the splitting of the ^{13}C MAS NMR lines of the central carbons. A distortion of the organic lattice occurs below about 200 K when the motion of the ethylene groups is frozen. The incommensurate character of the distortion is implied by the inhomogeneous broadening of the NMR lines. This feature rules out the commensurate nature claimed from earlier diffuse X-ray scattering experiments.

Received: September 11, 1997
Final version: March 6, 1998

[1] T. Ishiguro, K. Yamaji, *Organic Superconductors*, Springer, Berlin **1990**.
[2] J. Williams, *Science* **1991**, *252*, 1501.
[3] A. M. Kini, U. Geiser, H. H. Wang, K. D. Carlson, J. M. Williams, W. K. Kwok, K. G. Vandevoort, J. E. Thompson, D. L. Stupka, D. Jung, M. H. Whangbo, *Inorg. Chem.* **1990**, *29*, 2555.
[4] D. Jérome, *Science* **1991**, *252*, 1509.
[5] U. Geiser, A. Kini, H. Wang, M. Beno, J. Williams, *Acta Crystallogr. C* **1991**, *47*, 190.
[6] U. Geiser, A. M. Kini, H. H. Wang, M. A. Beno, J. M. Wiliams, *Physica C* **1991**, *174*, 475.
[7] Y. Nogami, J. Pouget, H. Ito, T. Ishiguro, G. Saito, *Solid State Commun.* **1994**, *89*, 113.
[8] H.Mayaffre, *Ph.D. Thesis*, Université Paris XI, **1996**.
[9] P. Wzietek, H. Mayaffre, D. Jérome, S. Brazovskii, *J. Phys. I (Paris)* **1996**, *6*, 2011.
[10] H. Mayaffre, P. Wzietek, D. Jérome, C. Lenoir, P. Batail, *Europhys. Lett.* **1994**, *28*, 205.
[11] S. D. Soto, C. Slichter, H. Wang, U. Geiser, J. Williams, *Phys. Rev. Lett.* **1993**, *70*, 2956.
[12] J. Larsen, C. Lenoir, *Org. Synth.* **1993**, *256*.
[13] M. Mehring, *High Resolution NMR in Solids*, Springer, Berlin **1983**.
[14] J. Herzfeld, A. Berger, *J. Chem. Phys.* **1980**, *73*, 6021.
[15] T. Klutz, I. Hennig, U. Haeberlen, D. Schweitzer, *Appl. Magn. Res.* **1991**, *2*, 441.
[16] S. D. Soto, C. Slichter, A. Kini, H. Wang, U. Geiser, J. Williams, *Phys. Rev. B* **1995**, *52*, 10364.
[17] A. Kawamoto, K. Miyagawa, Y. Nakazawa, K. Kanoda, *Phys. Rev. Lett.* **1995**, *74*, 3455.
[18] A. Vainrub, private communication.
[19] F. Artzner, private communication.
[20] T. Emge, P. Leung, M. Beno, A. Schultz, H. Wang, L. Sowa, J. Williams, *Phys. Rev. B* **1984**, *30*, 6780.
[21] A. Vainrub, S. Vija, E. Lippma, V. Prigodin, R. Beha, M. Mehring, *Phys. Rev. Lett.* **1992**, *69*, 3116.
[22] A. Vainrub, I. Kheinmaa, E. Yagubskii, *JETP Lett.* **1987**, *44*, 317.

Fabrication of Magnetic Spider Silk and Other Silk-Fiber Composites Using Inorganic Nanoparticles**

By *Eric L. Mayes*, *Fritz Vollrath*, and *Stephen Mann**

Spider dragline silk is a semicrystalline biopolymer with a unique combination of high tensile strength, high elasticity, and high modulus. The 0.2 to 10 μm diameter silk fibers have a higher breaking energy than other natural or synthetic fibrous polymers, far exceeding that of high tensile steel and Kevlar on a weight-for-weight basis.[1] Thus, silk fibers could have important applications in impact-proof textiles or other structural fabrics where strong, flexible materials are desirable. Moreover, the inherent biocompatibility of silk could be exploited in the preparation of new strong biomaterials for use in artificial tendons or non-allergenic sutures.[2] A further possibility might be to modify the properties of silk fibers by integration with those of other materials to give functionalized hybrid composites with enhanced or entirely new applications. For example, cross-linking of dragline silk fibers with organic polymeric precursors produces an apparent improvement in the tensile strength.[3]

Although silk is a highly hydrophobic, insoluble biopolymer, it has recently been shown that dragline spider silk can undergo a reversible transformation to a supercontracted state when placed in water or polar organic solvents.[4] These observations suggest a possible general route to the functionalization of silk fibers by aqueous-based interactions with the modified supercontracted state. In this paper we describe a specific approach in which hybrid silk materials are prepared by binding inorganic nanoparticles to the surface and near-surface regions of silk fibers immersed into colloidal sols.

Our main focus has been on the fabrication of magnetic spider silk fibers. Bundles of ca. 200 individual silk fibers were prepared by cutting 3 cm lengths of dragline spider silk from a continuous spool produced by *Nephila edulis*. We used dragline silk originating from the Major Ampullate glands, and the threads were drawn mechanically from immobilized but fully awake spiders at a speed of 2 cm/s onto either 1 cm diameter glass tubes or photographic slide frames. These bundles were suspended by tweezers and

[*] Prof. S. Mann, E. L. Mayes
Department of Chemistry, University of Bath
Bath BA2 7AY (UK)
Prof. F. Vollrath
Department of Zoology
Universitetsparken B135, DK-8000 Aarhus (Denmark)

[**] We thank Dr. T. Kearney and Dr. D. Goddard of BNFL plc for support of a postgraduate studentship to ELM, Dr. S. L. Burkett for preparation of the hydrophobic gold colloid, H. B. Joergensen for the preparation of dragline silk fibers, and Dr. Z. Shao for setting up and calibrating the mechanical gauge.

  0935-9648/98/1007-0801 $ 17.50+.50/0

mechanically lowered into either a water or water/methanol sol of 10 to 20 nm diameter superparamagnetic magnetite (Fe_3O_4) particles for 2 min. Alternatively, single fibers, mounted across a twin-pronged variable caliper,[5] were mechanically submerged into the nanocolloidal suspensions. After submersion, the fibers were slowly withdrawn from the colloidal sol and allowed to dry in air at ambient temperatures. The resulting dark brown fibers were coated with a dense coherent film of the magnetite nanocrystallites (Figs. 1A and B). High magnification images (e.g., Fig. 1C) showed that the magnetite–silk composites displayed some surface roughness, indicating that the thickness of the mineral films was substantial. The mineralized fibers, however, retained their natural flexibility without significant disruption of the magnetite coating (Fig. 1D). Moreover, the combination of intrinsic mechanical and fabricated magnetic properties enabled dried fibers to be oriented in the presence of an external magnetic field because fibers suspended against gravity tracked the position of a strong magnet. This was observed by fixing the fibers with tweezers in the presence of a 1.5 cm diameter neodymium–iron–boron slug (Fig. 2).

Mineralized fibers were embedded in epoxy resin and thin-sectioned for scanning electron microscopy (SEM) and energy dispersive X-ray (EDX) analysis studies using a JEOL 6310 SEM operating at 20 kV. The intensity of the iron Kα peak was determined for four different cross-sections of each sample. EDX analysis of sectioned magnetite–silk fibers showed high intensities for the iron Kα absorption around and possibly within the surface regions of the composites (Fig. 3). Analysis of the iron Kα peak intensities of cross-sectioned fibers showed that similar iron adherence was achieved for composites prepared from water or water/methanol solvents. Samples that were extensively washed in water or water/methanol for 2 min remained

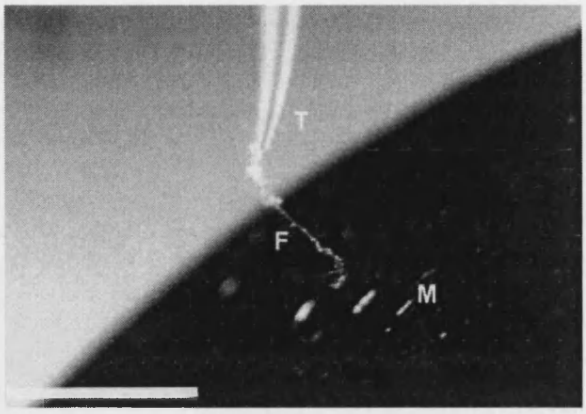

Fig. 2. Optical image illustrating magnetic attraction of a magnetite–silk fiber (F) to an external magnet (M).The fiber is held at the end of a vertically aligned pair of tweezers (T). Scale bar = 5 mm.

dark brown in color but had reduced iron contents as shown by EDX analysis of cross-sectioned material; similar observations were made for magnetite–silk fibers that had been sonicated for 1 h in water or water/methanol mixtures.

Stress–strain gauge measurements on individual magnetite–silk fibers showed negligible differences between the mechanical properties of the composite materials and unmineralized spider silk fibers (Fig. 4). The stress–strain properties determined from the breaking strength measurements were typical of natural silk (Table 1).[3] The breaking strengths were similar regardless of coating or solvent used in the preparations, but slight differences existed in the initial modulus and breaking elongation. The fibers exposed to water showed a slightly higher initial modulus, whereas the fibers prepared from methanol/water mixtures had a slightly higher breaking elongation. These mechani-

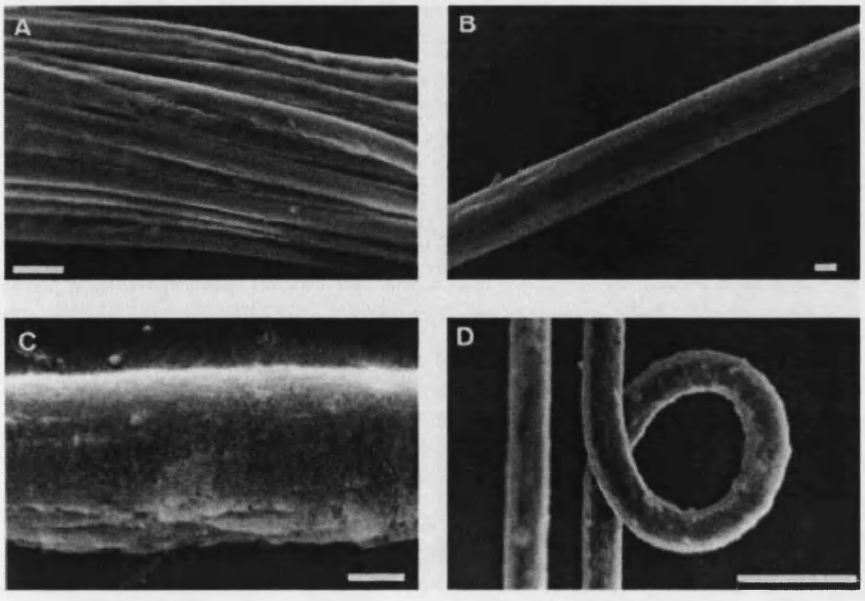

Fig. 1. SEM images of magnetite-coated silk fibers. A) Low magnification image showing bundle of magnetite-coated spider silk fibers, scale bar = 10 μm. B) Individual silk fiber with magnetite surface film, scale bar = 1 μm. C) Higher magnification image showing surface texture of the magnetite layer, scale bar = 1 μm. D) Magnetite–silk fiber displaying retained flexibility without significant loss of the mineral phase, scale bar = 10 μm

0935-9648/98/1007-0802 $ 17.50+.50/0

ADVANCED MATERIALS

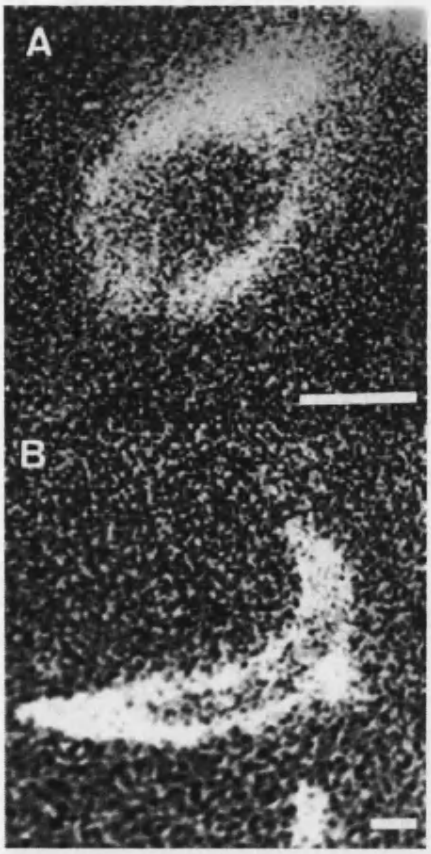

Fig. 3. Energy dispersive X-ray spatial mapping images for iron in magnetite–silk fibers sectioned A) approximately perpendicular to and B) oblique to the fiber axis. Scale bar = 1 μm in both images.

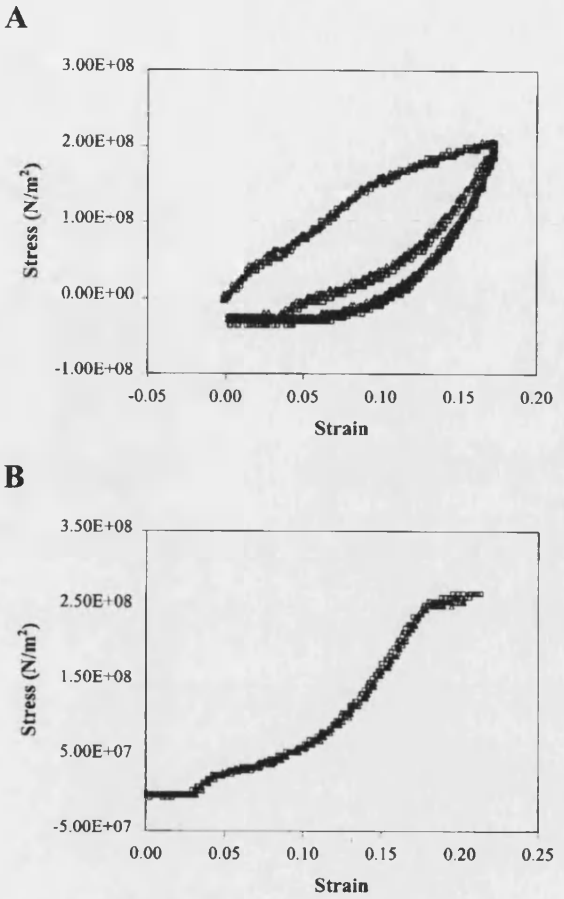

Fig. 4. Stress–strain curves for a control (unmodified) silk fiber (triangles) and magnetite-coated silk fiber (squares) showing A) hysteresis and B) breaking points.

cal properties were consistent with recent studies of *Araneus diadematus* dragline silk exposed to different solvents.[4]

We also prepared inorganic-silk fibers from colloids consisting of hydrophobic nanoparticles. Bundles of fibers, as well as individual fibers mounted on twin-pronged calipers, were submerged for 2 min in a 2-propanol sol of 2 nm gold particles that were surface-functionalized with 4-mercaptophenol.[6] Air drying of the dipped samples produced dark purple fibers with uniform and stable metal coatings (Fig. 5A). The gold coating was particularly resilient to subsequent washings with water and sonication. A similar procedure was used for the fabrication of inorganic-silk fibers coated in hydrophobic 5 nm diameter particles of cadmium sulfide. The semiconductor particles were prepared by chemical precipitation in reverse micelles formed from heptane/water/surfactant mixtures. Immersion of silk fibers into these dispersions produced pale white mineralized fibers that were covered in a homogeneous coating of CdS (Fig. 5B). The mechanical properties of both the Au- and CdS-coated silk fibers were essentially the same as determined for the unmodified silk (Table 1).

Table 1. Mechanical properties of *Nephila edulis* dragline silk–magnetite composites.

	Initial modulus [$\times 10^9$ N/m²]	Breaking strength [$\times 10^8$ N/m²]	Breaking elongation [%]
Control bare silk	1.1 ± 0.1	2.5 ± 0.1	22 ± 2.0
Magnetite (H_2O)	1.5 ± 0.2	2.2 ± 0.3	18 ± 2.0
Magnetite (CH_3OH/H_2O)	1.1 ± 0.1	2.3 ± 0.2	28 ± 1.0
Gold	1.2 ± 0.3	2.8 ± 0.1	25 ± 7.0
Cadmium sulfide	1.4 ± 0.3	2.2 ± 0.4	19 ± 2.0
Silica	1.9 ± 0.5	2.9 ± 0.3	22 ± 5.0

Finally, we prepared silk fibers coated in the electroconducting polymer polypyrrole by a two-step procedure involving Fe^{III}-catalyzed oxidative polymerization. Iron-coated fibers were prepared by dipping fibers in a 1 M $FeCl_3$ solution for 30 min and air-drying overnight. The resulting fibers were brown in color due to the formation of an iron oxide surface coating during drying of the Fe^{III} salt solution. The mounted fibers were then submerged in pyrrole for 2 min, removed, and rinsed with water to quench polymerization. After drying in air, dark greenish-black fibers coated in polypyrrole were produced (Fig. 5C). Although the Fe^{III} layer appeared to be stable, the polymer coating

  0935-9648/98/1007-0803 $ 17.50+.50/0

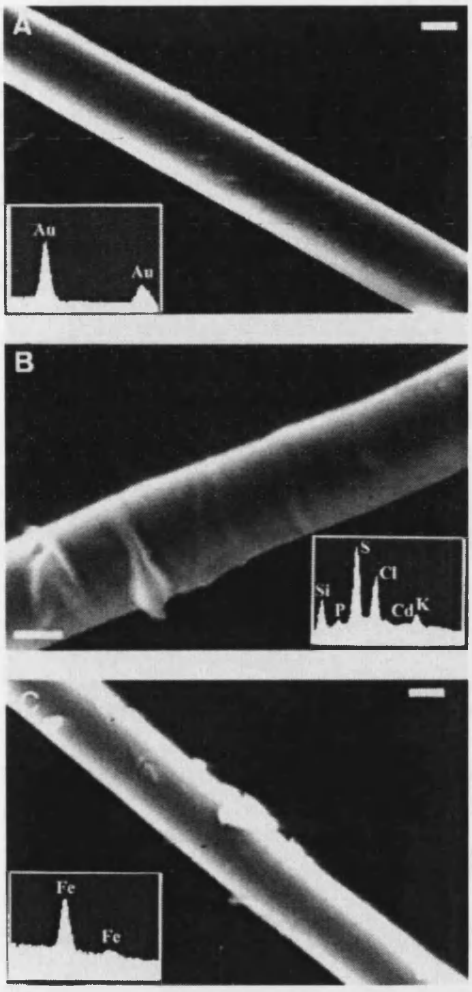

Fig. 5. SEM images and corresponding EDX analysis spectra for silk fiber composites prepared with nanoparticle coatings of A) hydrophobic gold, B) surfactant-coated CdS, and C) polypyrrole. Scale bars = 1 μm in all micrographs.

could be partially removed by sonication or mechanical flexing.

Our results indicate that mineral-coated silk fibers can be readily produced by a straightforward approach using nanoparticle suspensions. The method is versatile, easy to perform, and environmentally benign, suggesting that a wide range of silk-fiber hybrids could be routinely fabricated by this approach. At first sight, the use of dragline spider silk as a fibrous template for the adsorption and consolidation of thin films of magnetite nanoparticles is somewhat surprising, as the hydrophobic nature of the biopolymer should be incompatible with the charged and hydrated nature of the iron oxide surfaces. Indeed, use of hydrophobic nanoparticles, such as ligand-capped Au or surfactant-encapsulated CdS clusters, dispersed in organic solvents improved the wetting and mechanical stability of the inorganic coatings. It remains the case, however, that the magnetite coatings were well-defined and relatively stable when adsorbed from aqueous solutions. One possibility is that there are hydrogen bonding interactions at the oxide–silk interface. Recent observations have shown that immersion of spider silk fibers in water and other polar solvents induces reversible structural changes, consistent with hydrogen bonding networks within the near-surface structure of the silk.[4] In principle, oxo and hydroxyl species on the mineral surface could bind to polar amino acids that are exposed by interaction with solvent molecules. The collective outcome of such processes will be dependent on the binding site density and this is probably enhanced by the small size of the oxide nanoparticles, which generates a relatively large number of polar surface sites owing to the high surface area to volume ratio. Moreover, the small dimensions appear to be important for determining the structural integrity of the coatings, presumably because the nanoparticles give rise to close packed and highly consolidated aggregates during drying. In contrast, coatings prepared from aqueous suspensions of sub-micrometer size particles, such as colloidal silica, were extremely friable and flaked off the silk fibers during manipulation of the sample (data not shown). Similar considerations were discussed for nanocolloids used for the fabrication of ordered silica macrostructures within bacterial templates.[7]

Silk-fiber materials that combine the natural strength and elasticity of the biopolymer with physical properties such as magnetism, electrical conductivity, or semiconductivity might be useful as smart structural fabrics in a range of applications. Silk composites with magnetic properties, for example, could be integrated into devices concerned with audio reproduction where strong fabrics that respond to a magnetic field are required. We plan to continue to explore this system with the use of hydrophobic magnetic materials to achieve uniform coatings with high magnetization. Recently, evidence of an interesting hierarchical tube/core microstructure within the dragline silk has been reported,[8] suggesting that these micro-architectures could be used in future work to integrate inorganic components within silk fibers to produce biopolymer composites with significantly increased mineral loadings.

Experimental

A colloidal magnetite (Fe_3O_4) sol was prepared according to a previously reported procedure [9] by dropwise addition of 50 mL of 1 M $Me_4NOH{\cdot}5H_2O$ to a stirred mixture of 2.1 M $FeCl_3{\cdot}6H_2O$ (2.3 g in 4 mL H_2O) and 6.0 M $Fe(NH_4)_2(SO_4)_2$ (1.69 g in 1 mL of 2 M HCl). The resulting black sol was stirred at room temperature for 1 h, then sonicated in a water bath for 1 h, and finally centrifuged at 20000 rpm for 2 h. The supernatant was decanted and the pellet resuspended in H_2O by sonication. The centrifugation and washing procedures were repeated and the resuspended sol was filtered through a 13 mm diameter, 0.2 μm cellulose nitrate membrane. The final colloidal solution had a pH of 9.3. The negatively charged magnetite nanocolloid was used as a suspension either in water or in a 1:1 methanol/water mixture.

A nanocolloidal cadmium sulfide (CdS) sol was prepared in reverse micelles according to a previously reported procedure [10]. Reverse micelles were prepared by dissolving 1.67 g of AOT surfactant in 65 mL of heptane,

0935-9648/98/1007-0804 $ 17.50+.50/0

ADVANCED MATERIALS

followed by dropwise addition of 338 μL of H_2O while stirring vigorously. The homogeneous mixture was purged with nitrogen and 5 μL of 1 M $Cd(NO_3)_2 \cdot 4H_2O$ was then added via a microliter syringe to 10 mL of the stirred reverse micelle solution. 5 μL of 1 M Na_2S was slowly added and the solution was stirred for 20 min. Particle sizes were determined by UV-vis spectroscopy.

Mechanical testing was performed on single fibers of the inorganic-silk composites, which were attached to the twin arms of a custom-built stress–strain gauge using cyanoacrylate adhesive, and hysteresis cycles and breaking strength measurements were performed at ambient conditions of 29 °C and 34 % relative humidity. The measured stress was normalized using fiber diameters determined by SEM (mean diameter = 3.1±0.5 μm). The custom stress–strain gauge consisted of a FORT 10 force transducer (World Precision Instruments) and a Pen Motor Assembly (Hewlett Packard).

Received: December 1, 1997

[1] J. M. Gosline, M. E. DeMont, M. W. Denny, *Endeavour* **1986**, *10*, 37.
[2] M. A. Colgin, R. V. Lewis, *Chem. Ind.* **1995**, *12*, 1009.
[3] D. L. Dunaway, B. L. Thiel, C. Viney, *J. Appl. Polym. Sci.* **1995**, *58*, 675.
[4] Z. Shao, F. Vollrath, *Inst. Mater. (London)* **1997**, 262.
[5] T. Kohler, F. Vollrath, *J. Exp. Zool.* **1995**, *271*, 1.
[6] M. Brust, J. Fink, D. Bethell, D. J. Schiffrin, C. Kiely, *J. Chem. Soc., Chem. Commun.* **1995**, *16*, 1655.
[7] S. A. Davis, S. L. Burkett, N. H. Mendelson, S. Mann, *Nature* **1997**, *385*, 420.
[8] F. Vollrath, T. Holtet, H. C. Thoegersen, S. Frische, *Proc. R. Soc. London B* **1996**, *263*, 147.
[9] R. Massart, *IEEE Trans. Magn.* **1981**, *17*, 1247.
[10] R. R. Chandler, S. R. Bigham, J. L. Coffer, *J. Chem. Educ.* **1993**, *70*, A7.

Rapid, Solid-State Metathesis Routes to Metal Carbides**

By *Artur M. Nartowski, Ivan P. Parkin,* Alan J. Craven,* and *Maureen MacKenzie*

Transition metal carbides are inert, hard, refractory, conducting ceramics that find widespread usage in industry as components of cutting tools, crucibles, and catalysts.[1] They also play a crucial role in the formation and properties of hard steels.[2] Transition metal carbides are conventionally made by combination of the elements at elevated temperatures (>1500 °C) for extended time periods. For example, commercial grade WC used in abrasive pastes is synthesized at 2800 °C from the elements under a hydrogen atmosphere.[3] Molecular precursor routes to metal carbides have been developed in which the chemistry of the precursor decomposition has been tailored by introducing a molecular "Achilles heel" to promote carbide formation.[4,5]

We have been interested in finding straightforward, quick, low external energy routes to inorganic materials.[6] Kaner and co-workers first reported a new method of synthesizing inorganic materials by a solid-state metathesis (SSM) reaction[7] (Eq. 1).

$$Li_xQ_y + MCl_x \rightarrow MQ_y + x\,LiCl \quad (1)$$

(Q = N, P, As, O, S, Se, Te)

In this communication we report the first solid-state metathesis reactions for the formation of transition metal carbides via a fast (10 s), single-step reaction.

Thermal initiation of a mixture of calcium carbide with anhydrous metal chloride inside an evacuated ampoule either at the melting point of the halide or at 450 °C produces a transient red melt that, on cooling, forms a black solid with some calcium chloride layered on the surface (within 2–10 s). Trituration of the solid with methanol and water removes the coproduced calcium chloride and leaves a black or gray transition metal carbide that does not require any further annealing to induce crystallinity. In such reactions, carbon is coproduced, as shown for the reaction of VCl_3 and CaC_2 in Equation 2. This coproduced carbon was not detected in the triturated carbide product (by scanning electron microscopy (SEM), microanalysis, or X-ray diffraction (XRD)) and detailed inspection of the ampoule reveals that the carbon has phase separated from the vanadium carbide as a black layer on top of the coproduced $CaCl_2$.

$$8\,VCl_3 + 12\,CaC_2 \rightarrow V_8C_7 + 12\,CaCl_2 + 17\,C \quad (2)$$

An alternative carbiding reagent, Al_4C_3, was also investigated. Its reactions with transition metal halides were not as exothermic as those of CaC_2 but, after annealing for 2–3 days at 800–1000 °C, always resulted in the formation of phase-pure, crystalline carbides of transition metals. Here the reactions were again promoted by the melting of the transition metal halide. When the reactions were performed inside evacuated ampoules under a temperature gradient, the coproduced aluminum halide sublimed out from the carbide product (Eq. 3).

$$3\,ZrCl_4 + Al_4C_3 \rightarrow 3\,ZrC + 4\,AlCl_3 \quad (3)$$

The products were identified by X-ray powder diffraction (Table 1, Figs. 1a and b). The same single phase carbide products—stoichiometric ZrC, TiC, and WC and substoichiometric V_8C_7 and Mo_2C—were obtained for both the CaC_2 and Al_4C_3 reactions. An exception, however, was noted for the reactions of WCl_4 and $MoCl_5$ with CaC_2. These showed some W_2C and Mo as minor second phases in addition to the principal phases WC and Mo_2C. The metal carbides were indexed (Table 1) and showed good agreement with previous literature measurements.[3] Crystallite sizes as assessed by X-ray line broadening were of the or-

[*] Dr. I. P. Parkin, A. M. Nartowski
Department of Chemistry
University College London
20 Gordon Street, London WC1H 0AJ (UK)
Dr. A. J. Craven, Dr. M. MacKenzie
Department of Physics and Astronomy
University of Glasgow
Glasgow G12 8QQ (UK)

[**] The authors thank the EPSRC for grants GR/L06850 and GR/K93600.

  0935-9648/98/1007-0805 $ 17.50+.50/0

Organizing Nanometer-scale Magnets with Bacterial Threads

C. J. Smith, M. Field, C. J. Coakley and D. D. Awschalom
Department of Physics, University of California, Santa Barbara CA 93106, USA

N. H. Mendelson
Department of Molecular and Cellular Biology, University of Arizona, Tucson AZ 85721, USA

E. L. Mayes, S.A. Davis and S. Mann
School of Chemistry, University of Bath, Bath BA2 7AY, UK

***Abstract*— Macroscopic magnetic bacterial threads are formed in which 10 nm Fe_3O_4 particles are intercalated between cell walls. A mutant strain of bacteria is used which forms long filaments of joined cells. Using a drawing technique these strands can be bound together to form a solid thread which can be used as a superstructure to template magnetic particles. Dipping a thread into a ferrofluid solution allows the thread to rehydrate and draw the magnetite particles between the filaments. Cross-sectional images of the redrawn threads show the strands of cells form an ordered structure along the length of the fiber and reveal the magnetic particles embedded between the cell walls. The composite bacterial thread is superparamagnetic with a blocking temperature $T_B \sim 175$ K. Below this temperature the magnetization displays a field-dependent hysteresis indicating anisotropic behavior.**

***Index Terms*— Bacterial thread, Biomineralization, Magnetic microstructure.**

I. Introduction

Nanometer-scale ferromagnets can be patterned using lithographic techniques such as electron beam fabrication or local deposition using a scanning tunneling microscope [1], as well as the use of clusters and implantation techniques [2]. Another possible method is to use biological systems to direct the self-assembly of ordered magnetic structures. Certain organisms, such as magnetotactic bacteria [3-5], assimilate magnetic material and create microscopic magnets. Others create complex inorganic structures through biomineralization [4, 6], an approach that might be used as a template for artificial magnetic structures. In this work an ordered biological system based on bacteria is used as the framework for a ferromagnetic microstructure. Bacterial threads, typically of order 100 microns in diameter and several tens of centimeters long (figure 1), are fabricated by pulling many strings of cells together from out of a culture solution [7]. This structure is then dipped into a colloidal suspension containing 10 nm magnetite particles allowing the inorganic material to diffuse between the strings of cells and the thread to acquire magnetic properties. The resulting structure has a high density of magnetic particles arranged continuously along the thread, surrounding the strands of cells. This paper examines the microstructure and magnetic properties of the resulting bacterial thread.

Manuscript received October 17, 1997.
This work is supported by the AFOSR F49620-96-1-0018 and has made use of the MRL central facilities supported by the NSF under DMR-9123048.
NHM was supported by RR07912 from the National Center for Research Resources, NIH.

II. Fabrication of Bacterial Threads

The bacterial component used for the superstructure of the thread is *Bacillus subtilis* strain FJ7, a mutant which exhibits suppressed cell separation. *Bacillus subtilis* is a rod shaped (Gram positive) organism with cells of approximately 0.7 μm diameter and up to 4 μm in length [8]. In the mutant strain the cell grows by cylinder elongation at a constant diameter, but after the cell wall grows inward to create a septum in the middle of the cell length, no cell separation occurs. This results in the formation of long multi-cellular filaments which can contain thousands of cells [9], where each filament has one continuous cell wall linking the cells all the way down its length. This mutant strain of bacteria can be cultured so that filaments intertwine to form web like structures [7]. Using a thin wire hook these webs can be drawn out from the surface of their culture solution by slowly raising the hook at rates of up to 22 mm/min [10]. The filaments are compressed by surface tension into a thread at the fluid/air interface with all the filaments aligned parallel to the threads axis by the drawing action and, once dry, form a brittle solid. A typical bacterial thread contains $\sim 10^{10}$ cells

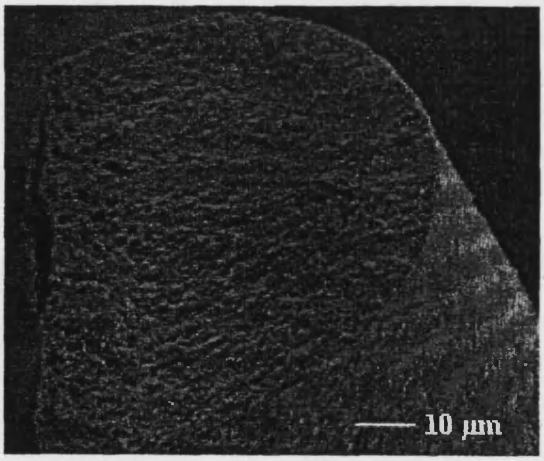

Fig 1. SEM micrograph of a cleaved bacterial thread

within 10^4 filaments, all arranged as a hierarchy of cylinders: cells attached end to end forming filaments, which are in turn close packed together making up the thread [7, 11].

Inorganic components can be added to a thread in two ways. Firstly the inorganic substance can be added to the web culture and a bacterial thread drawn with the inorganic component intercalated between the cell walls. Previous experiments added soluble metal salts ($FeCl_3$, $CaCl_2$ or $CuCl_2$) to the web culture which allowed the in situ mineralization of the filaments in the web as the metal binds to the cell walls, and the subsequent drawing of the mineralized strands into a fiber known as a "bionite" [8]. For this experiment a second method was used; a predrawn thread is dipped in to a solution containing the inorganic substance, the thread rehydrates and the strands loosen whilst van der Waals forces draw the fluid and the inorganic component into the thread. Subsequent drying of the thread produces a mineralized bacterial thread.

In this experiment the thread was impregnated with an aqueous colloidal suspension of Fe_3O_4 particles, prepared in air from an alkali solution of $FeCl_3.6H_20$ and $Fe(NH_4)_2(SO_4)_2$ salts [12]. TEM images show the particles to be approximately spherical, and measurements of 100 sampled particles reveals the size distribution to be symmetric with a mean particle diameter of 9.4 ± 2.4 nm.

III. Experimental Results and Discussion

Cross-sectional images of both magnetic and non-magnetic bacterial threads taken using AFM and SEM (figure 2) provide a method to examine the interior structure. The images show cells of typical diameter ~ 0.5 microns, slightly less than that reported for a single cell in culture [8] indicating some compression on drawing the fiber, and length ~ 4 microns (longitudinal image, not shown). A cross-section of a single thread reveals ~ 10^4 strands of cells in roughly close-packed order (figure 2(a)). All the cells are oriented so that their long dimension lies along the thread, a consequence of the production of strands of cells in the culture and the drawing technique. The magnetic bacterial thread shows the Fe_3O_4 particles embedded between the cell walls (figure 2(b)) in contrast to the regular bacterial thread with only close-packed cells (figure 2(c)). Examining several different areas of the magnetic bacterial thread samples shows the thickness of the magnetic layer between the cell walls to range between two and ten magnetite particles. Using this figure and the measured dimensions of the cells, the density of magnetite particles is estimated to be ~ 10^{18} particles/cm^3 and the volume fraction of magnetic material to be 7%. The samples are sufficiently magnetic to cling to a strong NdFeB permanent magnet (strength $4\pi M_s$ = 12300 G) against their own weight at room temperature.

The magnetic properties of a section of magnetic bacterial thread approximately one millimeter in length were measured using a SQUID magnetometer. The sample was cooled from room temperature to 5K in zero field. After applying an

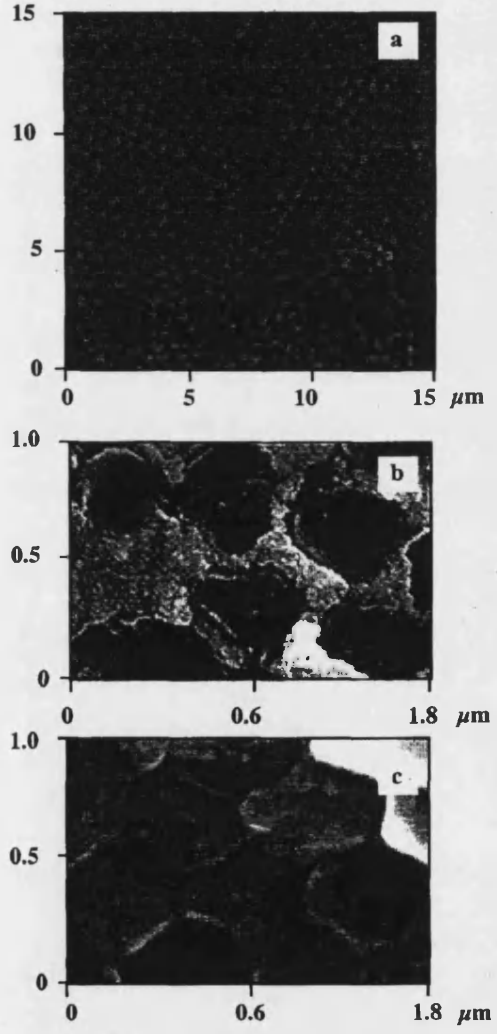

Fig 2. (a) AFM cross sectional image of cleaved bacterial thread (b ,c) Magnified SEM cross-sectional images of a cleaved magnetic (2b) and non-magnetic (2c) bacterial thread

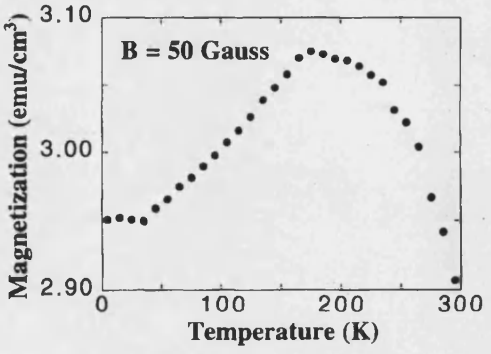

Fig 3. Magnetization versus temperature for a zero field cooled magnetic bacterial thread in a field of 50 Gauss applied along the length of the thread

external field of 50 Gauss along the length of the sample, the magnetization in the direction of the field was measured as a function of temperature (figure 3). The magnetization data shows a peak value at a temperature, $T_B \sim 175K$, corresponding to the blocking temperature of a superparamagnetic assembly of particles. The measured blocking temperature is an order of magnitude larger than an estimate of the single particle energy barrier calculated using the bulk value of magnetocrystalline anisotropy (13 K), indicating the particles are weakly interacting.

Above the blocking temperature the magnetization versus applied field shows a very small anisotropy with angle (not shown), measured parallel and perpendicular to the thread axis, due to the sample shape. To estimate both the number of particles and the moment per particle, the data for parallel and perpendicular measurements was averaged to remove the effects of this anisotropy. The magnetization, M_H, was then fitted using a Langevin function ($M_H = N\mu\, L(\mu H/k_BT)$) where N is the number of particles present, μ is the moment per particle and L is the Langevin function. This analysis gives a particle density of $1.3x10^{18}$ particles/cm^3 and which agrees well with our original estimate of $1x10^{18}$ particles/cm^3 from the cross-sectional SEM images. From this value of the particle density, we obtain a volume fraction estimate of 5%. The moment per particle from this fit to the Langevin function is $1.98x10^{-16}$ emu, which compares to a value of $2.05x10^{-16}$ emu calculated for a ten nanometer diameter particle using the magnetization of bulk magnetite [4] and a value of $2.62x10^{-16}$ emu from the magnetite in magnetotactic bacteria [5] (scaled with volume).

Below the blocking temperature the bacterial thread magnetization displays a field dependent hysteresis which changes as a function of angle indicating anisotropic behavior (figure 4). The anisotropy is larger below the blocking temperature compared with that above which is due solely to the sample shape. This suggests the distribution of easy axes is not truly random and there is a preferential orientation of the easy axes along the length of the thread. Compressional stress created on drawing the bacterial thread may cause the distribution of easy axes to be peaked along the fiber.

The hysteresis curve of a randomly oriented assembly of single domain Stoner-Wohlfarth magnets have a remanence that is exactly half of the saturation magnetization [13, 14]. At zero field the magnetization of each particle lies along it's easy axis, the remanence is then computed from the average of $\cos(\theta)$ where θ is the angle between a particle's easy axis and the direction in which the magnetization is measured. For a random distribution of easy axes the average of $\cos(\theta) = \langle\cos(\theta)\rangle = 1/2$, the Stoner-Wohlfarth result. The measured value of the remanence should give a direct measure of $\langle\cos(\theta)\rangle$, the angular distribution of the easy axes. The hysteresis loops of the bacterial thread measured at different angles show a maximum remanence of 0.313 (normalized to the saturation magnetization) with the field oriented parallel to the bacterial thread, and a minimum of 0.256 with the field perpendicular to the thread (figure 4). These two values show a difference attributable to a non-random distribution of easy axes, but are both clearly less than 1/2, further suggesting that the particles are weakly interacting within the thread.

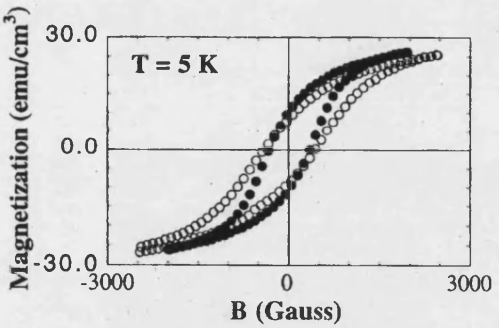

Fig 4. Magnetization versus field on magnetic bacterial thread sample at 5 Kelvin with the field applied parallel to (full circles) and perpendicular to (open circles) the length of the thread

IV. CONCLUSIONS

Bacterial threads were created with magnetic particles intercalated between the cell walls. Cross-sectional AFM and SEM images show the presence of the magnetic particles embedded between the cell walls in the thread. Magnetization data reveals the bacterial thread to be superparamagnetic with anisotropic behavior.

REFERENCES

[1] D.D. Awschalom, D.P. DiVincenzo, and J.F. Smyth, *Science*, vol. 258, pp. 414 - 421, 1992.

[2] J. Shi, S. Gider, K.L. Babcock, and D.D. Awschalom, *Science*, vol. 271, pp. 937 - 941, 1996.

[3] R. Blakemore, *Science*, vol. 190, pp. 377-379, 1975.

[4] J.L. Kirschvink, D.S. Jones, and B.J. MacFadden, in *Topics in Geobiology*, vol. 5, F.G. Stehli, Ed. New York: Plenum Press, 1985.

[5] B.M. Moskowitz, R.B. Frankel, P.J. Flanders, R.P. Blakemore, and B.B. Schwartz, *J. of Magn. Magn. Mater.*, vol. 73, pp. 273-288, 1988.

[6] S. Mann and G.A. Ozin, *Nature*, vol. 382, pp. 313-318, 1996.

[7] J.J. Thwaites and N.H. Mendelson *Proc. Natl. Acad. Sci.*, vol. 82, pp. 2163-2167, 1985.

[8] N.H. Mendelson*Science*, vol. 258, pp. 1633 - 1636, 1992.

[9] N.H. Mendelson, in *Biomimetic Materials Chemistry*, S. Mann, Ed.: VCH Publishers, 1996, pp. 279 - 313.

[10] S.A. Davis, S.L. Burkett, N.H. Mendelson, and S. Mann, *Nature*, vol. 385, pp. 420 - 423, 1997.

[11] N.H. Mendelson and J.J. Thwaites *Jour. Bacteriolgy*, vol. 171, pp. 1055 - 1062, 1989.

[12] R. Massart, *IEEE Trans. Mag.*, vol. 17, pp. 1247 - 1248, 1981.

[13] E.C. Stoner and E.P. Wohlfarth, *Phil. Trans. Roy. Soc. (London)*, vol. 240, pp. 599-642, 1948.

[14] A.H. Morrish, *The Physical Principals of Magnetism*. Robert E. Krieger Publishing Company, 1965.

Chem. Mater. **1998,** *10,* 2516−2524

Brittle Bacteria: A Biomimetic Approach to the Formation of Fibrous Composite Materials

Sean A. Davis,[†] Harish M. Patel,[†] Eric L. Mayes,[†] Neil H. Mendelson,[‡] Gabriella Franco,[†] and Stephen Mann*,[†]

Department of Chemistry, University of Bath, Bath, BA2 7AY, U.K., and Department of Molecular and Cellular Biology, University of Arizona, Tucson, Arizona 85721

Received April 16, 1998. Revised Manuscript Received July 2, 1998

Organized bacterial superstructures have been used as 3-D templates for the fabrication of ordered inorganic−organic fibrous composites. Preformed magnetic (Fe_3O_4) and semiconducting (CdS) inorganic nanoparticles were incorporated into macroscopic threads of *Bacillus subtilis* by reversible swelling of the superstructure in colloidal sols. The air-dried mineralized fibers consisted of a closely packed array of 0.5 μm diameter multicellular bacterial filaments, each of which was coated with a 30−70 nm thick layer of aggregated colloidal particles. Inorganic patterning of the interfilament spaces was influenced by the surface charge of the nanoparticles used. Whereas negatively charged magnetite colloids gave good infiltration and replication of the bacterial superstructure, the neutral-ligand-capped CdS colloid, although internalized to some extent, was preferentially localized at the surface of the thread. Positively charged sols of TiO_2, in contrast, did not penetrate the swollen fiber but produced coherent surface coatings of uniform thickness. Attempts to pattern the deposition of CdS using molecular precursors by exposing a Cd(II)-containing bacterial fiber to H_2S gas produced an uneven surface coat of CdS particles. Removal of the bacterial component from the magnetic composite by heating at elevated temperatures resulted in structural collapse.

Introduction

A central objective of biomimetic materials chemistry is to develop new strategies for the synthesis of materials and composites that exhibit the organizational and functional specificity exemplified by biological minerals such as bones, shells, and teeth.[1,2] Some progress has been made toward developing biomimetic approaches to the formation of inorganic materials with controlled size, shape, orientation, and polymorphic structure.[3,4] Current research is also investigating routes to the synthesis of inorganic materials with complex form[5,6] and higher-order hybrid assemblies,[7−10] often reminiscent of the hierarchical structures seen in nature. A generic approach to these biomimetic materials involves the inorganic replication of a preformed organic assembly possessing an extended and patterned architecture. In this paper we develop this strategy by using a bacterial template with reversible swelling properties to fabricate fibrous bioinorganic composites consisting of organized arrays of magnetic or semiconducting nanoparticles.

Bacterial threads can be produced from a mutant strain of the bacterium *Bacillus subtilis,* which has a cylinder-shaped cell, 0.8 μm in diameter and 4 μm in length. In fluid cultures, the mutant strain, which exhibits suppressed cell separation, can only grow by elongation at constant diameter along the cylinder axis to produce long multicellular filaments that intertwine to form weblike structures (Figure 1). Drawing these web structures from the culture medium results in compaction of the individual filaments at the fluid−air interface to give a macroscopic bacterial thread, often several decimeters long and 0.1−0.2 mm wide.[11,12] The air-dried thread consists of a superstructure of multicellular filaments aligned parallel to the thread axis and arranged in a pseudohexagonal-packed configuration, reminiscent of the organization of cylindrical surfactant micelles in the H_I liquid−crystal lyotropic phase, albeit on a length scale 2 orders of magnitude greater. A

* To whom correspondence should be addressed.
† University of Bath.
‡ University of Arizona

(1) Sarikaya, M.; Aksay, I. A. *Biomimetics: Design and Processing of Materials;* AIP Series in Polymers and Complex Materials; AIP Press: New York, 1995.
(2) Mann, S. *Biomimetic Materials Chemistry,* VCH Publishers: New York, 1996.
(3) Mann, S. *J. Mater. Chem.* **1995**, *5*, 935.
(4) Heuer, A. H.; Fink, D. J.; Laraia, V. J.; Arias, J. L.; Calvert, P. D.; Kendall, K.; Messing, G. L.; Blackwell, J.; Rieke, P. C.; Thompson, D. H.; Wheeler, A. P.; Veis, A.; Caplan, A. I. *Science* **1992**, *255*, 1098−1105.
(5) Mann, S.; Ozin, G. A. *Nature* **1996**, *382*, 313−318.
(6) Mann, S. *J. Chem. Soc., Dalton Trans.* **1997**, 3953.
(7) Aksay, I. A.; Trau, M.; Manne, S.; Hunma, I.; Yao, N.; Zhou, L.; Fenter, P.; Eisenberger, P. M.; Gruner, S. M. *Science* **1996**, *273*, 892.
(8) Antonietti, M.; Göltner, C. *Angew. Chem., Int. Ed. Engl.* **1997**, *36*, 910.
(9) Mann, S.; Burkett, S. L.; Davis, S. A.; Fowler, C. E.; Mendelson, N. H.; Sims, S. D.; Walsh, D.; Whilton, N. T. *Chem. Mater.* **1997**, *9*, 2300.
(10) Combs, N.; Khushalani, D.; Oliver, S.; Ozin, G. A.; Shen, G. S.; Sokolov, I.; Yang, H. *J. Chem. Soc., Dalton Trans.* **1997**, 3941.
(11) Mendelson, N. H.; Thwaites, J. J. *MRS Symp. Proc.* **1990**, *174*, 171.
(12) Thwaites, J. J.; Mendelson, N. H. *Proc. Natl. Acad. Sci. U.S.A.* **1985**, *82*, 2163.

S0897-4756(98)00285-3 CCC: $15.00
Published on Web 08/29/1998

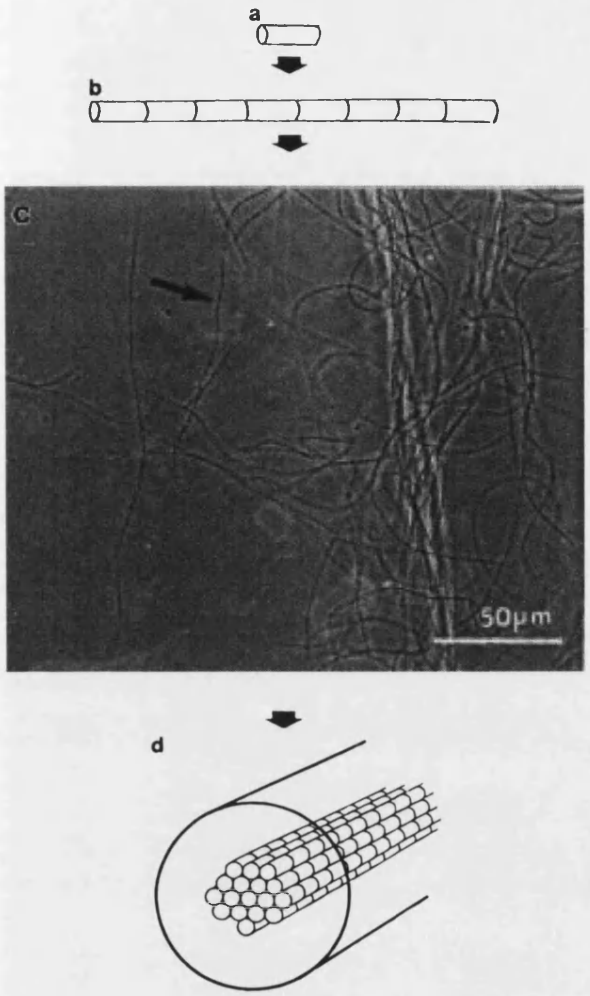

Figure 1. Different levels of cellular organization in bacterial thread. (a) individual rod shaped cells of *B. subtilis*, (b) growth at constant diameter to produce multicellular filaments, (c) optical micrograph of cultured bacteria showing intertwined filaments with weblike structures, and (d) withdrawing of multicellular filaments through the air–water interface produces macroscopic bacterial thread with organized internal superstructure.

typical bacterial thread can contain in excess of 10^{10} cells and 50 000 filaments arranged as a cell → filament → thread hierarchy of cylindrical building units.[13]

The strong metal-binding ability of the cell wall of *B. ubtilis*[14] has been utilized for the mineralization of multicellular bacterial filaments prior to drawing of the macroscopic composite fiber.[15] For example, addition of soluble metal salts of iron and calcium directly to unwashed web cultures resulted in the formation of precipitates on the filaments within the web culture.[16] Analysis of fibers drawn from these mineralized web structures indicated a metal content of 10–16 wt % deposited in the form of mineral phases such as Fe_2O_3 and $CaCO_3$. However, no precipitation was observed on the filaments prior to drawing into a fiber when washed webs or copper salts were used. The corresponding drawn fibers contained mineral deposits formed by solution evaporation, but the metal loadings were significantly reduced. The internal microstructure of the composite fibers produced from mineralized webs (both washed and unwashed) was not systematically studied.

In recent studies, we have been investigating an alternative method to the fabrication of organized bacterial–mineral composites that is based on reversible swelling of unmineralized threads in the presence of preformed inorganic nanoparticles.[17] Our objective is to exploit the underlying organization of the thread as a template for producing composites with an extended, ordered microstructure. This was achieved by loading the bacterial thread with colloidal suspensions of ceramic nanoparticles, followed by air-drying to consolidate the inorganic mineral and to replicate the interfilament spaces in the form of a continuous inorganic framework. Moreover, removal of the bacterial template by calcination produced a silica fiber with ordered macroporous channels. We also infiltrated the organic superstructure with a colloidal dispersion of a surfactant-templated mesostructured silica phase (MCM-41) to illustrate how bacterial templates could be used in hierarchical processing. An ordered macroporous fiber with channel walls of periodic mesoporous silica was obtained after calcination.[17] Here we describe the use of a preformed bacterial thread for the production of fiberlike composites containing Fe_3O_4, CdS, or TiO_2 nanoparticles.

Experimental Section

Production of Bacterial Thread. The cultures of *B. subtilis* strain FJ7(II) were grown at 20 °C in 100 mm diameter plastic Petri dishes containing 16 mL of tryptose blood (TB) medium, consisting of tryptose (10 g/L), beef extract (3 g/L), and NaCl (5 g/L), supplemented with uracil (20 mg/L).[18] Decimeter-long bacterial threads were produced by slowly pulling the web from solution using a thin wire hook, withdrawn at 22 mm min^{-1} by a rate-controlled motor, and were left to dry in air.

Synthesis of Magnetite (Fe_3O_4) Nanoparticles. A magnetite colloid was prepared in alkaline media according to the general procedure described elsewhere.[19] An aqueous solution containing iron(III) chloride hexahydrate (4 mL, 0.0085 mol) and ammonium iron(II) sulfate hexahydrate (1 mL, 0.0043 mol, in 2 M HCl) was added to 50 mL of 1 M tetramethylammonium hydroxide. The resulting black suspension was stirred for 1 h at room temperature and then placed in an ultrasonic bath for 1 h. The colloid produced was centrifuged at 20 000*g* for 1 h. The supernatant was decanted and the sediment resuspended in 20 mL of water by sonication. The black dispersion obtained was filtered through a 0.2 μm pore cellulose nitrate membrane filter. The particle size of the approximately spherical particles was 9.1 ± 2.4 nm as determined by transmission electron microscopy. Electron diffraction data [d_{hkl} = 0.500 nm (111), 0.305 nm (220), 0.259 nm (311), 0.216 nm (400)] were consistent with magnetite.

Synthesis of Cadmium Sulfide (CdS) Nanoparticles. A CdS colloid was prepared by the following procedure:[20] cadmium acetate (2.712 g, 0.0118 mol), thiourea (0.263 g, 0.00346 mol), and 3-mercapto-1,2-propanediol (0.945 cm^3,

(13) Mendelson, N. H.; Thwaites, J. J. *J. Bacteriol.* **1989**, *171*, 1055.
(14) Beveridge, T. J.; Murray, R. G. E. *J. Bacteriol.* **1976**, *127*, 1502.
(15) Mendelson, N. H. *Science* **1992**, *258*, 1633.
(16) Mendelson, N. H.. In *Biomimetic Materials Chemistry*; Mann, S., Ed.; VCH Publishers: New York, 1996; pp 279–313.
(17) Davis, S. A.; Burkett, S. L.; Mendelson, N. H.; Mann, S. *Nature* **1997**, *385*, 420.
(18) Mendelson, N. H. *Proc. Natl. Acad. Sci. U.S.A.* **1976**, *73*, 1740.
(19) Massart, R. *IEEE Trans. Magnet.* **1981**, *17*, 1247.
(20) Chemseddine, A.; Feaheiley, M. L. *Thin Sol. Films* **1994**, *247*, 3.

0.0113 mol) were mixed together with dimethylformamide (200 cm^3) for approximately 1 h, under a flow of argon. The mixture was then heated to 100−130 °C for 20 min and allowed to cool for 30 min. This heating−cooling cycle, which decomposes the thiourea and generates S^{2-} ions, was repeated, and on the third heating cycle, a white precipitate of CdS formed. The precipitate was isolated by centrifugation, washed with acetone followed by diethyl ether (to remove residual Cd(II) ions), and finally dried in vacuo. The particle diameter determined by TEM was 3.4 ± 0.7 nm. XRD measurements of films and powders prepared from the dispersion indicated that the CdS nanoparticles adopt the ZnS blende structure [d_{hkl} = 0.336 nm (111), 0.290 nm (200), 0.206 nm (220), 0.175 nm (311)].

Synthesis of Titania (TiO_2) Colloid. Colloidal titania was prepared by hydrolysis of titanium tetraisopropoxide under a nitrogen atmosphere using the procedure described previously.[21] Titanium(IV) isopropoxide (1.25 mL, 0,00424 mol) was added to 0.25 mL of 2-propanol in a syringe. This mixture was added dropwise over 5 min to 10 mL of distilled, deionized water while the mixture stirred vigorously. Ten minutes after the final alkoxide addition, 0.05 mL of 70% nitric acid was added. The hydrolysis mixture was then stirred for 8 h at 80 °C to remove the 2-propanol. The mean particle diameter from TEM studies was 8.2 ± 2.2 nm. Electron diffraction indicated that the major phase present was the anatase polymorph of TiO_2 [d_{hkl} = 0.355 nm (101), 0.238 nm (004), 0.231 nm (112), 0.191 nm (200), 0.169 nm (105)]. A small amount of brookite, also a polymorph of TiO_2, was also detected [d_{hkl} = 0.292 nm (121)].

Preparation of Mineralized Bacterial Composites from Preformed Nanoparticles. Fiber composites were prepared by dipping 5 cm long samples of prewashed bacterial thread into a colloidal dispersion of inorganic nanoparticles (Fe_3O_4, CdS, or TiO_2) for between 5 and 120 min. Samples were then carefully removed from the colloid-containing solution and allowed to dry in air for at least 24 h prior to analysis. Reverse tweezers were used to hold the bacterial thread throughout the process. During the dipping process, the tweezers were held so that the tip was not immersed in the dispersion, and the portion of bacterial thread being held remained dry, which aided the recovery of the composite fiber. Consequently, a portion of the loaded thread remained bare and this was removed from the air-dried samples before further analysis.

A portion of a magnetite−bacterial thread composite was placed in a crucible and heated in air to 600 °C in an oven. The temperature was increased in 50 °C increments at 30 min intervals. The oven was turned off after 2 h and allowed to cool to room temperature before the product was recovered.

Preparation of Mineralized Bacterial Composites by in Situ Deposition. A 5 cm long portion of a prewashed bacterial thread was dipped into a 1.0 M cadmium chloride solution for 2 h, redrawn, and allowed to dry in air overnight. The Cd-containing bacterial thread was then placed in a desiccator and exposed to a constant supply of H_2S, generated from the reaction of Na_2S(s) with HCl(aq), for 7 days.

Characterization. Scanning electron microscopy (SEM) and energy-dispersive X-ray analysis (EDXA) were performed using a JEOL 6310 SEM operated at 15 keV. Samples were prepared for analysis using one of two different methods. First, air-dried uncoated samples were mounted onto aluminum stubs using circular carbon adhesive pads for EDX analysis and then gold-coated in an Edwards S150B sputter-coater for 4 min for imaging studies. Second, resin-embedded samples were mounted onto aluminum stubs using a carbon "gum" and gold-coated for 2 min, after which a carbon paste was applied between the gold coat and the stub to enhance the electrical conductivity of the resin blocks. Elemental distribution maps were generated by EDX analysis and corresponding secondary electron images obtained.

(21) O'Regan, B.; Moser, J.; Anderson, M.; Gratzel, M. *J. Phys. Chem.* **1990**, *94*, 8720.

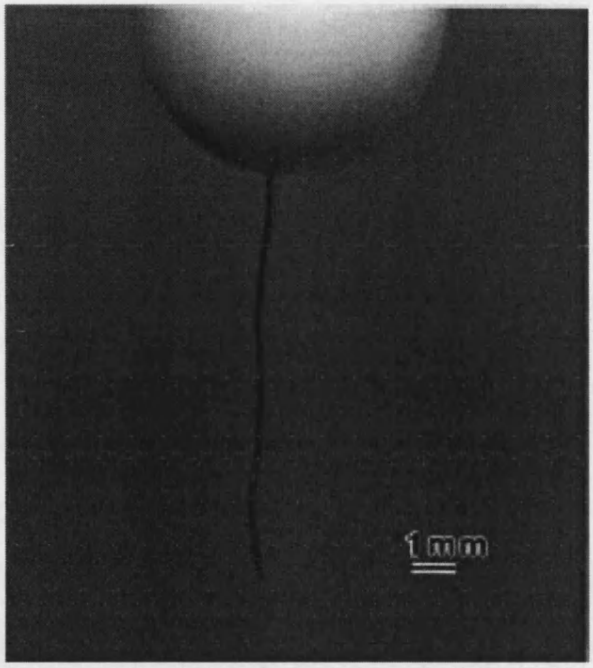

Figure 2. A bacterial−magnetite fibrous composite attracted to and vertically suspended from a permanent bar magnet.

Thin sections of the composite fibers were prepared for transmission electron microscopy (TEM) analysis by dehydrating a 1 cm length of the material for 1 h in 50 mL of 50:50 MeOH/H_2O containing 0.5 mL of silane to aid adhesion between the sample and resin. After drying in air for 90 min, the fiber was transferred to a sample bottle, covered in TAAB hard resin, and placed in a rotator for at least 12 h to allow infiltration of the resin into the fiber. The sample was then placed in an embedding mold and covered with fresh resin, which was polymerized in an oven at 60 °C for 2 days. Sections were prepared using a diamond knife on an OMU3 ultramicrotome. Thin sections were cut perpendicular to the fiber axis to a thickness of typically 50−100 nm (silver−gold interference colors). Sections were collected on Formvar-covered, carbon-coated, 3 mm slotted copper grids and left unstained. TEM imaging, selected area electron diffraction studies, and EDXA were performed on a JEOL 2000FX analytical TEM operated at an accelerating voltage of 200 keV.

X-ray diffraction data were recorded from whole samples, using a Phillips X-ray powder diffractometer with Cu Kα (l = 1.5405 Å) radiation.

Results

Bacterial−Magnetite Fibrous Composites. Dipping of bacterial threads into a ferrofluid of magnetite nanoparticles resulted in visible swelling of the biological superstructure without loss of structural integrity. The swollen fiber was withdrawn through the air−liquid interface to produce a compact black fiber that was initially pliable due to its high moisture content. Drying in air gave a consolidated, brittle fiber of similar size to the unmineralized bacterial thread. The iron loading in the dried sample was 19 wt %, as determined by atomic absorption spectrometry. The mass loading of magnetite in the composite was calculated as 26 wt %, by assuming a chemical composition of Fe_3O_4. The composite fibers were sufficiently magnetic that they responded and tracked to an external magnetic field and could be suspended vertically under the poles of a bar magnet (Figure 2). Further details on the superpara-

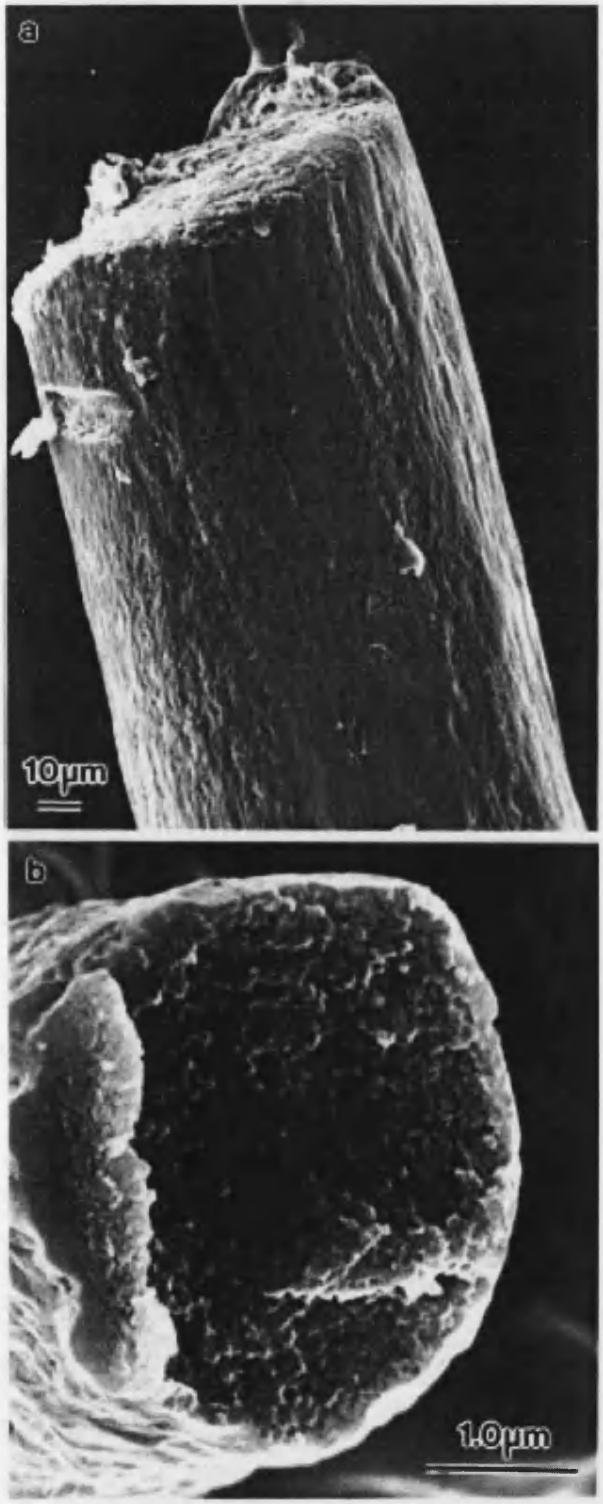

Figure 3. SEM images of (a) the external surface and (b) cross section of a bacterial–magnetite fibrous composite.

magnetic properties of the composite fibers are reported elsewhere.[22]

The surface and internal texture of the individual composite fibers (Figure 3) was significantly different than that of the unmineralized bacterial thread. A thin mineral coating, which gave peaks for iron by energy-dispersive X-ray analysis (data not shown), obscured the

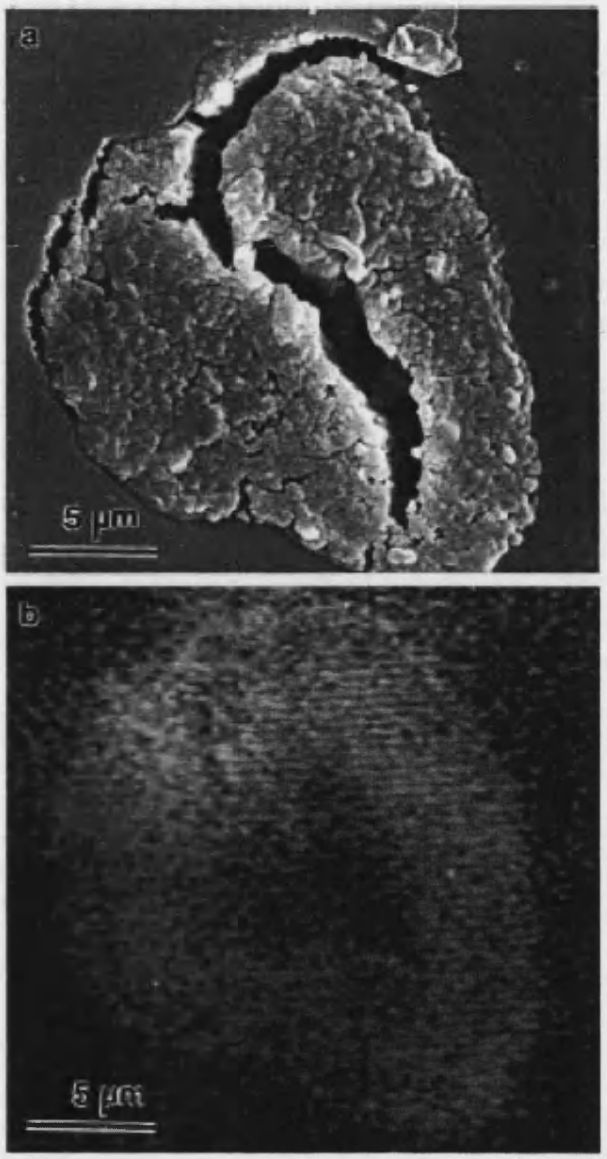

Figure 4. (a) SEM image of a resin-embedded bacterial–magnetite composite imaged in cross section. (b) Corresponding elemental distribution map for iron.

underlying bacterial cells. The fibers appeared uniformly dark in cross section, indicating that the mineral phase was not restricted to the surface of the fiber. This was confirmed by mapping the iron distribution of a sample in cross section (Figure 4), as well as TEM imaging of the central region of thin transverse sections (Figure 5). The TEM data showed that discrete magnetite nanoparticles were concentrated around and between the multicellular filaments of the bacterial superstructure to produce an extended and interconnected microskeletal framework. The thickness of the mineral walls was typically between 50 and 70 nm.

Removal of the bacterial template by high-temperature curing produced an intact but extremely brittle black fiber. Any attempt to manipulate the sample resulted in collapse of the structure.

(22) Smith, C. J.; Field, M.; Coakley, C. J.; Awschalom, D. D.; Mendelson, N. H.; Mayes, E. L.; Davis, S. A.; Mann, S. *IEEE Trans. Magn.* **1998**, *34*, 988.

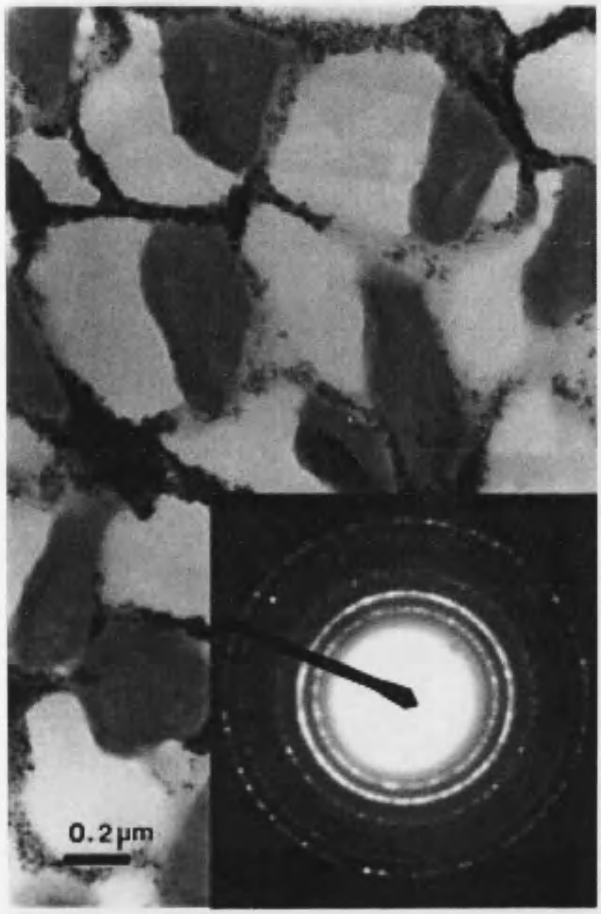

Figure 5. TEM image of a transverse thin section of a bacterial–magnetite composite fiber showing aggregated Fe_3O_4 nanoparticles (darkest areas in the micrograph) within the interfilament spacings. Inset: associated selected-area diffraction patterns confirming the presence of magnetite [d_{hkl} = 0.492 nm (111), 0.300 nm (220), 0.253 nm, 0.212 nm].

Bacterial–CdS Fibrous Composites. Dipping bacterial thread into an aqueous suspension of CdS nanoparticles produced a fiber that was not significantly different than the original bacterial thread in appearance. SEM microscopy of the composite fiber revealed that the fiber surface consisted of partially disorganized filaments and discrete, randomly distributed micron-scale mineral aggregates (Figure 6), which contained Cd and S (EDX data not shown). Thus, the CdS colloid produced localized aggregates rather than a uniform coating of the fiber surface. However, elemental mapping indicated that the inorganic phase was dispersed throughout the bacterial thread (Figure 7), although a higher concentration was observed near to the edge of the fiber due to the surface aggregates. TEM micrographs of transverse thin sections (Figure 8) showed that the bacterial filaments were comparatively well-ordered in the center of the fiber, in contrast to their surface organization. Higher magnification images (Figure 8b) revealed 30–40 nm thick electron dense regions surrounding individual filaments that were attributed to closely packed arrays of the CdS nanoparticles. No electron diffraction patterns could be recorded from these areas due to the low localized concentration of the colloidal particles.

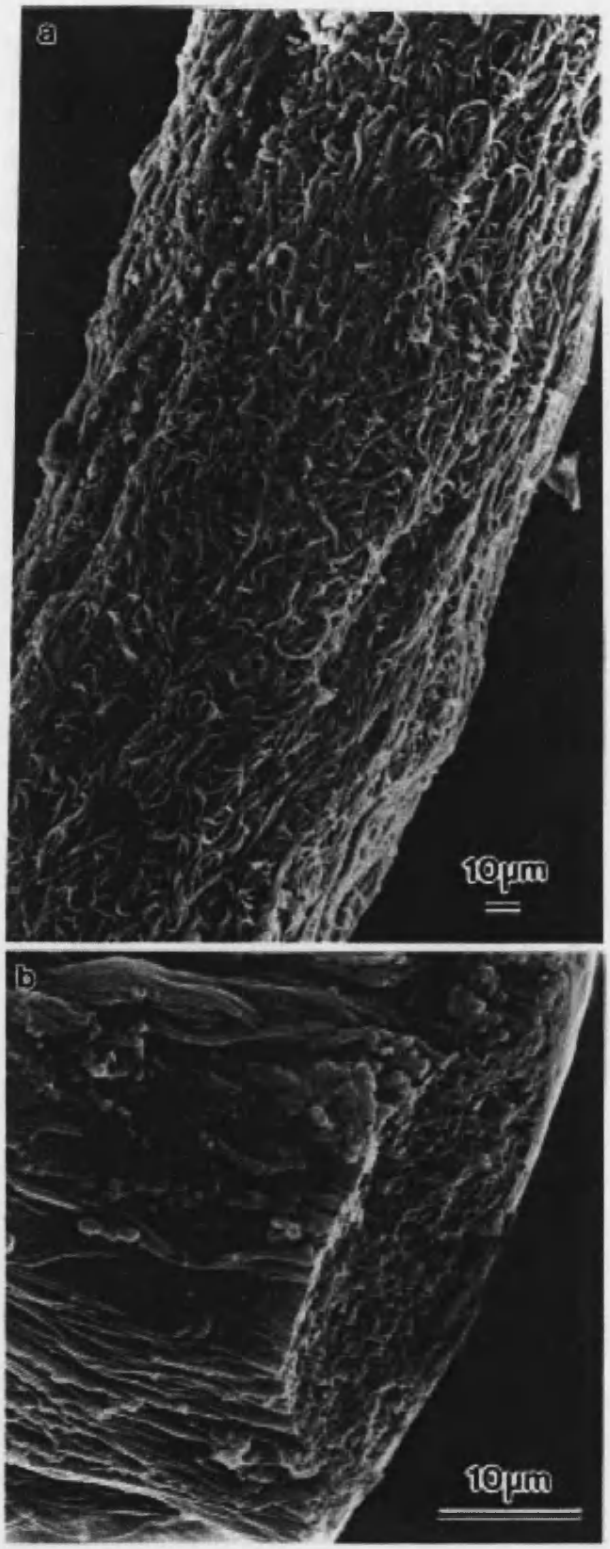

Figure 6. (a) SEM of the surface of a bacterial–CdS composite fiber. (b) Higher magnification image showing detail of a fractured surface.

In Situ Mineralization of CdS in the Bacterial Thread. Dry fibers, produced after dipping bacterial thread into aqueous $CdCl_2$ solution, were white and of similar diameter to the native material. Although Cd was detected by EDX analysis (data not shown), no

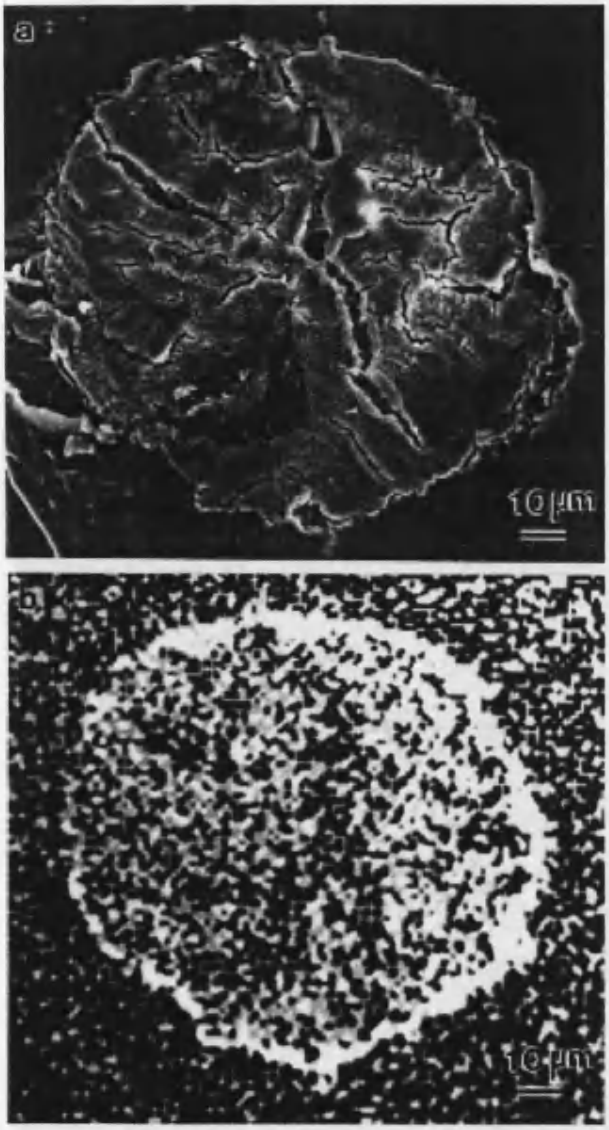

Figure 7. (a) SEM of a bacterial–CdS composite imaged parallel to the fiber axis. (b) Corresponding elemental distribution map for Cd.

mineral phases, such as a $CdCl_2$ evaporite, were observed by SEM examination of the fiber surface, which consisted of disorganized bacterial filaments. The Cd-containing bacterial thread developed a yellow coloration when exposed to H_2S. Examination of the fiber by SEM revealed an uneven surface coating which consisted of a mass of platelike, and smaller discrete crystals (Figure 9). Elemental mapping indicated that Cd and S were not evenly distributed throughout the fiber but were concentrated near the surface (Figure 10). X-ray diffraction (XRD) of the composite fiber indicated the presence of a crystalline CdS phase with the ZnS blende structure [d_{hkl} = 0.335 nm (111), 0.298 nm (200), 0.206 nm (220)]. TEM imaging of thin sections clearly showed the presence of a surface coating about 60 nm thick (Figure 11). Electron diffraction data recorded from this area were consistent with the XRD data. Cadmium sulfide particles were also identified at much lower loadings in the center of the thread by EDX analysis (data not shown).

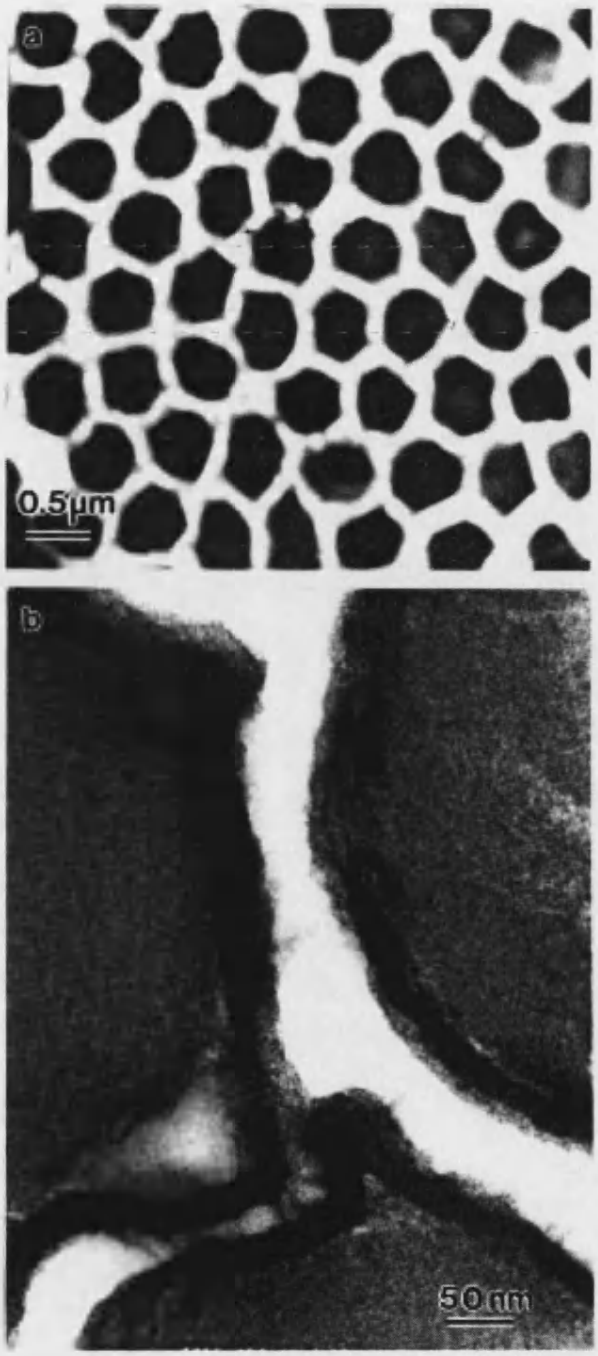

Figure 8. (a) Low-magnification TEM micrograph of a transverse thin section of a bacterial–CdS composite showing the ordered arrangement of the bacterial filaments near the center of the fiber. (b) Higher magnification image of individual bacterial filaments showing a densely packed array of CdS nanoparticles on the cell walls.

Bacterial–Titania Fibrous Composites. A pale white fiber was produced by dipping bacterial thread into an aqueous dispersion of titania nanoparticles. Examination of the surface of the fiber by SEM revealed a distinct mineral coating (Figure 12), which appeared smooth and of quite uniform thickness. The apparent platelike morphology originated from shrinkage of a thin mineral film during drying which caused extensive cracking, predominantly perpendicular and parallel to

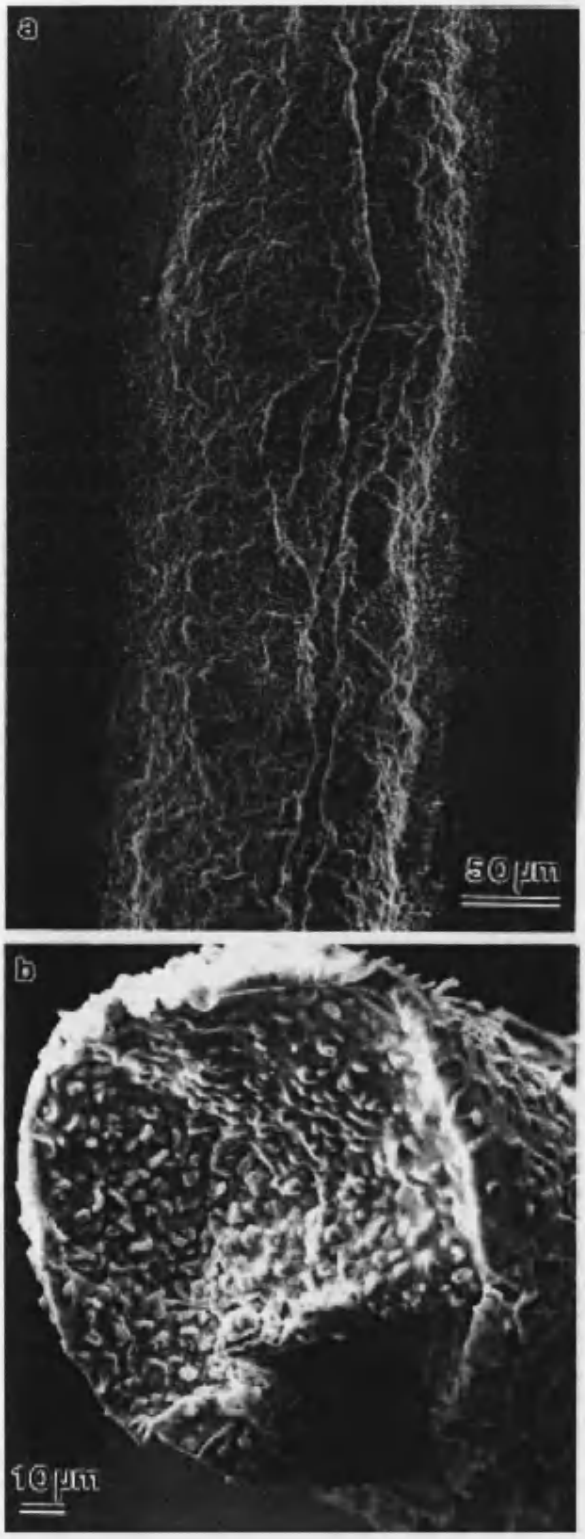

Figure 9. (a) SEM of the surface of a bacterial thread mineralized in situ with CdS. (b) Higher magnification image of the tip of a composite fiber.

the fiber axis. The characteristic texture of the underlying bacterial thread was visible between some of the mineral plates. X-ray analysis indicated the presence of Ti and P (data not shown). Lattice spacings obtained by XRD of the composite fiber were the same as those

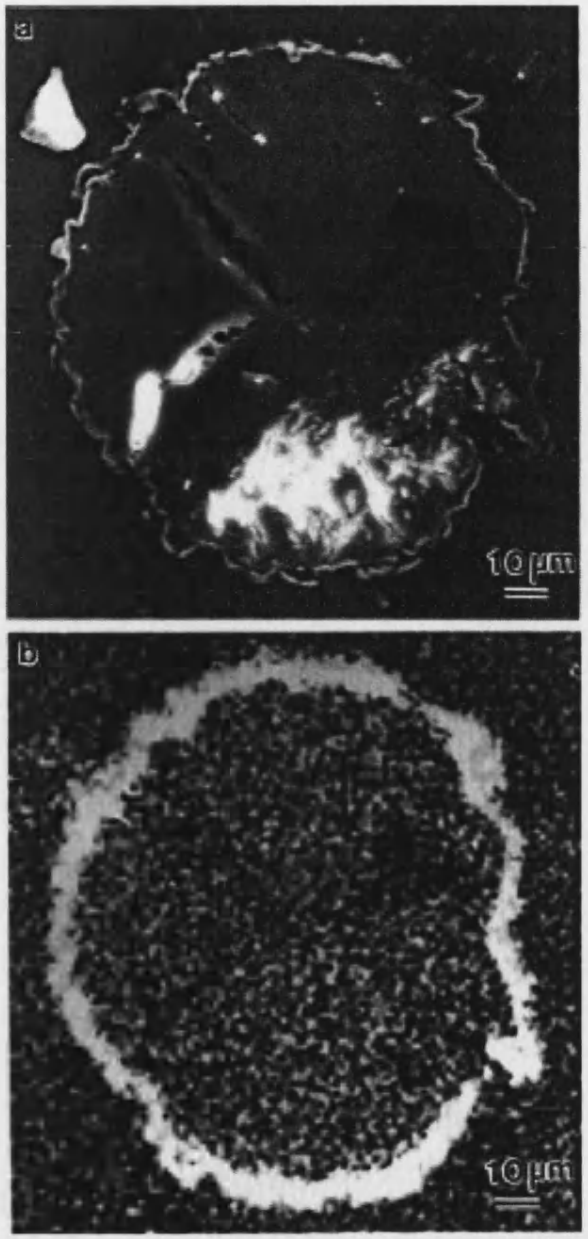

Figure 10. (a) SEM image of an in situ mineralized bacterial–CdS composite fiber viewed in cross section. (b) Corresponding elemental distribution map for S.

obtained from the TiO_2 colloid ($d = 0.350$ nm, 0.304 nm, 0.238 nm, 0.190 nm, 0.168 nm, 0.148 nm). The mineral phase was therefore identified as being predominantly anatase.

The distinct surface coating was clearly discernible by SEM examination of a sample in cross section (Figure 13). When compared with the corresponding elemental distribution map for titanium, it was clear that the mineral phase was present only at the surface of the macroscopic thread. No infiltration into the center of the thread was observed. The thickness of the surface coating was estimated as 0.5–5 μm. TEM studies of different regions of transverse thin sections of the fiber indicated a densely consolidated surface coat (Figure 14) and negligible infiltration of TiO_2 between the coaligned bacterial filaments.

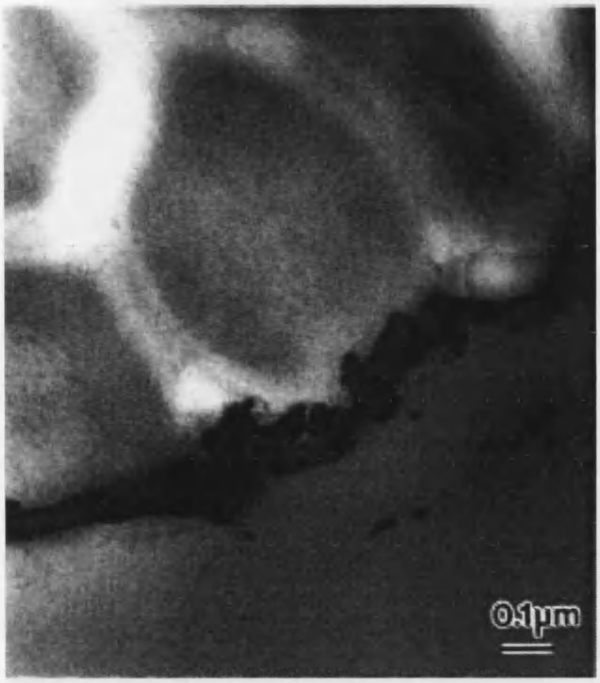

Figure 11. TEM image of the outer edge of a bacterial–CdS composite fiber mineralized in situ. The mineral phase forms a distinct surface coating.

Discussion

The technique of utilizing organic templates for the fabrication of fibrous hybrids is currently being explored in a number of systems. Often, preformed static templates are surface-coated to produce biomimetic composite materials; for example, composite magnetite–textile polyester fibers[23] and magnetic spider silk threads[24] have been prepared by absorbing magnetite particles onto the surface of the (bio)polymers. Similarly, hollow ceramic cylinders have been fabricated by calcining silica-[25] or aluminum hydroxide-coated[26] phospholipid tubules.

In contrast, the work described here illustrates that organized organic superstructures with reversible swelling properties can be exploited in the preparation of mineral-infiltrated fibrous composites, provided that the surface charge of the inorganic phase is appropriately tailored. The bacterial filaments are negatively charged due to the predominance of carboxylate groups on the cell membrane. Thus, colloids with a net positive surface charge, such as TiO_2, tend to deposit only on the external surface of the macroscopic bacterial thread, to give uniform coatings, whereas a negatively charged colloid, such as magnetite or silica,[17] penetrates into the interior of the thread to produce an organized inorganic phase that is patterned within the interspaces between the multicellular filaments. Presumably in this case, repulsive forces between the nanoparticles and cell membranes give rise to good infiltration and swelling when the superstructure comes into contact with sol. The extent of infiltration of the CdS nanoparticles was less than that observed for the magnetite colloid but greater than for the TiO_2 system, which is consistent with the presence of uncharged polar hydroxylated ligands on the surface of the CdS nanocrystals.

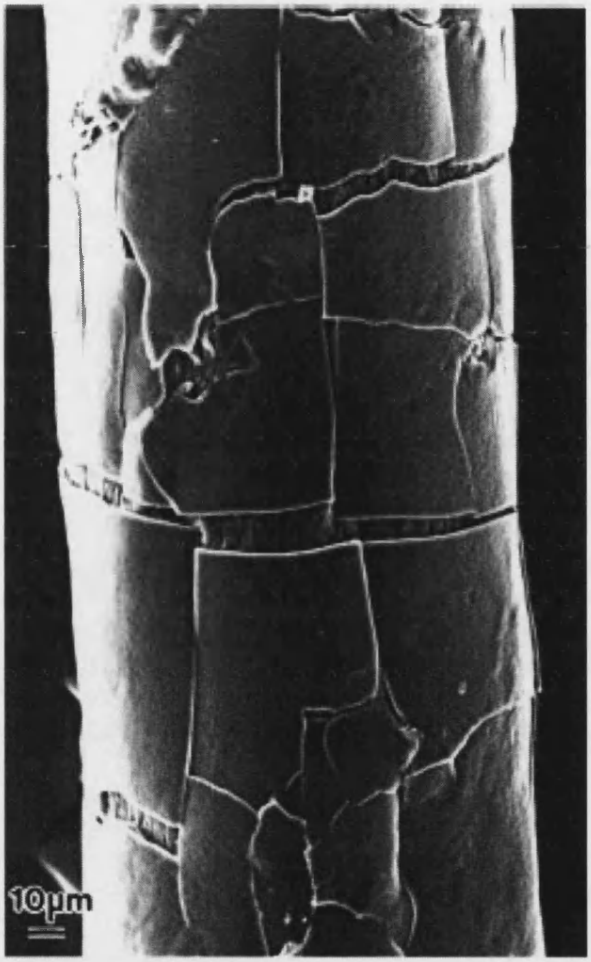

Figure 12. SEM image of the surface of a bacterial–titania composite fiber.

When the bacterial thread is redrawn from the sol, particles become trapped between or adhere to the multicellular filaments such that they are retained and consolidated within the interfilament spaces on drying. The idealized structure would therefore consist of a well-ordered, close-packed array of uniform diameter bacterial filaments that are separated by an interpenetrating, continuous inorganic phase of uniform thickness. In reality, only small areas within the composite have such an idealized structure, because the superstructure is disordered to some extent by the hydration and air-drying process.[12] This is manifested as a lowering in packing density of the bacterial component and a corresponding reduction in the long-range periodicity. Furthermore, the formation of a continuous wall structure requires particle–particle aggregation and fusion into an extended network; although this was observed for amorphous silica nanoparticles,[17] the crystalline magnetite domains remain only loosely associated such that calcination of the composite did not produce a stable porous inorganic replica of the bacterial superstructure.

(23) Forder, C.; Armes, S. P.; Simpson, A. W.; Maggiore, C.; Hawley, M. *J. Mater. Chem.* **1993**, *3*, 563.
(24) Mayes, E. M.; Vollrath, F.; Mann, S. *Adv. Mater.* **1998**, *10*, 801.
(25) Baral, S.; Schoen, P. *Chem. Mater.* **1993**, *5*, 145.
(26) Chappell, J. S.; Yager, P. *J. Mater. Sci. Lett.* **1992**, *11*, 633.

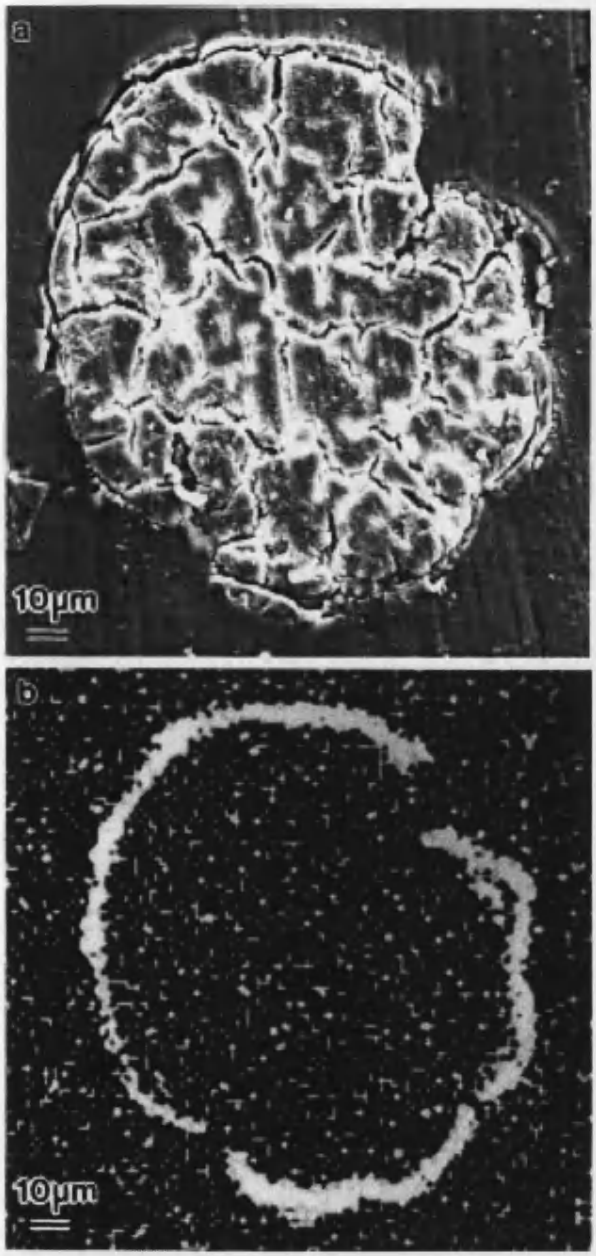

Figure 13. (a) SEM of a bacterial–titania composite embedded in resin and cut perpendicular to the fiber axis. (b) Corresponding Ti distribution map.

In situ deposition of CdS nanoparticles within the bacterial superstructure produced an uneven surface coat with negligible penetration of the thread interior. Swelling of the dry thread in a $CdCl_2$ solution gives rise to partial separation of the multicellular filaments along with strong Cd(II) binding to the highly charged groups present in the bacterial cell wall, which are known to sequester many different metals.[14] To some extent, these interactions disrupt the superstructure, as shown by changes in the surface texture of the threads after air-drying. Subsequent reaction with H_2S gas is diffusion-limited because of the preferential formation of a crust of CdS particles at or near the external surface of the bacterial thread. Although, there is only partial transformation to CdS near the center of the fiber, it should be possible in future experiments to control the diffusion processes to produce fully mineralized CdS–bacterial composites by in situ precipitation.

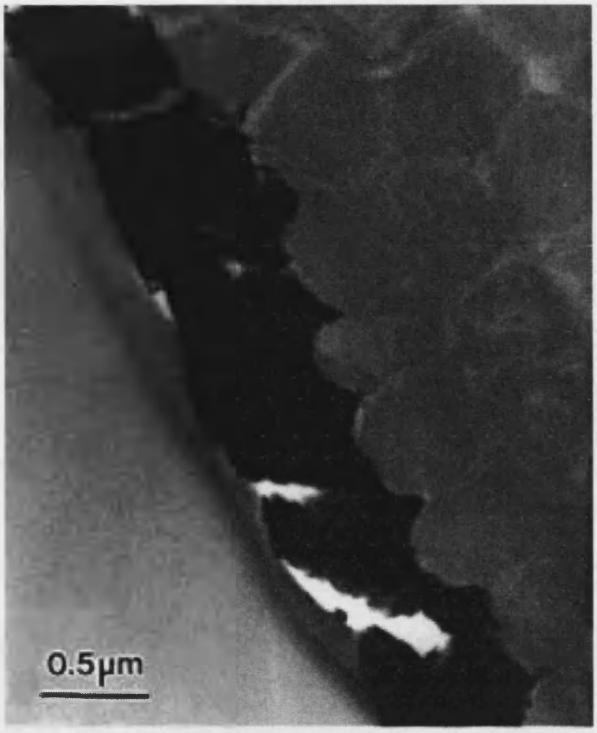

Figure 14. TEM image of a transverse thin section of a bacterial–titania composite fiber showing a uniform consolidated mineral coating at the fiber surface.

Conclusions

The results presented in this paper indicate that bacterial superstructures with reversible swelling properties can be used as 3-D templates for the fabrication of ordered inorganic–organic fibrous composites containing nanoparticles with magnetic (Fe_3O_4) or semiconducting (CdS) properties. Further studies are in progress to establish the optimum conditions for mineral infiltration with different types of inorganic nanoparticles. In the long term, we aim to integrate biotechnological and materials chemistry processes for the fabrication of a wide range of hybrid materials exhibiting patterned microstructures and morphological complexity.

Acknowledgment. We thank BNFL (S.A.D and E.L.M), Leverhulme Trust (S.A.D), EPSRC (H.M.P), the Arizona Agricultural Experimental Station Hatch (N.H.M), and the University of Bath (G.F) for financial support. We also thank K. K. W. Wong for assistance with TEM studies of CdS systems, T. Douglas for help with web cultures and magnetite preparations, and D.J. Riley for helpful discussions.

CM9802853

APPLIED PHYSICS LETTERS VOLUME 73, NUMBER 12 21 SEPTEMBER 1998

Ordering nanometer-scale magnets using bacterial thread templates

M. Field, C. J. Smith, and D. D. Awschalom[a)]
Department of Physics, University of California, Santa Barbara, California 93106

N. H. Mendelson
Department of Molecular and Cellular Biology, University of Arizona, Tucson Arizona 85721

E. L. Mayes, S. A. Davis, and S. Mann
School of Chemistry, University of Bath, Bath BA2 7AY, United Kingdom

(Received 1 May 1998; accepted for publication 23 July 1998)

Nanometer-scale ferromagnetic particles (Fe_2O_3, Fe_3O_4) are dispersed within a mutant bacterial chain which is drawn into a macroscopic fiber "rope." Cross-sectional scanning electron microscopy images reveal that the iron oxide particles are intercalated between the walls of the bacterial cells which are bundled into parallel threads. The field-dependent switching is seen to markedly sharpen when the synthesis is conducted within an applied magnetic field. © *1998 American Institute of Physics.* [S0003-6951(98)03338-5]

An ordered magnetic microstructure may be fabricated by either a "top down" approach by depositing bulk material and using standard lithographic techniques or a "bottom up" approach by assembling nanometer-scale ferromagnets created by chemical synthesis. The first method allows direct spatial control and can produce individual magnets as small as 10–100 nm using electron beam lithography[1] or local deposition with a scanning tunneling microscope.[2] The second approach includes magnetic clusters and implanted ion species[3] over which there is little spatial control beyond direct masking, but can produce structures of smaller dimensions. An alternative strategy is to use biological self-assembly techniques, such as that used by magnetotactic bacteria to create inorganic magnets within a living cell.[4–6] Other biological systems are able to produce complex inorganic structures through biomineralization,[5,7] which might be directed to create artificial magnetic structures. Here an ordered bacterial structure is used as a template for nanometer scale iron oxide particles, and subsequently characterized by scanning electron microscopy (SEM) and magnetometry. Moreover, conducting the synthesis within an applied magnetic field produces macroscopic bacterial fibers with clear magnetic anisotropy.

The bacterium used to create the skeleton for templating is the mutant FJ7 strain of *bacillus subtilis*. A single *bacillus subtilis* bacterium is a rod shaped organism, with cells of approximately 0.7 μm in diameter and up to 4 μm in length.[8] The mutant strain exhibits suppressed cell separation where the cell reproduces by elongation at a constant diameter but, after the cell wall grows inward to create a septum in the middle of the cell length, no separation occurs and the cells remain linked. Repeated cell division thus leads to long multicellular filaments which can contain thousands of cells linked end on end with a common cell wall down the length of the strand.[9] The bacteria is cultured to produce many filaments that are intertwined forming a web on the surface of the culture medium.[10] Dipping a small wire hook into the medium and withdrawing it slowly brings out many strands of cells, where the surface tension at the fluid/air interface compresses the filaments into a thread with parallel strands. The fiber can be drawn from the culture medium at rates of up to 22 mm/min,[11] and on drying in air for several hours forms a brittle solid. A drawn bacterial thread is typically on the order of 100 μm in diameter and can be several tens of centimeters long, having aspect ratios $>10^4$:1. A thread contains $\sim 10^{10}$ cells within $\sim 10^4$ filaments arranged as a hierarchy of cylinders: cells attached end to end forming filaments which are in turn close packed composing the thread.[10,12] Figures 1(a) and 1(b) shows two SEMs of a cleaved bacterial thread with a magnified cross-sectional im-

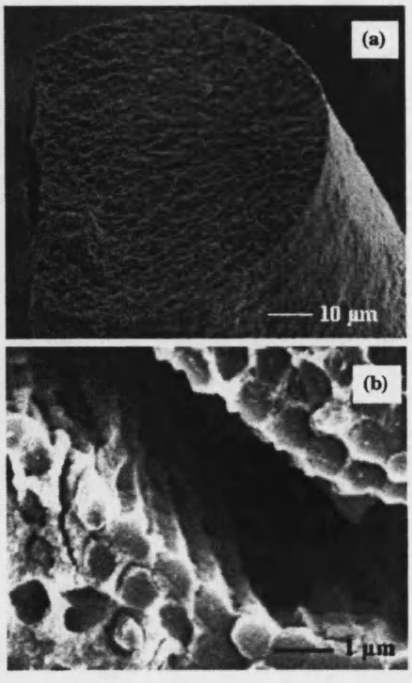

FIG. 1. Scanning electron micrographs of a cleaved bacterial thread showing (a) end facet and (b) internal cell structure.

[a)]Electronic mail: awsch@lotemp.physics.ucsb.edu

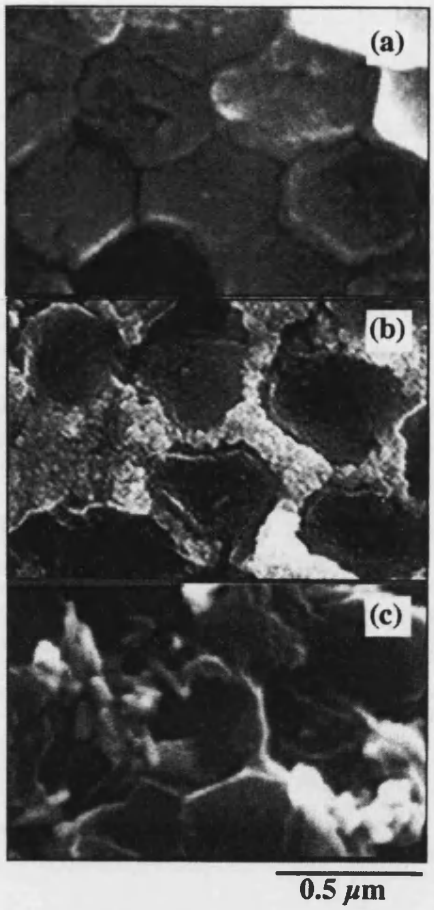

FIG. 2. SEM cross-sectional images of an assembled bacterial thread (a) before dipping, (b) dipped in the Fe_3O_4 ferrofluid and dried in zero field, (c) dipped in the γ-Fe_2O_3 ferrofluid and dried in zero field.

age shown in Fig. 2(a). Dipping a dried bacterial thread into a fluid rehydrates the sample and allows the cell strands to loosen. Any inorganic particles present in the liquid, such as the magnetic particles in a ferrofluid, are drawn between the cell walls by van der Waals forces and become incorporated in the structure upon drying. Two types of nanometer scale iron oxide particles were introduced into bacterial threads by dipping, small spherical magnetite (Fe_3O_4) particles and larger maghaemite (γ-Fe_2O_3) needle shaped particles.

An aqueous colloidal suspension of Fe_3O_4 particles is prepared in air from an alkali solution of $FeCl_3.6H_2O$ and $Fe(NH_4)_2(SO_4)_2$ salts.[13] Transmission electron microscopy images show these particles to be approximately spherical, and measurements of 100 sampled particles reveal a symmetric size distribution with a mean particle diameter of 9.4 ± 2.4 nm. Using the magnetization of bulk magnetite the mean magnetic moment of a single particle is estimated to be 2.05×10^{-16} emu. These particles are small enough to be superparamagnetic at room temperature, with an estimated blocking temperature, T_B, of 14 K calculated using the bulk value of magnetocrystalline anisotropy. The γ-Fe_2O_3 particles are commercially available in powder form, and were dispersed in distilled water using a detergent and ultrasound.[14] Each particle is needle shaped with an average length of 350 nm and width of 60 nm (acicularity ratio of 6:1). Due to their size and geometry, these particles are single domain with an estimated mean magnetic moment of 4.35×10^{-13} emu using the magnetization of bulk maghaemite.

Bacterial threads are dipped in one of the two colloidal solutions for 60 s and allowed to dry in air, with a further undipped control sample kept for comparison. The intercalation is performed in either zero field or a 4000 G field applied along the long axis of the thread. The energy difference between the easy and hard axes of a γ-Fe_2O_3 particle in a field of 4000 G is several orders of magnitude greater than the thermal energy even at the elevated temperature ($T = 325$ K) within the electromagnet used to apply the field. Hence the γ-Fe_2O_3 particles will align their easy axes parallel to the applied field; however the magnetic field will not affect the nominally spherical Fe_3O_4 particles, as the superparamagnetic moment can orientate itself freely in space without producing a torque on the particle. Figure 2 shows three SEM micrographs of cleaved bacterial threads dried in zero field, including: (a) an assembled bacterial thread before dipping, indicating the characteristic hexagonal close packing of the cells, (b) a thread dipped in the Fe_3O_4 ferrofluid, the gray material between the cell walls composed of Fe_3O_4 magnetic particles, and (c) a thread dipped in the γ-Fe_2O_3 ferrofluid where the individual particles are visible.

The magnetic properties of sections of magnetic bacterial thread approximately 1 mm in length are measured in a rf superconducting quantum interference device (SQUID) magnetometer. The temperature dependence of the magnetic moment of both magnetic samples is measured in a 50 G applied field after a zero field cool from 400 to 5 K. The Fe_3O_4 doped sample showed a peak moment at a temperature of $T_B \sim 175$ K corresponding to the blocking temperature of an assembly of superparamagnetic particles. In contrast, the γ-Fe_2O_3 sample displayed no change in magnetic moment as a function of temperature as expected for noninteracting single domain particles below T_B. Magnetic studies of the Fe_3O_4 sample are reported elsewhere,[15] together with a measurement of the particle density (1.3×10^{17} particles/cm^3) and a moment per particle of 1.98×10^{-16} emu, compared to 2.05×10^{-16} emu estimated from fitting the paramagnetic response above T_B. The measured blocking temperature is an order of magnitude greater than the estimate obtained using the bulk value of magnetocrystalline anisotropy (14 K), which may be due to dipolar interactions between nearest neighbors. The SEM images confirm that the particles lie only in the volume between the cell walls, in which case the particle density estimate suggests the particles are almost close packed.

The angle-dependent magnetization was measured for each sample at 5 K as a function of field. The host bacterial thread was not measurably magnetic, the moment being below the background level of the sample holder ($\sim 10^{-8}$ emu/G). In contrast, both the Fe_3O_4 and γ-Fe_2O_3 magnetic bacterial threads have a saturation magnetization of ~ 25 emu/cm^3 at 2000 G and display a field dependent hysteresis which changes as a function of angle between the applied field and the thread orientation. The concentration of magnetic particles can be estimated by dividing the saturation magnetization by the moment per particle, giving a den-

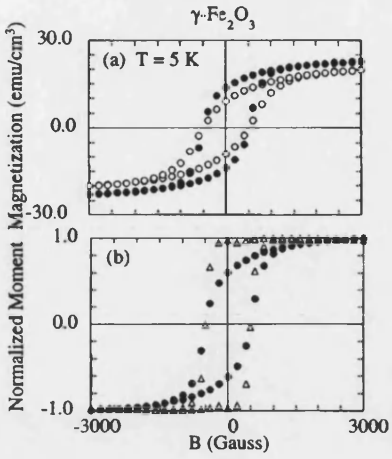

FIG. 3. Results for the γ-Fe_2O_3 thread measured at $T=5$ K: (a) magnetization vs applied field measured parallel (open circles) and perpendicular (closed circles) to the thread axis, (b) normalized moment vs applied field measured parallel to the thread for field dried (open triangles) and zero field dried (closed circles).

sity of 1.3×10^{17} cm^{-3} for the Fe_3O_4 bacterial thread, agreeing with the value obtained by fitting the paramagnetic response above T_B,[15] and a density of 5.1×10^{13} cm^{-3} for the γ-Fe_2O_3 sample. Despite the different concentrations the magnetic volume fraction of 5% is approximately the same in each case. The sample shape, approximately a cylinder of acicularity ratio 12:1 with a demagnetizing factor of 0.2,[16] accounts for some of the observed angle dependency of the hysteresis shape in each sample. In the Fe_3O_4 sample the anisotropy is larger below T_B compared with that above (not shown),[15] which can be accounted for by the sample shape. This suggests that the distribution of easy axes is not random and there is a preferential orientation along the thread. Compressional stress created during the drawing of the thread may cause the distribution of easy axes to be peaked along the thread; alternatively, in the case of the γ-Fe_2O_3 particles their shape may cause partial alignment on drying a thread. The distribution of easy axes within the thread can be studied by observing the sample's remanent field. A randomly oriented set of independent single domain Stoner–Wohlfarth magnets has a remanence of exactly half the saturation magnetization.[16,17] At zero field the moment of each particle lies along its easy axis and the remanence is computed from the average value of $\cos(\theta)$, where θ is the angle between the easy axis and the direction in which the total moment is measured. For a random distribution $\langle\cos(\theta)\rangle=0.5$, and the measured remanence should give a direct measure of $\langle\cos(\theta)\rangle$, the mean angular distribution of easy axes. This value is independent of the exact value of the shape dependent demagnetizing factor since the measurement is performed in zero field.

The normalized remanence of the Fe_3O_4 sample dried in zero field shows a maximum of 0.313 with the field orientated parallel to the thread and a minimum of 0.256 with the field perpendicular to the thread.[15] The difference in these two values is attributable to a nonrandom distribution of easy axes, but are both clearly less than 0.5. This suggests that the particles are weakly interacting within the thread, in agreement with the measured T_B. Repeating these measurements on Fe_3O_4 threads that have been dried in applied fields show no difference, since the drying is done above T_B.

Figure 3(a) shows the results for the γ-Fe_2O_3 sample dried in zero field. The sample displays a maximum normalized remanence of 0.603 with the field applied along the thread and a minimum of 0.453 in the perpendicular direction, which can be analyzed directly in terms of the independent particle model with a slight nonrandom distribution of easy axes. On drying in a 4000 G field along the length of the thread, Fig. 3(b) shows the maximum normalized remanence with the field applied in the same direction markedly increasing from 0.603 to 0.97. The distribution of the easy axes has become strongly maximized along the thread axis.

We have created a magnetic microstructure by using a bacterial thread as a superstructure to template magnetic particles, where cross-sectional SEM images show the magnetic particles embedded between the cell walls. Magnetization data demonstrate that the bacterial thread is anisotropic, an effect which is dramatically increased on drying the system in an external field to orientate the easy axes of single domain particles.

This work was supported by AFOSR Grant No. F49620-96-1-0018. N.H.M. One of the authors, N.H.M., was supported by Grant No. RR07912 from the National Center for Research resources, NIH.

[1] Y. D. Park, J. A. Caballero, A. Cabbibo, J. R. Childress, H. D. Hudspeth, T. J. Schultz, and F. Sharifi, J. Appl. Phys. **81**, 4717 (1997).
[2] D. D. Awschalom, D. P. DiVincenzo, and J. F. Smyth, Science **258**, 414 (1992).
[3] J. Shi, S. Gider, K. L. Babcock, and D. D. Awschalom, Science **271**, 937 (1996).
[4] R. Blakemore, Science **190**, 377 (1975).
[5] *Magnetite Biominerialization and Magnetoreception in Organisms*, edited by J. L. Kirschvink, D. S. Jones, and B. J. MacFadden (Plenum, New York, 1985), Vol. 5.
[6] B. M. Moskowitz, R. B. Frankel, P. J. Flanders, R. P. Blakemore, and B. B. Schwartz, J. Magn. Magn. Mater. **73**, 273 (1988).
[7] S. Mann and G. A. Ozin, Nature (London) **382**, 313 (1996).
[8] N. H. Mendelson, Science **258**, 1633 (1992). The bacillus subtilis bacterium is Gram positive.
[9] N. H. Mendelson, in *Biomimetic Materials Chemistry*, edited by S. Mann (VCH, Berlin, 1996), pp. 279–313.
[10] J. J. Thwaites and N. H. Mendelson, Proc. Natl. Acad. Sci. USA **82**, 2163 (1985).
[11] S. A. Davis, S. L. Burkett, N. H. Mendelson, and S. Mann, Nature (London) **385**, 420 (1997).
[12] N. H. Mendelson and J. J. Thwaites, J. Bacteriol. **171**, 1055 (1989).
[13] R. Massart, IEEE Trans. Magn. **17**, 1247 (1981).
[14] The particles are available from Kromachem Ltd., UK, as Pferrox 2228. The detergent used as a surfactant was the "Joy" brand marketed by Procter and Gamble. After sonification this mixture would remain in suspension for approximately 5 mins, which was sufficient time to dip a bacterial thread.
[15] C. J. Smith, M. Field, C. J. Coakley, D. D. Awschalom, N. H. Mendelson, E. L. Mayes, S. A. Davis, and S. Mann, IEEE Trans. Magn. **34**, 988 (1998).
[16] A. H. Morrish, *The Physical Principals of Magnetism* (Krieger, Malabar, FL, 1965).
[17] E. C. Stoner and E. P. Wohlfarth, Philos. Trans. R. Soc. London **240**, 599 (1948).

JOURNAL OF MATERIALS SCIENCE LETTERS 19 2000 1085–1088

Functional micro-concrete: The incorporation of zeolites and inorganic nano-particles into cement micro-structures

S. L. COLSTON, D. O'CONNOR, P. BARNES
Industrial Materials Group, Department of Crystallography, Birkbeck College, University of London, Malet Street, London WC1E 7HX, UK

E. L. MAYES, S. MANN
School of Chemistry, University of Bristol, Bristol BS8 1TS, UK

H. FREIMUTH, W. EHRFELD
IMM Institute of Microtechnology, GmbH, Carl-Zeiss-Strasse 18-20, D-55129 Mainz-Hechsteim, Germany

Recent advances in lithographic techniques have resulted in the creation of a variety of micro-structures with functions ranging from electromagnetic band-gap modification to micro-reactors [1, 2]. Previous work [3] by the authors has demonstrated the potential of cements as a new medium for micro-structures, indeed competing very favorably with previously used ceramic materials. Micron-scale resolution is achieved for micro-features in the plane of the molds, the replication being of the order of 100% of the mold dimensions, while in the vertical direction the replication is 90–100% depending on the height of the features. The mechanism by which the walls form smooth surfaces and intersections with sub-micron dimensions is essentially hydrate growth outwards from the initial cement grains towards the mold faces. The reproduction of micro-features in the early work was however not always found to be consistent, the greatest problem being a tendency for micro-features to crack and break free as a result of *shrinkage* or mechanical stressing during demolding. Therefore one of the aims of this more recent investigation has been to improve the replication and strength of the cement micro-structures by adjustment of several production parameters. A second aim has been to exploit cement as a binder of functional materials such as zeolites/catalysts and magnetic phases; it could be said that in this mode the functional material effectively replaces the aggregates of more commonplace mortars and concretes, but on a scale that is compatible with micron-sized features.

As stated, the first aim has been to realize a significant improvement in the quality of basic cement microstructures, as measured by a variety of characterization techniques including profilometry, scanning electron microscopy/X-ray fluorescence analysis, microhardness and synchrotron radiation tomographic energy-dispersive-diffraction imaging [4]. All microstructures reported here were formed in a PMMA mold and removed from the mold by heat treatment; the production parameters that have been varied in this investigation are:

- *Heating cycle:* To facilitate removal of the microstructure from the PMMA mold the heating cycle was extended to 15 °C/hour plus set 400 °C for 3 h. This procedure reduced the stresses on the composite structure and incidence of bulk fracture.
- *Water content:* Increases in the water content from 30 to 50% improved replication in the vertical dimension, although resulting air entrainment needed to be minimized.
- *Latex admixture:* Increasing amounts (20 to 40%) of latex in the dispersions were shown to promote growth of calcium hydroxide, rather than calcium silicate hydrate, over the micro-feature surfaces.
- *Organo-clay additives:* Inclusion of a range of synthetically prepared organo-magnesium silicate clays (containing alkyl, epoxy, methacrylate or polymethacrylate groups covalently linked to the inorganic clay layers) to the cement mix markedly improved the strength of the microstructures. Whether this improvement arises from the effects of dispersion, aggregation, slower hydration or other chemical changes is not known.

These variations were tested using PMMA molds designed for optoelectronic applications and produced by the LIGA process [1, 2] in which the micro-features generally consisted of channels and pits of widths 50–250 μm and vertical depths of 100–130 μm. The resulting micro-structures possess greatly improved strength (less brittle and easy to handle), dimensional replications of 100% in both the vertical and horizontal directions and with smooth calcium hydroxide-rich surfaces on the micro-features. Fig. 1 illustrates some examples with excellent feature replication and indeed these are among the best achieved for any ceramic material to date.

The second aim, of incorporating additional phases within the micro-structure, has now been extensively explored with a range of passive (spheriglass) and functional (zeolites, magnetic and protein nano-particles) materials. Mostly these materials mix easily with the cement though it is necessary in some cases to alter the water content where the added material has a high water uptake and which would otherwise reduce the flow of the mix into the mold; the details are given in

0261–8028

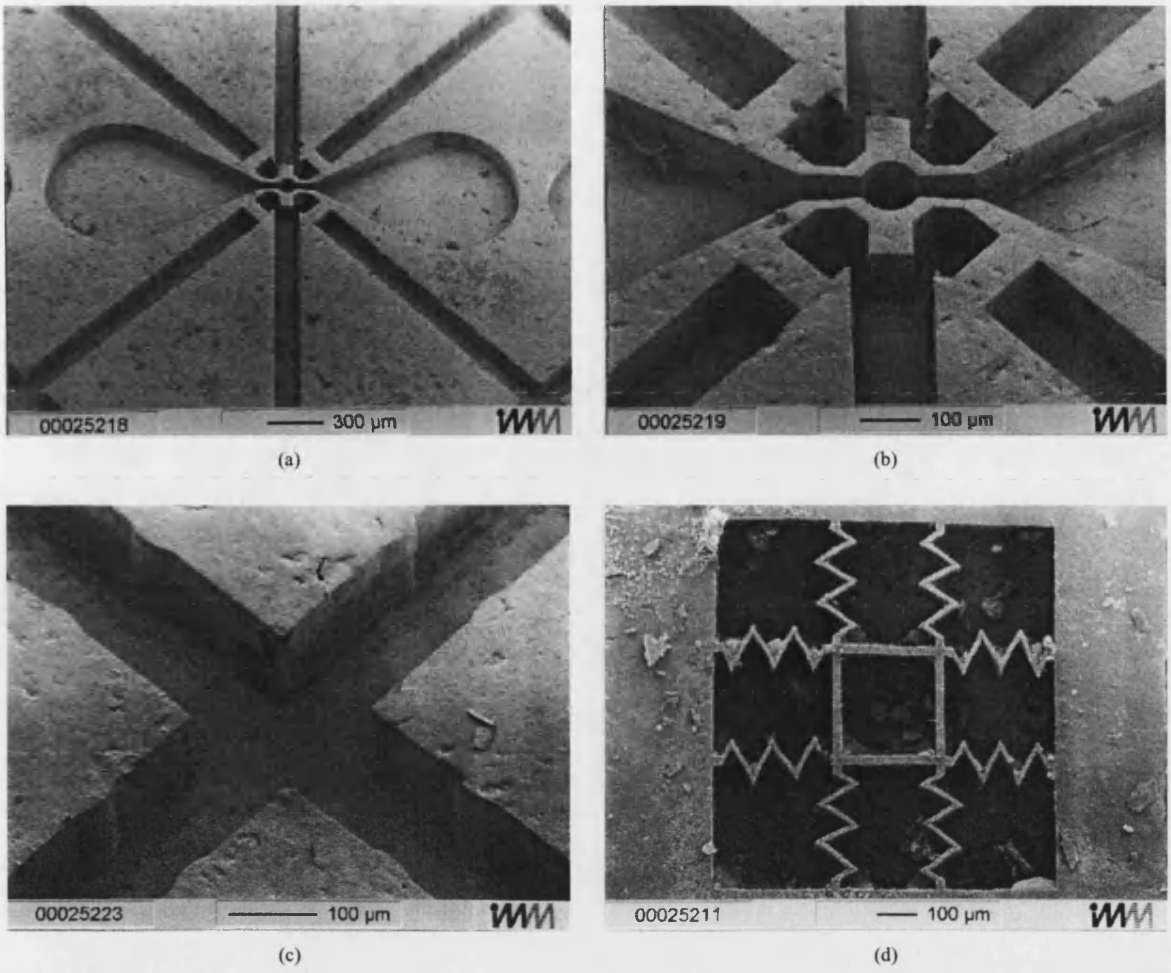

Figure 1 SEM micrographs of micro-structures made from synthetic organo-clay/latex/cement mixes. (a), (b) and (c) show, at different magnifications, the reproduction of micro-features obtained from a mold design for an optical coupler; in the case of (c) excellent replication is evident for the 8 designed humps protruding out from the channel wall sides by about 5 μm; (d) gives an example of a thin-walled (12–13 μm) spring-like structure.

Table I. The inclusion of spheriglass in this list was as a visible marker to demonstrate the effectiveness of the water and latex to "carry" materials into the mold features. However the obvious outstanding interest in this project was to see whether *functional* phases might be chaperoned by the cement medium into the micro-features.

The first kind of functional material considered was that of zeolites which are now widely used in industry for processes such as dehydration of gases, molecular separation within liquids and gases, catalytic breakdown of long-chain (petro-chemical) hydrocarbons and detoxification. The two natural zeolites used, mordenite and clinoptilolite, have a variety of applications such as

TABLE I Details of the various materials blended with Portland cement to form composite micro-structures

Material	Form	Particle size	Typical level of addition (by weight)
Ordinary Portland cement (OPC)	Powder	10–100 μm range, 20 μm average	
Styrene-butadiene latex	Liquid emulsion	0.2 μm average	20% solid polymer
Organo-clays	Slurry	1–50 μm	2–5% clay
Mordenite (zeolite)	Powder	<75 μm	20, 50, 80%
Zeolite 3A (K-exchanged)	Powder	0.5–5 μm	90%
Clinoptilolite (zeolite)	Powder	1–10 μm	80%
Spheriglass	Powder of hollow spheres	3.5–5 μm	10%
Magnetite	Colloidal	~10 μm	3 ml
Ferritin	Native horse spleen (Sigma 10.2 mg/ml)	~12 μm	3 ml

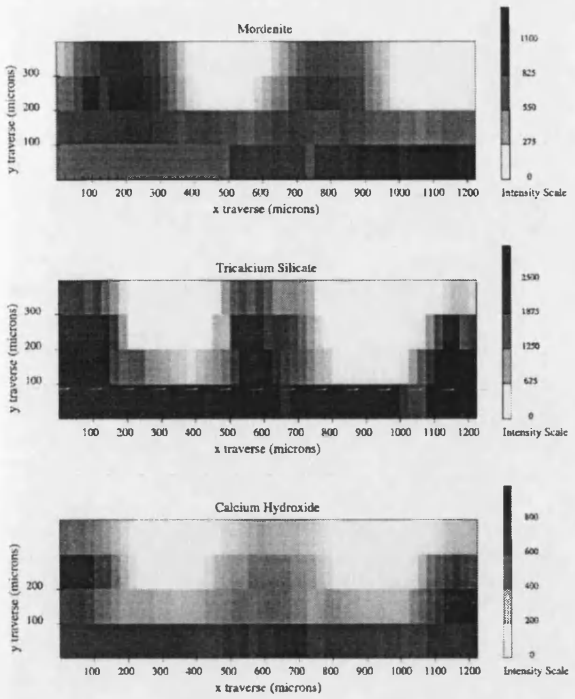

Figure 2 Two-dimensional composition maps across (perpendicular to) a series of parallel cement/zeolite/latex micro-channels, obtained using SR-TEDDI (synchrotron radiation—tomographic energy dispersive diffraction imaging). The tricalcium silicate and calcium hydroxide maps represent the locations of unhydrated and hydrated portland cement and, with the zeolite (mordenite) phase, form the micro-features which are seen to be compositionally homogenous at the TEDDI-pixel scale of 25 μm.

the adsorption and containment of heavy ions in detoxification by water filtration and nuclear waste treatment. Fig. 2 shows how the incorporation of one of these zeolites, mordenite, into a micro-structure can be characterized using a novel technique, SR-TEDDI [4] (synchrotron radiation—tomographic energy dispersive diffraction imaging). The micro-structure in question consisted of parallel sided micro-channels/walls, 100 μm high by 100 μm wide, which are faithfully reproduced by the zeolite/cement composite. The SR-TEDDI technique yields compositional maps based on energy-dispersive diffraction patterns, and was configured in this study to yield cement/mordenite 2-dimensional maps perpendicular to (across) the channel/wall direction. Three phases are shown in Fig. 2, the tricalcium silicate and calcium hydroxide maps being representative of unhydrated and hydrated cement phases respectively [5] and which, together with the mordenite map, demonstrate two essential points: (i) that the mordenite structure is retained in spite of the calcium rich/alkali environment of the hydrating cement and the subsequent heat treatment; (ii) that a homogeneous distribution of mordenite is obtained within the micro-features and bulk/substrate. In practice the mordenite can be bound into these micro-features using quite low concentrations of Portland cement though the structure becomes noticeably brittle if less than about 20% cement is used. Also we note that the tricalcium silicate is largely absent from the channel features as expected since the smaller grains would enter these features and are more reactive than the larger grains.

The second kind of functional material considered was that of hydrophilic inorganic and bio-inorganic nano-particles. The first of this type of material was a hydrophilic magnetite colloid, which has been recently employed in inorganic-organic fiber composites [6, 7]. This colloid behaves as a super-paramagnet, meaning that it responds to a magnetic field but only retains a permanent moment at very low temperatures. The second of this type of material was a naturally occurring protein called ferritin that is involved in iron storage in many living organisms. This protein is a hollow sphere, 12 nm in diameter which encases an 8 nm diameter iron oxide core in the form of a hydrated ferric oxide. We note that the protein appears to remain intact during cement curing, indicating the possibility of incorporating other biologically interesting proteins. Both of these materials were readily incorporated into the cement microstructures; and we have been able to study these composite micro-structures using conventional SEM/microprobe analysis since the Fe-K_α fluorescence peak from the inorganic phases is sufficiently strong. Fig. 3 shows the SEM micrograph and associated Ca-, Si- and Fe-fluorescence maps from a cement/latex/ferritin microstructure. Although there is granularity within the cement fraction at the 5 μm scale, as evident from the Ca- and Si-maps (particularly in the case of the calcium hydroxide micro-crystallites), the iron particles are still found (Fig. 3d) to be evenly distributed over the surfaces of the micro-structures.

In conclusion we find that latex/cement mixes are capable of dispersing and carrying functional materials as micro- or nano-particles within the micro-features. In some applications the placement of these materials, such as zeolites, at the surfaces may well be critical if their physical property or functionality requires direct contact with a gas or liquid medium. A further

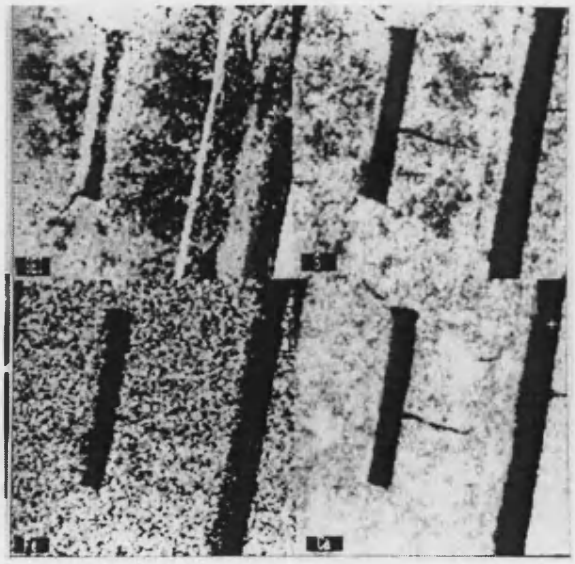

Figure 3 SEM micrograph and corresponding X-ray fluorescence maps (Ca, Si, and Fe as indicated) for a cement/latex/ferritin composite. The dark rectangular regions correspond to channels similar to those in Fig. 1. Although granularity is evident, particularly at the areas of strong Ca- and weak Si-signals which are indicative of calcium hydroxide crystallites, the Fe-containing particles are evenly distributed throughout the microstructural surfaces.

potential of these micro-structures, which has yet to be exploited, is that since cement is porous one could in principle "engineer" the porosity of the micro-features by deliberately altering the latex design or water content of the mix. One can then conceive of operations in which gas/liquid flow proceeds through the cement matrix pores to reach the zeolites contained in the interior. Similarly, one can envisage drug sensors that use immobilized proteins within a porous and microstructured matrix. Also, exploiting the magnetic properties of a magnetite composite cement, one could conceive of actuators with catalytic or filtration properties. This opens up a variety of "inorganic membrane" possibilities involving mixed length scales at the nanometre (zeolites, proteins), sub-micron (cement pores) and 10–100 micron (micro-features) levels. We believe that these prototype composites give promise for a variety of "next-generation" functional materials and microstructures suitable for filtration, catalysis, sensor and (electro)magnetic applications.

Acknowledgments

The authors wish to acknowledge the help given by the EPSRC for granting, the CLRC and ESRF for synchrotron beam-time, and the facilities of the Institute of Micro-mechanics. We thank Dr. Nicola Whilton for the synthesis and gift of the clay samples.

References

1. G. FEIERTAG, W. EHRFELD, H. FREIMUTH, G. KIRIAKIDIS, H. LEHR, T. PEDERSEN, M. SCHMIDT, C. SOUKOULIS and R. WEIEL, "Photonic Band Gap Materials, Vol. 63–69" (Kluwer Academic Publishers, Netherlands, 1996).
2. F. SCHLUTH, *Dechema Monographs* **132** (1996) 71.
3. S. L. COLSTON, P. BARNES, H. FREIMUTH, M. LACHER and W. EHRFELD, *J. Mater. Sci. Lett.* **15** (1996) 1660.
4. C. HALL, P. BARNES, J. K. COCKCROFT, S. L. COLSTON, D. HAUSERMANN, S. D. M. JACQUES, A. C. JUPE and M. KUNZ, *Nucl. Instrum. & Meth. in Phys. Res.* **B140** (1998) 253.
5. I. JAWED, J. SKALNY and J. F. YOUNG, in "Structure and Performance of Cements," edited by P. Barnes (Applied Science Publishers, London, 1983) p. 237.
6. M. FIELD, C. J. SMITH, D. D. AWSCHALOM, N. H. MENDELSON, E. L. MAYES, S. A. DAVIS and S. MANN, *Appl. Phys. Letters* **73** (1998) 1740.
7. E. L. MAYES, F. VOLLRATH and S. MANN, *Advanced Materials* **10** (1998) 801.

Received 14 May
and accepted 15 December 1999